AN EXERGETIC COMPARISON OF COPPER EXTRACTION FROM CHALCOPYRITE CONCENTRATES BY PYROMETALLURGY AND HYDROMETALLURGY

by

Paul Mather

A Dissertation

Submitted to the Faculty of Purdue University

In Partial Fulfillment of the Requirements for the degree of

Doctor of Philosophy

School of Materials Engineering

West Lafayette, Indiana

December 2020

THE PURDUE UNIVERSITY GRADUATE SCHOOL

STATEMENT OF COMMITTEE APPROVAL

Dr. Matthew J. M. Krane, Chair

School of Materials Engineering

Dr. Kenneth H. Sandhage

School of Aeronautics and Astronautics

Dr. Kevin P. Trumble

School of Materials Engineering

Dr. Neera Jain

School of Mechanical Engineering

Approved by:

Dr. David F. Bahr

Dedicated to my beautiful wife Madelyn

ACKNOWLEDGEMENTS

I owe more than I can say to my wife, parents, and friends. A large deal of gratitude is owed to the Freeport-McMoRan Inc. (our funding source) and the FMI Tucson Technology Center staff, namely Dr. Jodie Robertson and Tom Bolles, as well as the FMI Miami Smelter staff, namely David Jones, Brandon Steinborn, Avi Nanda, and Alex Piatkiewicz, for making this work possible. Finally, I can't say enough in gratitude to the Order of Preachers, namely the St. Tom's staff and Fr. Donald Bramble of the Western Province. *Laudare, benedicere, praedicare*!

TABLE OF CONTENTS

LIST OF TABLES

LIST OF FIGURES

ABSTRACT

Copper is an essential metal in today's economy, due to its superior electrical and thermal conductivities, alloying properties, and chemical uses. Most copper is produced *via* mining and refining, and most copper is found in the earth's crust as chalcopyrite, $CuFeS_2$. Typically, chalcopyrite is concentrated and fed to a high temperature pyrometallurgical process which produces >99.99% purity copper cathodes. Recently, Freeport-McMoRan Inc. has implemented a hydrometallurgical autoclave-leaching process that takes chalcopyrite concentrate and produces copper cathodes. It is imperative that these pyrometallurgical and hydrometallurgical processes be modeled and compared so that the extraction industry can best decide which technology to apply in the future. This work presents transient, reduced-order models for the comparison of the two processes using exergy balances. Exergy is typically thought of as the maximum work extractable from a system as it spontaneously reacts to the state of the surrounding environment; for extractive processes, it is also helpful to think of exergy as the minimum work required to effect a concentration, *e.g.* of copper. Exergy balances are thus similar to first law balances, but they comment on the location and magnitude of useful energy flows, instead of energy flows in general. For the baseline case, this work found that the pyrometallurgical process up to 99.5% copper anode stored 54% of the fed exergy in product, lost 20% of the fed exergy, and destroyed the remaining 26%. In contrast, the hydrometallurgical process up to 30 grams-per-liter copper pregnant-leach-solution stored 5% of the fed exergy in product, lost 9% of the fed exergy, and destroyed the remaining 86%. The effects of process variations are also looked at. It is recommended that this work be incorporated in whole-plant exergy balances to more precisely examine the tradeoffs between the pyrometallurgical and hydrometallurgical routes of copper extraction from chalcopyrite concentrates.

CHAPTER 1. INTRODUCTION

1.1 Overview of Copper Extraction

Copper has been an essential part of human culture since prehistory [1]. Now, it is primarily used for its electrical conductivity. The future can only expect to see demand for copper grow. There are several reasons for this, which include but are not limited to:

1. Increasing global industrialization
2. Increased popularity of electric vehicles
3. Antiviral and antibiotic properties of copper surfaces (ref)

Some examples of additional uses of copper are for alloys, artwork, and antifouling paints.

Despite the increasing demand of metallic copper worldwide, transient models of many of the copper extraction steps have not been published. Models that are transient, reduced-order, and computationally cheap have the potential to add much value to the copper production process, as well as be useful learning tools. This dissertation will present transient, reduced-order models for the main chemical reactors involved in the traditional pyrometallurgical extraction of copper from copper sulfide concentrate, as well as Freeport-McMoRan Inc.'s concentrate leach process (CLP), which extracts copper from copper sulfide concentrates hydrometallurgically.

Historically there two routes to producing 99.99% purity copper cathode from copper bearing ores. These are the high-temperature pyrometallurgical process (smelting, converting, fire refining and casting, electrolysis) and the low temperature hydrometallurgical process (leaching, solvent extraction, electrowinning). The type of process used depends on the ore type being processed, which are usually either sulfide or oxide ores. Leaching at ambient temperature is typically much cheaper than smelting; however, to-date there has been no economic low-temperature leaching process developed and industrially proven for chalcopyrite-based ores.

When oxides are leached, the copper readily dissolves. However, the thermodynamics of sulfide leaching at ambient temperature and pressure are such that a solid-sulfur shell will develop on the ore particles, preventing the leaching agents from reaching the core of unreacted mineral. This halt to the leaching process for sulfides typically occurs before copper extractions reach 30 % .

The autoclave leaching process for copper avoids this behavior by leaching in temperature and pressure conditions such that the sulfur converts to aqueous sulfate, thereby ensuring that the leaching solution always has access to fresh mineral surface. This thesis compares the pyrometallurgical route to copper extraction and FMI's concentrate leach process (fig. 1.1 and 1.2). Both the CLP and smelting require communition and flotation upstream, so the comparison will only look at processing steps subsequent to concentrate formation. The chief metric used to make the comparison in this work will be exergy. The industrial data for the pyrometallurgical processing steps was provided by Brandon Steinborn, Senior Supervisor of Converter Operations, at the FMI Miami, Arizona Smelter. Industrial data for the concentrate leach process was provided by Pranav Attavar, Metallurgist II, who is with the FMI Tucson Technology Center.

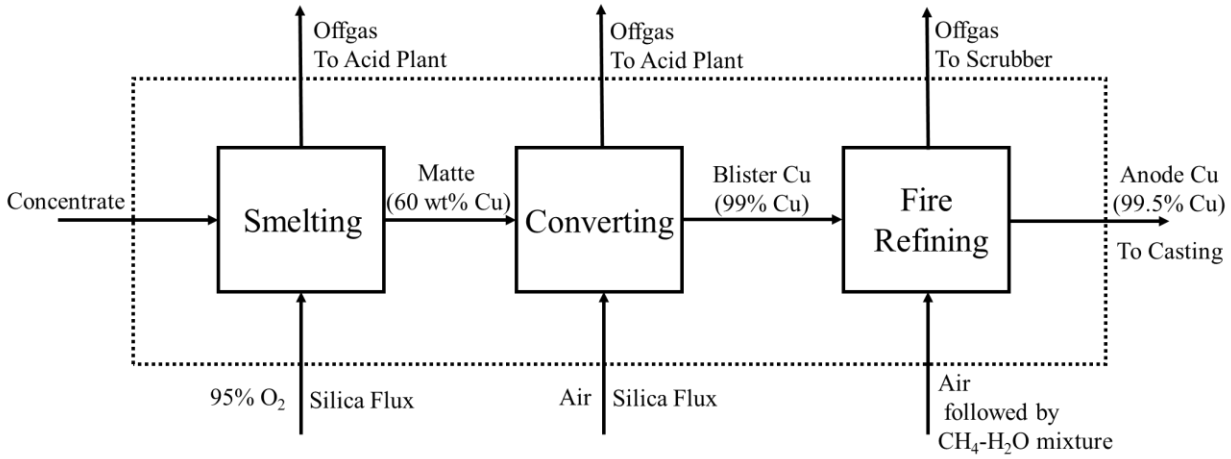

Figure 1.1 – Schematic of the pyrometallurgical process for copper extraction for copper sulfide concentrates. The three unit operations in the dashed box are modeled in this work

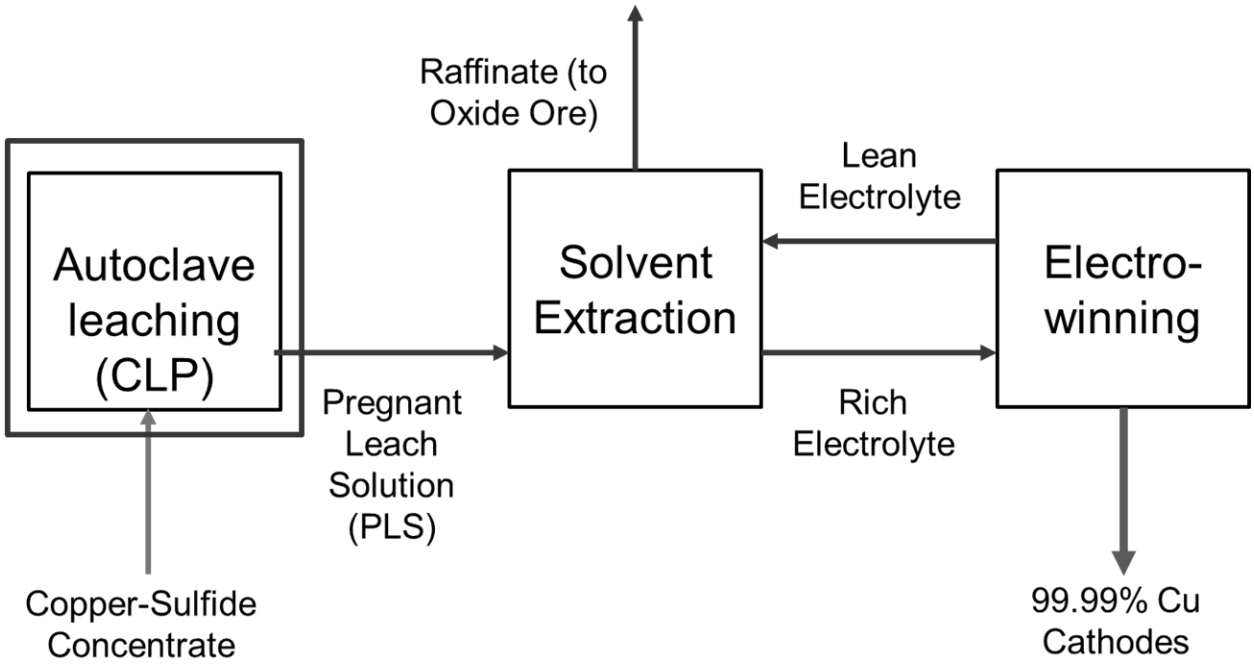

Figure 1.2 – Overview of the hydrometallurgical route to copper extraction from copper-sulfide ores. The current work models autoclave leaching.

1.2 Exergy — What It is and Why It is Useful

Exergy is the maximum amount of work an amount of heat or matter could do if it was allowed to react spontaneously with a reference environment until equilibrium was achieved [2]. This reference environment is also referred to as the dead-state. Shaft work or electricity can be used for any application requiring heat, but the converse is not true; therefore, the first two types of energy are more useful than the last. In this light, a first law analysis of a process accounts for the magnitude of the processes' energy flows, an exergy analysis accounts for their quality. Additionally, it describes the maximum potential for work recovery from each process stream.

Thinking of exergy as the maximum work which can be extracted from a process stream while it reacts spontaneously with its environment until they are in equilibrium is useful for evaluating processes such as power generation, but is not ideal for the purposes of metal extraction. There the goal is to take a material found in nature and make it chemically very different from the environment. Because exergy can be regarded as a measure of how different a process stream is from the dead state, its definition in extractive-metallurgical processes is more useful as the minimum work required to change material from the environmental condition to a purified state.

Obviously, a 99.99% pure copper ingot is significantly different (and has much higher economic value) than copper found chemically bound in very dilute ore. As such, the purer, free copper has much higher exergy. Fig. 1.3 shows the exergy value for copper at the end of each unit operation in a pyrometallurgical extraction route. The chart gives a qualitative sense of the change in minimum exergy cost for each part of copper extraction; as the change in copper concentration in the product stream between each operation decreases, less impurity is being separated from copper, so one would expect the exergetic cost of the steps to decrease with rising copper purity. On this basis, one would expect, for example, smelting to require more exergy than converting, and converting more than fire refining. These considerations become important when multiple unit operations in copper extraction are considered together.

There has been minimal published work on modeling the exergetic performance of the unit operations in copper extraction. This work attempts to partially fill this hole in the literature by doing exergy balances on the most chemically intense processes in the pyrometallurgical process and CLP for copper extraction.

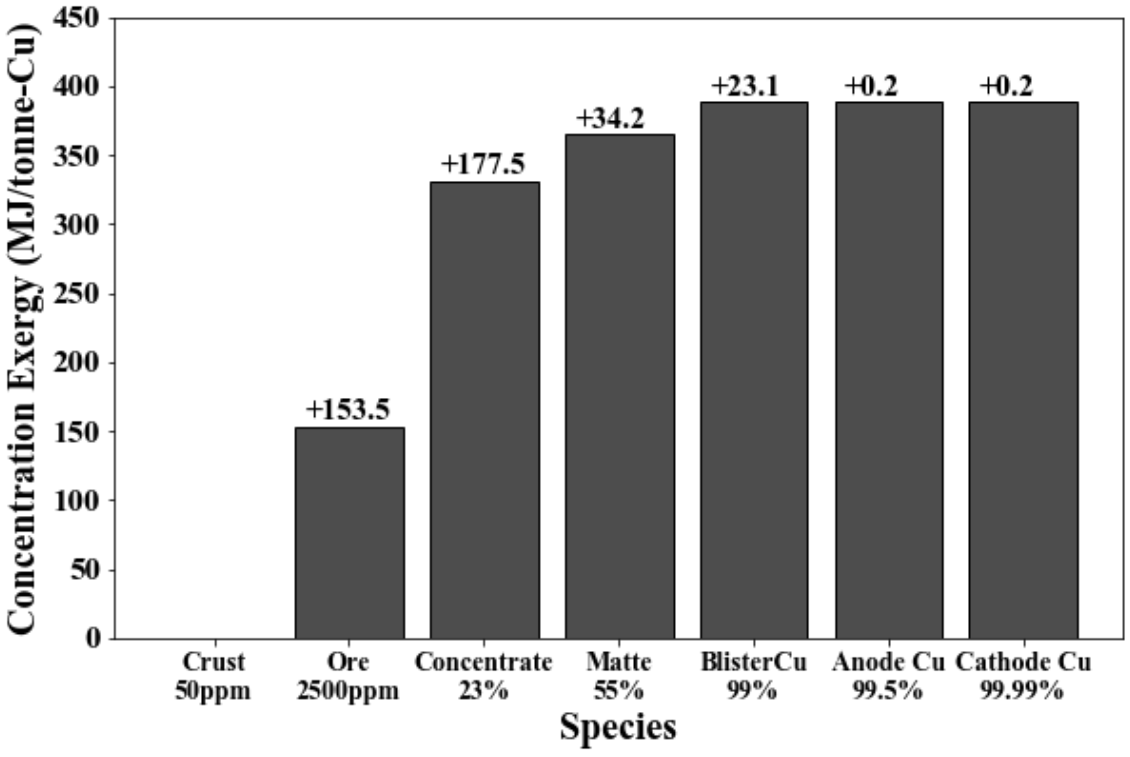

Figure 1.3 - Minimum work required, or concentration exergy, for each unit operation to pyrometallurgical extraction per tonne of copper in the copper bearing material

1.3 Bath Smelting

The first step in the pyrometallurgical route to copper after ore concentration is smelting. This step separates iron and sulfur from concentrates of Cu-Fe-S minerals by oxidation reactions into a copper sulphide and iron sulphide bearing matte, an iron bearing slag, and SO_2 rich offgas. The matte is sent to copper converters to remove the remaining iron and sulfur, the slag is landfilled, and the offgas is sent to a sulfuric acid plant. Both the matte and offgas are considered product streams; the reason the offgas is a product is that the sulfuric acid produced from is often essential to maintaining the economic viability of a smelter. As of 2011, IsaSMELT furnaces, which are bath furnaces, had an annual throughput of about 9.5 Mt [2]. Figure 1.4 shows a schematic of a bath smelting furnace. For more of an overview, Errington et al. have presented the history of copper IsaSMELTs along with some process flow diagrams[3], as well as an overview of process technology, minor element distribution data, and some improvements Cyprus Mining made to the Miami, Arizona smelter in the 1990's. [4]. The growth of the copper smelting industry worldwide warrants investigations into the energetic performance of smelters and has prompted creation of smelting models.

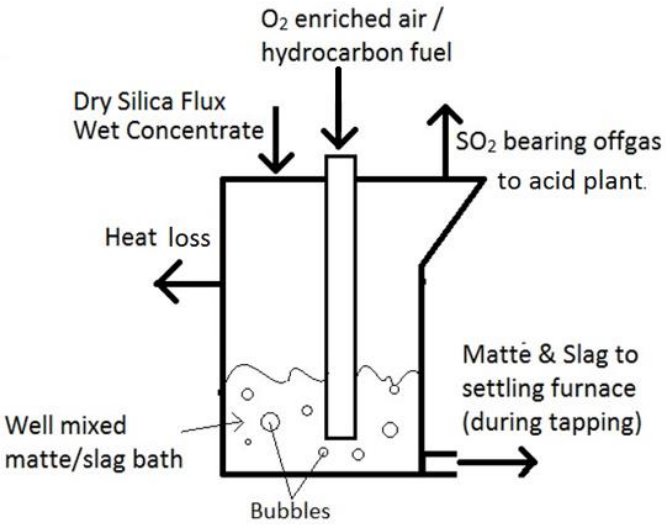

Figure 1.4 - Schematic of input and output streams of an IsaSMELT

Copper smelting has been the subject of numerous modeling efforts for several decades. The models most germane to this paper are those for IsaSMELT furnaces. Alvear et al. produced a mass-balance model to help show that IsaSMELTs can be used profitably [5]. Alvear et al. in a different work[6] provide minor element distribution data for IsaSMELT furnaces, which shows

that IsaSMELT furnaces may be especially good at managing Arsenic. One of the most thorough models of IsaSMELT furnaces is that of Nagamori et al. [3]. These authors made a chemical equilibrium based model of the furnace and used it to predict minor element distributions among the slag, matte, and offgas at a fixed temperature. In general for copper smelters, modeling that looks at constant temperature operation has been done several times [3,7–12]. These include further equilibrium based minor element distribution studies [7], equilibrium based major-element distributions[8,9], steady-state heat and mass balances used to estimate required smelter feed rates [10], heat transfer models [11], and plant-wide mass balance models which include a smelter [12]. However, it appears this paper is the first publicly published model of IsaSMELT furnaces that looks at unsteady melt temperature and phase compositions.

In addition to the mass and heat balance models done for IsaSMELTs, models of fluid dynamics have been used to simulate details of flow and heat and mass transfer for other smelting furnaces. Perhaps the best example of these is that of Sohn and coworkers [13–15], who developed a CFD model copper flash smelting in the early 1990's. They were able to estimate the two dimensional temperature profile of the gas and particle phases down the inlet shaft height, as well as make contours for oxygen and sulfur dioxide content over the shaft length and radius. They were also able to estimate the extent of minor element volatilization along the shaft length. Such flash furnace modeling was later augmented by Itagaki et al [16], who gave estimates for fractional conversion of sulfur along the shaft length, as well as the distribution of minor elements to the slag, matte, and gas phases as functions of oxygen enrichment of the blown gas. Although the modeling work is very well developed, such kinetic models are not directly applicable to IsaSMELTs because IsaSMELTs add the concentrate and air directly to the bath, which is so strongly agitated it can be considered perfectly mixed to a first approximation.

This modeling work differs from these others in its primary goals. These goals include the development of a simple and fast model to estimate the transient temperature and compositions of the matte, slag, and gas phases. To accomplish this goal, the model performs an equilibrium mass balance in the presence of material additions and removals from the furnace and an energy balance. Only the major elements of copper, iron, sulfur, oxygen, and silica are included. Another contribution of this work is its use of *exergy* to characterize the energetic performance of IsaSMELT furnaces.

Two works representing significant progress in modeling the energetic performance of copper smelters are those of Coursol et al. [17,18]. These papers give detailed plantwide and furnace specific energy balances, respectively—and of key interest to this work, fuel equivalents of electrical energy. One motivation for these types of conversions is that one Joule of electricity typically takes several times that amount of energy in the form of a fuel at a powerplant to produce. Using these conversions in an energy balance thus gives the balance a global character and a more precise measure of the value of its constituent energy flows. Coursol et al. showed that modern smelting plants (which include some equivalent of smelting, converting, and fire-refining) perform within 0.9 MJ fuel equivalent per tonne of produced anode copper of each other, flash smelting requiring approximately 10.7 MJ/tonne-Cu and bottom-blown smelting requiring 11.6 MJ/tonne [18].

The current study presents a transient, reduced order model of copper bath smelting, to be used in conjunction with reduced order models of the other copper extraction steps in future work. This study looks at a baseline case, from which operating parameters such injected gas oxygen grade and total air injection rate are varied in parametric studies. The effect of these variations on temperature, phase composition, and exergetic performance are examined. An exergy balance on the smelting process is included as well.

1.4 Peirce-Smith Converting of Copper Matte

Copper matte converting falls between smelting and fire-refining in the pyrometallurgical route to 99.99% pure copper cathode. Peirce-Smith converting, currently the most popular copper matte converting technology worldwide [19], has two steps. The first refines the matte to nearly pure Cu_2S, *i.e.* "white metal", and the second refines the white metal to 99% Cu purity ("blister copper"). The slag blow oxidizes the ferrous sulfide in the matte to sulfur dioxide gas and an iron bearing slag. The copper blow oxidizes the white metal to sulfur dioxide gas and liquid copper. Matte from smelting/slag-cleaning and a slag-forming flux is fed into the converting furnace via a ladle. Plant air, sometimes combined with industrial oxygen, is blown into the melt via tuyeres to provide the oxygen for reaction. The furnace can rotate to pour off formed slag as needed. Once blister copper is had, the melt is transferred via ladel to anode/fire-refining [20]. Hoboken converting is similar to Peirce-Smith converting, but instead of offgas being sucked out of the furnace mouth into a hood, a Hoboken converter removes offgas from the furnace through

ventilation in the furnace sidewall. For the purposes of the model presented in this work, Hoboken and Perice-Smith converting are indistinguishable. The products of converting are the produced white-metal and liquid copper, and the sulfur dioxide bearing offgas. The offgas is a product because it is used to produce economically valuable sulfuric acid.

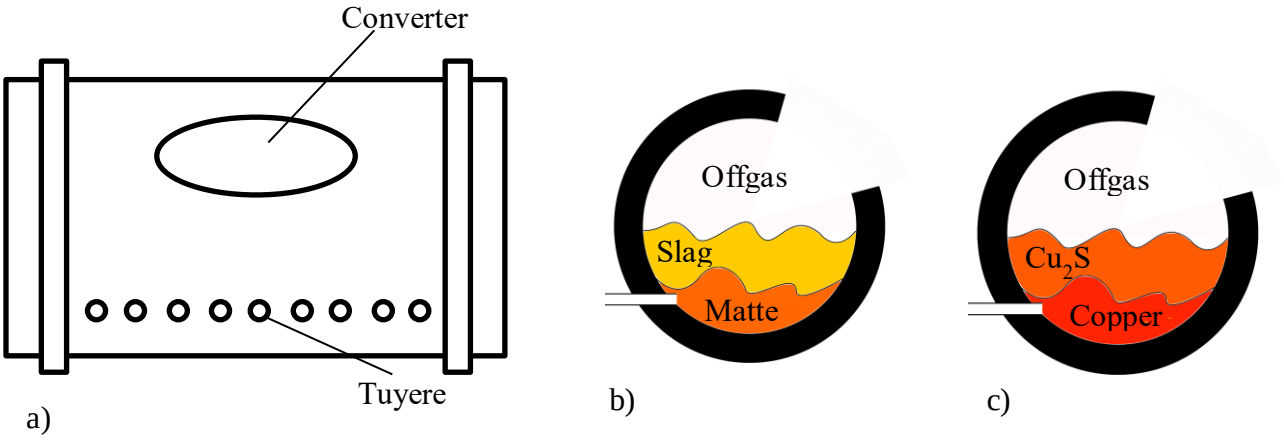

Figure 1.5 - Schematic of (a) a Peirce-Smith Converter and the (b) slag and (c) copper blows

Kyllo [21], and Kyllo and Richards [22,23] have produced transient models of copper converting, which give temperature and phase composition histories. The models include a large number of parameters for helping establish mass transfer rates between the matte, slag, and gas phases. These authors were able to show partial agreement between their models and industrial data. Their model contrasts with the work of Aminizadeh and Mansouri [24], who model the slag blow by assuming perfect mixing of the melt and that all of the FeS in the matte oxidizes to FeO only. These authors also include a simple radiation heat transfer model for estimating the rate of heat loss from the furnace. The model presented in the present paper contrasts with these others in that it assumes perfect mixing of all the phases, takes heat loss to be a constant, and estimates converter behavior based on equilibrium between the matte, slag, and gas phases. This last point is important, because a significant fraction of the oxygen added to a converter will go to magnetite and Cu_2O formation.

Models of copper matte converting equilibrium allow the transient phase compositions of a converter to be estimated. Many models of copper matte converting thermodynamics have been made. Perreti gave an early analysis of the thermodynamics of the copper converting process and

demonstrated that bottom blowing of converters is prone to lead to metallic copper solidifying in the tuyeres [25]. Eriksson and Bjorkman conducted quantitative equilibrium studies on the copper-matte, fayalitic-slag system that produced activity coefficients for copper matte smelting and the slag blow of converting [26]. Much recent work has been done on slag thermodynamics by Nikolic et al. [27–33], who have provided much liquidus and solubility data for slags containing both SiO_2 and CaO, which frequently occur in copper converting systems. This work will only consider slags comprised of SiO_2, FeO, Fe_3O_4, and Cu_2O, so the work of Eriksson and Bjorkman is perfectly suited to it. The more recent work provides grounds for expansion of the model presented here, should this be desired.

Many authors have also looked at minor element deportment in the converting process. Chaubal et al. [34] used computer simulations to look at the deportment of lead and estimated that between 50-90% of lead in the starting matte of converting reports to offgas when converting is done at 1300 ℃. Chaubal and Nagamori also used computer simulations to look at the deportment of arsenic and antimony [35] and were able to provide estimations of the fraction of arsenic and antimony removed from the matte on the basis of converting temperature and starting matte copper grade. Chaubal et al. [36] have also looked at minor element deportment in flash smelting and converting and were able to provide estimations for the percentage elimination of arsenic, antimony, lead, and bismuth to each phase in copper converting as functions of matte copper grade, converting temperature, and oxygen grade of injected oxygen gas.

The only work that looks at exergy in converting appears to be that of Pineda and Plascencia [37], who examined how changes to the exergy flows through converting might change converting SO_2 emissions. They concluded that increasing oxygen enrichment should increase the available exergy from converting reactions and reduce SO_2 emissions. It must be mentioned that Peirce-Smith and Hoboken converts have a practical O_2 grade limit of 26%, beyond which tuyere line corrosion is greatly accelerated. Additionally, as will be shown in this work, higher oxygen grades lead to greatly increased, likely harmful converting temperatures.

The current study presents a transient, reduced order model of a Peirce-Smith copper converting furnace only, to be used in conjunction with reduced order models of the other copper extraction steps in future work. This study looks at a baseline case, from which operating parameters such injected gas oxygen grade and oxygen efficiency are varied in parametric studies. The effect of these variations on temperature, phase composition, and exergetic performance are

examined. In particular, the amplitude of the temperature cycles, also called “thermal cycling,” will be of interest. This is because higher amplitudes of thermal cycles cause greater furnace refractory wear, decreasing converter campaign life. Although beyond the scope of the model presented here, minor element behavior is growing in importance for copper extraction, and it could be interesting to add minor element behavior to the model presented in this work.

1.5 Fire Refining

The pyrometallurgical route to 99.99 wt% copper cathode sheet, starting from concentrate, can be broken into: smelting, converting, fire/anode refining, anode casting, and electrolysis. Copper fire refining is a purification process that removes dissolved sulfur and oxygen from the molten “blister” copper produced by converting; this blister copper is approximately 99% wt. pure Cu, 0.5% wt. dissolved oxygen, about 450 ppm dissolved sulfur, and the balance is minor elements. The sulfur and oxygen must be removed to prevent their combination into sulfur dioxide gas during anode casting, which would ruin the anode quality by the formation of casting porosity or “blisters” [38]. A common practice now is to remove sulfur *via* injection of the copper melt with air, followed by removal of the dissolved oxygen *via* injection of natural-gas stream mixtures or in some cases, liquid hydrocarbon fuels. Once the copper has been reduced, it is referred to as “anode copper” and is ready for casting into anodes for the electrolysis process. Figure 1.6 shows a schematic of a fire refining vessel.

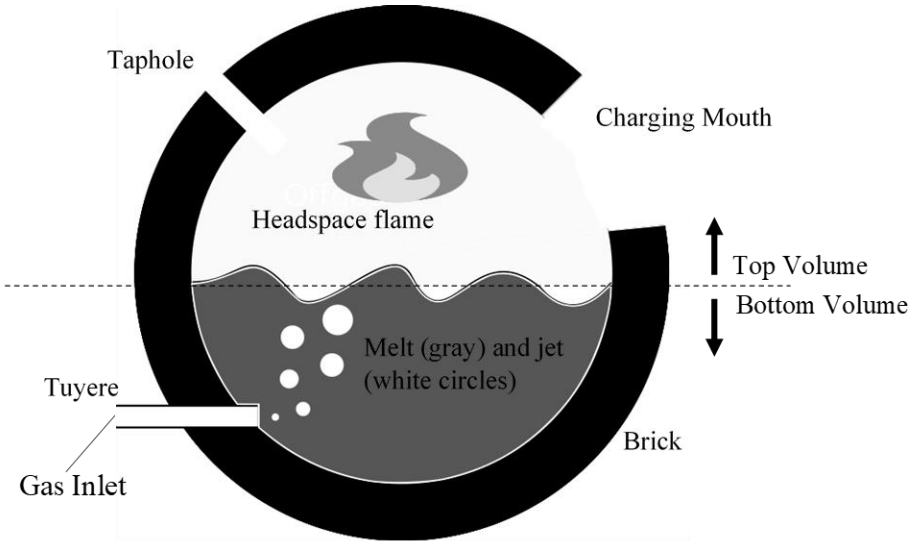

Figure 1.6 - Schematic of a copper fire refining furnace

Process models calibrated to industrial data have potential for giving improved process control, rapid process change evaluation, and the discovery of new operating modes that could increase production or decrease costs. It appears there have been no publically available models for the desulfurization step of fire-refining. Diaz-Damacillo et al. made a model for the reduction of blister copper [39] that estimates reduction as linear to about 400 ppm dissolved oxygen, after which reduction is liquid phase mass transport controlled. The authors were able to fit their model to several sets of industrial data; however, this does not mean their model is validated like they claim. These authors simply provided a linear model and exponential model with a large number of uncertain parameters that make the model easy to fit, though not necessarily physical. This model also does not account for injected bubble growth or homogenous gas phase reactions in the injected jet. Currently, there do not appear to have been any models that include these features available in the open literature for the reduction step of copper fire refining.

Several authors have studied copper desulfurization and deoxidation in a laboratory setting. Nanda and Geiger [40] studied copper reduction using carbon monoxide and were able to show that their system was liquid phase mass transport controlled between 500 ppm dissolved oxygen and 50 ppm dissolved oxygen. Andreini et al. [41] also studied copper deoxidation with carbon monoxide and these authors make the argument that the process is liquid phase mass transport controlled even above 5,000 ppm dissolved oxygen. Ohno [42] and Marin et al. [43] have studied

copper reduction *via* graphite, and both authors came to the conclusion that CO, formed from the graphite, was the chief reducing agent. Marin and Utigard studied copper reduction by top blowing of reducing flames [44] and found that gas phase mass transport control was rate limiting for this system above dissolved oxygen contents of 0.3 wt%. Goyal et al. have performed laboratory studies on the desulfurization and reduction steps of copper fire refining [45]. Importantly, they show that porous plugs probably do not lead to fine bubble dispersions in the copper refining system under typical gas injection conditions because the surface tension of copper is high enough that the formed microbubbles rapidly agglomerate. Kolczyk et al. modeled the fluid dynamics model of copper reduction [46]; these authors concluded that the melt is well-mixed during reduction, an assumption that will be used in the present study. None of the aforementioned authors look at injection of natural-gas/steam mixtures, which are especially important due to their actual industrial use and conversion of soot into reducing gases.

One area of interest in copper fire refining is the use sonic injection of gas. Kapusta [47] has presented a thorough review of this methodology and compared it to the current ubiquitously used bubbling injection. Kapusta showed that sonic jets have much greater penetration into the melt, which may help prevent tuyere line corrosion as less reaction would occur at the tuyere lines. Sonic jetting may greatly improve reduction times both by increasing the mixing of the melt and increasing jet-melt interfacial area. Enriquez et al. have performed plant trials under what they believed (on the basis of nozzle geometry and applied pressure) to be sonic injection conditions, and the results appear promising [48]. Because of the interest in this development, this model includes two different bubble injection regimes: spherical-cap bubbles, such as might be expected with traditional bubbling injection, and spherical microbubbles, such as expected from sonic injection of gas.

Overall, it appears that to-date there have been no published models of the natural-gas and steam injection system in copper fire refining. This system has two major advantages over natural-gas only injection. The first is that the soot formed by methane pyrolysis is rapidly consumed by the carbon-steam reaction, so the steam lowers the amount of combustible solid fed through the offgas handling system of the furnace. The second benefit is that the carbon-steam reaction produces two moles of reducing gas for every mole of solid carbon consumed. As such, each mole of injected methane ultimately leads to four moles of reducing gas in the natural-gas and steam

system, as opposed to two moles of reducing gas in the natural-gas only system. The current work will use injection of natural-gas/steam mixtures.

This paper provides simple reacting flow models for copper desulfurization and reduction in fire-refining. The model is intended to be amenable to calibration *via* Bayesian inference [49], which could provide a powerful tool for making estimations with known reliability for refining process. To this end, models were sought which minimize the number of uncertain parameters. This makes calibration of the models cheaper and minimizes the risk of model overfitting, which is where a model has so many parameters it can be tightly fit to an arbitrary set of data. Sensitivity analyses that include exergy balances were done on both models. Proposals for shortening process times, reducing natural gas consumption, and reducing soot production are made.

1.6 Autoclave Leaching

Roughly 80% of copper is produced *via* mining and refining, and of this quantity most is produced *via* smelting and refining of chalcopyrite based concentrates [50]. Recently, a novel industrial process for extracting copper from chalcopyrite has been developed. Over the last 20 years, Freeport-McMoRan Inc. has been a major contributor to the development of the autoclave leaching of chalcopyrite concentrate [51–53], and currently owns and operates the sole industrially-sized such plant. Autoclave leaching is the dissolution of targeted mineral species in aqueous solution at temperatures above the boiling point of water. This is done in vessels that are horizontal cylinders (autoclaves) and can withstand pressures up to about 30 bar. Autoclave leaching has been applied for the past several decades to various processes, such as gold ore pretreatment [54], zinc extraction [55], and nickel extraction [56]; high temperature and pressure is needed for sulfide leaching because at low temperature, elemental sulfur forms and coats the partially leached concentrate, greatly slowing down the leaching rate [57].

Autoclave leaching of copper-sulfide concentrates, also called the concentrate leach process (CLP), is similar to other autoclave leaching processes. The key difference is that copper-sulfide bearing concentrates instead of pyritic gold ores or other materials is fed to the vessel. Figure 1.7 shows a schematic of the autoclaves used for the CLP. The autoclaves are long horizontal cylinders with six evenly-sized compartments that are mechanically agitated. Oxygen enriched air, about 98.5% O_2, is fed to the autoclave to drive the leaching reactions. Plant water is

also fed to the autoclave to control temperature. The CLP has economics that appear competitive with smelting [51]. Both processes have advantages and disadvantages. Autoclave leaching of copper avoids SO_2 emissions; smelting produces SO_2 which may be used to make H_2SO_4 and requires less oxygen from oxygen plants per mole of copper refined. A quick and thorough overview of CLP technology in general and as applied to chalcopyrite leaching can be found in McDonald and Muir's work [58].

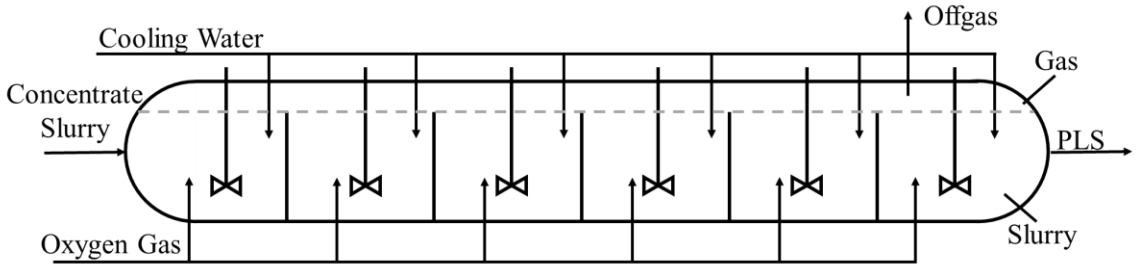

Figure 1.7 - Schematic of a CLP autoclave. The cooling water and oxygen is added through the bottom of each compartment

There have been numerous models autoclave leaching processes made, albeit not for copper extraction, and the model used for this paper is based on these efforts. Steady-state and transient models have been made. Several papers have been published on steady-state modeling of gold pretreatment and zinc extraction autoclaves [10–12,13]. These models describe the distribution of residence times the particles flowing through the autoclave would be expected to have; these residence time distributions are used to calculate extractions and heat generations. The steady-state modeling contrasts to the transient "population-balance" method (PBM) [63–66]. The population balance method tracks the transient particle size distribution present in each tank and calculates transient extraction rates amongst other performance variables.

Crundwell [67] and Woodward [56] have reviewed the two methods of autoclave leaching modeling, both mentioning that the steady-state modeling appears easier, though at the sacrifice of transient results. That said, the PBM is capable of producing both transient and steady-state results and for this reason, despite the additional computational resources required, was used to model the CLP. Additionally, Bayesian inference was used to calibrate the rates of mineral particle shrinkage as described in chapter 6. This allows the uncertainty of the model with respect to these rates to be quantified.

This study aims to provide an assessment of the performance of the CLP that can be used to compare this process to other copper-extraction routes. The current study presents a transient, reduced-order exergy model of a chalcopyrite-based concentrate pressure leaching process, similar to the CLP employed by Freeport-McMoRan Inc., to be used in conjunction with reduced order models of solvent extraction and electrowinning in future work. This study looks at a baseline case for which the exergetic performance of the process is evaluated. Additionally, operating parameters such as tank size are varied. The effect of these variations on copper extraction, cooling water addition rate, required oxygen addition are assed.

CHAPTER 2. BATH SMELTING MODEL

2.1 Model Description

The model made is for bath smelting in an IsaSMELT (figure 2.1). Detailed descriptions of these furnaces can be found in Schlesinger[68]. This model gives temperature, composition, and material flow histories for all streams entering, accumulating, and leaving the modeled furnace. The model is transient and assumes that all phases reach equilibrium within each time-step [69,70]. The model conserves mass and energy, finds the equilibrium of the matte, slag and gas phases, and calculates the exergy destroyed and lost for each time-step.

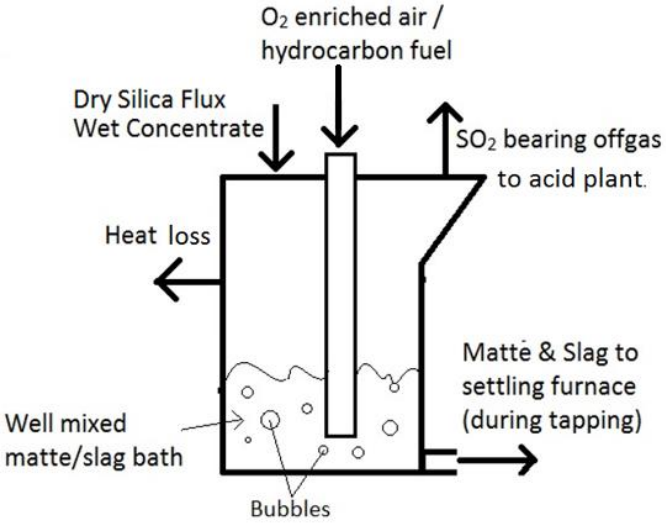

Figure 2.1 - Schematic of input and output streams of an IsaSMELT

2.1.1 Domain and Chemistry

The geometry of the IsaSMELT furnace modeled here is similar to those used in industry [68]. The vessel is a large cylinder (radius 1.875m, height 10m), providing a maximum volume for matte, slag, and gas of at 110 m^3. A schematic of this bath furnace is provided in figure 2.1, which also shows major inputs and outputs. The operation of this furnace is semi-batch; material is continuously fed to the furnace, but tapping of the mixed matte and slag only occurs about every half hour. Offgas is continuously removed from the furnace.

The IsaSMELT furnace takes wet concentrate, which can be approximated as $CuFeS_2$ (chalcopyrite), FeS_2 (pyrite), and SiO_2 (silica), with about 10 wt% H_2O, and oxidizes the iron to FeO and Fe_3O_4 with oxygen enriched air (95% O_2 and 5% N_2).

$$2CuFeS_{2(concentrate)} + O_{2(g)} \rightarrow 2FeS_{(matte)} + 2CuS_{0.5(matte)} + SO_{2(g)} \quad (2.1)$$

$$FeS_{2(concentrate)} + O_{2(g)} \rightarrow FeS_{(matte)} + SO_{2(g)} \quad (2.2)$$

$$FeS_{(matte)} + 1.5O_{2(g)} = FeO_{(slag)} + SO_{2(g)} \quad (2.3)$$

$$FeO_{(slag)} + 0.167O_{2(g)} = FeO_{1.333(slag)} \quad (2.4)$$

Dry silica flux is added to form a fayalitic slag, to which any condensed oxides report. The equilibrium constant of equation 2.3 is about four orders of magnitude times that of equation 2.5 at 1473K, and thus very little copper is oxidized compared to iron. As such, nearly all of the copper reports to the matte.

$$CuS_{0.5(matte)} + 0.75O_{2(g)} = CuO_{0.5(slag)} + 0.5SO_{2(g)} \quad (2.5)$$

In addition to equations 2.1-5, the slag forming reaction of FeO and SiO_2 also occurs:

$$2FeO + SiO_2 = 2FeO \cdot SiO_2 \quad (2.6)$$

Equation 2.6 was originally included in the model, but it was found that this had a negligible impact on the model results due to the low enthalpy and entropy of this reaction. It was thus excluded to enhance model speed. IsaSMELT furnaces also accommodate natural gas combustion at the lance tip, used to control melt temperature.

$$CH_{4(g)} + 2O_2 = CO_{2(g)} + 2H_2O_{(g)} \quad (2.7)$$

The IsaSMELT is distinguished from other copper smelting furnaces in that it blows the oxygen enriched air directly into the melt, thus strongly agitating the melt and encouraging an approximation of perfect mixing. The result of smelting is the Cu-rich, Fe-poor matte phase (Cu_2S, FeS), Fe-rich, Cu-poor slag phase (FeO, Fe_3O_4, Cu_2O, SiO_2), and SO_2 rich offgas (with N_2, CO_2, and H_2O). This last phase is sent to a sulfuric acid plant which is not included in this model. It is assumed that the smelting bath and gas are each perfectly mixed and that the smelting kinetics are fast enough that the furnace is in chemical equilibrium at any time [69–73].

2.1.2 Thermochemical Mass Balance on the Melt and Gas Volume

The equations for the equilibrium-molar balance for Cu, Fe, S, and O at any time are

$$N_{Cu} = N_{CuS_{0.5}} + N_{CuO_{0.5}} \tag{2.8}$$

$$N_{Fe} = N_{FeS} + N_{FeO} + N_{FeO_{1.333}} \tag{2.9}$$

$$N_O = N_{FeO} + 1.333N_{FeO_{1.333}} + 0.5N_{CuO_{0.5}} + 2N_{SiO_2} + 2N_{O_2} + 2N_{SO_2} + 2N_{CO_2} + 2N_{H_2O} \tag{2.10}$$

$$N_S = 0.5N_{CuS_{0.5}} + N_{FeS} + N_{SO_2}\,. \tag{2.11}$$

In equations 2.8-11, N_i is the total moles of species i in the furnace. The equilibrium constants for equations 2.3-5, which deal with the slag production and its equilibrium with matte, are

$$K_3 = \exp\left(\frac{-\Delta G_3}{RT}\right) = \frac{a_{FeO} f_{SO_2}}{a_{FeS} {f_{O_2}}^{1.5}} = \frac{(\gamma_{FeO} X_{FeO}) P_{SO_2}}{(\gamma_{FeS} X_{FeS}) {P_{O_2}}^{1.5}} \tag{2.12}$$

$$K_4 = \exp\left(\frac{-\Delta G_4}{RT}\right) = \frac{a_{FeO_{1.333}}}{a_{FeO} {f_{O_2}}^{0.167}} = \frac{\gamma_{FeO_{1.333}} X_{FeO_{1.333}}}{\gamma_{FeO} X_{FeO} {P_{O_2}}^{0.167}} \tag{2.13}$$

$$K_5 = \exp\left(\frac{-\Delta G_5}{RT}\right) = \frac{a_{CuO_{0.5}} {f_{SO_2}}^{0.5}}{a_{CuS_{0.5}} {f_{O_2}}^{0.75}} = \frac{\gamma_{Cu_2O} X_{Cu_2O} {P_{SO_2}}^{0.5}}{\gamma_{Cu_2S} X_{Cu_2S} {P_{O_2}}^{0.75}} \ . \tag{2.14}$$

In equations 2.12-14, K_i is the equilibrium constant of equation i, ΔG_i is the gibbs free energy of reaction of equation i, a_i, f_i, γ_i, X_i, and P_i are the activity, fugacity, activity coefficient, mole fraction, and partial pressure, respectively, of species *i*. Thermodynamic data for the gibbs free energies of the species used to calculate the Gibbs free energy of reactions, as well as molar enthalpy and molar entropy data, is taken exclusively from Barin[74]. All silica added to the furnace reports as silica in the slag, so the moles of Si are not distributed at all to the matte. The definition of mole fraction for species *i* in phase *k* is

$$X_{i,k} = \frac{N_{i,k}}{\sum_j N_{j,k}} \ . \tag{2.15}$$

In equation 2.15, $X_{i,k}$ and $N_{i,k}$ are the mole fractions and total moles respectively of species *i* in phase *k*; $\sum_j N_{j,k}$ is the sum of all the moles of each species *j* in phase *k*, *i.e.*, the total moles in phase *k*. Activity coefficient expressions for equations 2.12-14 can be found in in Table 2 of Bjorkman and Eriksson [26]. Because Bjorkman and Eriksson use different species stoichiometries for Cu_2S, Cu_2O, and Fe_3O_4, one will have to either convert their activities to be in terms of the species in this paper (the much more common notation) or employ their species stoichiometries in computational model.

The rates of accumulation of copper, iron, oxygen, and sulfur are given by

$$\frac{dN_{Cu}}{dt} = \dot{N}_{Cpy,in} \tag{2.16}$$

$$\frac{dN_{Fe}}{dt} = \dot{N}_{Cpy,in} + \dot{N}_{Py,in} \tag{2.17}$$

$$\frac{dN_O}{dt} = 2\dot{N}_{O_2,in} + 2\dot{N}_{SiO_2,in} + \dot{N}_{H_2O,in} - 2\dot{N}_{O_2,out} - 2\dot{N}_{SO_2,out} - \dot{N}_{H_2O,out} - 2\dot{N}_{CO_2,out} \tag{2.18}$$

$$\frac{dN_S}{dt} = 2\dot{N}_{Cpy,in} + 2\dot{N}_{Py,in} - \dot{N}_{SO_2,out} \,. \tag{2.19}$$

In equations 2.16-19, $\dot{N}_{i,in}$ is the molar flowrate of species *i* into the furnace, $\dot{N}_{i,out}$ is the molar flowrate of species *i* out of the furnace, the subscript "cpy" denotes the mineral chalcopyrite ($CuFeS_2$), and the subscript "py" denotes the mineral pyrite (FeS_2). Equations 2.16-19 are ODEs. These equations can be solved by knowing process inputs.

2.1.3 Energy Balance

Calculating the transient temperature of the furnace requires an energy balance to be coupled with the mass balance. Energy enters the smelter with the feed streams and leaves with the offgas; heat also leaves the furnace through the furnace wall due to heat transfer. Heat in the condensed phases remains until tapping or heat loss through the furnace walls. The energy balance takes the form

$$\frac{dH}{dt} = \sum_i \dot{N}_{i,in} h_{i,in} - \sum_j \dot{N}_{j,out} h_{j,out} - \dot{Q}_{out} \tag{2.20}$$

where *H* is the total enthalpy contained in the furnace contents (gaseous and condensed phases) and $\dot{Q}_{out}$ is the heat transfer out of the furnace. The temperature can be calculated at any time from the total enthalpy in the furnace

$$H = \sum_i h_i N_i = \sum_i (A_i + B_i T) N_i \,. \tag{2.21}$$

The total enthalpy in the furnace in a given time-step is $H_{furnace}$, and a linear variation of molar enthalpy is assumed. Rearranging eqn. 2.21 yields the temperature as a function of total enthalpy and species molar amounts

$$T = \frac{H - \sum_i A_i N_i}{\sum_i B_i N_i} \,. \tag{2.22}$$

2.1.4 Exergy Balance

The exergy added to a process has one of three fates. It can be carried out of the process as in the product (here, the matte), which is defined by the purposes of the process. Other exergy streams leaving the system, but that do not serve the direct purpose of the process, are said to be losses. Exergy lost by the process may be recovered by downstream operations, but if it is not, that exergy is destroyed as the stream is thermally and chemically dispersed into the environment. Finally, exergy can be destroyed/annihilated and not recovered. This destruction of the ability of an energy stream to do useful work can be seen, for example, in the drop in temperature during the spontaneous transfer of heat. So, unlike energy, which is always conserved when transferred or changed, exergy always experiences an irreversible degradation when transferred or changed, as no process is completely reversible. The "exergetic efficiency" of a process is defined as the fraction/percentage of exergy put into that process which leaves in a product stream.

Exergy also comes in several types; the two primarily important for copper smelting are thermal and chemical exergy. The third, mechanical exergy is not important here because the pressure of the smelting vessel is at atmospheric pressure. Thermal exergy is the potential work recoverable during spontaneous heat transfer to the environmental temperature. Chemical exergy is the potential recoverable work by reaction of matter to the environmental composition at environmental pressure and temperature. In general, the specific exergy of some matter at the dead state pressure (1 atm) is the sum of its thermal and chemical exergy,

$$e_i = h_i - h_{i,0} - T_0\left(s_i - s_{i,0}\right) + b_i\,, \tag{2.23}$$

where e_i is the specific exergy of species *i*, h_i is the specific enthalpy of species *i*, $h_{i,0}$ is the molar enthalpy of species *i* at the dead state temperature, T_0 is the environmental temperature, s_i is the molar entropy of species *i*, $s_{i,0}$ is the molar entropy of species *i* at the dead state temperature, and b_i is the chemical exergy of species *i*. It can be seen that the molar exergy is the difference between the total energy released on bringing the material to the reference temperature (the enthalpy difference terms) and the part of that energy that goes to reducing the material's entropy; to this quantity the chemical exergy is then added. The chemical exergy itself is equal to Gibbs free energy of reaction of the chemical species in question to its dead-state decomposition products at the dead-state composition; for example, the chemical exergy of metallic copper would be found

by the Gibbs free energy of the dissolution of metallic copper in water to the environmental cupric ion concentration [75].

Energy being transported by heat transfer also has an exergy content equal to

$$\dot{E}_Q = \dot{Q}\left(1 - \frac{T_0}{T}\right), \tag{2.24}$$

where $\dot{E}_Q$ is the rate of exergy transfer, $\dot{Q}$ is the rate of heat transfer, and T is the temperature of the heat source.

The total rate of exergy destruction is the difference between the rate of exergy input and exergy lost and accumulated

$$\dot{E}_{des} = \sum_i \dot{n}_{i,in} e_{i,in} - \sum_j \dot{n}_{j,out} e_{j,out} - \frac{dE_{furnace}}{dt} - \dot{Q}\left(1 - \frac{T_0}{T_t}\right). \tag{2.25}$$

In these equations, $\dot{E}_{des}$ is the rate of exergy destruction in the furnace, *i* and *j* are chemical species fed into and out of the furnace respectively, $\frac{dE_{furnace}}{dt}$ is the rate of exergy accumulation in the furnace, $\dot{n}_{j,out} e_{j,out}$ also represents the exergy lost with some material flow of species *j* out of the furnace.

The rate of exergy accumulation in the furnace is given by

$$\frac{dE_{furnace}}{dt} = \frac{d}{dt}\left(\sum_i e_i N_i\right), \tag{2.26}$$

where e_i is the molar exergy of species *i* at the temperature, pressure, and composition of its bearing phase in the furnace (*e.g.* Cu_2S in the matte) and N_i is the total moles of species *i* in the furnace. Equation 2.26 is simply the derivative of the total exergy contained in the matter in the furnace with respect to time.

2.1.5 Property Data

2.1.5.1 Thermodynamic Data for Species

For species thermodynamic properties, the work of Barin [74] was exclusively used to keep a consistent reference state. Data from this work in or near the temperature range of smelter operation was linearly best-fit for each species to provide simple, temperature dependent expressions of $h_i = A_i + B_i T$, where h_i is molar enthalpy of species i, and A & B are constants; specifically, B_i is the heat capacity of the i near 1473K. Molar entropies and Gibbs free energies were found using the estimated heat capacities and standard expressions for these terms.

2.1.5.2 Activity Coefficient Data

Activity coefficients for the condensed species were taken from Table 2 of Eriksson & Björkman's work [26].

2.1.5.3 Heat Flows

Experience with industrial smelters shows that they can be run at steady state. A simple analysis of conduction through the vessel walls shows that heat flow out does not change significantly in the range of possible operating temperatures of the smelter. This constancy is due to the small process temperature range (about +/- 50K) compared to the difference between the operating temperature (about 1450K-1500K) and the environmental temperature (298K). For the baseline case, similar to the Miami smelter and described later, a value of $\dot{Q} = 17.5\text{MW}$ keeps the bath temperature steady at 1473K, and so that value is used throughout this study. This value is somewhat higher than the estimate made in other studies, such as Coursol et al. [17,18], who estimate $\dot{Q} = 7\text{MW}$. More heat is certainly required to be lost in our baseline to maintain steady temperature, as the baseline oxygen grade is 95%, compared to the 45% used by Coursol et al. Physically, this extra heat loss could be facilitated by a water cooling jacket such as that actually employed by the Miami smelter; it appears a water cooling jacket is not employed by the furnaces looked at in Coursol et al.

2.1.6 Solution Method

The smelting model is a combined system of ordinary differential equations (with respect to time) and algebraic equations. The ordinary equations are addressed *via* knowledge of material addition rates to the furnace and the assumption that the furnace behaves as a closed system in a time-step. This latter assumption allows the offgassing rate to be calculated. It can be assumed that some amount of gas is in equilibrium with the melt. As such, the offgassing done in a timestep can be calculated as the difference between the total moles of gas in the closed system at the end of a timestep and the amount of gas taken to be in equilibrium with the melt. One can see that as the timestep size goes to zero, this difference goes to zero as well, so the method is valid. With this in mind, the algorithm used to implement the model is as follows:

1. Silica, wet concentrate, methane, and oxygen-enriched air are added to the furnace, giving:

$$N_{i,PA} = N_{i,0} + \dot{N}_{i,in}\Delta t \tag{2.27}$$

   where $N_{i,PA}$ is the moles of species i in the furnace after material addition (post addition), $N_{i,0}$ is the amount of material at the start of the timestep, $\dot{N}_{i,in}$ is the flowrate of species i into the furnace, and Δt is the timestep size.
2. An initial guess for the amount of reactions 3-5 is made, assuming the furnace now behaves as a closed system, and the moles of each species are updated.
3. Equations 2.8-14 and 20 are simultaneously solved using Newton's method; this gives the equilibrium temperature, phase compositions, and molar phase amounts at equilibrium and before offgassing.
4. Offgassing at the end of each time step to bring to the total moles of gas-phase to the amount estimated to be in equilibrium with the melt. For example, if 0.1 kmole are estimated to be in equilibrium with the melt, and 0.13 kmole are found in the furnace after step 3, the offgassing rate is calculated to be 0.03 kmole for that timestep. The offgas composition is taken to be the gas-phase composition at the end of step 3.

One immediately wonders how much of an affect the amount of gas estimated to be in equilibrium with the melt has on the model results. To assess this, the amount of gas was varied

from 1 kmole (approximately 100 m^3 of gas, or the entire furnace volume not occupied by melt) to 0.01 kmole. It was found that this parameter, over this range, had a negligible affect on the smelter results. As such, the intermediate value of 0.1 kmole was chosen. One may also wonder how the time-step size affects the model results. The timestep was varied over the range from 0.005s to 0.5s, and it was found that this change also had a negligible effect on the results, so the value of 0.5s was chosen. Finally, Newton's method was implemented in python *via* the scientific python library's fsolve function [76], which is a wrapper of the Hybrid Quasi-Newton's Method code developed by Argonne National Laboratories [77].

2.2 Results and Discussion

2.2.1 The Baseline Case

A baseline-case for smelter behavior was simulated using the conditions in Table 2.1. To align our study with industrial practice, conditions are similar to values from the FMI Miami smelter averaged over a period of four weeks. Base case furnace composition is shown in table 2.2. Mole fractions of $CuS_{0.5}$, $CuO_{0.5}$, and $FeO_{1.333}$ were converted to mole fractions of Cu_2S, Cu_2O, and Fe_3O_4 to keep in line with the formalism usually employed in when giving smelter modeling results. The average rate of offgas production for the baseline case was 0.1 kmole/s.

Table 2.1 - Parameter values used for the base case

Parameter	**Value**
Blast Oxygen Grade (Mole Fraction)	0.95
Dry Concentrate Feed Rate (kmole-$CuFeS_2$/s)	0.17 (92.3 dry tph)
Dry Concentrate Silica Grade (Wt. Fraction)	0. 07
Dry Concentrate Pyrite Grade (Wt. Fraction)	0.09
Concentrate Moisture Grade (Wt. Fraction H_2O)	0.1
Oxygen Addition Rate (kmole-O_2/s)	0.32 (470 Nm^3/min)
Silica Addition Rate (kmole-SiO_2/s)	0.07 kmole/s (15.1 tph)
Methane Addition Rate (kmole-CH_4/s)	0.009 (13.2 Nm^3/min)
Q_L (MW)	17.5

Table 2.2 - Initial furnace composition for the baseline case. Initial temperature was 1476.5K

Species	Initial Amount (kmole)
Cu_2S	156
FeS	62.0
FeO	130.
Fe_3O_4	10.7
Cu_2O	0.0333
SiO_2	90.5
O_2	$2.65x10^{-10}$
SO_2	$4.86x10^{-2}$
N_2	$3.45x10^{-3}$
CO_2	$1.85x10^{-3}$
H_2O	$4.61x10^{-2}$

The initial furnace condition for the baseline case is presented in table 2.2. The initial furnace temperature was taken to be 1476.5 K. Industrial IsaSMELT furnaces operate in a semi-batch way: a bath of smelted material is built, and after say 30 minutes, about half of the bath volume is tapped. The initial condition was found by mimicking this process; the initial composition corresponds to the cyclic steady state found by running multiple smelting-tapping cycles with the model using the parameter values in table 2.1. The initial quantity of melt corresponds to approximately 1 m of melt depth. Changes to this initial condition, for example, varying the initial temperature of the furnace by +/- 25K, did not change the steady state reached. Such changes merely imposed a transient of approximately 20 minutes to go from the initial condition to the steady state composition presented in table 2.2.

The purpose of the smelter is to remove Cu_2S (in liquid form) from the chalcopyrite ($CuFeS_2$) to be desulfurized in the subsequent converting process. By the end of the baseline process (t = 30 min), the product of the smelter (the matte) is at 82 wt% Cu_2S, or 56 wt% Cu; the rest is FeS. Only 0.002 wt% of the slag is Cu (as Cu_2O), so 0.02% of the copper fed to the smelter

is dissolved in the slag. In a real system, more copper will report to the slag, as small droplets of matte will be entrained in the slag due to the agitation of the bath in the smelting furnace. A settling process after tapping can be used to recover some that matte. The estimated copper grade of the matte is lower than that found at some smelters [68], but is similar to FMI's Miami smelter. The high O_2 grade used here and at Miami does not directly affect the matte grade. Matte grade is determined by the ratio of the oxygen addition rate (not grade) to iron addition rate *via* the concentrate. As such, changes to the oxygen grade will not affect the matte grade if the total oxygen addition rate is kept constant. However, one positive result of using higher O_2 grades is the reduction of N_2 addition. Although the inert N_2 has some cooling effect, less of it in the offgas allows for a larger volume flowrate of SO_2 in the offgas, thereby allowing higher production rates in a volume constrained gas handling system.

Table 2.3 - Steady-state composition of the furnace phases for the baseline case

Phase	Species	Mole Fraction	Weight Fraction
Matte	Cu_2S	0.72	0.82
	FeS	0.28	0.18
Slag	FeO	0.56	0.42
	Fe_3O_4	0.046	0.080
	Cu_2O	0.0014	0.002
	SiO_2	0.39	0.51
Gas	O_2	$2.7x10^{-9}$	-
	SO_2	0.49	-
	N_2	0.035	-
	CO_2	0.018	-
	H_2O	0.46	-

The exergy input to the smelter is shown in figure 2.2. The smelter uses approximately 28400 MJ/tonne-Cu fed to the smelter of exergy, most of which comes from chalcopyrite (84%).

The next most significant exergy source is pyrite (12%). The injected methane and oxygen provide less than 2.5% of the total exergy to the system. In the input gas stream, most of the exergy is in the methane, in spite of its small mole fraction (0.026) in that flow. The other species are relatively inert or close to the environmental composition. All of the input exergy is chemical, as the inlet streams are at the dead state temperature.

Figure 2.3 shows the distribution of exergy leaving the process with each stream. Exergy fed to the process has three different fates. The first fate is as process product, which is the matte (Cu_2S and FeS) and offgas (SO_2, N_2, H_2O, CO_2, and O_2) for smelting. The exergy in the matte is used to drive the subsequent copper extraction process, converting. The exergy in the offgas is used in the production of sulfuric acid, a valuable smelter product. 45% of the exergy fed to the process leaves with the product matte, and another 26% leaves with product offgass. The second fate of exergy is as losses, which for the smelter is slag (FeO, Fe_3O_4, Cu_2O, and SiO_2) and heat loss through the furnace walls. The exergy that is lost could theoretically be recovered and used to drive some process, but is not; rather, this exergy is allowed to spontaneously go to the dead state and so is ultimately destroyed. Exergy destruction is the final fate. Exergy is destroyed in a process due to entropy generation, such as by chemical reaction. Approximately 1% of the exergy fed to the smelter is destroyed. This likely happens by using reaction heat to bring added material to process temperature. Because the temperature of the smelting operation is about five times that of the dead-state, and the amount of added material that doesn't contribute to reaction is comparatively small (N_2 and H_2O in the concentrate are <5%) of the material fed to the smelter, the exergy destroyed in the smelter for the base case is also small.

Overall, 71% of the exergy fed to the smelting process leaves as a product stream, which is arguably a very good efficiency. The smelter used approximately 28400 MJ/tonne-Cu fed to the smelter in order to make matte, about 810 times the minimum theoretical exergy required as per figure 1.3. What this suggests is that there may be some as of yet undiscovered copper extraction technology that is less exergetically intense than smelting, or that there may be some way to reduce the intensity of smelting. This is important because processes that are less exergetically intense typically require less capital and are cheaper to operate. As such, there appears to be room for much future progress in making copper's extraction less intense and cheaper. However, this must be considered in light of the 71% efficiency of current smelting operation; this baseline case has shown that current smelting operations arguably do a good job of making use of the exergy fed to

them. Arguably, it is preferable to have a more exergetically intense process that is more efficient, than a less exergetically intense process that wastes much of the exergy fed to it. This consideration must be bourne in mind when assessing new copper extraction technologies from an exergetic point of view.

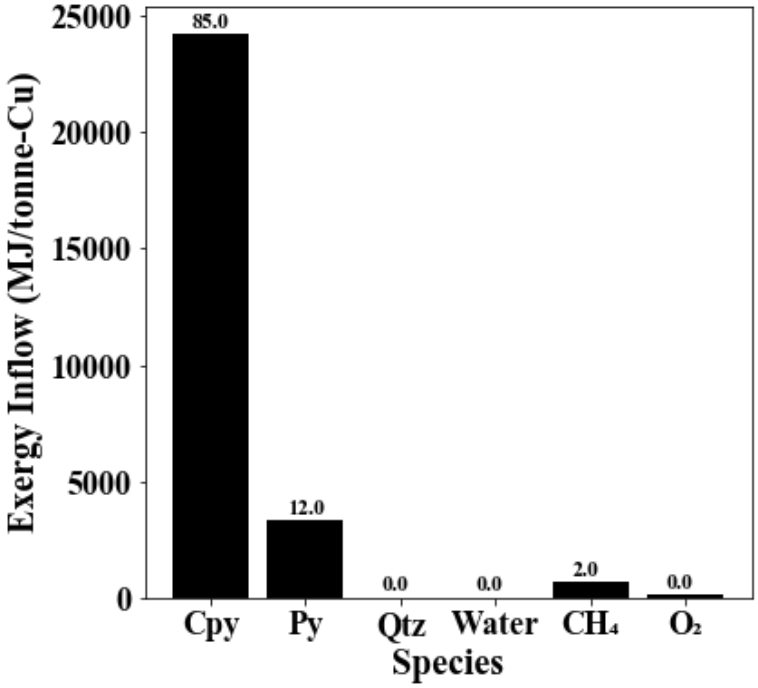

Figure 2.2 - Exergy inflow rate for each species added to the furnace. Numbers on top of bars are percentages of total exergy fed, which is 28400 MJ/tonne-Cu fed to the smelter

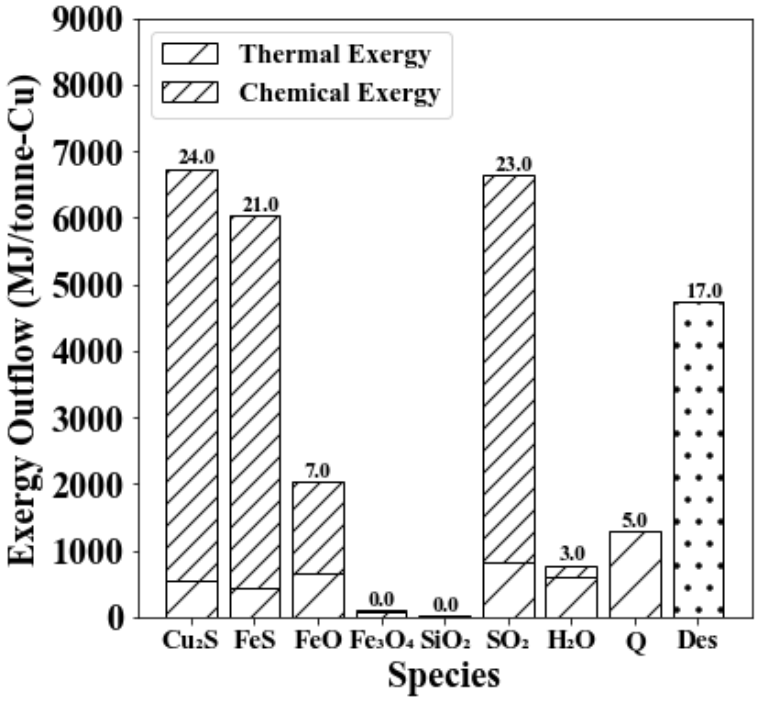

Figure 2.3 - Distribution of exergy flows out of the smelting vessel. Species with negligible exergy contents were left out to make the chart cleaner. Numbers on top of bars are percentages of total exergy in product, lost, and destroyed, which is 28400 MJ/tonne-Cu fed to the smelter

2.2.2 Oxygen Injection Rate Variation

The rate of oxygen addition was varied +/- 5% about the base line case value of 0.32 kmole-O_2/s. The composition of the injected gas was kept constant (95% O_2), so increasing the oxygen injection rate also increased the nitrogen injection rate.

Figure 2.4 shows the effect of changing the oxygen injection rate on the matte composition. Increasing the oxygen injection rate from 95% of the baseline value to 105% of the baseline value increased the terminal Cu_2S fraction of the matte from 0.53 to 0.58. The same change in rate of oxygen injection decreased the FeS fraction of the matte from 0.47 to 0.42. The reason for this change is that the oxidation of FeS to FeO is roughly 30000 times more favored than the oxidation of Cu_2S to Cu_2O at the temperature of smelting. As such, increasing the oxygen injection rate will cause enrichment of Cu_2S in the matte.

Figure 2.5 shows the effect of changing the oxygen injection rate on the dissolved-Cu_2O content of the slag. The increase in oxygen injection rate from 95% of the baseline to 105% of the baseline caused the mole fraction of dissolved Cu_2O in the slag to go from 0.0005 to 0.0011. This

is equivalent to the percentage of copper added to the smelter reporting to the slag changing from 0.08% to 0.4%, a fivefold increase. However, by producing more slag in the smelter, less slag will be produced in the converting operations, where the terminal dissolved Cu_2O content in the slag can be upwards of 0.02. A combined mass balance of smelting and converting operations is needed to ascertain the optimal smelter matte grade to target.

Figure 2.6 shows the effect of changing the oxygen injection rate of the smelter offgas composition. Increasing the oxygen injection rate from 95% of the baseline case to 105% of the baseline case caused the mole fraction of SO_2 in the offgas to change from 0.476 to 0.497. The reason for this increase is that practically all of the injected oxygen goes to SO_2 production. The benefit or cost of changes to the SO_2 grade of the offgas will ultimately be determined by the smelter acid plant. The rate of change of the offgas composition is much greater than the rate of change of the condensed phase compositions. The reason for this is that there is substantially less moles of gas than condensed phases due to the large specific volume of the smelter gas. As such, a given amount of reaction will cause much more rapid changes in the gas phase composition than condensed phase compositions.

Figure 2.7 shows the effect of oxygen injection rate on temperature. Changing the oxygen injection rate from 95% of the baseline to 105% of the baseline caused the terminal temperature to change from 1405K to 1545K. This range of temperatures is enough to significantly impact both smelter thermodynamics, and partially explains the increase in dissolved Cu_2O in the slag. The difference in favorability between Cu_2S oxidation and FeS oxidation decreases with increasing temperature. This temperature change is also enough to impact furnace refractory/freeze-lining behavior and lance integrity. The sensitivity of temperature to oxygen injection rate could be partially mitigated by using a lower oxygen grade in the injected gas, but this would decrease smelter production capacity due to the increased offgas load. Decreasing the oxygen grade of the injected gas would also require more fuel to be added to the smelter to make up the heat balance, which will consume more oxygen and further increase the offgas load.

Figure 2.8 shows a comparison of the exergy fates for the two oxygen injection cases. Higher oxygen injection shifts exergy from leaving the smelter with product matte to product offgas (as SO_2), losses as slag (as FeO), and being destroyed. The increase in exergy leaving the smelter with the offgas and slag is due to higher quantities of SO_2 and FeO being formed with higher oxygen injection rate. The increase in exergy destroyed is due to the increase in FeS

oxidation to FeO. Although this behavior appears unfavorable, it should be remembered that the exergy destruction in the converters subsequent to smelting will have decreased.

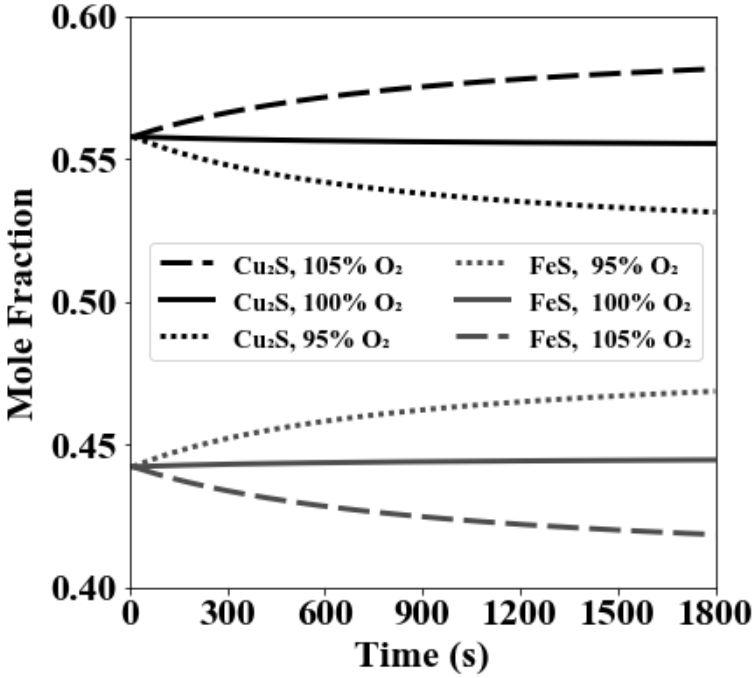

Figure 2.4 - Effect of oxygen injection rate on matte composition

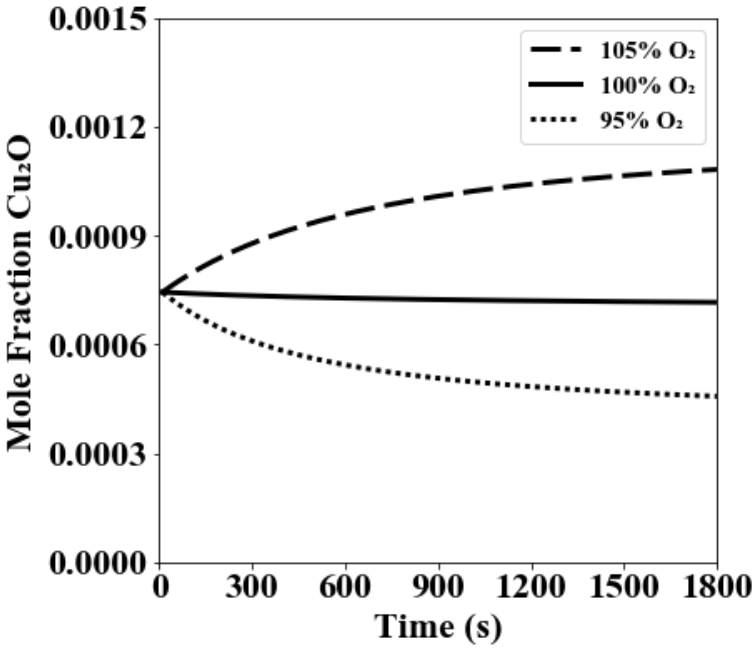

Figure 2.5 - Effect of oxygen injection rate on slag dissolved-Cu2O content

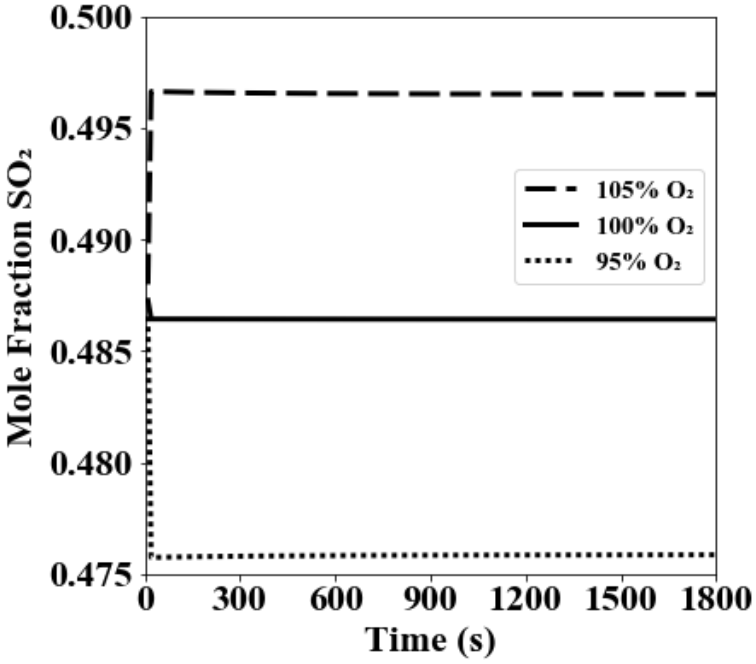

Figure 2.6 - Effect of oxygen injection rate on offgas SO2 content

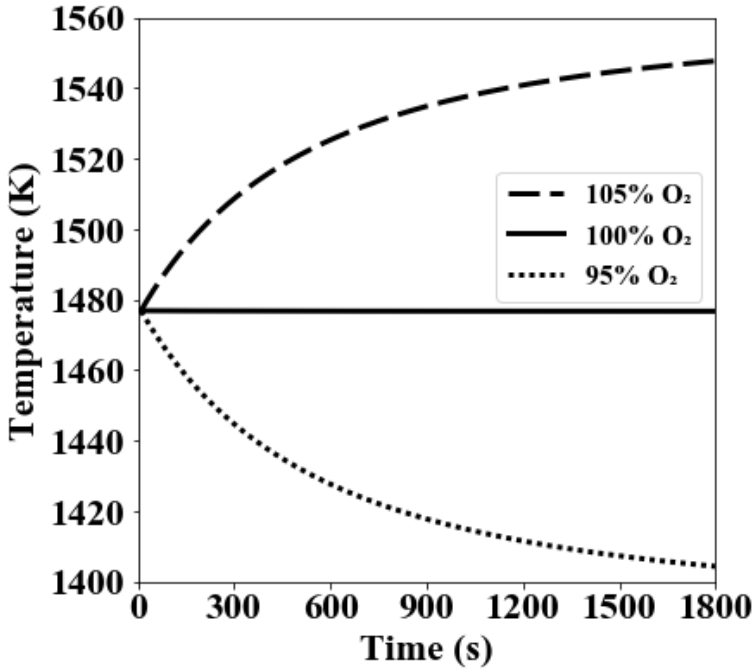

Figure 2.7 - Effect of oxygen injection rate on temperature

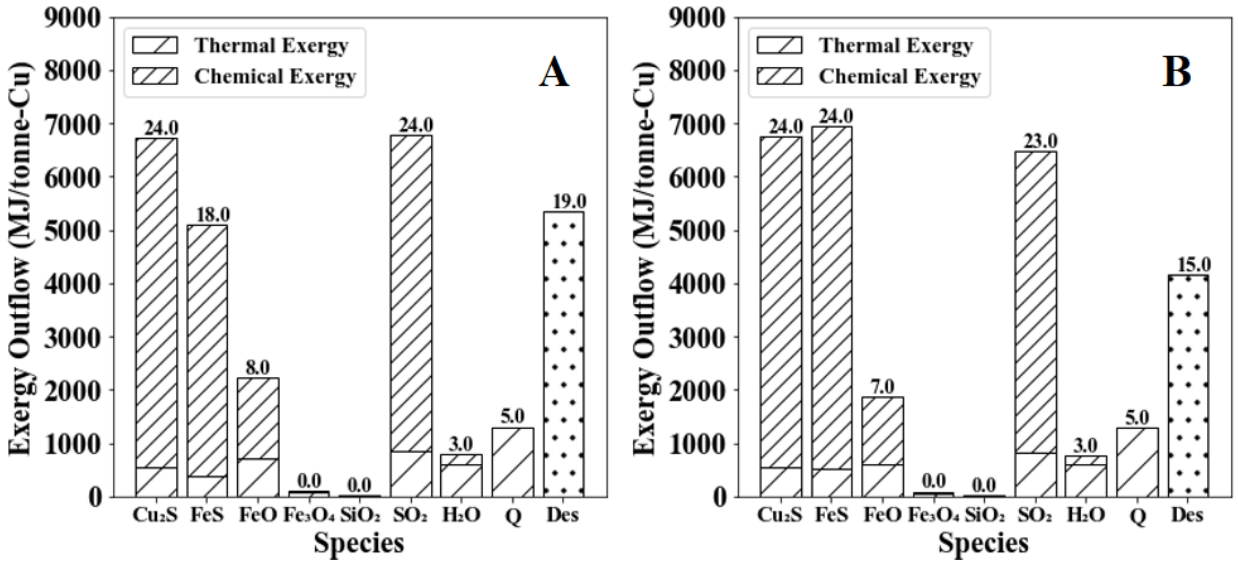

Figure 2.8 - Comparison of the exergy fates for A) the 105% of baseline oxygen injection and B) the 95% of baseline oxygen injection cases

2.2.3 Oxygen Grade Variation

The oxygen grade of the injected gas was changed over the range from 0.65 to 1.0 molar fraction O_2 in the injected gas. The injection rate of oxygen was kept constant, so the lower oxygen grade cases had a higher total injection rate of gas due to the added injected nitrogen. As mentioned earlier, smelter operators prefer higher oxygen grades as less nitrogen minimizes the offgas load of the smelting furnace on the plant gas handling system, allowing more load from the converters and other furnaces and increasing production capacity.

Figure 2.10 shows the effect of oxygen grade on the temperature history of the smelter. Decreases in oxygen grade cause significant drops in temperature. This is caused by the increased heat demand of the added nitrogen. One notices that the rate of temperature drop decreases with decreasing temperature. Heat loss is treated as a constant in the model, so this effect is not caused by decreasing heat loss. Rather, as the temperature decreases, less heat is required to bring the added material to temperature, so the rate of cooling decreases. When temperature increases, more heat is required to bring the added material to temperature, so the heating rate slows. Additionally, as the temperature of the bath lowers, the oxidation reactions become more favored and more exothermic, and this effect partially makes up for the heat demand of the nitrogen. When the oxygen grade is increased, the temperature of the smelter increases at a decreasing rate. The

temperature increases because there is less nitrogen consuming heat. The rate of temperature increase decreases because the oxidation reactions become less favored and less exothermic with increasing temperature. Overall, the tendency of the smelting reactions' favorability and heat of reaction to oppose changes in temperatures is helpful for maintaining a desired steady state.

Another important result from the oxygen grade study is the effect oxygen grade has on the SO_2 grade of the offgas; this is shown in figure 2.11. The offgas from smelting is sent to a sulfuric acid plant, and it is important for the sulfuric acid plant to dilute the smelting and converting offgas to low enough SO_2 levels. The reason for this is that the acid plant employs catalyst beds to convert SO_2 to SO_3, a highly exothermic reaction, and too high of SO_2 grades entering this process can cause nonoptimal or even damaging temperatures to develop. Being able to estimate the SO_2 grade coming off the smelter assists with process control at the acid plant.

One can see that the SO_2 grade of the smelter offgas increases approximately linearly with oxygen grade. At an oxygen grade of 1.0, the offgas is comprised almost entirely of SO_2, formed during reactions, and water vapor from the concentrate. The remaining gas is the water vapor and carbon dioxide from combustion of the methane. This result is a link to a study of the coupled downstream acid plant, as well as other copper extraction studies.

Decreasing the oxygen grade of the injected gas from 1.0 to 0.65 increased the fraction exergy leaving with nitrogen by 0.01. This change is shown in figure 2.12. There was a negligible change in the fraction of exergy destroyed. The total exergy leaving with the matte, slag, and remainder of the offgas decreased by a fraction of 0.01. The distribution of exergy between the smelting species besides nitrogen did not significantly change. Overall, changes to the oxygen grade over the range studied did not have a significant effect on the exergetic performance of the smelter.

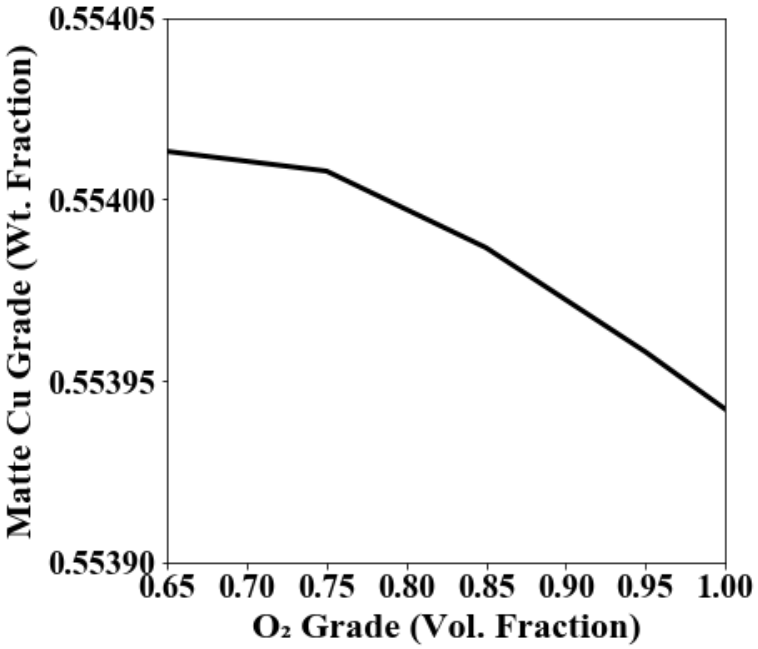

Figure 2.9 - Matte copper grade versus oxygen grade of the injected gas

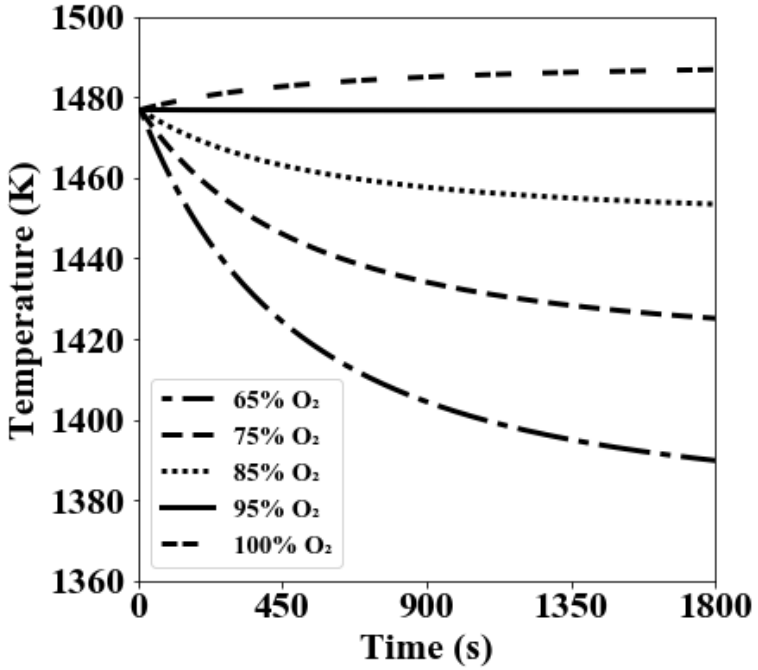

Figure 2.10 - Effect of injected gas oxygen grade on temperature

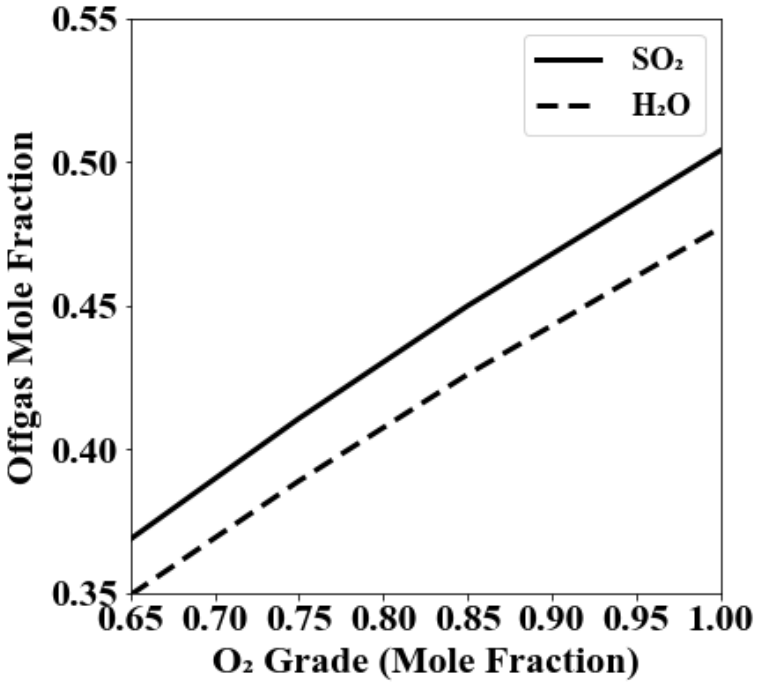

Figure 2.11 Terminal Partial Pressure of SO_2 in the smelter as a function of oxygen grade

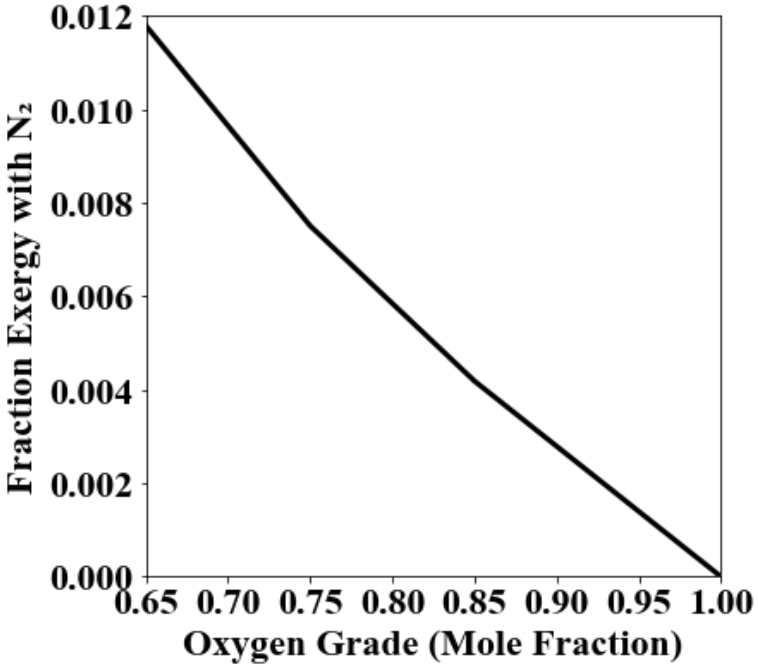

Figure 2.12 - Fraction of exergy leaving the smelting furnace in nitrogen gas

2.2.4 Pyrite Grade of Concentrate Variation

Pyrite is a common mineral present in porphyry copper ore bodies and a significant amount of it makes it through flotation and into the smelted concentrate. Pyrite is presumed to react according to equation 2.2. This reaction is exothermic at smelting temperatures and produces SO_2 gas while consuming oxygen. This said, one should not presume higher fractions of pyrite in the concentrate lead to higher smelting temperatures.

Two cases were run with base case parameters except variations in pyrite additions; the pyrite grade of the dry concentrate was varied +/- one percent. The chalcopyrite/copper addition and so production rate was kept constant, so the total amount of concentrate being fed to the smelter with pyrite grade. Changes to the pyrite addition over this range had less than a 1% effect on terminal phase compositions. Figure 2.13 shows the effect of the changes to the pyrite grade on temperature. Less pyrite in the concentrate means less concentrate needs to be added to keep the same copper production rate. As such, less heat goes to bring the concentrate to temperature and the bath temperature increases. The opposite holds true when more pyrite is in the concentrate.

Figure 2.14 shows the effect of dry-concentrate pyrite grade on matte composition. Increasing the dry-concentrate pyrite grade from 0.08 to 0.10 caused the terminal matte Cu_2S fraction to decrease from 0.57 to 0.54, and the terminal matte FeS fraction to increase from 0.43 to 0.46. The reason for this change is that less oxygen is available for FeS oxidation when more pyrite is present. Smelters could mitigate the decrease in matte Cu_2S grade caused by higher concentrate pyrite grades by injecting more oxygen (see section C). However, this will increase the offgas load of the smelter, thereby limiting smelter production.

Figure 2.15 shows the effect of dry-concentrate pyrite grade on smelter exergetic performance. Increasing the concentrate pyrite grade from 0.08 to 0.10 caused the fraction of exergy leaving the smelter with SO_2 to increase by 0.003, the fraction leaving with FeS to increase by 0.03, and the fraction destroyed to decrease by 0.03. The higher exergy leaving with SO_2 is caused by the stoichiometry of equations 2.1-5; more pyrite addition with a fixed oxygen addition causes greater SO_2 production and so greater exergy loss with SO_2. The same holds true for FeS. The fraction of exergy destruction decreases with increasing concentrate pyrite grade both because the actual amount of exergy destruction decreases and the total exergy flow through the smelter increases. Less absolute exergy is destroyed in the smelter with higher concentrate pyrite grade because there is less FeS oxidation, a reaction which destroys more exergy at smelting

temperatures than FeS_2 conversion to FeS (of which there is more). If additional oxygen were added to make up for additional pyrite addition and bring the fraction of Cu_2S in the matte to the desired level, the exergetic performance of the smelter would mimic the base case. As such, higher pyrite grades in the concentrate do not actually improve exergetic performance of a smelter. Overall, consideration of this exergy result and the decrease in copper production capacity associated with higher concentrate pyrite grades shows that smaller concentrate pyrite grades are better for smelting operations.

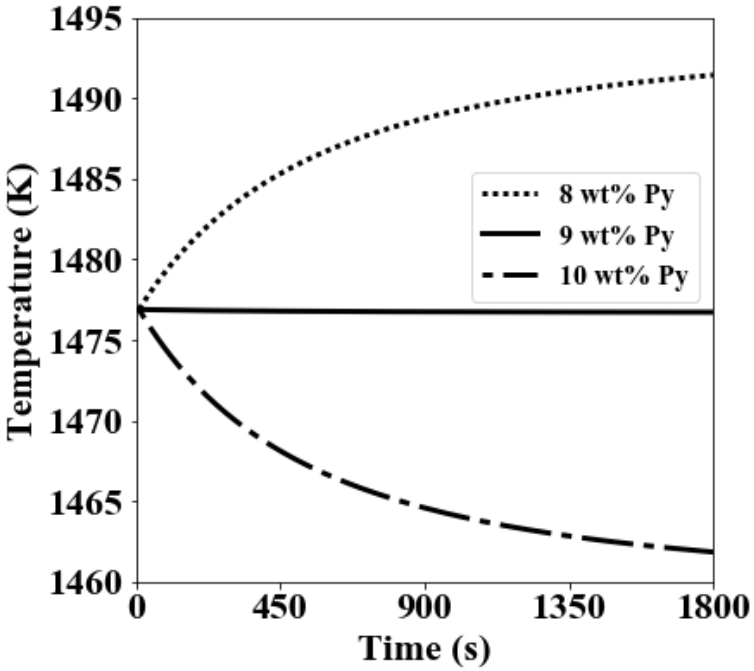

Figure 2.13 - Effect of changes to the dry-concentrate pyrite grade on smelter bath temperature

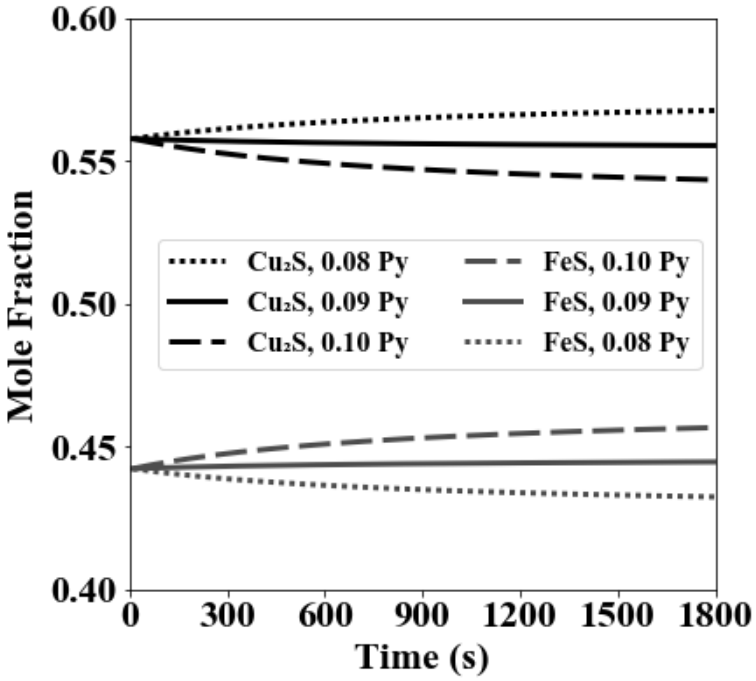

Figure 2.14 - Effect of changes to the dry-concentrate pyrite grade on matte composition

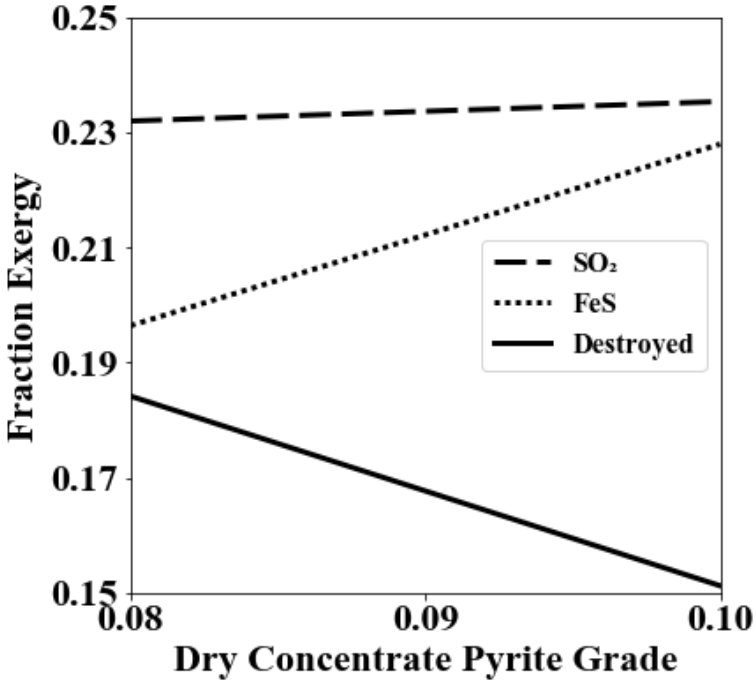

Figure 2.15 - Effect of concentrate pyrite grade on fraction of exergy leaving the smelter with SO_2, FeS, and as destructions

2.2.5 Silica Grade of Concentrate Variation

Two cases were run with dry concentrate silica grades of 0.06 and 0.08 mole fraction of the dry concentrate for the low and high cases. The chalcopyrite/copper addition and so production rate was kept constant, so the total amount of concentrate being fed to the smelter with pyrite grade. The results of this study show that these variations in silica grade had less than a 2% effect on terminal slag composition and less than an 0.2% effect on terminal matte composition. There was no noticeable effect on gas composition. The effect of varying silica grade on temperature is shown in figure 2.16. Increasing the silica grade requires more concentrate to be added to keep the same copper production rate, so temperature decreases due to the increased heat demand of bring more concentrate to temperature. The opposite effect holds true for decreases to the silica grade. The effect of concentrate silica grade on smelter exergetic performance was negligible over the range examined.

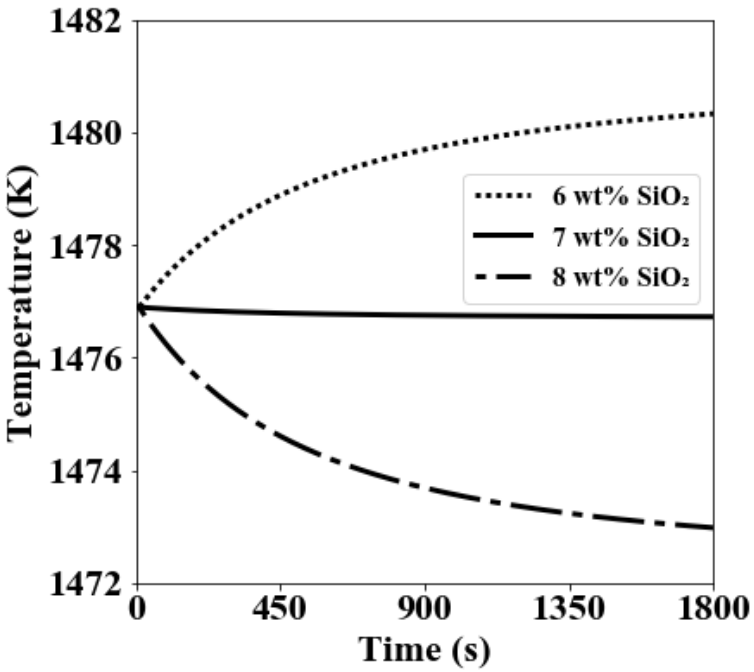

Figure 2.16 - Effect of dry silica grade of concentrate on bath temperature

2.3 Conclusions and Recommendations

A transient, reduced order equilibrium model of copper bath smelting was developed. The model successfully estimated transient phase compositions and furnace temperature for a parametric the study, the baseline for which was similar to industrial practice.

It was found that smelter phase compositions, temperature, and exergetic performance were strong functions of the oxygen injection rate. Condensed phase compositions were nearly independent of injected gas oxygen grade. Furnace temperature was a strong function of injected gas oxygen grade. Offgas SO_2 and H_2O mole fractions increased with the injected gas oxygen grade and were strong functions of it. Changes to the concentrate pyrite grade of +/- 1% had a significant impact on smelter performance. Increases to the concentrate pyrite grade decreased smelter temperature, Cu_2S mole fraction of the matte, and fraction of exergy destroyed. Increases to the concentrate pyrite grade increased the fraction of exergy leaving the smelter in FeS and SO_2. Changes to the concentrate silica grade of +/- 1% about the baseline had a negligible impact on smelter performance.

From the results, we make the following observations and recommendations:

1. Injected gas oxygen grade should be maximized. This decreases the offgas load of the smelting furnace, increasing possible production of copper at the smelter as whole.
2. Efforts on recovering exergy should be targeted at the smelter offgas and heat loss. Such recovery for the offgas is generally done *via* a waste-heat boiler above the smelter and at the sulfuric acid plant. Recovery of exergy from the heat loss is done at some operations *via* a cooling water jacket.
3. Although there is significant lost thermal and chemical exergy in the slag, there does not appear to be an economic way to recover either from this material at present.
4. Careful control of the injected oxygen rate is needed to ensure steady operating temperature. Changes to oxygen injection rate in light of changes to the concentrate composition should be done slowly, as the smelting system naturally resists temperature change.
5. While this study sheds light on the behavior of bath smelters, real performance gains require coupling this work with similar models of other unit operations, such as converting, and investigating tradeoffs throughout a plant.

CHAPTER 3. PEIRCE-SMITH CONVERTING

3.1 Model Description

Peirce-Smith converting (figure 3.1) has two steps: the first is the slag blow, in which the oxygen enriched plant air reacts with FeS in copper matte to remove the iron and produce a fayalitic slag. The second is the copper blow in which the oxygen enriched plant air reacts with the matte, now nearly pure Cu_2S, to produce blister copper (99% Cu). The model furnace geometry is a large horizontal cylinder with an internal diameter of 4m, a length of 12m, and an internal furnace volume of approximately 150 m^3, similar to industrial furnaces.

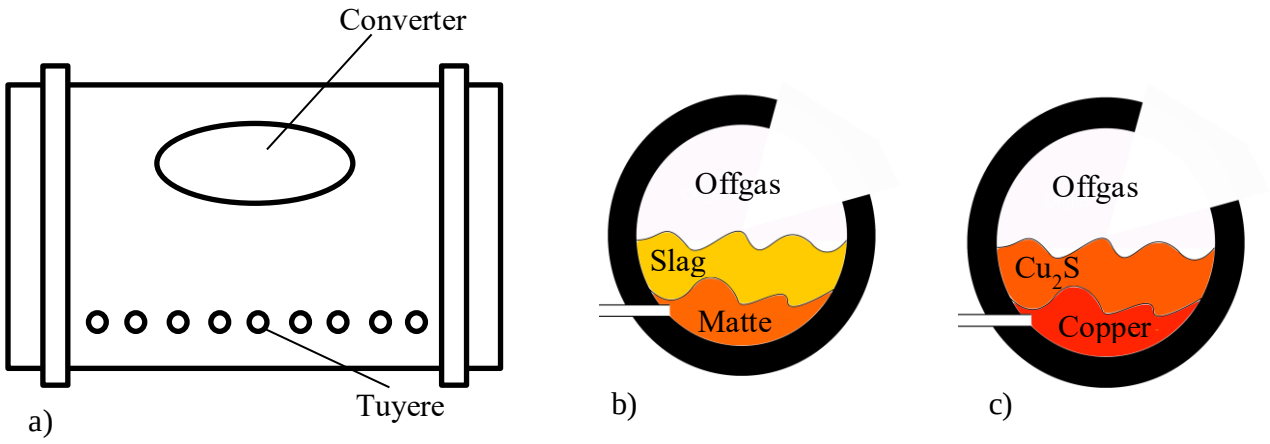

Figure 3.1 - Schematic of (a) a Peirce-Smith Converter and the (b) slag and (c) copper blows.

3.1.1 Slag Blow Regime

The principal chemical reaction in the slag blow is the conversion of iron sulfide in the copper-bearing matte to iron oxide in the slag:

$$FeS_{(matte)} + 1.5O_{2(g)} = FeO_{(slag)} + SO_{2(g)} \tag{3.1}$$

where it can further oxidize to magnetite:

$$6FeO_{(slag)} + O_{2(g)} = 2Fe_3O_{4(slag)} \tag{3.2}$$

As the blow continues, more and more copper is also oxidized and reports to the slag:

$$Cu_2S_{(matte)} + 1.5O_{2(g)} = Cu_2O_{(slag)} + SO_{2(g)} \quad (3.3)$$

Unlike smelting, where the content of dissolved copper in the slag may be 0.1-0.2 wt%, converting operations can see terminal dissolved copper contents of up 10 wt%. The tradeoff to the higher copper losses is needed so that the matte will be nearly pure Cu_2S ("white metal"). Converting operations minimize dissolved copper losses in the slag by periodically pouring off the slag during the slag-blow. This works because what matters for the thermodynamics is the composition and not quantity of the slag. Pouring off the slag intermittently ensures that at the end of converting, a small amount of slag at the high copper fraction is produced, rather than a large amount of slag with the same high copper fraction. To recover the copper plants can also recycle the converting slag to the settling furnaces that follow smelting. This works because the matte grade in contact with the slag in the settling furnaces has a much lower copper grade than converting matte, so some copper should redissolve into the settling matte from the converting slag. Finally, a silica flux is added to the melt to facilitate the formation of the slag:

$$2FeO + SiO_2 = 2FeO \cdot SiO_2 \quad (3.4)$$

Equation 3.4 was originally included in the model, but its enthalpy and entropy of reaction are small enough that it was found to have a negligible impact on the model results. It was thus excluded to enhance model speed. The slag is still comprised of Cu_2O, FeO, Fe_3O_4, and SiO_2, but added SiO_2 is taken to dissolve into the slag without any reaction.

3.1.2 Thermochemical Mass Balance for the Slag Blow during Air Injection

The slag blow is a highly transient process in which the iron in copper matte is continuously oxidized to produce fayalitic slag. Additionally, the slag blow is typically divided into four sub-blows. For the first sub-blow, the furnace is filled approximately half full with copper matte. This amount optimizes use of the furnace volume and helps minimize total copper dissolution in slag. Then, air and silica are continuously added into the furnace for a set period of time. After this

period, the slag is dumped out of the furnace into ladles, and more matte is added. The newly added matte is at the composition of the matte found in the settling furnace preceding converting. Air and silica are then added to the furnace again for another set a period of time. This process of adding matte and injecting air and silica, followed by pouring off the slag, repeats three times until the copper rich phase of the melt has become nearly pure Cu_2S, called white metal.

The thermodynamics of each cycle during the slag blow is governed by the same physics, although with different initial conditions. The equations for the equilibrium-molar balance for Cu, Fe, S, and O at any time are :

$$N_{Cu} = N_{CuS_{0.5}} + N_{CuO_{0.5}} \tag{3.5}$$

$$N_{Fe} = N_{FeS} + N_{FeO} + N_{FeO_{1.333}} \tag{3.6}$$

$$N_O = N_{FeO} + 1.333N_{FeO_{1.333}} + 0.5N_{CuO_{0.5}} + 2N_{SiO_2} + 2N_{O_2} + 2N_{SO_2} \tag{3.7}$$

$$N_S = 0.5N_{CuS_{0.5}} + N_{FeS} + N_{SO_2} \tag{3.8}$$

I

n equations 3.5-8, N_i is the total moles of species i in the furnace. The equilibrium constants for equations 3.1-3, which deal with the slag production and its equilibrium with matte, are:

$$K_1 = \exp\left(\frac{-\Delta G_3}{RT}\right) = \frac{a_{FeO} f_{SO_2}}{a_{FeS} {f_{O_2}}^{1.5}} = \frac{(\gamma_{FeO} X_{FeO}) P_{SO_2}}{(\gamma_{FeS} X_{FeS}) {P_{O_2}}^{1.5}} \tag{3.9}$$

$$K_2 = \exp\left(\frac{-\Delta G_4}{RT}\right) = \frac{a_{FeO_{1.333}}}{a_{FeO} {f_{O_2}}^{0.167}} = \frac{\gamma_{FeO_{1.333}} X_{FeO_{1.333}}}{\gamma_{FeO} X_{FeO} {P_{O_2}}^{0.167}} \tag{3.10}$$

$$K_3 = \exp\left(\frac{-\Delta G_5}{RT}\right) = \frac{a_{CuO_{0.5}} {f_{SO_2}}^{0.5}}{a_{CuS_{0.5}} {f_{O_2}}^{0.75}} = \frac{\gamma_{Cu_2O} X_{Cu_2O} {P_{SO_2}}^{0.5}}{\gamma_{Cu_2S} X_{Cu_2S} {P_{O_2}}^{0.75}} \tag{3.11}$$

In equations 3.9-11, K_i is the equilibrium constant of equation i, ΔG_i is the Gibbs free energy of reaction of equation i, a_i, f_i, γ_i, X_i, and P_i are the activity, fugacity, activity coefficient, mole fraction, and partial pressure, respectively, of species *i.* All silica added to the furnace reports as silica in the slag, so the moles of Si are not distributed at all to the matte. The definition of mole fraction for species *i* in phase *k* is:

$$X_{i,k} = \frac{N_{i,k}}{\sum_j N_{j,k}} \tag{3.12}$$

In equation 3.12, $X_{i,k}$ and $N_{i,k}$ are the mole fractions and total moles, respectively, of species *i* in phase *k* (*i* includes SiO_2 for the slag); $\sum_j N_{j,k}$ is the sum of all the moles of each species *j* in phase *k*, *i.e.*, the total moles in phase *k*. Activity coefficient expressions for equations 3.9-11 can be found in in Table 2 of Bjorkman and Eriksson [26] and appendix A.

During blowing, the rates of accumulation of copper, iron, oxygen, and sulfur are given by.

$$\frac{dN_{Cu}}{dt} = 0 \tag{3.13}$$

$$\frac{dN_{Fe}}{dt} = 0 \tag{3.14}$$

$$\frac{dN_{O,A}}{dt} = \theta\left(2\dot{N}_{O_2,in}\right) + 2\dot{N}_{SiO_2,in} - 2\dot{N}_{O_2,out} - 2\dot{N}_{SO_2,out} \tag{3.15}$$

$$\frac{dN_S}{dt} = -\dot{N}_{SO_2,out} \tag{3.16}$$

In equation 3.15, $N_{O,A}$ is the moles of active oxygen in the converting furnace, and θ is the oxygen efficiency of the slag blow. In converting operations, some of the added oxygen short-circuits through the melt as unreacted bubbles; the percentage of added oxygen that does not short-

circuit and so is available for reaction is referred to as the oxygen efficiency. Oxygen efficiency is estimated in industrial operations by comparing the air addition rate and oxide formation rate in the slag. In equations 3.15 and 16, $\dot{N}_{i,in}$ and $\dot{N}_{i,out}$ are the molar flowrates of species *i* into and out of the furnace, respectively. In between sub-blows, when the furnace is cooling, the rate of sulfur and oxygen in and out of the furnace are zero, as there is no material flow into or out of the furnace. As soon as blowing stops, pouring of the slag is simulated by reducing the amount of slag in the furnace to 1% of its value at the end of blowing. After cooling for seven minutes, matte at 1380K is added to the furnace. The furnace temperature and equilibrium composition are updated, and the matte-slag-gas mixture is allowed to continue cooling for another seven minutes. Then, another slag sub-blow commences, unless the total slag-blow time has reached 13820s, when the copper blow commences. The time of 13,820 swas found to be the time at which the composition of the matte exceeded 99.9% Cu_2S. Table 3.1 shows the furnace schedule used in the model, which is similar to practice at Miami.

Table 3.1 - Model Furnace Schedule for the Slag Blow

Event	Time Range (s)
First Sub Slag Blow	0 - 3600
Slag Pour & Cooling	3600 - 4020
Matte Addition (60% of Initial Matte)	4020
Cooling	4020 - 4440
Second Sub Slag Blow	4440 - 7440
Slag Pour & Cooling	7440 - 7860
Matte Addition (40% of Initial Matte)	7860
Cooling	7860 - 8280
Third Sub Slag Blow	8280 - 10980
Slag Pour & Cooling	10980 - 11400
Matte Addition (20% of Initial Matte)	11400
Cooling	11400 - 11820
Final Sub Slag Blow	11820 - 13820
Final Slag Pour	13820

3.1.3 Energy Balance for the Slag Blow

Calculating the transient temperature of the furnace requires an enthalpy balance to be coupled with the mass balance. During air injection, enthalpy enters the converter with the feed streams and leaves with the offgas; heat also leaves the furnace through the furnace wall due to heat transfer. Heat in the condensed phases is continuously lost to heat transfer. The enthalpy balance takes the form:

$$\frac{dH}{dt} = \sum_i \dot{N}_{i,in} h_{i,in} - \sum_j \dot{N}_{j,out} h_{j,out} - \dot{Q}_{out} \tag{3.17}$$

where H is the total enthalpy contained in the furnace contents (gaseous and condensed phases) and $\dot{Q}_{out}$ is the heat transfer out through the furnace. The temperature can be calculated at any time from the total enthalpy in the furnace:

$$H = \sum_i h_i N_i = \sum_i (A_i + B_i T) N_i \ . \tag{3.18}$$

The total enthalpy in the furnace in a given time-step is $H_{furnace}$, and a linear variation of molar enthalpy is assumed. Rearranging eqn. 3.18 yields the temperature as a function of total enthalpy and species molar amounts:

$$T = \frac{H - \sum_i A_i N_i}{\sum_i B_i N_i} \ . \tag{3.19}$$

Equations 3.17 to 19 coupled with the equations 3.1 to 16 can now be used to estimate the state of the converting furnace at any point during air injection in the slag blow. When the slag is poured off, the total enthalpy in the furnace is adjusted according to

$$\Delta H_P = -0.99 N_{S,bp} \sum_i X_i h_i \ . \tag{3.20}$$

In equation 3.20, ΔH_P, is the enthalpy removed from the furnace in the poured slag, $N_{S,bp}$ is the total moles of slag before pouring, X_i is the mole fraction of each slag species i, and h_i are the molar enthalpy of each slag species i. The right hand side of equation 3.20 is multiplied by 0.99 because 99% of the slag in the furnace is assumed to be poured off. After the slag is poured off air injection ceases; no material enters or leaves the furnace, so the energy balance takes the form:

$$\frac{dH}{dt} = -\dot{Q}_{out} \tag{3.21}$$

After several minutes, matte is added to the furnace. The enthalpy of the furnace changes according to:

$$\Delta H_{MA} = N_{MA} \sum_i X_i h_i \tag{3.22}$$

In equation 3.22, ΔH_{MA} is the change in furnace enthalpy caused by matte addition, N_{MA} is the total moles of matte being added, X_i is the mole fraction of the species in the matte being poured into the furnace, and h_i is the specific enthalpy of the matte being poured into the furnace at the temperature of the poured in matte.

3.1.4 Copper Blow Regime

The domain of copper blow is the same as for the slag blow. When the copper blow is first initiated, Cu_2S is oxidized to liquid copper with dissolved sulfur and sulfur-dioxide gas:

$$\mathrm{Cu_2S_{(l)}} + \left(\frac{1 - 3X_{Mon}}{1 - X_{Mon}}\right)\mathrm{O_{2(g)}} = 2\,\mathrm{Cu_{(l)}} + \left(\frac{2X_{Mon}}{1 - X_{Mon}}\right)\mathrm{S_{(Cu)}} + \left(\frac{1 - 3X_{Mon}}{1 - X_{Mon}}\right)\mathrm{SO_{2(g)}} \tag{3.23}$$

X_{Mon} is the mol fraction of sulfur dissolved in the liquid copper phase at the copper rich edge of the Cu-S binary system monotectic [78]. Equation 3.27 happens when the total melt composition is under the monotectic. Once the composition of the melt has reached the copper-rich side of the monotectic, dissolved sulfur is oxidized to sulfur-dioxide gas:

$$S_{(Cu)} + O_{2(g)} = SO_{2(g)} . \quad (3.24)$$

The temperature-dependent value for X_{Mon} is approximated by a parabola:

$$X_{Mon} = -4.80\text{x}10^{-7}T^2 + 1.32\text{x}10^{-3}T + 7.41\text{x}10^{-2} . \quad (3.25)$$

In practice, it is likely that there will be some mixing between the formed copper phase and the white metal. This means reactions 3.27 and 28 happen simultaneously. Because the exact extent of mixing is not known, the copper blow was modeled both with equations 3.27 and then 28 happening in sequence, and perfect mixing of the copper and white-metal phases. The overall reaction that occurs with perfect mixing is:

$$Cu_2S + O_2 = 2Cu + SO_2 \quad (3.26)$$

The base case result for the copper blow is for the perfect mixing case. This is compared to the otherwise equivalent case with no mixing.

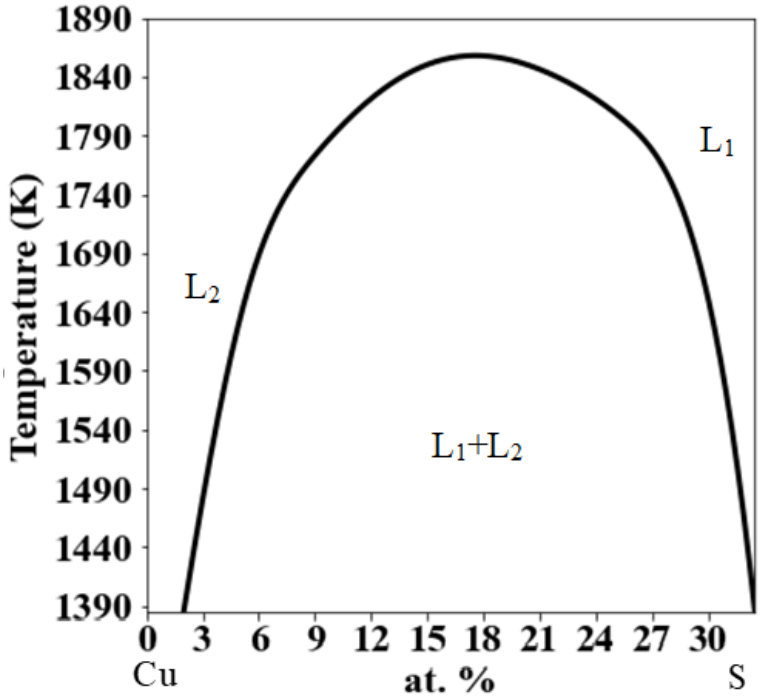

Figure 3.2 - Sketch of the Cu-S binary system at the compositions of the copper blow [78]

3.1.5 Mass Balance for the Copper Blow

The copper blow mass balance is similar to the slag blow mass balance, but without equilibrium constant relationships. Equilibrium constant relationships are not needed because extent of equation 3.30 is always one; when no mixing of the copper and white metal is assumed equation 3.29 can be used to precisely account for the extent of equation 3.27. The mass balance equations thus are:

$$\frac{dN_{Cu}}{dt} = 0 \tag{3.27}$$

$$\frac{dN_S}{dt} = -\dot{N}_{O_2,in} \tag{3.28}$$

It is assumed that all of the copper that is in the furnace at the start of the copper blow remains in the furnace. Because no equilibrium calculation is being done, it is simply assumed that all the formed gas leaves the furnace as the off-gas at the same rate it is generated.

3.1.6 Heat Balance for the Copper Blow

Equations 3.17-19 are used for the copper-blow heat balance and temperature calculation, although the chemical species used are those found in equations 3.27, 28, and 30. Additionally, because the furnace volume is lower and liquid copper and white metal have lower emissivities than slag, it is expected that the heat transfer out of the furnace during the copper blow will be lower than in the slag blow [24]. The values used for the heat transfer are given in the results section.

3.1.7 Property Data

3.1.7.1 Thermodynamic Data for Species

For species thermodynamic properties, the work of Barin [74] to linearly best-fit temperature dependent expressions for molar enthalpy:

$$h_i = A_i + B_i T, \tag{3.29}$$

where h_i is molar enthalpy of species *i*, and A & B are constants; specifically, B_i is the heat capacity of the *i* near 1473K. Molar entropies and Gibbs free energies were found using the estimated heat capacities and standard expressions for these terms.

3.1.7.2 Activity Coefficient Data

Activity coefficients for the condensed species were taken from Table 2 of Eriksson & Björkman's work [26].

3.1.7.3 Heat Flows

The heat transfer in a converting furnace is a complex topic. To simplify the model, a constant heat transfer rate was chosen such that the terminal temperature of the baseline case of the slag blow would be within 10K of the terminal temperature given by the compared industrial data. This approach allows the model output to be usefully compared to the industrial data, because the temperature histories produced throughout the slag blow will not necessarily equal the industrial data for the same amount of slag blow time. So while the model has been fit to one temperature data point, it has not been fit to the remaining temperature data points, making a comparison between the model and industrial temperature histories useful from a validation standpoint.

3.1.8 Exergy Balance for the Slag and Copper Blows

Exergy is added to the converting operation as copper matte. There is a negligible amount of exergy in the added flux and air. The exergy added to a process has one of three fates. It can be carried out of the process as in the product, which is defined by the purposes of the process. For converting, the matte, copper, and sulfur-dioxide bearing offgas are products because these are all revenue sources for the plant. Other exergy streams leaving the system, but that do not serve the direct purpose of the process, are said to be losses. For converting, these are the slag and heat transfer out of the furnace. Exergy lost by the process may be recovered by downstream operations, but if it is not, that exergy is destroyed as the stream is thermally and chemically dispersed into the environment. Finally, exergy can be destroyed/annihilated and so is not recoverable. This destruction of the ability of an energy stream to do useful work can be seen, for example, in the

drop in temperature during the spontaneous transfer of heat. So, unlike energy, which is always conserved when transferred or changed, exergy always experiences an irreversible degradation when transferred or changed, as no process is completely reversible. Please see section 2.1.4 for further discussion on exergy balances.

3.1.9 Solution Method

The solution method used for the slag blow is the same as used for the smelting furnace except for the initial condition. The furnace initializes with a certain amount of matte at the composition of the settling furnace preceding converting. A guess for the offgas composition is made; because the total amount of gas in the converting furnace is on the same order as the amount of reaction in 10s of converting, the offgas composition will rapidly go to its practical value. A small amount of slag (*e.g.* 1 kmole) is also taken to be in equilibrium with the matte and gas. This small amount of slag is necessary for solving the thermochemical mass balance and does not affect the results. The copper blow is solved by Euler's method.

3.2 Results for the Slag-Blow

3.2.1 Base Case

This case was run with parameters similar to those used at an industrial smelter. The smelter in question is the Freeport-McMoRan Inc. smelting plant located in Miami, Arizona. The parameter values used are listed in Table 3.2. Temperature and composition histories were examined. Additionally, an exergy balance was done for the average converter performance over the whole slag blow. The results are presented in figures 3.3 through 3.7.

Table 3.2 - Parameter values used for the base case

*Refers to time = 0

Parameter	Value
Initial* Cu_2S (kmole)	840
Initial Fes (kmole)	660
Initial FeO (kmole)	5.80
Initial Fe_3O_4 (kmole)	0.06
Initial Cu_2O (kmole)	0.01
Initial SiO_2 (kmole)	4.00
Initial P_{O_2} (atm)	3.0×10^{-9}
Initial P_{SO_2} (atm)	0.40
Initial P_{N_2} (atm)	0.60
Initial Temperature (K)	1380
Air Feed Rate (kmole/s)	0.943
Air Oxygen Grade	0.21
Oxygen Efficiency	0.84
Silica Feed Rate (kmole/s)	0.075
Heat Loss Rate (MW)	6.5

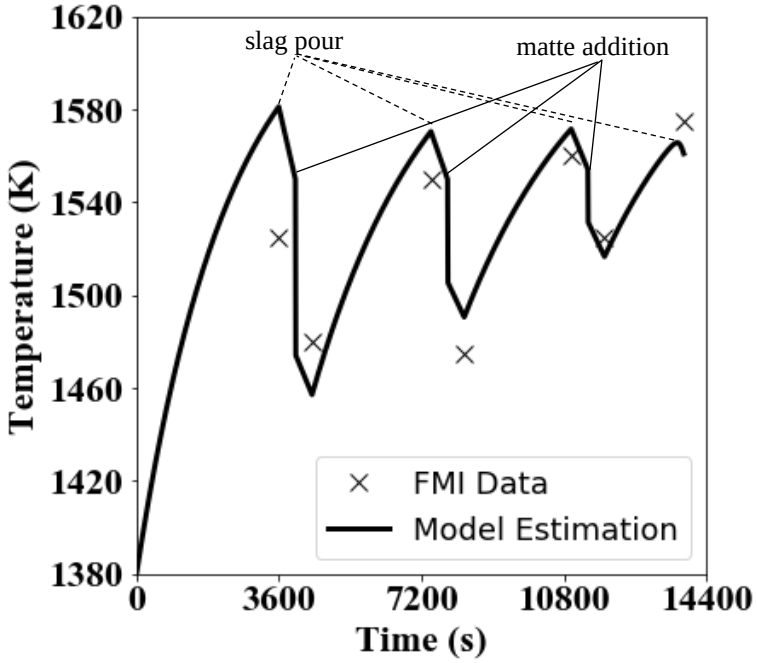

Figure 3.3 – Temperature history of the melt for the base case and corresponding FMI data.

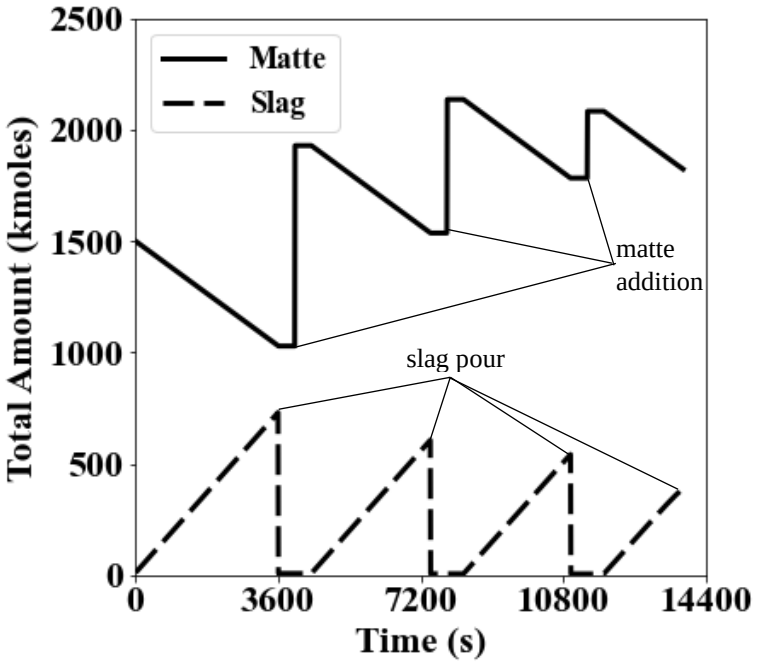

Figure 3.4 - Quantity histories for the matte and slag during the slag blow

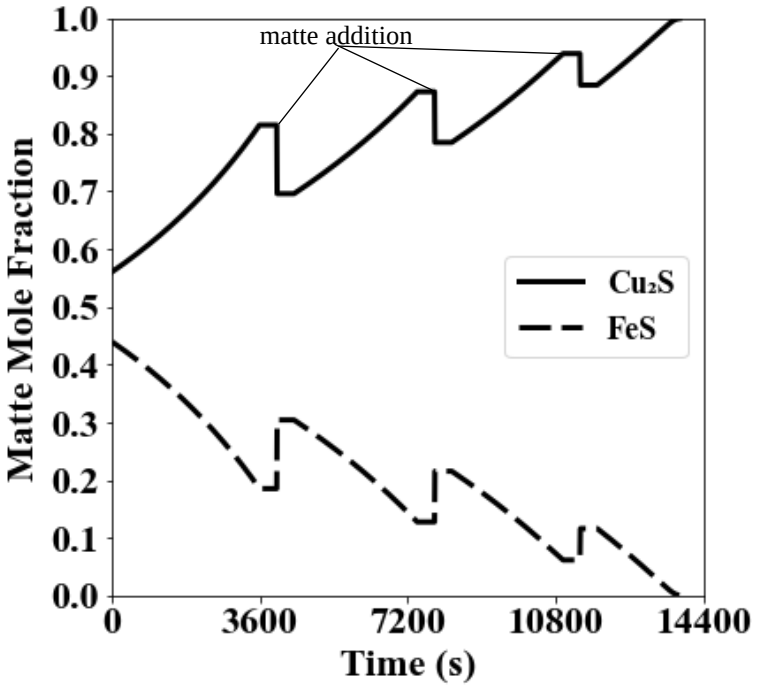

Figure 3.5 – Matte composition history for the base case

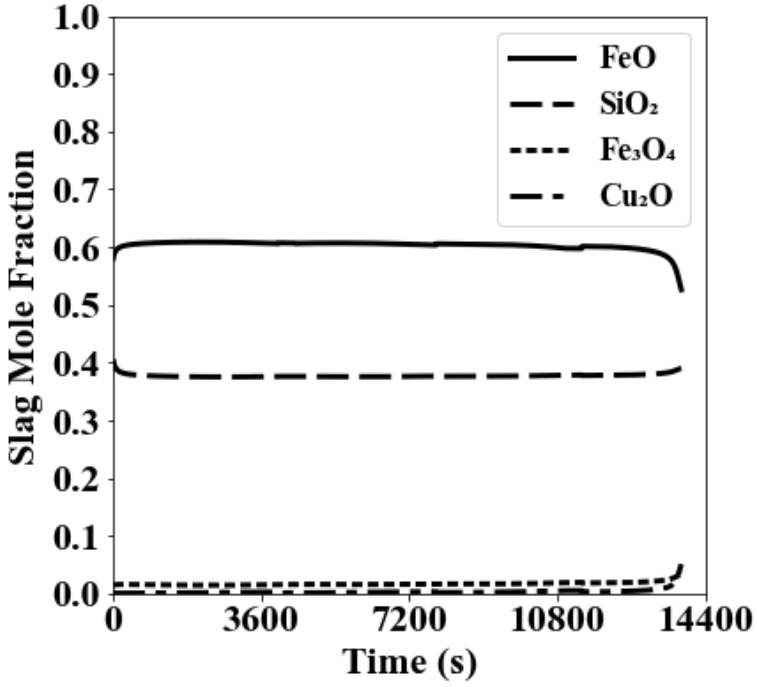

Figure 3.6 - Slag composition history for the base case

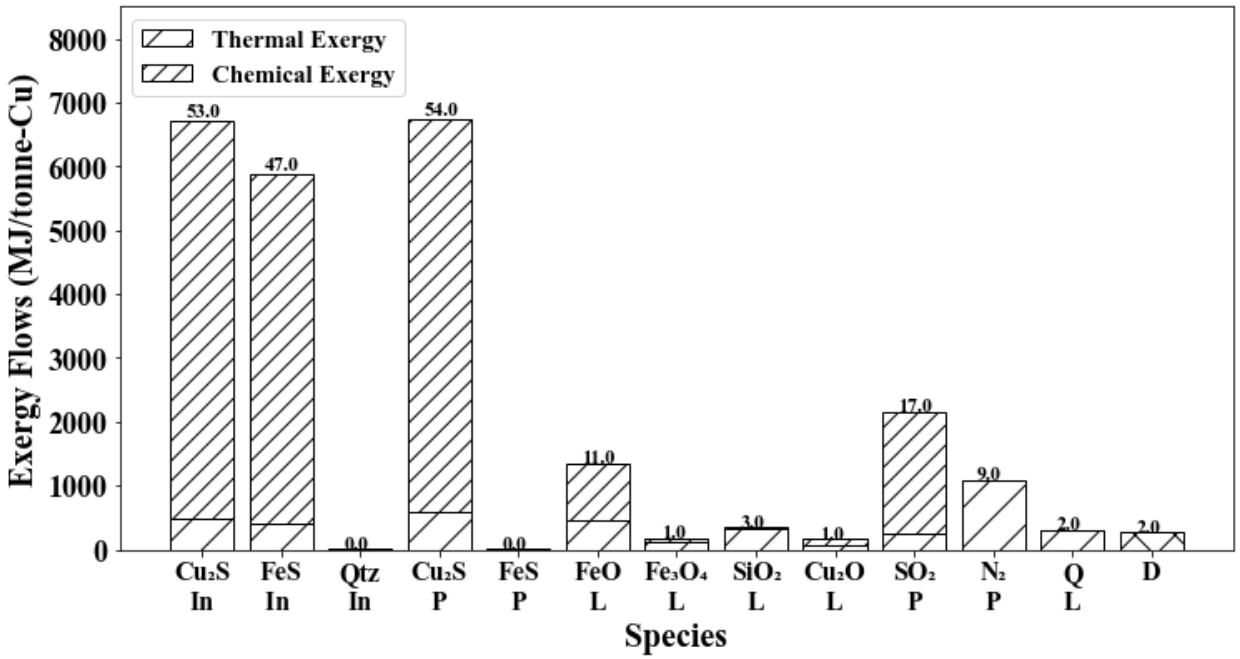

Figure 3.7 - Exergy fed ("In",Cu_2S, FeS, Qtz), exergy that goes with product ("P",Cu_2S, SO_2, N_2), exergy lost ("L", FeO, Fe_3O_4, SiO_2, Cu_2O, Q), and destruction (D) for the base case. Labels on tops of bars are the percentages of inflow or outflow

The first result of interest is the furnace temperature history and its comparison to the Freeport-McMoRan Data. The model shows temperature rising during air injection, due to the exothermic chemical reactions taking place. The temperature steadily falls after slag pouring and matte addition due to heat transfer out of the furnace. The temperature sharply drops when matte is added, because the added matte is at 1380K. Overall, the model appears to perform favorably with respect to the given temperature data. This close agreement is in spite of probable uncertainty in the optical pyrometry measurements and in the estimation of the oxygen efficiency. Furthermore, the reported amounts of slag and matte transferred in the plant only estimated to within 10%.

The temperature history shows some interesting features. First, one can see that the rate of temperature increase during the blows decreases as the temperature rises. The reason for this is that as the temperature of the furnace increases, more heat is required to bring the injected air and silica to temperature; additionally, the reactions become less exothermic. After the blow, the temperature of the furnace falls rapidly and even more so after the new matte addition. However, the rate of temperature decrease is faster at the higher temperature, *i.e.* after the slag is poured off, than after matte addition. The reason for this is that the total quantity of matter in the furnace is

less before than after matte addition, so the same rate of heat transfer causes a lower rate of temperature decrease after matte addition. The temperature falls at the very end of the simulation because nearly all of the FeS has been converted to iron oxides, so the much less exothermic Cu_2S oxidation has begun in earnest, and this reaction is much less exothermic than FeS oxidation.

Figure 3.4 shows the matte composition history for the baseline case. As oxidation of the matte occurs, FeS is converted to FeO and SO_2, so the grade of Cu_2S in the matte increases, but not monotonically. Added matte contains more Fe than the partially converted liquid in the vessel, so the Cu_2S grade decreases with matte addition. By the end of the slag blow the matte has successfully been converted to white metal (Cu_2S).

Figure 3.5 shows the slag composition history. The composition of the slag is relatively constant throughout the slag blow, although just before the process is complete, the grade of Cu_2O in the slag begins to rapidly increase. This oxidation begins as the matte has run out of FeS to oxidize.

The gas phase composition remains mostly flat throughout the entire slag blow with occasional bumps when new matte is added. The SO_2 grade of the converting offgas (12%) is about five times lower than the SO_2 grade of smelting offgas when smelting is done with 95% oxygen enrichment in the injected air. However, the total offgassing rate of a single converting furnace is about three times higher than for the modeled smelting furnace. Such information is helpful to the operation because it provides the sulfuric acid plant with a better idea of how much dilution of the incoming gas from the smelter and converters is needed.

Figure 3.7 shows the results of the exergy balance for the baseline case. The exergy fed to the process entirely comes from the matte produced *via* smelting and settling. Eighty percent of this fed exergy leaves the process as product white metal and offgas. Sixteen percent leaves the process as losses in slag, and two percent leaves the process as losses in heat transfer. It presently appears impractical to recover the exergy lost to slag. Although slag can be recycled to recover copper, the exergetic content of the slag negligibly changes, and the slag is dumped with all of it thermal and chemical exergy. A water cooling jacket may be able to recover some of the exergy lost to heat transfer, but this appears impractical because this exergy stream is so small. Two percent of the fed exergy is destroyed.

3.2.2 Air Injection Rate Variation

Changes to the air injection rate are the simplest way to change production rate in a converting operation. The air injection rate was varied +/- 5% about the baseline case value. Figure 3.8 shows the effect of variation to the air injection rate on process temperature. Higher air injection rates lead to more rapid temperature increase because more oxygen is available for FeS oxidation.. The terminal temperature is lower for the higher air injection rate case because the FeS finishes oxidation sooner than the baseline, and so more Cu_2S oxidation (which is less exothermic than FeS oxidation) occurs. Cu_2S oxidation is not sufficient to make up for the heat required to bring the added air to temperature and lost to heat transfer.

Figures 3.9 and 10 show the influence of air injection rate on the composition of the matte and slag, respectively. Higher air injection lead to quicker attainment of white-metal; however, with the refining time is kept the same between the cases, the terminal Cu_2O fraction of the last slag produced increases by a dramatic 25%. These results show the importance of careful control of the converting time. The change in air injection rate had a negligible impact on the slag composition before white-metal oxidation, offgas composition, and the exergetic performance of the operation.

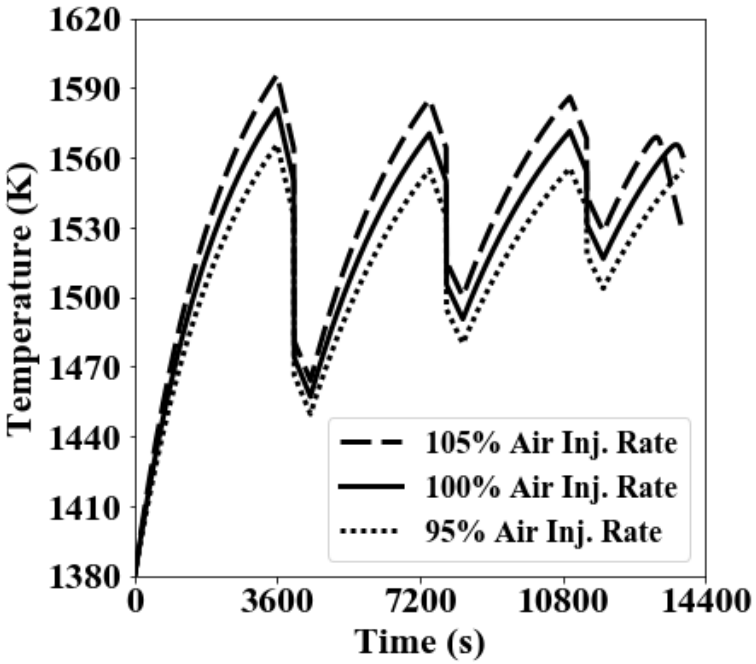

Figure 3.8 - Temperature histories for the air injection rate variation study

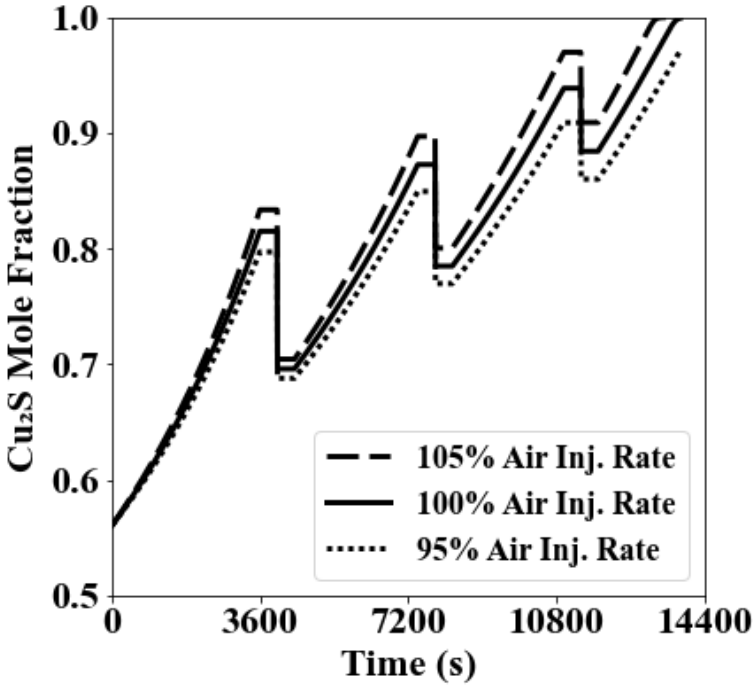

Figure 3.9 - Composition history of the matte for the air injection rate study

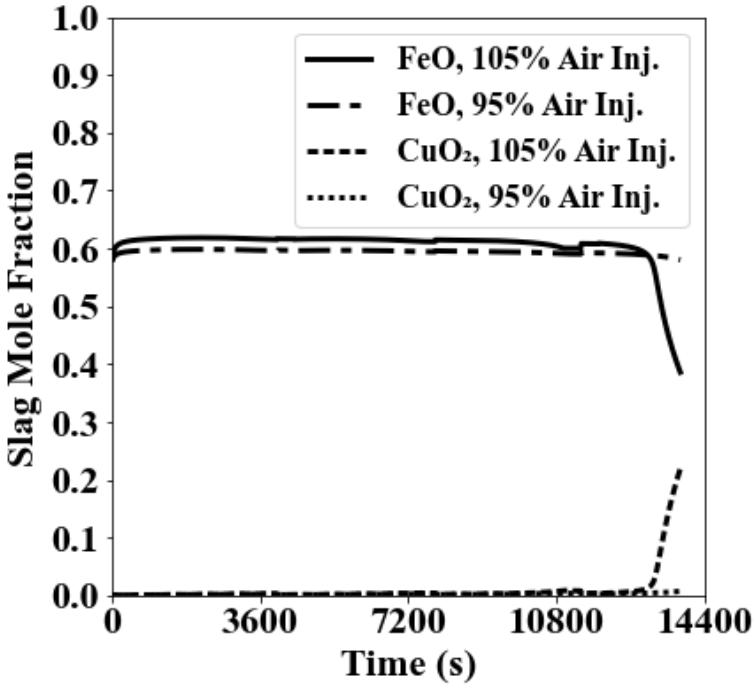

Figure 3.10 - Composition history for the slag for the air injection study

3.2.3 Oxygen Grade Variation

Many converting operations have the option to enrich the oxygen grade of the air being injected to the converters. This can be helpful if there is a large amount of revert material that the converters need to dispose of (additional revert requires more heat) or if there is a critical need for the small amount of offgassing capacity that higher oxygen grades free to be used elsewhere in the plant. However, the extent to which oxygen enrichment is possible is limited both by refractory corrosion around the tuyeres and by the effect of heating. When bubbling injection is used, 26% O_2 in the injected gas being taken as a maximum [79–82]. The cases studied in this section increased the oxygen grade of the injected gas to 22% and 23%. The total oxygen injection rate was kept constant so that Cu_2S oxidation at the end of the slag blow would not start to predominantly occur. It is expected that an operating plant would likewise decrease the total air injection rate when the oxygen grade is increased. Overall, this modeling work showed (fig. 3.11) that a one percentage increase in the injected gas oxygen grade leads to a 30 K increase in terminal operating temperature. Finally, changes to the O_2 grade had negligible effects on the condensed phase compositions and only a small effect on the offgas composition, lowering the nitrogen grade by about a percentage point and replacing it with sulfur dioxide. Negligible effects were also seen in the exergetic performance of converting.

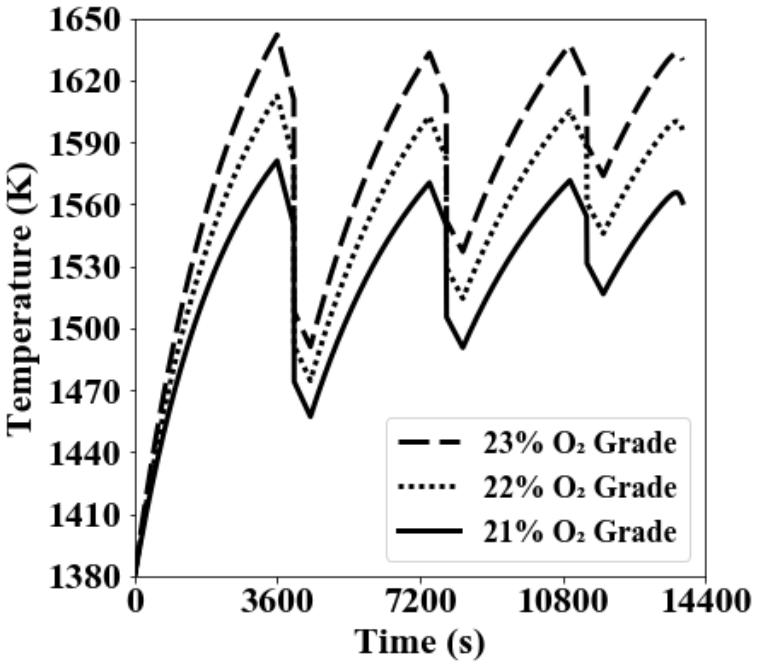

Figure 3.11 – Temperature histories for the oxygen grade variation study

3.2.4 Silica Addition Variation

The effect of changes to the silica addition rate was studied over the range of 0.065 kmole/s SiO_2 addition (14.0 tonnes/hr) to 0.085 kmole/s (18.4 tonnes/hr). It was found that changes to the silica addition rate had a negligible influence on the composition histories in the converter and on the exergetic performance of the converter. The terminal Cu_2O fraction in the slag increased by 0.1%, from 5.0% to 5.1%. over the silica addition rate range studied due to the thermodynamics of the slag phase. The increase in silica addition over the range studied decreased the temperature (fig. 3.12) at the end of each slag sub-blow by about 40K because more heat was used bringing silica to temperature. Higher silica addition was thus helpful in the sense that it lowered the amplitude and average temperature of the temperature histories. However, high silica addition caused higher dissolved copper grades in the slag and also causes larger volumes of slag in the furnace (because more slag forming material is added to the furnace) and increased total cost of raw materials.

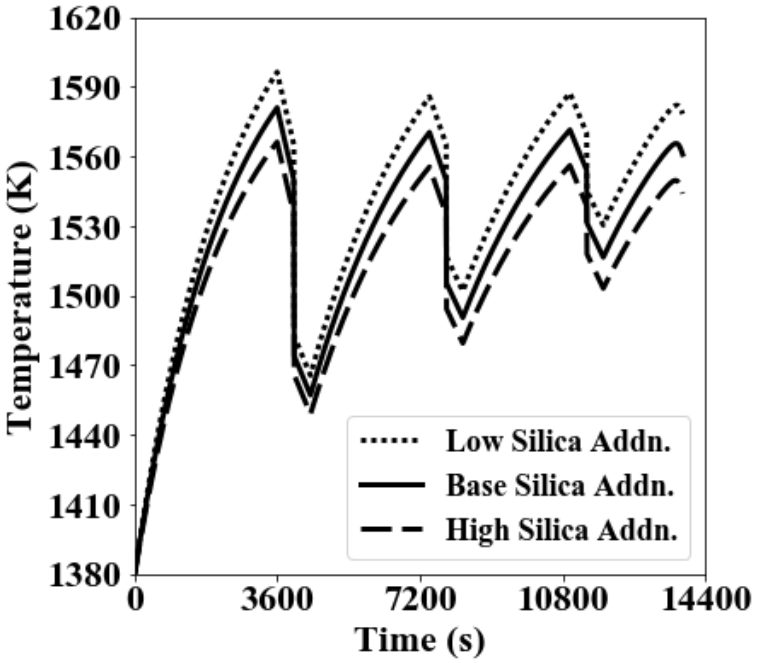

Figure 3.12 - Temperature histories for the silica addition rate study. Low Silica corresponds to 0.065 kmole SiO_2 per second addition; base silica addition is 0.075 kmole SiO_2 per second; high silica addition is 0.085 kmole SiO_2 per second

3.2.5 Starting Matte Composition Variation

The starting matte composition was varied to have base case molar amounts of FeS or Cu_2S, and +/- 20% initial molar amounts of the other species. Table 3.3 shows the values of the parameters used for each study. The oxygen addition rate was changed for the cases with high and low FeS such that the oxygen addition rate to initial FeS ratio stayed the same as base case.

Table 3.3 - Parameter levels used in the initial composition variation cases

Case	Initial Cu_2S (kmoles)	Initial FeS (kmoles)	X_{Cu_2S}
High Cu_2S	1008	660	0.604
Low Cu_2S	672	660	0.504
High FeS	840	792	0.515
Low FeS	840	528	0.614

Changes to the initial matte composition and corresponding changes to the oxygen addition rate had a significant effect on the temperature histories; temperature histories for the first slag sub-blow are shown in figure 3.13. Higher amounts of FeS in the initial matte required more FeS oxidation per time, leading to a more rapid temperature increase despite the greater initial thermal mass (due to more melt) in the furnace. Higher amounts of Cu_2S led to more gentle temperature increases due to an increase in the ratio of thermal mass to amount of FeS oxidation per time. Overall, these results strongly suggests that operators may wish to look at increasing the copper grade of the matte that leaves the smelting furnace. This would shorten converting time for the same converting air injection rate (*i.e.*, same offgasing rate in the converters) and weaken the thermal cycling that occurs in these furnaces, possibly extending converter campaign life as well. The smelting furnace operators could increase matte grade by increasing the oxygen-enriched air injection rate. Regarding the composition, all cases reached white-metal after the same total converting time. This is because the oxygen injection rate to initial FeS ratio was kept constant for all cases. The amount of dissolved copper lost to slag negligibly varied between the cases, because each case was stopped before white-metal would start to be oxidized.

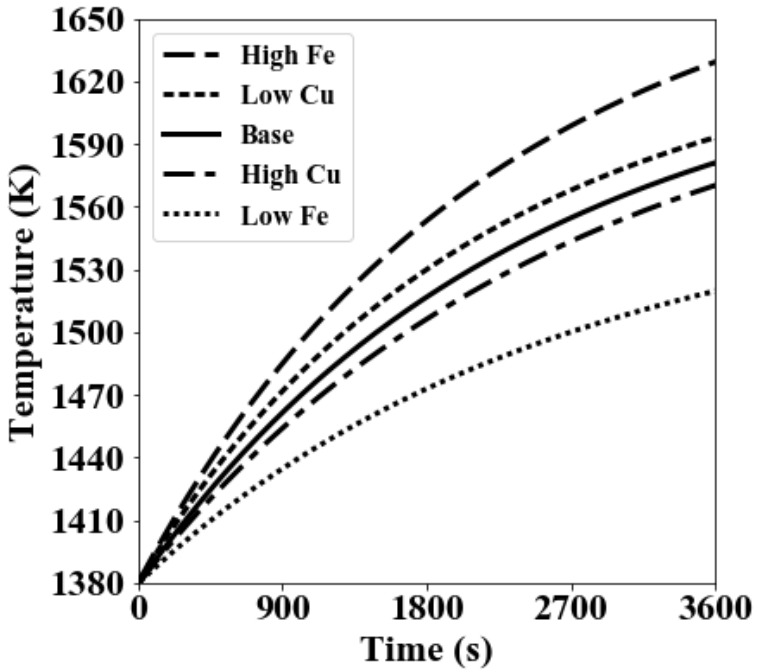

Figure 3.13 - Temperature histories for the initial matte composition variation cases. Only the first slag sub-blow is plotted for clarity

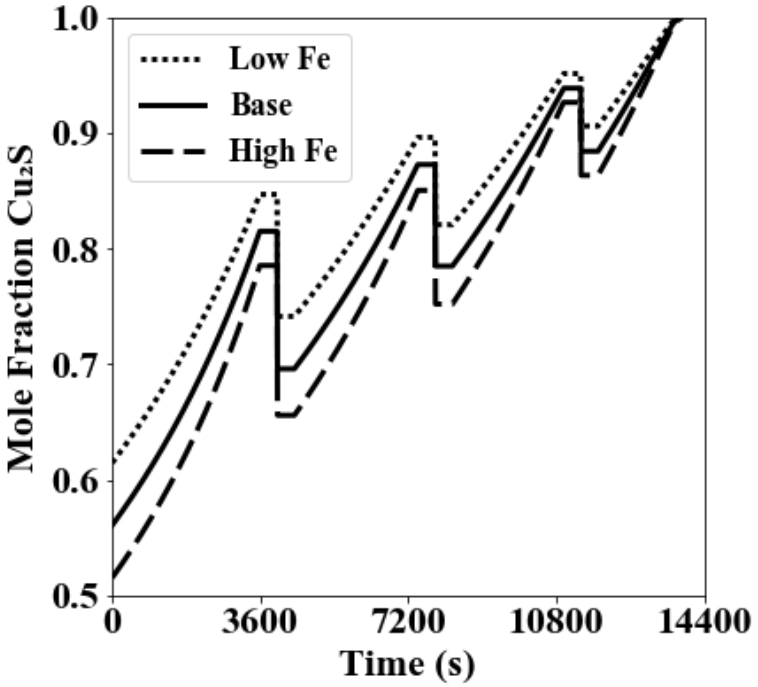

Figure 3.14 - Matte Composition histories for the initial matte composition variation cases. The low Cu case overlays the high Fe case, and the high Cu case overlays the low Fe case

3.2.6 Oxygen Efficiency Variation

One parameter in this model is not a physical input but rather a numerical factor used to estimate the fraction of added oxygen used in the reactions. This oxygen efficiency, θ, was varied +/- 10% from the base-case value of 84%; the rate of air injection was kept constant between all the cases. Temperature histories are shown in figure 3.15. A 10% increases in the oxygen efficiency caused an approximately 110K increase in terminal temperature. The reason for this is that more FeS oxidation happens per time. The last 2000s of the 94% oxygen efficiency case saw a large amount of white metal (Cu_2S) oxidized to Cu_2O, which explains the temperature decrease. Figure 3.16 shows that a 10% increase to the oxygen efficiency led to an increase in SO_2 content of the offgas from 12.5% to 14% because more SO_2 is being produced per time, which in turn happens because more FeS is being oxidized per time.

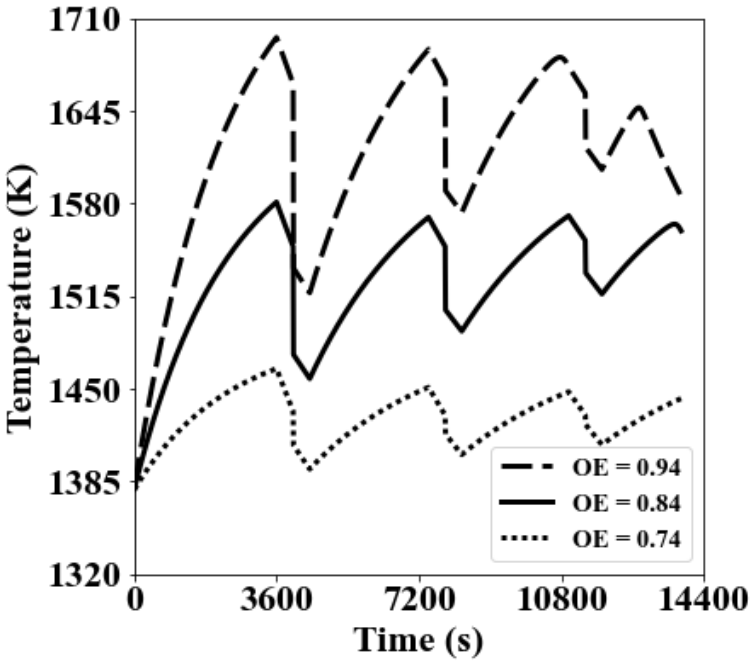

Figure 3.15 – Temperature histories for the oxygen efficiency variation cases

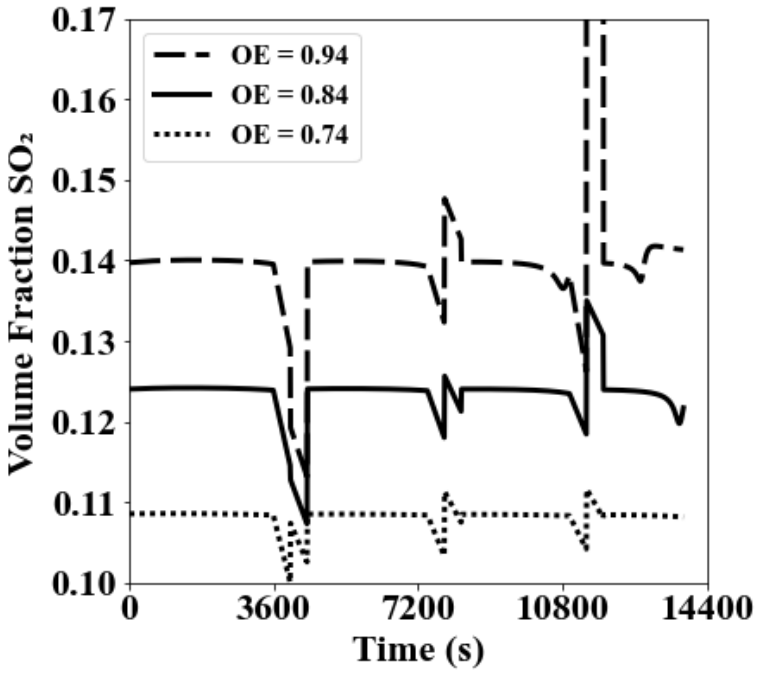

Figure 3.16 - Offgas composition histories for the oxygen efficiency variation cases

3.2.7 Heat Loss Variation

Although converting operations do not have direct control over the rate of heat loss from the converter, it is another furnace performance parameter which must be estimated. To evaluate the sensitivity of the model furnace behavior, the rate of heat loss was varied +/- 1 MW around the base-case value of 6.5 MW. The results of this study are shown in figure 3.17, which shows that higher heat loss rates decrease thermal cycling and the average temperature of the converter. Composition histories and exergetic performance did not significantly change over the heat loss range studied.

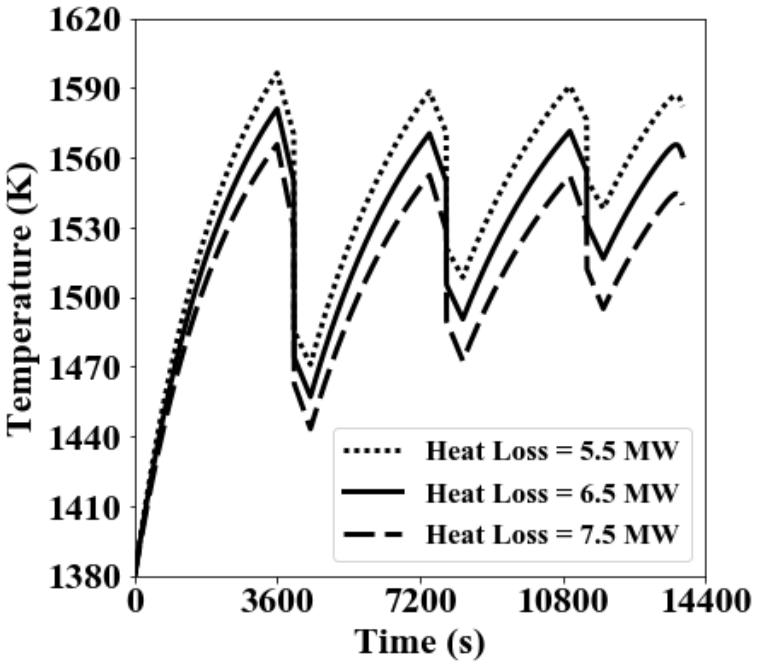

Figure 3.17 - Temperature histories for the heat loss variation study

3.3 Results for the Copper-Blow

For the copper blow, the behavior of the converter with variations in oxygen efficiency, oxygen grade, total oxygen injection rate, and heat loss rate was examined. For the baseline case, model performance with perfect mixing of the white metal and liquid copper and model performance with no mixing of these phases was compared. It will be shown that the perfect mixing case corresponds much more closely to industrial practice. Because of this, only perfect-mixing behavior is shown for the cases other than the baseline.

3.3.1 The Baseline Case

Table 3.4 shows the parameter values used for the base case. The initial amount of Cu_2S corresponds to the total Cu_2S added to the converter over the course of the slag blow. The air injection rate is the same as used in the base case of the slag blow. The nwq oxygen efficiency is about 10% higher than for the slag blow, based on estimations by the Miami Smelter. The rate of heat loss is expected to be lower during the copper blow than during the slag blow due to the reduction of furnace volume occupied by melt as well as the higher emissivity of liquid copper over slag [24].

Figure 3.18 shows the temperature histories for a perfectly mixed melt and the melt with no mixing of the liquid copper and white-metal phases for the base case parameter values. For the case with no mixing, the temperature gradually decreases over the course of several hours when the total melt composition is under the monotectic. Once the monotectic is exited and the melt is single phase metallic copper, the temperature rapidly increases due to the 140 MJ/kmole increase in magnitude of enthalpy of reaction from equations 3.27 to 28. This rapid increase in temperature is not observed by the FMI converters anywhere in the copper blow. It seems likely that the assumption of reactions only occurring in one phase at a time does not actually hold in a real converter, allowing significant amounts of the excess reaction heat observed at the end of blow to be spread out over a much larger period. The temperature history shown when perfect mixing of the two phases is assumed is much closer to the industrial data in that there is no rapid temperature increase. The industrial data plotted in figure 3.18 is the average of three converting copper blows at the FMI Miami smelter; the spread for any given data point was at most +/- 50K.

Table 3.4 - Parameter levels used in the baseline case

*1460K is the average initial temperature of the received data

Parameter	Value
Initial Cu_2S (kmole)	1848
Air Injection Rate (kmole/s)	0.943
O_2 Grade of Injected Air	0.21
Oxygen Efficiency	0.95
Rate of Heat Loss (MW)	4.5
Initial Temperature (K)*	1460

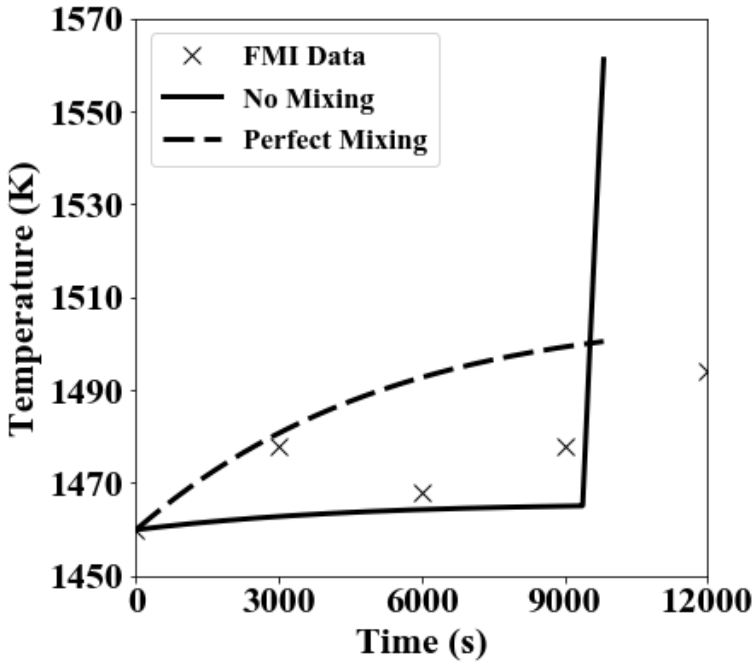

Figure 3.18 - Temperature histories for the copper-blow base cases

Figure 3.19 shows the composition history of the melt during the copper blow with no mixing of the copper and white-metal phases. When no mixing occurs, the amount of dissolved sulfur gradually builds in the melt and is completely depleted in last 500s of converting. When perfect mixing occurs, the Cu and Cu_2S are both pure and the amount of dissolved sulfur is zero at all times.

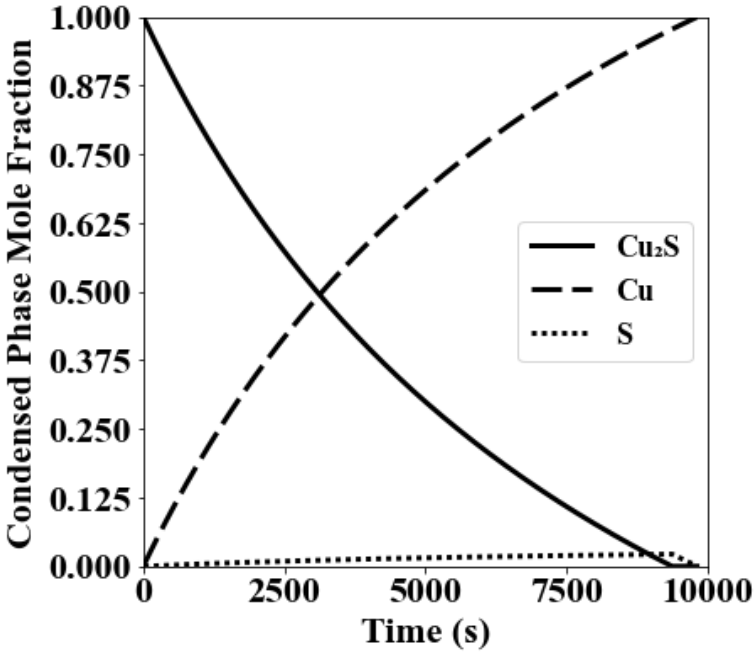

Figure 3.19 - Composition history of the condensed phases during the copper blow with no mixing

The offgas composition is effectively constant over the copper blow, at 79% nitrogen, 20% sulfur dioxide, and 1% oxygen. Oxygen is present in the offgas due to an oxygen efficiency of less than one.

Figure 3.20 shows the exergy balance for the base case. The exergy balance shows that 90% of the fed exergy leaves the process as product exergy in the blister copper and the offgas. Only 2% of the input exergy is lost (as heat transfer). Some thermal exergy may still be recoverable from the offgas product, as sulfuric acid plants require input gas temperatures to be around 900K. The exergy destruction is 8%.

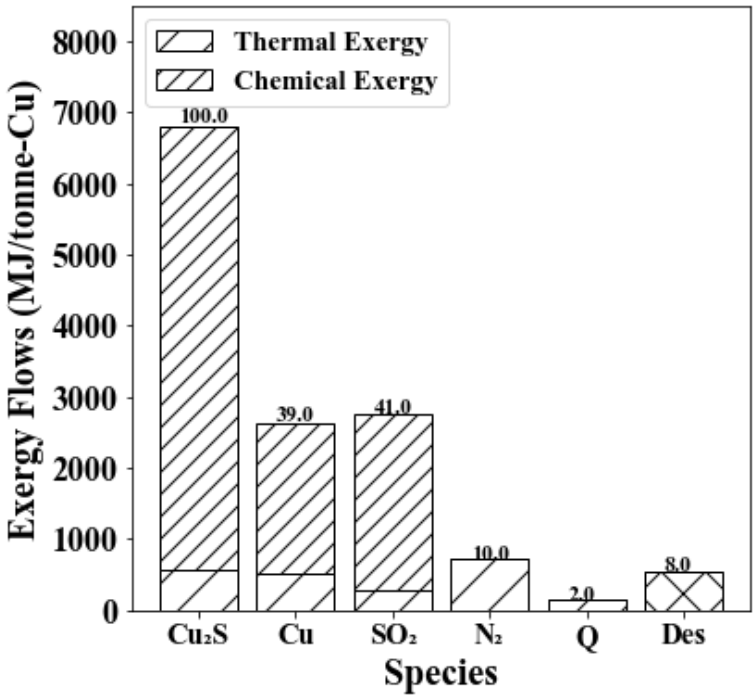

Figure 3.20 - Exergy balance for the copper-blow base case. Fed exergy: Cu_2S. Product exergy: Cu, SO_2, N_2. Lost exergy: heat transfer (Q). Destroyed exergy: Des. The exergy of dissolved sulfur and oxygen in the offgas was negligible, and so not included for clarity

3.3.2 Oxygen Grade Variation Cases

The oxygen grade of the injected air was increased to 22% and 23% from the base case value of 21%. The results of this study are shown in figure 3.21. The results show that single percentage increases to the oxygen grade cause increases to the terminal temperature of the copper blow on the order of 50 K, which amplifies the deleterious effects of thermal cycling. The main advantage of using a higher oxygen grade in the copper blow is the decrease in the offgas load of the converting operations. As such, unless the plant has a critical need for offgassing capacity to be directed away from the converter, it is recommended that oxygen enrichment in the copper blow not be used. Changes to the oxygen grade of the injected gas over the range studied had a negligible impact on composition histories and exergetic performance of the converter.

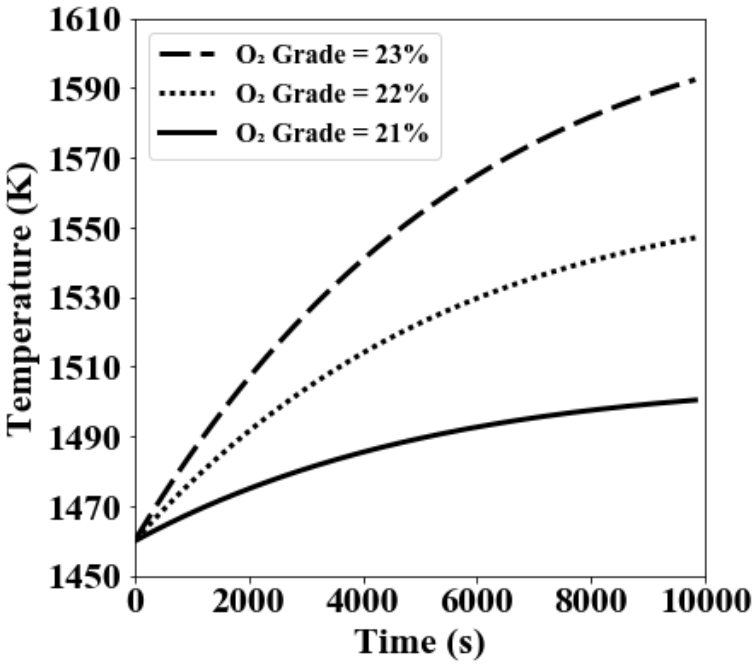

Figure 3.21 - Temperature histories for the O_2 grade variation cases

3.3.3 Air Injection Rate Variation Cases

The air injection rate was varied +/- 20% from its base case value of 0.943 kmole/s. Temperature histories for this variation are shown in figure 3.22. There is a tradeoff between production time and thermal cycling. Higher air throughput lead to shorter converting times, and thus higher maximum production, but also higher temperatures. This means increased thermal cycling. Changing the air injection rate had a proportional effect on the composition histories; 20% higher air injection rate led to a 20% faster copper blow. As such, another tradeoff is between production rate and required offgas load. Higher production rates require higher offgas load, which could be partially mitigated by using oxygen enrichment, but as mentioned in section B, will lead to increased thermal cycling. Changing the air injection rate over the range studied had a negligible impact on the exergetic performance of the copper blow.

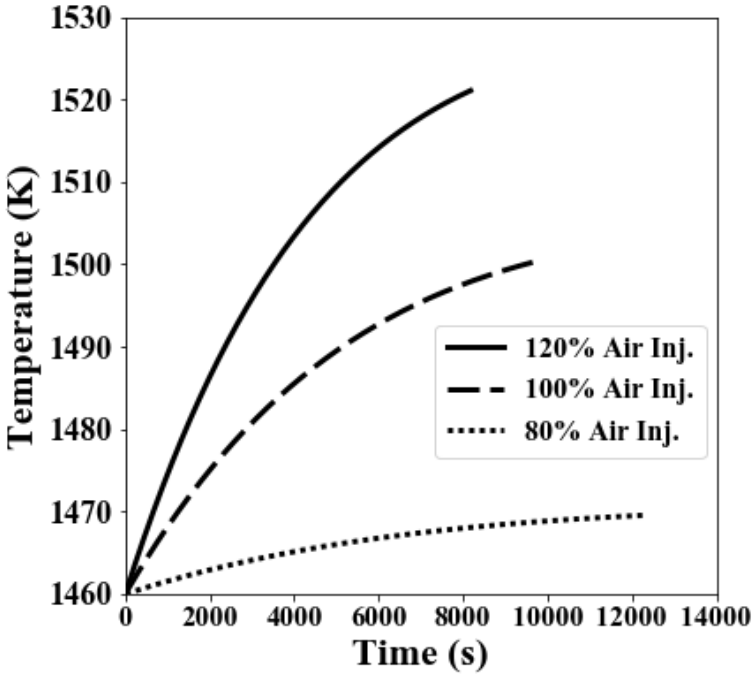

Figure 3.22 - Temperature histories for the air injection rate variation cases

3.3.4 Effect of Changes to Oxygen Efficiency

The oxygen efficiency of the copper blow was varied +/- 5% about the base case value of 95%. Although converting operations do not have direct control over the oxygen efficiency, variation to this parameter is interesting for analyzing model performance. The temperature history for the oxygen efficiency study is shown in figure 3.23. An increase to the oxygen efficiency of 5% (oxygen efficiency equal to 100%) led to a terminal temperature increase of 60K and an increase in production rate. Decreasing the oxygen efficiency by 5% (oxygen efficiency of 90%) caused a terminal temperature decrease of 50K and decrease in production rate. These results arae because the total oxygen injection rate was maintained while more oxygen was available for reaction. Changes to the oxygen efficiency over the range studied had a negligible impact on exergetic performance.

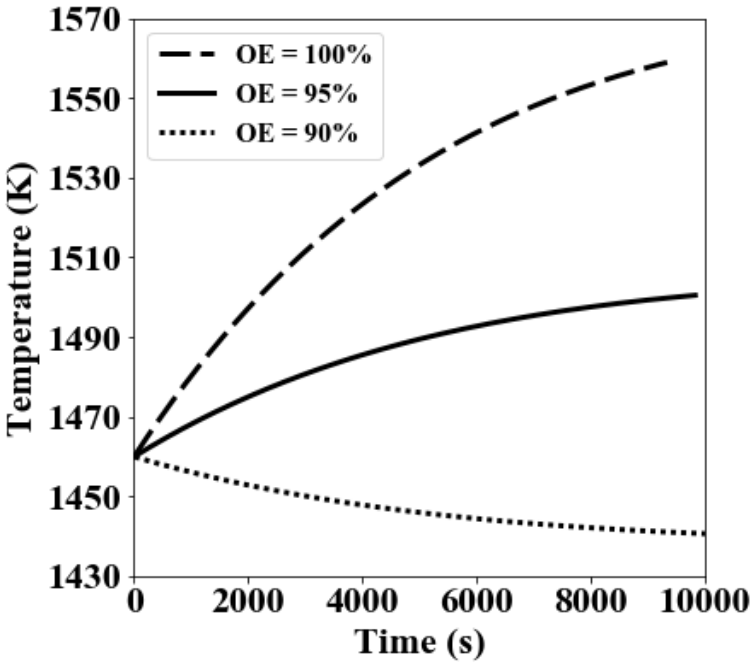

Figure 3.23 - Temperature histories for the oxygen efficiency cases

3.3.5 Heat Loss Variation Cases

Although the plant does not have direct control over the converter heat loss rate, variation of this parameter is interesting in terms of model performance. The heat loss was varied +/- 1 MW from its base case value of 4.5 MW. The results of this study are shown in figure 3.24. It is seen that 1 MW changes produce terminal temperature changes of about 30 K. Changes to the heat loss rate had negligible effects on the composition histories. The higher heat loss rate caused a less than 1% increase in exergy lost with heat loss, and a less than 1% decrease in exergy leaving with the copper and offgas. The decrease to the heat loss had the opposite effect.

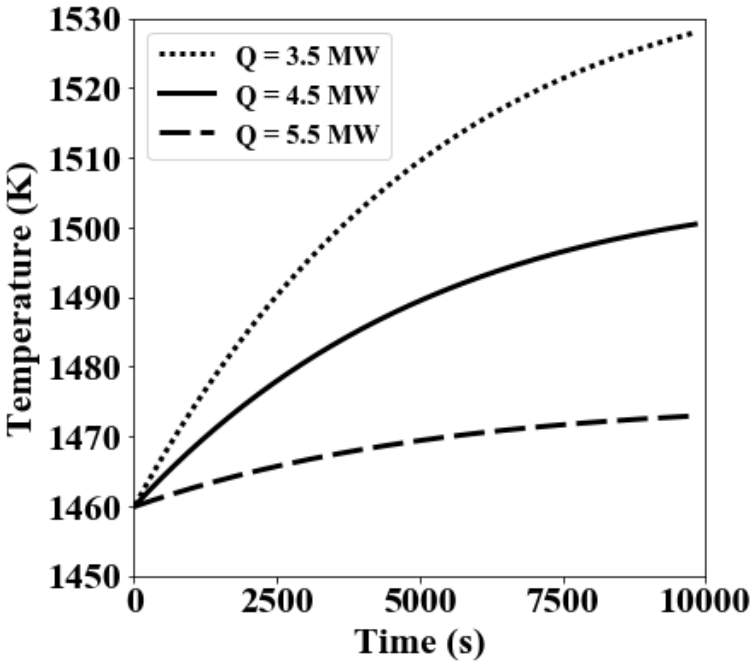

Figure 3.24 - Temperature histories for the heat loss variation cases

3.4 Conclusions and Recommendations

A transient equilibrium model was made for the slag blow of Peirce-Smith/Hoboken converting with a fayalitic slag system. A transient model was also made for the copper blow of Peirce-Smith/Hoboken converting. The models successfully estimated transient temperatures and phase compositions for a parametric study, the baseline of which was similar to industrial practice.

It was found that converter temperature and phase compositions were strong functions of air injection rate. Converter temperature was also a strong function of injected-air oxygen grade, oxygen efficiency, and heat loss rate, whereas converter phase compositions were weak functions of these parameters. For the slag blow, it was found that converter temperature and phase compositions were strong functions of the composition of the matte being added to the furnace.

From the results, we make the following observations and recommendations:

1. Attempts should be made to minimize thermal cycling in the converters. As such, injected gas oxygen grade should not be increased unless there is a critical need for the offgassing capacity this frees

2. Plantwide copper production under a fixed maximum offgas load can be increased by increasing the matte grade fed to the converters. This is because smelting furnaces can use oxygen enriched air, allowing the same amount of copper purification with less offgas production than converters. This has the added benefit of decreasing the thermal cycling in the converters.
3. Improvements to oxygen efficiency free offgas load in the converters but also cause greater thermal cycling for a constant copper production rate
4. Eighty percent of the exergy fed to the slag blow of converting leaves with product, and about 90% of the exergy fed to the copper blow of converting leaves with product. The most promising source of exergy recovery is the converting offgas (a product because of the economic value of the sulfuric as produced from it), as sulfuric acid plants require inlet gas at a temperature lower than that produced by converting.

CHAPTER 4. COPPER FIRE REFINING

Copper fire refining is a two step process. The first step removes residual dissolved sulfur left at the end of converting. The second step removed the dissolved oxygen. At the end of reduction, the liquid copper is cast as anodes which are ready for electrolysis. This chapter will examine the desulfurization step first, followed by reduction.

4.1 Desulfurization of Blister Copper

4.1.1 Model Description

4.1.1.1 Model Conditions

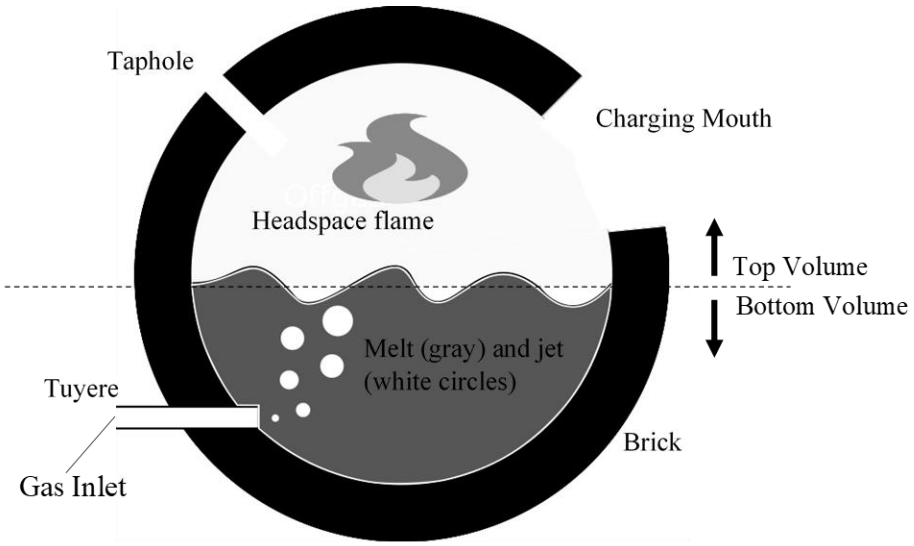

Figure 4.1 - Schematic of a copper fire refining furnace

The model divides the vessel into three distinct regions (Figure 4.1): the liquid copper melt ("bottom volume"), a bubble-jet that goes through the melt (the jet is gas only), and the furnace headspace ("top volume"). The melt and the headspace each are considered spatially homogeneous in temperature and composition within their respective regions; the jet is modeled as a 1D flow reactor along the jet's height. Chemical reaction rates, bubble geometry and velocity, and the

associated jet-species flow rates are modeled. Chemical reactions occur either within the jet or heterogeneously at the jet-melt interface.

4.1.1.2 Desulfurization Chemistry and Kinetics

Desulfurization is effected by the conversion of dissolved sulfur and oxygen to gaseous SO_2, which then leaves the melt once it reaches gas-melt interface:

$$\underline{S} + 2\underline{O} \rightarrow SO_{2(g)} \tag{4.1}$$

Oxygen present in the liquid copper fed to fire-refining, and additional oxygen dissolves from the injected air:

$$O_{2(g)} \rightarrow 2\underline{O} \tag{4.2}$$

Also present in the gas phase of the system is nitrogen gas, which has negligible solubility in liquid copper. There are no well-established rate laws for equations 4.1-2. As such, any developed kinetic model will ultimately need to be calibrated on laboratory or industrial data. However, rate laws that capture expected behavior can still be useful for estimating process trends, which is done in this work.

4.1.1.2.1 Desulfurization Rate Law

A couple of observations [48] are important for the development of the desulfurization rate law:

1. The desulfurization rate is dependent on the dissolved sulfur content
2. The desulfurization rate is dependent on the dissolved oxygen content
3. The desulfurization rate is not dependent on the oxygen grade of the injected gas except as this changes the dissolved oxygen content of the melt

These observations suggest that dissolved SO_2 forms in the melt and then enters the jet at the jet-melt interface. If sulfur was reacted to SO_2 at the jet melt interface, observations 2 and 3 would not hold. The rate law used is

$$\dot{\omega}_{SO_2} = k_{SO_2} A\left(a_{SO_2,melt} - a_{SO_2}{}^*\right) \tag{4.3}$$

$$a_{SO_2,melt} = K_1\left(\gamma_{\underline{S}} X_{\underline{S}}\right)\left(\gamma_{\underline{O}} X_{\underline{O}}\right)^2, \tag{4.4}$$

where $\dot{\omega}_{SO_2}$ is the net generation rate of SO_2 gas in the jet per height, k_{SO_2} is a mass transport coefficient describing the rate of transport of dissolved SO_2 to the jet, *A* is the area of the jet-melt interface per height of the jet, $a_{SO_2,melt}$ is the equilibrium dissolved SO_2 activity in the melt based on the dissolved sulfur and oxygen activities, $a_{SO_2}{}^*$ is the activity of dissolved SO_2 in equilibrium with SO_2 in the jet, K_1 is the equilibrium constant of equation 4.1, γ_i is the activity coefficient of dissolved species *i* in the melt, and X_i is the mole fraction of dissolved species *i* in the melt. There is virtually no SO_2 solubility in copper under the conditions of copper desulfurization, so $a_{SO_2}{}^*$ is taken to be zero. The activity coefficients are taken as constants. This is because both dissolved species are assumed to be in the Henrian regime [83,84]. Taking all of these points into consideration, the rate law can be simplified to:

$$\dot{\omega}_{SO_2} = k^*_{SO_2} A X_{\underline{S}} X_{\underline{O}}{}^2 \tag{4.5}$$

$$k^*_{SO_2} = k_{SO_2} K_1 \gamma_{\underline{S}} \gamma_{\underline{O}}{}^2 \tag{4.6}$$

Where $k^*_{SO_2}$ is the mass transport coefficient for dissolved SO_2 lumped with the equilibrium constant and activity coefficients. An attractive feature of this rate law is that it has only one uncertain parameter, $k^*_{SO_2}$ (*A* is explicitly calculated).

4.1.1.2.1 Oxidation Rate Law

Industrial observation sees all of the added oxygen report as either dissolved copper or copper-oxide slag. The equilibrium phase for the Cu-O system at the partial pressure and temperature of the jet is the L_2 liquid phase [84]. As such, it would appear that there is not slag immediately in contact with the jet-melt interface. The equilibrium phase at all times during desulfurization for the bulk melt composition is the L_1 liquid phase. As such, any formed copper slag should dissolve into the melt when the melt is only comprised of Cu, S, and O (inclusion of minor elements may change slag stability, but this is beyond the scope of this model) and

equilibrium is reached. Because of this and the high degree of uncertainty as to what fraction of added oxygen reports as slag, this model assumes that all added oxygen reports as dissolved oxygen. Assuming the dissolution rate of oxygen is controlled by transport of the dissolved oxygen away from the jet melt interface, the following rate law can be used:

$$\dot{\omega}_{O_2} = k_{\underline{O}} A\left(X_{\underline{O}}^{*} - X_{\underline{O}}\right) \tag{4.7}$$

where $\dot{\omega}_{O_2}$ is the rate of O_2 removal from the jet, $k_{\underline{O}}$ is a mass transport coefficient, A is the interfacial area of the jet and melt per height of jet, $X_{\underline{O}}^{*}$ is the concentration of dissolved oxygen in equilibrium with the jet, and $X_{\underline{O}}$ is the bulk dissolved oxygen concentration. $X_{\underline{O}}$ is small enough (more than two orders of magnitude less) compared to $X_{\underline{O}}^{*}$ that $X_{\underline{O}}$ can be safely neglected. This allows equation 4.8 to be transformed to:

$$\dot{\omega}_{O_2} = k_{O_2} A C_{O_2} \tag{4.8}$$

$$k_{O_2} = \frac{k_{\underline{O}} X_{\underline{O}}^{*}}{Y_{O_2}} \tag{4.9}$$

where k_{O_2} is a proportionality constant for describing the O_2 dissolution rate as a function of C_{O_2}, concentration of oxygen in the jet. Equations 4.8 and 9 make a first order approximation for the relationship between oxygen concentration in the jet and dissolved oxygen content at the jet-melt interface. The simplification given by these equations makes for an oxygen dissolution model with only one uncertain parameter.

4.1.1.3 Mass And Momentum Conservation Laws for the Jet

The model tracks the concentrations and flowrates of oxygen, nitrogen, and sulfur dioxide along the jet height. It is assumed that diffusion in the jet is negligible because the melt blocks gas-diffusion between bubbles and the bubbles are small relative to the length of the jet. In the direction along the jet (z), the continuity equation is:

$$\frac{\partial(C_i A_x)}{\partial t} + \frac{\partial(C_i w A_x)}{\partial z} = \dot{\omega}_i A_x \,, \tag{4.10}$$

where C_i is the concentration of species i, A_x is the cross-sectional area of the gas in the bubble jet at height z, w is the bubble velocity, and $\dot{\omega}_i$ is the net generation rate of species i via chemical reaction in kmoles/m^3-s. Continuity is used to solve the concentrations of the chemical species in the jet as well as the concentration of bubbles at any point along the jet. $\dot{\omega}_{bubbles}$ is zero because bubble generation or destruction is assumed to not occur.

Two types of bubbles are modeled: microbubbles (spheres) and spherical-cap bubbles. The upward velocity (w) of spherical-cap bubbles in the jet is found according to Wegener and Parlange [85], who derived analytical expressions for rising spherical cap bubbles under steady flow. When microbubbles are modeled, the upward velocity is found using Bond's modification of Stokes' law [86] for spherical bubbles undergoing steady flow. Although both velocity expressions are a simplification of jet momentum conservation, they capture the expected bubble radius dependency of the bubble velocity while also giving a first order approximation of injected bubble vertical velocities. The equations for the rising bubble vertical velocity are

$$w_{sc} = \frac{2}{3}\left[\frac{2 g r_{bub}(1-\cos\theta)}{\sin^2\theta}\right]^{\frac{1}{2}} \tag{4.11}$$

$$w_{mb} = \frac{1}{3}\frac{g \rho_{Cu} {r_{bub}}^2}{\mu_{Cu}} \tag{4.12}$$

where w_{sc} is the spherical-cap bubble velocity, w_{mb} is the microbubble velocity, g is the terrestrial acceleration due to gravity (9.8 m/s^2), r_{bub} is the bubble radius in meters, θ is the spherical-cap bubble angle (50°), ρ_{Cu} is the density of the liquid copper at 1400K (8000 kg/m^3), [87], and μ_{Cu} is the dynamic viscosity of liquid copper at 1400K ($4 \cdot 10^{-3}$ Pa·s). The velocity of microbubbles is much more sensitive to changes in the bubble radius than spherical-cap bubbles due to the difference in dependency on bubble radius, as shown in figure 4.2.

Bubble radius along the jet is found from the ideal gas law, in which the total pressure at a given height is the hydrostatic pressure of the melt, and the moles of gas per bubble are found by taking the ratio of the concentration of gas to the concentration of bubbles:

$$V_{sb} = \frac{C_{gas}}{C_{bub}} \frac{RT_{melt}}{P_{jet}} = \frac{\pi}{3}(2 + \cos\theta)(1 - \cos\theta)^2 {r_{bub}}^3 \tag{4.13}$$

$$V_{mb} = \frac{C_{gas}}{C_{bub}} \frac{RT_{melt}}{P_{jet}} = \frac{4}{3}\pi {r_{bub}}^3 \tag{4.14}$$

$$C_{gas} = \sum_i C_i \tag{4.15}$$

$$P_{jet} = P_0 + g\rho_{Cu}(L - z) \tag{4.16}$$

$$A_{sb} = 2\pi r^2(1 - \cos\theta)C_{bub} \tag{4.17}$$

$$A_{mb} = 4\pi {r_{bub}}^2 C_{bub} \tag{4.18}$$

where V_{sb} and V_{mb} are the volume of gas per spherical-cap and micro bubble respectively at height z along the jet respectively; $\frac{C_{gas}}{C_{bub}}$ is the ratio of the concentration of gas to the concentration of bubbles at height z; P_{jet} is the hydrostatic pressure of the melt at height z above the tuyere insertion point; A_{sb} and A_{mb} are the surface area of the jet-melt interface per height of jet at an arbitrary height for spherical-cap and microbubbles respectively. One may note that the surface area of the spherical cap bubble on the wake-side has been ignored. This choice was made because this area is highly uncertain, and it is also moving away from the melt. Additionally, if the mass transfer coefficient is calibrated, the exact area of the bubbles does not need to be known. For both spherical-cap bubbles and microbubbles, the rate of sulfur dioxide transport ultimately goes as:

$$\dot{\omega}_{SO_2} = k_{SO_2} B {X_{\underline{O}}}^2 X_{\underline{S}} {r_{bub}}^2 \tag{4.19}$$

where B is the constant giving the surface area per bubble radius squared for a given bubble geometry. As such, an arbitrary change to B will cause an inversely proportional change to the calibration of k_{SO_2}. Finally, the molar flowrate of any species anywhere in the jet is given by the product of the bubble velocity and the concentration of that species:

$$\dot{N}_i = wC_i \tag{4.20}$$

There are some important points regarding equations 4.10-20. First, the surface area to volume ratio of microbubbles is much larger than for spherical-cap bubbles due to the smaller size of the microbubbles. This leads to modeled jet interfacial areas about two orders of magnitude greater for microbubbles than for spherical-cap bubbles; suggesting one of two possibilities: either there are different k_{SO_2} and $k_{\underline{O}}$ values for each bubbling regime, or microbubble injection is actually orders of magnitude faster than spherical-cap bubble injection. The latter does not seem to be the case [48], so the former is assumed in this model. Additionally, the bubble velocity as a function of height will be different for spherical-cap bubbles and micro bubbles. Figure 4.2 shows how injected gas velocity changes over the height of one meter of liquid copper for different initial bubble radii in the spherical-cap bubble and microbubble regimes. The moles of gas in the bubbles (for a given initial radius) is kept constant over the jet height for figure 4.2. The radii of the bubbles were chosen so that the initial velocities of the microbubbles and spherical cap bubbles would be equal. Microbubbles have a higher acceleration than spherical-cap bubbles. This counteracts the effects of the higher surface area to volume ratios for microbubbles to small degree, as these bubbles spend less total time in the melt than the spherical cap bubbles, so they have less time to participate in reaction.

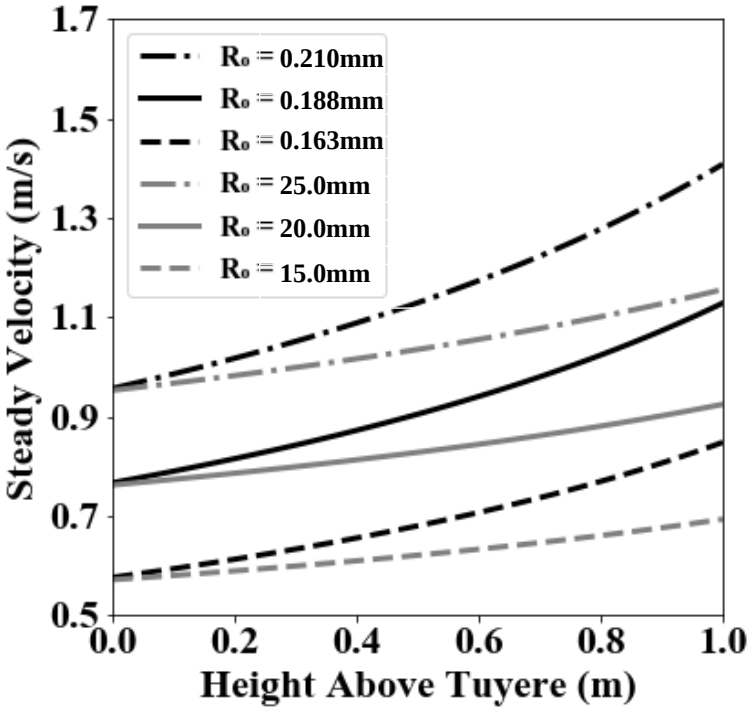

Figure 4.2 - Estimated bubble velocity for spherical-cap bubbles (gray) and microbubbles (black) with a constant bubble molar amount of gas over the height of 1 m of depth of liquid copper

4.1.1.4 Mass Conservation for the Melt

The melt is considered separately from the jet of blown-in gas; as such, the only mass flow into the melt is oxygen which has dissolved from the jet. Sulfur and oxygen can leave the melt and enter the jet as sulfur dioxide. Copper is neither added to nor removed from the furnace. The rate of change of the mass in the melt of copper, sulfur, and oxygen are thus:

$$\frac{dN_{Cu,melt}}{dt} = 0 \tag{4.21}$$

$$\frac{dN_{\mathrm{S}}}{dt} = -\int_0^L \dot{\omega}_{\mathrm{SO_2}}\, dz \tag{4.22}$$

$$\frac{dN_{\mathrm{O}}}{dt} = 2\int_0^L \left(\dot{\omega}_{\mathrm{O_2}} - \dot{\omega}_{\mathrm{SO_2}}\right) dz \tag{4.23}$$

where N_i is the molar amount of species i in the melt, $\dot{\omega}_{SO_2}$ and $\dot{\omega}_{O_2}$ are the molar rates of generation of sulfur dioxide and oxygen in the melt per length of melt height, respectively and L is the length of the jet. These two terms are described in greater detail in the desulfurization and oxidation kinetics sections.

4.1.1.5 Initial Conditions for the Melt During Desulfurization

The base case for the melt is initially comprised of 4091 kmoles (260 tonnes) of liquid copper that has a dissolved sulfur content of 890 molar ppm (450 wt. ppm) and a dissolved oxygen content of 11,000 molar ppm (2800 wt. ppm). The melt starts with a specified uniform temperature of 1398 K. Variations to this base case are stated in the results section.

4.1.1.6 Energy Conservation for the Melt And Jet

The melt and jet volumes are thermally lumped and taken to be at the same, uniform temperature. The energy inflow to this lumped volume is the enthalpy of the injected gas, and the net heat transfer to the melt. Energy outflows from the jet-melt lump are the gas leaving the melt and conduction through the furnace wall in contact with the melt. The overall transient heat balance is:

$$\frac{dH}{dt} = \sum_i \dot{N}_i h_i - \sum_j \dot{N}_j h_j - \dot{Q} \tag{4.24}$$

where H is the total enthalpy in the jet and melt, $\sum_i \dot{N}_i h_i$ is the total enthalpy entering the melt with the injected oxygen and nitrogen, and $\sum_j \dot{N}_j h_j$ is the total enthalpy leaving the melt with nitrogen, oxygen, and sulfur dioxide, and $\dot{Q}$ is the net heat transfer out of the melt. The equations and associated parameter values used to calculate the specific enthalpies of each species can be found in Appendix A. The work of Barin [74] was used for copper and the gas phase species, the work of Hallstedt et al. [84] was used for dissolved oxygen, and the work of Bale and Toguri [83] was used for dissolved sulfur. The mass of the jet is negligible compared to the mass of the melt, so it can be ignored for temperature calculations. If the enthalpy of each species is linearly approximated, the temperature can be modeled according to:

$$h_i = a_i + b_i T \tag{4.25}$$

$$T = \frac{H - \sum_i a_i N_i}{\sum_i b_i N_i} \tag{4.26}$$

where *i* now only denotes copper, dissolved oxygen, and dissolved sulfur. Testing was done which showed that neglecting dissolved sulfur and dissolved oxygen in eqn. 4.26 led to negligible changes in the temperature histories.

Table 4.1 - Molar enthalpies and entropies of the species used in the model. Temperatures used in the equations are in Kelvin. R is the universal gas constant. $X_{\underline{O}}$ and $X_{\underline{S}}$ are the mole fractions of dissolved oxygen and sulfur in the melt

Specie	**Specific Enthalpy (MJ/kmol)**	**Specific Entropy (MJ/kmol-K)**
Cu	-1.8 + 0.033T	0.085+0.038ln(T/1400)
N_2	-13.76+0.035T	0.24+0.034ln(T/1400)
O_2	-13.765+0.037T	0.26+0.037ln(T/1400)
SO_2	-319.896+0.057T	0.32+0.057ln(T/1400)
$\underline{S}$	59.921+0.019T	$0.239+0.019\ln(T/1400)+R\ln(1.005X_{\underline{S}}^{0.002})$
$\underline{O}$	$0.5h_{O_2}$-78.42-38.5R$X_{\underline{O}}$	$0.5s_{O_2}$-R[ln(100$X_{\underline{O}}$)+0.019($X_{\underline{O}}$-0.01)]

4.1.1.7 Initial Conditions for the Jet

The model considers desulfurization to start with the entrance of the first bubble into the melt. As such the jet length approaches zero as the time since gas injection start approaches zero. It takes approximately 2s for the jet to first reach the melt surface. The initial temperature of the jet is the initial melt temperature.

4.1.1.8 Boundary Conditions for the Jet

The chemical composition and flowrate of the jet is fixed at the jet inlet and is constant over the entire modeled time. Because the differential equations describing the jet are first order,

only one boundary condition is needed (a marching problem). The flowrates and compositions used for each study are given in the results section. Only oxygen and nitrogen are considered to comprise the injected gas. The composition and flowrate of the jet leaving the melt is variable and solved *via* mass conservation as described earlier. The concentration of bubbles at the jet inlet is given by taking the ratio of the bubble flowrate to the bubble vertical velocity at the jet inlet,

$$C_{bub}|_{z=0} = \left.\frac{\dot{F}_{bub}}{w}\right|_{z=0} \tag{4.27}$$

where C_{bub} is the concentration of bubbles (number of bubbles/m) and $\dot{F}_{bub}$ is the bubble flowrate (number of bubbles per second). The flowrate of bubbles at the inlet is approximated by assuming a monodispersion of bubbles; the initial bubble size used is given in the results section.

4.1.1.9 Heat Transfer in the Furnace

A steady state radiation heat transfer model was made for heat exchange between the melt, headspace brick, and headspace flame. The full details of the balance can be found in Mather's dissertation (ref dissertation). Essential to this model is the net heat transfer rate to the melt and out of the furnace. These are important for establishing an energy balance on the melt and for calculating exergy losses and destruction. Table 4.2 shows these values as a function of melt temperature. The values were found to produce very small melt temperature changes (less than 1 K) over the course of a three hour reduction cycle, as seen at FMI Miami Anode Plant.

Table 4.2 - Heat transfer values necessary for model reproduction

Melt Temperature (K)	Net Heat Transfer Rate to Melt (MW)	Net Heat Transfer Rate through Furnace Walls (MW)	Steady State Flame Temperature (K)
1373	-0.69	2.81	1849
1398	-0.73	2.86	1852
1423	-0.78	2.90	1855
1448	-0.82	2.95	1858
1473	-0.87	2.99	1862

4.1.1.10 Exergy Calculations

The exergy balance for the desulfurization step of fire refining is same as that used for the other unit operation in the current work. For desulfurization, exergy is fed to the process with the blister copper from the converters. Exergy leaves the process with the offgas and heat transfer out of the furnace.

4.1.1.11 Solution Method

The reacting flow system was solved *via* a forward-time, back-space solution method [88]. The timestep size used was 0.0005 seconds. The jet-depth increment used was 0.01 m. Use of this method makes sense because there is only one boundary condition for the jet (at the inlet).

4.1.2 Results and Discussion

A sensitivity study was conducted on the model. Each set of model parameters was looked at with both microbubbles and spherical cap bubbles. Varied parameters include oxygen grade of the injected gas, initial bubble size, starting composition of the melt, oxygen mass transport coefficient (OMTC) and sulfur dioxide mass transport coefficient (SMTC). Model performance is primarily assessed by the dissolved sulfur and oxygen content histories. The base case is looked at first. As an additional note, temperature was allowed to vary in this model. All cases except for the oxygen grade variation cases saw a linear change from the initial temperature of 1398 K to

1425 K. There was negligible change to the exergetic performance of the system over all the cases studied, so exergy results for the baseline case are presented last.

4.1.2.1 Base Case Results

The set of parameters used to model the base case for both microbubbles and spherical cap bubbles is presented in table 4.3. The values of the parameters used correspond approximately to those used in the work of Enriquez et al. [48]. The initial bubble size, spherical cap bubble angle, OMTC and SMTC are estimates used by the authors that cause model performance approximate to the industrial observation.

The model gives transient profiles of gaseous species concentrations along the jet height. Contours of the jet cross sectional area with respect to time and height along the jet are shown in figure 4.3. The cross sectional area of the microbubble jet varies much less over its height than the spherical cap bubble jet. The reason for this is that the microbubbles in this system tend to rise more quickly than spherical cap bubbles. This means there is less time for bubble growth in the microbubble jet case, so the jet expands less and thus has a more consistent cross sectional area over its height. Both types of jet see their cross-sectional area initially decrease. This is because the rate of oxygen consumption by the melt at higher depths is much greater than the rate of sulfur dioxide uptake to the jet; as such, the net amount of moles of gas in the jet initially decreases for both cases, causing a shrink in cross sectional and surface area. As the bubbles rise for each case, the decrease in pressure and the increase in total moles of gas per bubble (from SO_2 uptake to the jet) cause increases in the cross sectional area of the jet.

Figure 4.5 shows how the concentration of oxygen in the jet changes for each case with respect to time and height. The concentration of oxygen in the jet decreases exponentially with respect to time. The decrease is more rapid with respect to height for the spherical cap bubble case, as the bubbles travel more slowly in this case and thus the oxygen has more time to dissolve into the melt over any given height range. Figure 4.5 shows that the bubbling regime does not matter in terms of the total oxygen dissolution for the base case, as intended. Overall, the change in total dissolved oxygen content, 3000 ppm, corresponds to the values found by Enriquez et al. [48] for the industrial system they studied.

The SO_2 content of the jet as a function of height from tuyere insertion and time is shown in figure 4.6. The SO_2 concentration reaches a maximum at about 20 minutes of refining time at

the top of the jet. This result shows the effect of jet development (increasing SO_2 concentration as height increases) and the combined effect of oxygen dissolution and sulfur removal to/from the melt; the product $X_{\underline{S}}X_{\underline{O}}^2$ reaches a maximum at about 20 minutes.

Table 4.3 – Parameter values used for the base cases

Parameter	Spherical-Cap Bubbles	Microbubbles
Moles of Cu in Melt (kmole)	3918.	
Depth of Tuyere Submergence (m)	1.	
Initial Melt Temperature (K)	1398	
Total Gas Injection Rate (kmole/s)	0.020	
Injected Gas O_2 Grade (%)	0.21	
Initial Mole Fraction Dissolved Oxygen in Melt	0.011 (2800 wt. ppm)	
Initial Mole Fraction Dissolved Sulfur in Melt	$8.9\text{x}10^{-4}$ (450 wt. ppm)	
Initial Bubble Diameter (m)	$2\text{x}10^{-2}$	$1.68\text{x}10^{-4}$
Sph. Cap Bubble Angle (^{o})	50	-
$k_{\underline{O}}$ (1/s)	$1.5\text{x}10^{-4}$	$2.357\text{x}10^{-6}$
$k_{\underline{S}}$ (1/s)	3.5	$5.5\text{x}10^{-2}$

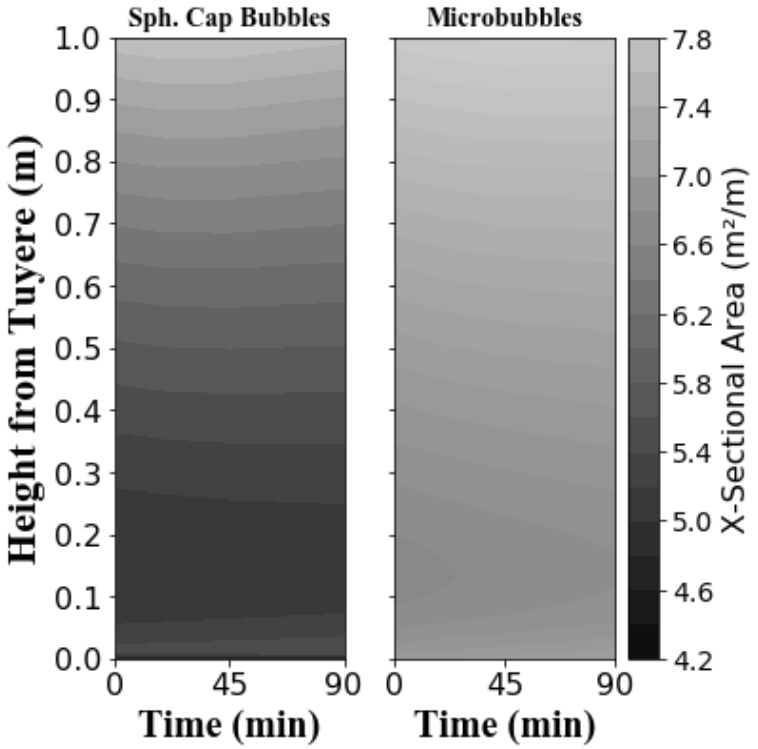

Figure 4.3 – Cross sectional area vs time and height from gas injection contours for the base case.

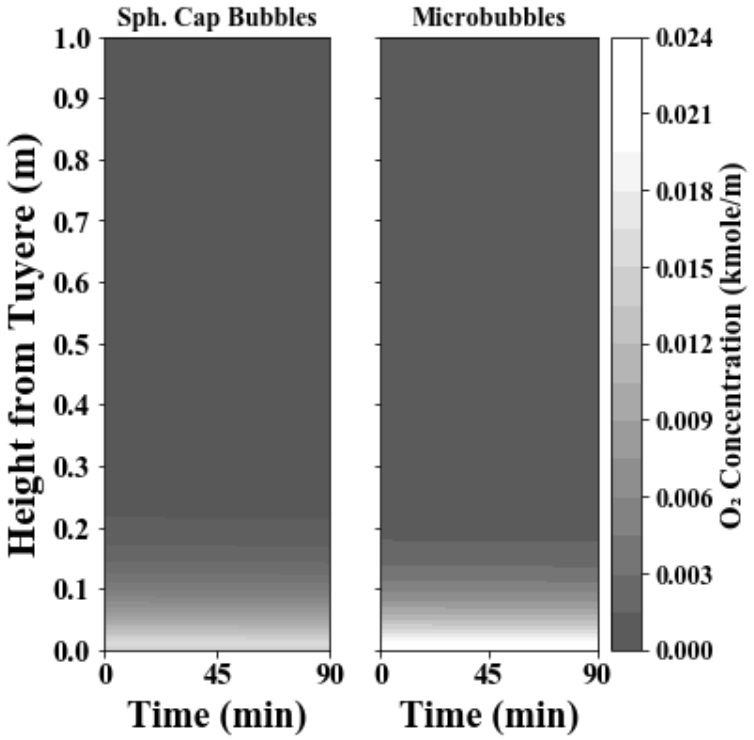

Figure 4.4 – Concentration of dissolved oxygen with respect to height from gas injection and time.

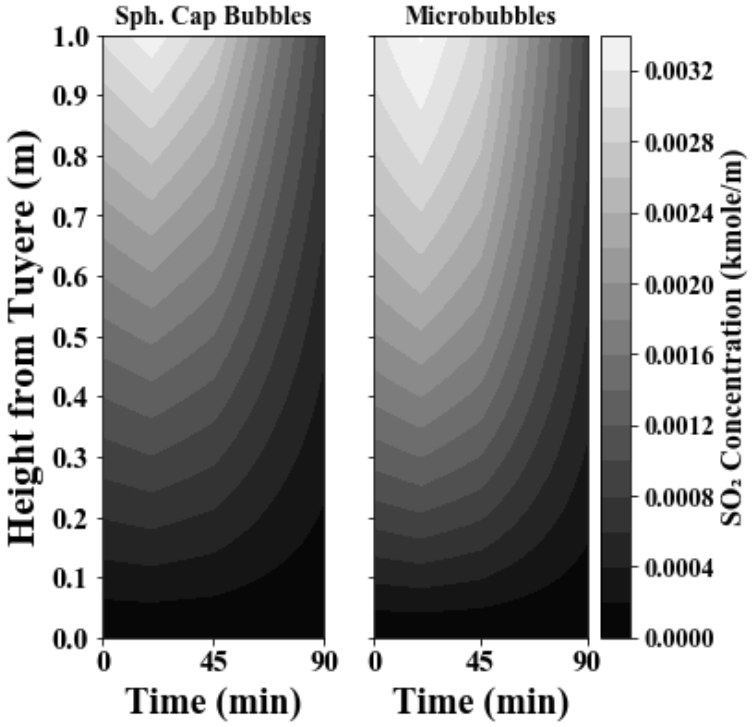

Figure 4.5 – Dissolved SO2 concentration as a function of refining time and height from tuyere submergence

4.1.2.2 Injected-Gas Oxygen Grade Variation Results

Cases were run in which the oxygen grade of the injected gas was varied down to 0.5%. Figure 4.7 shows histories of the dissolved oxygen content of the melt. With a lower oxygen grade in the injected gas and same total gas injection rate and refining time, the terminal dissolved oxygen content in the melt decreases with oxygen grade. Indeed, it can be seen that using 99.5% nitrogen as the injected gas causes almost no increase in dissolved oxygen content of the melt. Figure 4.8 shows a moderate increase in terminal dissolved sulfur concentration of about 100 ppm when the oxygen content of the injected gas is decreased to 0.5%. It should be remembered that the SMTC would ideally be calibrated, a higher SMTC would cause the terminal sulfur concentration to be closer for each case. Figure 4.8 is shows the expected result that lower average dissolved oxygen in the melt leads to a lower average SO_2 formation rate in the copper and thus lower sulfur removal rate from the melt. In practice, it may be possible to simply increase the total gas flowrate with lower oxygen grades. This would increase the jet-melt interfacial area and make-up for the decrease in desulfurization rate. Because there would be less oxygen in the injected gas, increasing the total gas injection rate would not increase dissolved oxygen in the melt. Overall, figures 4.7 and 4.8 show that it may very well be possible to conduct desulfurization with nearly pure nitrogen and greatly reduce the dissolved oxygen content at the end of desulfurization. The change in dissolved oxygen content of about 3000 ppm corresponds to about an hour to an hour and a half of time saved during the reduction step of fire refining. These results give support to the work of Enriquez et al. [48] and give motivation to study the effect of nitrogen injection during desulfurization at industrial sites.

Interestingly, desulfurization rate was worse for microbubble injection. The difference is due to the difference in bubble velocity for each type of bubble over the jet height. Both types of jets saw all added oxygen dissolved to the melt, so the difference is not dissolved oxygen content in the melt. Both cases also had the same initial dissolved sulfur in the melt. Furthermore, the OMTC and SMTC were not changed from their base case values. The only variable left is jet-melt interfacial area. Figure 4.9 gives contours for the jet cross-sectional (to which interfacial area is directly proportional) for the 0.5% O_2 grade in injected gas cases. The average interfacial area for the spherical-cap bubble case has increased as a fraction of its base-case value much more than for the microbubble case. Indeed, from the base case to the no oxygen injection case, the average cross sectional area for the spherical cap bubble case increased by a factor of 1.17, from 6.0 m^2/m

to 7.1 m^2/m; meanwhile the microbubble injection cases saw an increase by a factor of only 1.06, from 7.2 to 7.7. So, the spherical cap bubble case saw a much greater increase in the average of $k_S A$ than the microbubble case when the oxygen grade decreased. So, the larger surface area of the spherical cap bubble jet made up for the decrease in average X_O more than microbubble jet.

Figure 4.10 shows temperature histories for the oxygen grade variation cases. The temperature histories are dominated by oxygen dissolution, so there is practically no difference between the microbubble and spherical cap bubble cases. The key result shown is that the headspace flame is adequate for maintaining melt temperature even when there is almost no oxygen in the injected gas. This means the fear of freezing the melt when dropping oxygen grade should be mitigated.

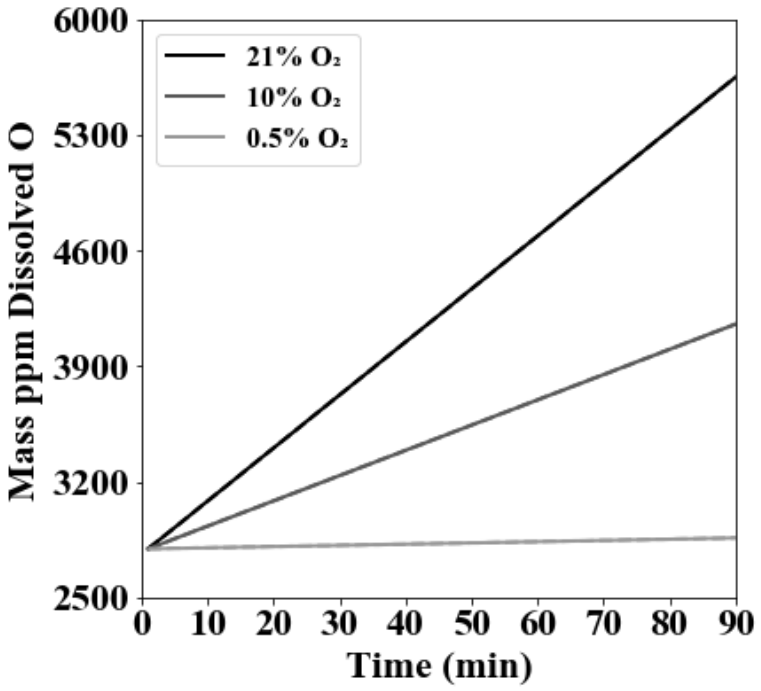

Figure 4.6 – Melt dissolved oxygen content histories for the oxygen grade variation cases. Solid lines correspond to spherical-cap bubble injection; dashed lines correspond to microbubble injection

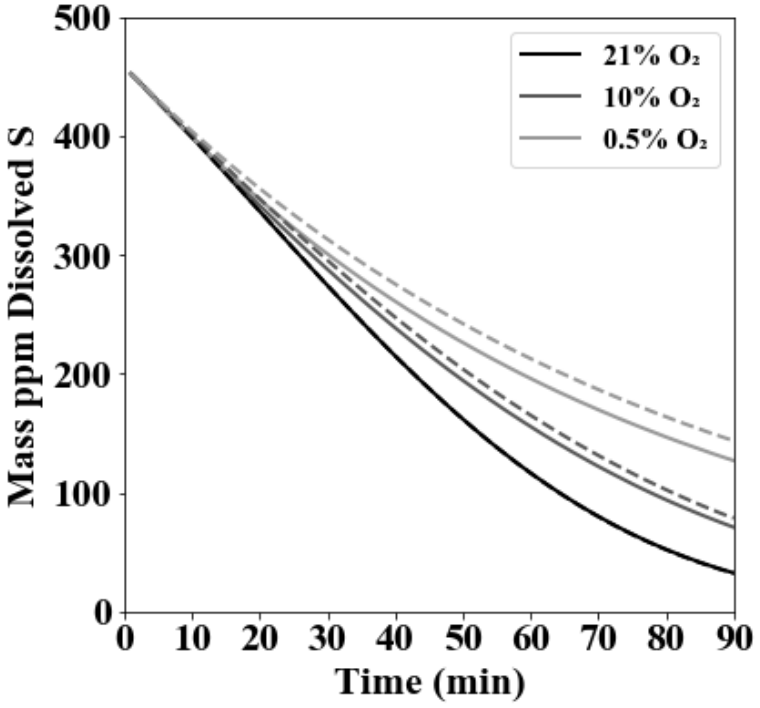

Figure 4.7 - Histories of dissolved sulfur concentrations of the melt for the injected gas oxygen grade variation cases. Solid lines correspond to spherical-cap bubble injection; dashed lines correspond to microbubble injection

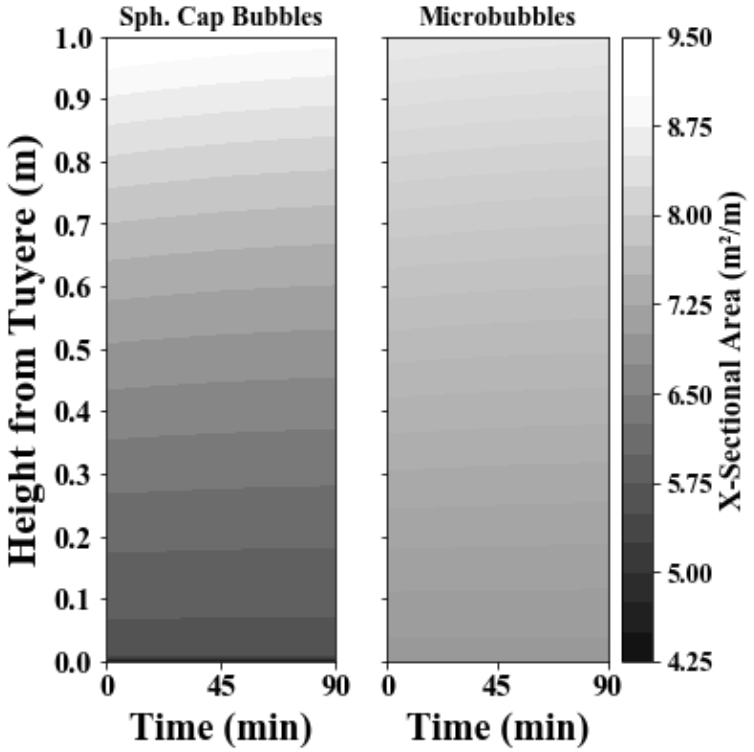

Figure 4.8 – Contours of the cross-area over time and height of jet from tuyere insertion for the 0.5% O2 in injected gas case

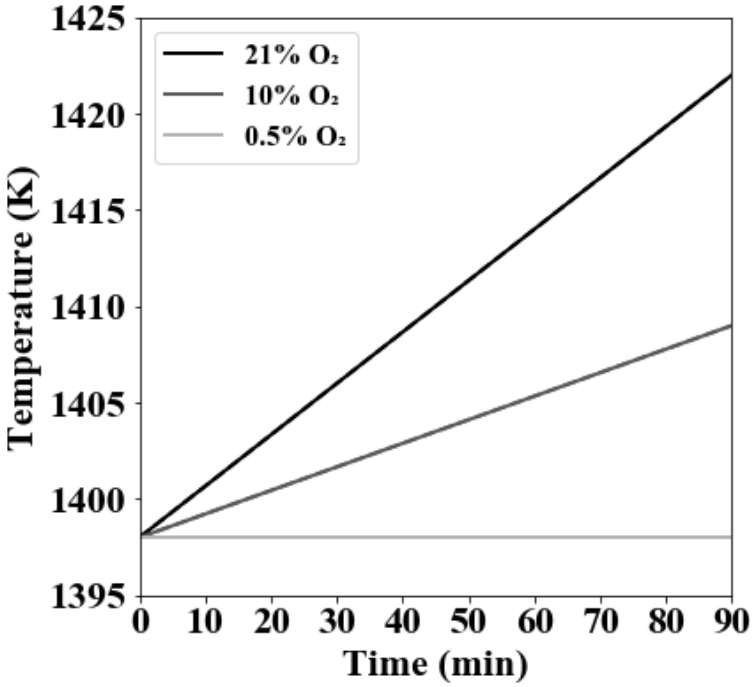

Figure 4.9 – Temperature histories for the O2 grade variation cases. Solid lines are for spherical cap bubbles and dashed lines are for microbubbles

4.1.2.3 Initial Bubble Size Variation

Bubble size was varied +/- 25% from the base case values for both spherical cap and microbubbles. This variation had no effect on the total amount of oxygen dissolved (100%). The variation in dissolved sulfur history is shown in figure 4.11. Larger bubbles caused slower desulfurization rates. The reason for this is that larger bubbles have a lower surface area to volume ratio and rise more quickly through the melt (which also causes narrower jets). As such, both the total volume of gas in the jet at any given time and its interfacial decrease with larger bubble sizes. Decreases to the interfacial area of the jet decrease the rate of SO_2 uptake to the jet.

The microbubble cases saw more dramatic changes to the desulfurization rate than the spherical cap bubble cases. This can be explained by figure 4.2, which shows that microbubble velocity is much more sensitive to radius than spherical cap bubble velocity. Overall, these results show that minimization of bubble radius will likely be beneficial for operating plants. Additionally, the results show that calibration of the initial bubble radius on data should lead to a much tighter fit for the microbubble case than the spherical cap bubble case. This is due to the increased sensitivity in desulfurization rate with respect to initial bubble radius for microbubbles.

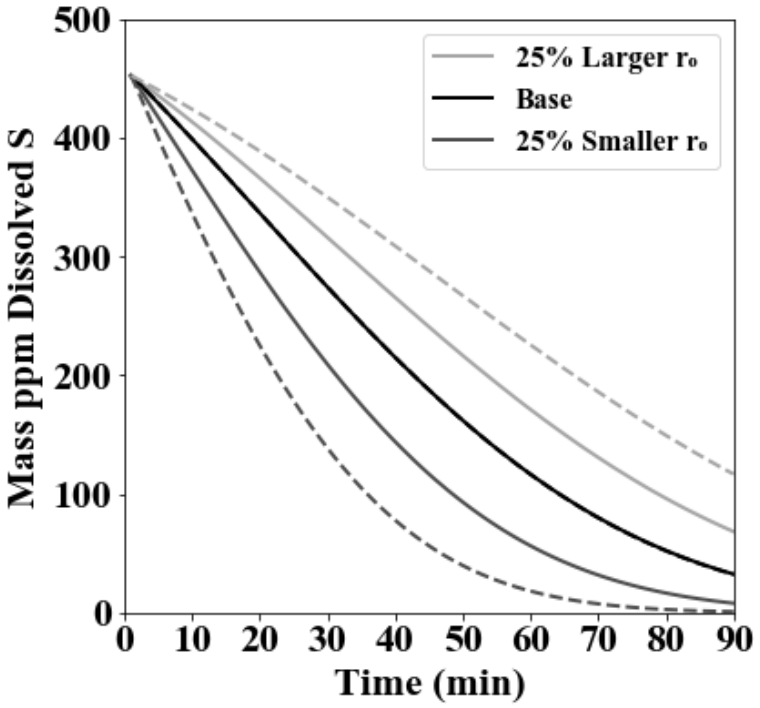

Figure 4.10 – Dissolved sulfur content histories for the bubble variation cases. Solid lines are for spherical cap bubbles and dashed lines are microbubbles. The base case bubble radius for spherical cap bubbles is 20 mm; the corresponding value for microbubbles is 168 μm

4.1.2.4 Starting Composition Variation

One case was run with high initial dissolved oxygen (3500 mass ppm) and low initial dissolved sulfur (300 ppm). Another case was run with low initial dissolved oxygen (2100 mass ppm) and high initial dissolved sulfur (600 ppm). These conditions correspond to slight decreases and increases in converting time respectively. The dissolved sulfur histories are shown in figure 4.12 and the dissolved oxygen histories are shown in figure 4.13. The higher initial sulfur content cases bring out the inflected nature of the dissolved sulfur histories. The desulfurization rate increases at first due to increases in the dissolved oxygen content of the melt, and then decreases due to the decrease in dissolved sulfur content.

The first important result is that increases to starting sulfur concentration can have a severely deleterious effect to refining operations; the 25% increase in starting sulfur more than doubled terminal sulfur. Although some dissolved sulfur is may be removed during reduction, it cannot be guaranteed that enough will be removed such that higher terminal sulfur in the desulfurization step will be effectively managed. As such, this result stresses the importance of

careful converter operation. Many plants use visual checks on a spoon sample to test when the copper blow of converting should cease; however, these results show that development and implementation of a more precise instrument for measuring dissolved sulfur in copper could lead to significant improvements in dissolved sulfur control. Such improvements could lead to improved cast anode quality.

Microbubbles and spherical cap bubbles were both studied, and the results show no difference between the two bubbling regimes. This is because the ratio of $k_{SO_2}A$ between the spherical cap and microbubble cases is not changed. Over very large sulfur composition changes, the changes to sulfur uptake could begin affecting bubble velocity, which would be different for spherical cap and microbubbles, and presumably lead to some difference in dissolved sulfur history. However, this affect is apparently very weak over the initial sulfur content range studied.

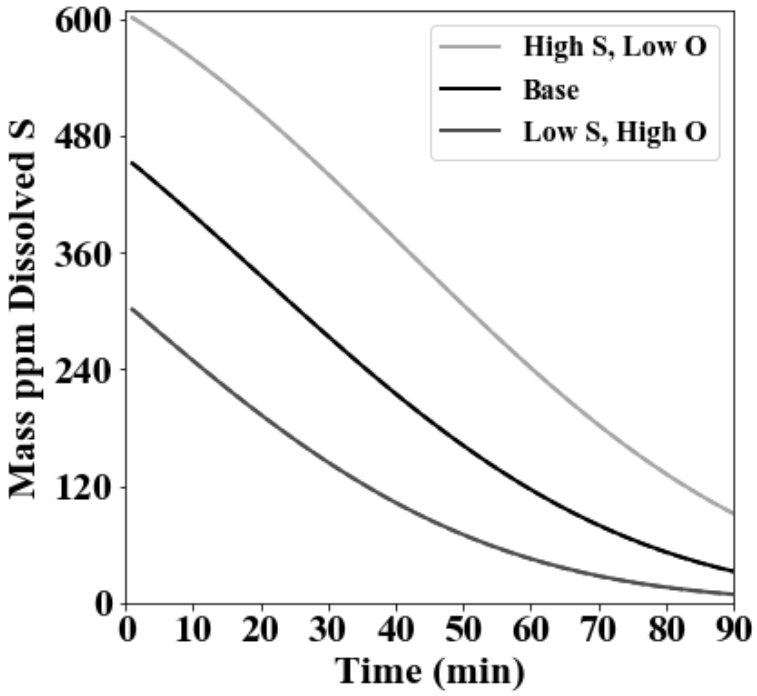

Figure 4.11 - Dissolved sulfur histories for the starting composition variation cases. Solid lines are for spherical cap bubbles and dashed lines are for microbubbles

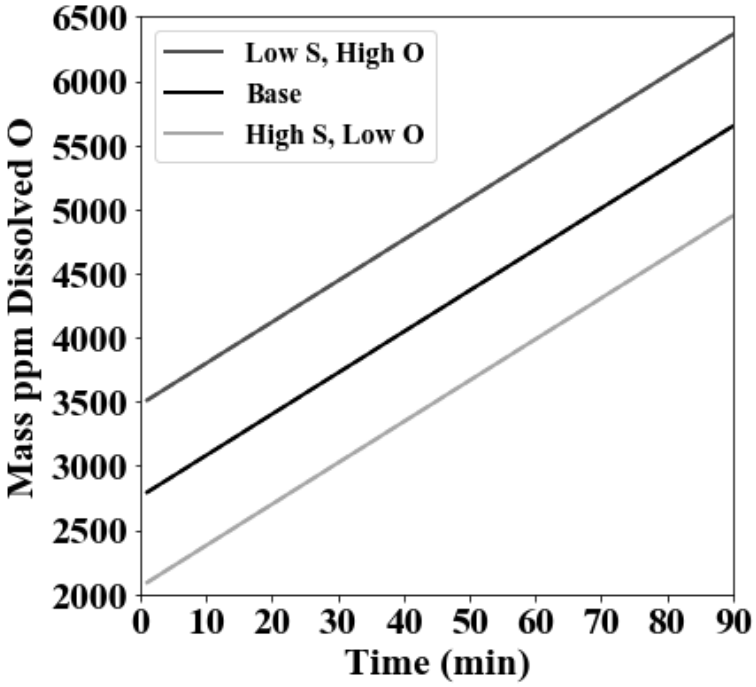

Figure 4.12 – Dissolved oxygen histories for the starting composition variation cases. Solid lines are for spherical cap bubbles and dashed lines are for microbubbles

4.1.2.5 Sulfur Mass Transport Coefficient Variation

The sulfur mass transport coefficient is a highly uncertain parameter. The sensitivity of the model to this parameter is an important piece of information for model calibration efforts. Figure 4.14 shows how the dissolved sulfur content histories change with +/- 20% changes in the SMTC. Decreasing the SMTC by 20% led to a 70% increase in terminal sulfur concentration. Increasing the SMTC by 20% led to a 40% decrease in terminal sulfur concentration. There was no difference between the spherical cap and microbubble cases because changes to k_{SO_2} do not affect the ratio of $k_{SO_2}A$ for the microbubble cases to $k_{SO_2}A$ for the spherical cap bubble cases.

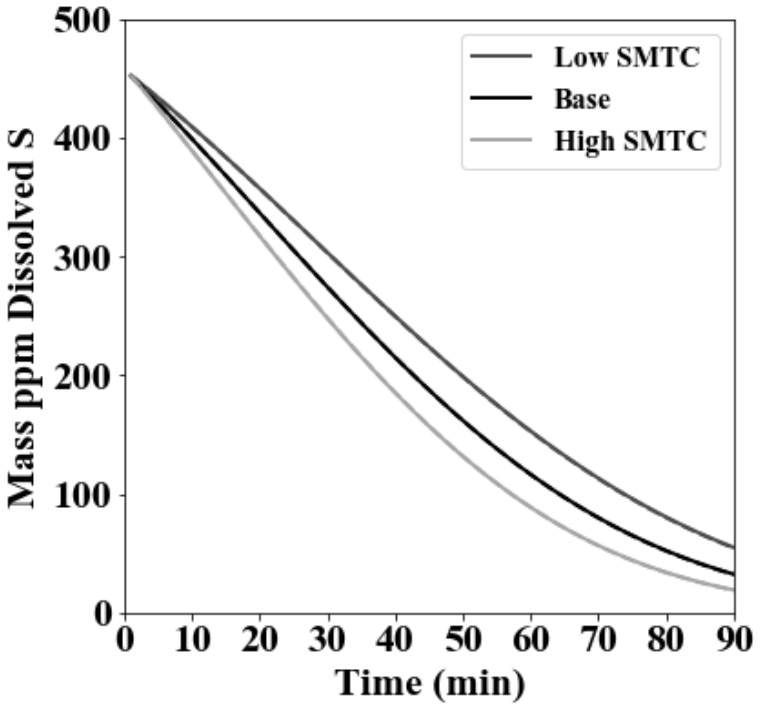

Figure 4.13 - Dissolved sulfur content histories for the sulfur mass transport coefficient variation cases. Solid lines are for spherical cap bubbles and dashed lines are for microbubbles

4.1.2.6 OXYGEN MASS TRANSPORT COEFFICIENT VARIATION CASES

The oxygen mass transport coefficient is a highly uncertain parameter. The sensitivity of the model to this parameter is an important piece of information for model calibration efforts. To study this, the OMTC was varied +/- 20% from its base case values. Changes to the oxygen mass transport coefficient over this range caused negligible changes in the dissolved sulfur and oxygen histories. Changes to the OMTC did lead to slight changes in the jet concentration profile histories, however all of the added oxygen still dissolved well before the top of the jet.

4.1.2.7 EXERGY PERFORMANCE OF THE BASE CASE

The exergetic performance of the base case was examined. The results for microbubbles and spherical cap bubbles are the same. The exergy feeds to copper fire refining desulfurization are the molten copper and natural gas (modeled as pure methane) used for the headspace burner; injected air at atmospheric pressure, even when pressurized, has negligible exergy content. Exergy leaves the process with the molten copper, the offgas, and heat transfer. Some exergy is also

destroyed. Table 4.5 shows the exergy feeds and outlets to the process. The exergy flowrate of copper was found by dividing the total copper addition by the total time of desulfurization. Overall, it is seen that the copper dominates the exergy balance. This is not surprising as it represents almost the entire mass added during desulfurization. The majority of the exergy lost is with the offgas, suggesting exergy recovery attempts should be targeted hear first. Very little exergy is destroyed due to the total material addition into the furnace being much smaller (<1%) than the initial amount of material in the furnace. Overall, the exergy flows from fire refining are much smaller than for smelting and converting (ref these papers). Copper smelting plants aiming to recovery exergy should target these latter operations before they target fire refining.

Table 4.4 – Exergy feeds and fates for the base case

Exergy Feed Stream	**Thermal Exergy Flow (MJ/tonne-Cu)**	**Chemical Exergy Flow (MJ/tonne-Cu)**	**Percentage of Fed Exergy**
Liquid Copper	452	2110	94.0
Methane	0	173	6.0
Exergy Fate			
Liquid Copper	463	2110	94.0
SO_2	0.498	4.11	0.0
N_2	58.6	0	2.0
CO_2	11.2	4.14	1.0
H_2O	17.7	3.96	1.0
Heat Loss	52.1	0	2.0
Destruction	9.92		0.0

4.1.3 Conclusions and Recommendations

A transient reduced order reacting flow model was made for the desulfurization step of copper fire refining. A sensitivity study was performed with respect to changes in injected gas oxygen grade, initial bubble size, initial melt composition, and mass transport coefficient values.

It was found that use of nearly pure nitrogen in the desulfurization step allowed for acceptable desulfurization rates. The results of the model lead to the following recommendations:

1. Attempts should be made in industry to replace some or all of the injected air with nitrogen from the smelter oxygen plant. This could save hours in the subsequent reduction step. Although decreases in the desulfurization rate may occur, these can be mitigated by increasing the total gas injection, which would not increase the oxidation of the melt as there would be almost no oxygen in the injected gas.
2. Attempts should be made to reduce initial bubble size. This could be done by using smaller tuyeres or attempting microbubble formation, *e.g.* by jetting the gas into the fire refiners instead of bubbling the gas in.
3. Laboratory and/or industrial data for the desulfurization step of fire refining should be collected so that this model can be calibrated. Calibrations are expected to be somewhat unique to each operation
4. Very little exergy is destroyed during desulfurization. Most of the lost exergy is with the offgas. Smelters should target the smelting and converting furnaces for exergy recovery before fire refining as the exergy loss from these former two unit operations is much greater than for fire refining

4.2 Reduction of Desulfurized Blister Copper

4.2.1 Model Description

4.2.1.1 Model Conditions

The model divides the vessel into three distinct regions (Figure 4.1): the liquid copper melt ("bottom volume"), a bubble-jet that goes through the melt (the jet is gas only), and the furnace headspace ("top volume"). The melt and the headspace each are considered spatially homogeneous in temperature and composition within their respective regions; the jet is modeled as a 1D flow reactor along the jet's height. Chemical reaction rates, bubble geometry and velocity, and the associated jet-species flow rates are modeled. Chemical reactions occur either within the jet or heterogeneously at the jet-melt interface.

4.2.1.2 Reduction Chemistry and Kinetics

There are several chemical reactions that occur homogenously in the injected-gas jet and heterogeneously at the jet-melt interface. The first of these reactions is the pyrolysis of methane, which produces soot and hydrogen gas, an important reductant:

$$CH_{4(g)} \rightarrow C_{(s)} + 2H_{2(g)} \tag{4.28}$$

Steam is injected with the natural gas to effect the carbon-steam reaction, which consumes the soot formed in eqn. 4.28 and produces more reducing gas:

$$C_{(s)} + H_2O_{(g)} \rightarrow CO_{(g)} + H_{2(g)}\,. \tag{4.29}$$

Soot can also be consumed by the Boudouard reaction:

$$C_{(s)} + CO_{2(g)} \rightarrow 2CO_{(g)}\,. \tag{4.30}$$

The last homogenous reaction considered is the water gas shift reaction:

$$CO_{(g)} + H_2O_{(g)} = CO_{2(g)} + H_{2(g)}\,. \tag{4.31}$$

All of the reducing gas species (CO, H_2, CH_4) present in the jet are thermodynamically favored to react with copper-dissolved oxygen at the jet-melt interface:

$$CO_{(g)} + \underline{O} \rightarrow CO_{2(g)} \tag{4.32}$$

$$H_{2(g)} + \underline{O} \rightarrow H_2O_{(g)} \tag{4.33}$$

$$CH_{4(g)} + 4\underline{O} \rightarrow CO_{2(g)} + 2H_2O_{(g)} \tag{4.34}$$

The rate laws and kinetic data for reactions 4.29-32 are respectively taken from Palmer et al. [89], Hüttinger and Merdes [90], Ergun [91], and Graven and Long [92]. In order, these are:

$$R_1 = 10^{\left(13-\frac{18600}{T\,[K]}\right)} C_{CH_4} \tag{4.35}$$

$$R_2 = \frac{2.1 \cdot 10^{-4} \alpha x P_{H_2O}[\text{bar}]}{1 + 0.167 P_{H_2O}[\text{bar}] + 7.06 P_{H_2}[\text{bar}] + 1.54\left(P_{H_2}[\text{bar}]\right)^2} \tag{4.36}$$

$$R_3 = 18\alpha \exp\left(\frac{-20906}{T\,[K]}\right) C_C \left(1 + \frac{C_{CO}}{C_{CO_2} K_1}\right)^{-1} \tag{4.37}$$

$$R_{4f} = 5 \cdot 10^{12} \exp\left(\frac{-33700}{T[K]}\right) C_{CO}^{\frac{1}{2}} C_{H_2O} \left(1 + 12000 C_{H_2}\right)^{-\frac{1}{2}} \tag{4.38}$$

$$R_{4r} = 9.5 \cdot 10^{10} \exp\left(\frac{-28700}{T[K]}\right) C_{H_2}^{\frac{1}{2}} C_{CO_2} (1 + 3600 C_{CO})^{-1} \tag{4.39}$$

$$x = 2.67 \cdot 10^{-4} T[K] - 0.676 T[K] + 429 \tag{4.40}$$

$$K_1 = 4 \cdot 10^4 \exp\left(\frac{-11600}{T[K]}\right) \tag{4.41}$$

In these equations, R_i is the rate of reaction i in kmol/s/m, C_i is the concentration of species i in kmol/m, T is the melt temperature in Kelvin, and α (m^2/kmole) and x (unitless) are scaling

parameters. The subscripts "*f*" and "*r*" for reaction 4 denote the forward and reverse rates, respectively. It is appropriate that such a scaling parameter be present as the specific surface area of the carbon formed in fire-refining is highly uncertain. Ultimately, α is probably best found via Bayesian calibration, should industrial observations be available for such a calibration. The value of α used is given in the results. x is a temperature scaling parameter for the carbon steam reaction found from Ergun's data [91]. It is applied to the data of Huttinger and Merdes because these authors only studied one temperature and the current work looks at temperature variations at a higher baseline temperature than used by Huttinger and Merdes [90].

It was assumed that the reduction rate of the melt was proportional to the difference between the oxygen concentration in the bulk melt and the oxygen concentration at the jet-melt interface. Furthermore, it was also assumed that any oxygen that reached the jet-melt interface was immediately consumed by a reduction reaction, so the concentration of dissolved oxygen at the jet-melt interface is zero. As such, the rate of oxygen removal from the melt per length of jet height is

$$\dot{\omega}_{\underline{O}} = -k_{\underline{O}} A X_{\underline{O}}\,, \tag{4.42}$$

Where $k_{\underline{O}}$ is a mass transfer coefficient at the jet-melt interface and A is the jet-melt interfacial area per height. It was assumed that the rate of oxygen consumption by each reducing reagent was proportional to the fraction of the jet-gas comprised by each reagent, *i.e.*:

$$R_5 = Y_{CO} k_{\underline{O}} X_{\underline{O}} \tag{4.43}$$

$$R_6 = Y_{H_2} k_{\underline{O}} X_{\underline{O}} \tag{4.44}$$

$$R_7 = \frac{Y_{CH_4} k_{\underline{O}} X_{\underline{O}}}{4} \tag{4.45}$$

With these rate expressions for equations 4.35-41, the rates of generation of the jet species ($\dot{\omega}_i$) in kmol/s/m during reduction are

$$\dot{\omega}_{CH_4} = -R_1 - R_7 \tag{4.46}$$

$$\dot{\omega}_{C} = R_1 - R_2 - R_3 \tag{4.47}$$

$$\dot{\omega}_{H_2} = 2R_1 + R_2 + R_{4f} - R_{4r} + R_6 \tag{4.48}$$

$$\dot{\omega}_{CO} = R_2 + 2R_3 - R_{4f} + R_{4r} - R_5 \tag{4.49}$$

$$\dot{\omega}_{H_2O} = -R_2 - R_{4f} + R_{4r} - R_{4f} + R_6 + 2R_7 \tag{4.50}$$

$$\dot{\omega}_{CO_2} = -R_3 + R_{4f} - R_{4r} - R_{4f} + R_5 + R_7 \tag{4.51}$$

4.2.1.3 Mass and Momentum Conservation Laws for the Jet

The model tracks the concentrations and flowrates of methane, steam, hydrogen, carbon monoxide, carbon dioxide and soot along the height of the jet. It is assumed that diffusion in the jet is negligible because the melt blocks gas-diffusion between bubbles and the bubbles are small relative to the length of the jet. In the direction along the jet (z), the continuity equation is

$$\frac{\partial(C_i A_x)}{\partial t} + \frac{\partial(C_i w A_x)}{\partial z} = \dot{\omega}_i A_x \,, \tag{4.52}$$

where C_i is the concentration of species i, A_x is the cross-sectional area of the gas in the bubble jet at height z, w is the bubble velocity, and $\dot{\omega}_i$ is the net generation rate of species i via chemical reaction in kmoles/m^3-s. Continuity is used to solve the concentrations of the chemical species in the jet as well as the concentration of bubbles at any point along the jet. $\dot{\omega}_{bubbles}$ is zero because bubble generation or destruction is assumed to not occur.

Two types of bubbles are modeled: microbubbles (spheres) and spherical-cap bubbles. The upward velocity (w) of spherical-cap bubbles in the jet is found according to Wegener and Parlange [85], who derived analytical expressions for rising spherical cap bubbles under steady flow. When microbubbles are modeled, the upward velocity is found using Bond's modification of Stokes' law [86] for spherical bubbles undergoing steady flow. Although both velocity expressions are a simplification of jet momentum conservation, they capture the expected bubble radius dependency of the bubble velocity while also giving a first order approximation of injected bubble vertical velocities. The equations for the rising bubble vertical velocity are:

$$w_{sc} = \frac{2}{3}\left[\frac{2gr_{bub}(1-\cos\theta)}{\sin^2\theta}\right]^{\frac{1}{2}} \tag{4.53}$$

$$w_{mb} = \frac{1}{3}\frac{g\rho_{Cu}{r_{bub}}^2}{\mu_{Cu}} \tag{4.54}$$

where w_{sc} is the spherical-cap bubble velocity, w_{mb} is the microbubble velocity, g is the terrestrial acceleration due to gravity (9.8 m/s^2), r_{bub} is the bubble radius in meters, θ is the spherical-cap bubble angle (50°), ρ_{Cu} is the density of the liquid copper at 1400K (8000 kg/m^3), [87], and μ_{Cu} is the dynamic viscosity of liquid copper at 1400K ($4\cdot10^{-3}$ Pa·s). The velocity of microbubbles is much more sensitive to changes in the bubble radius than spherical-cap bubbles due to the difference in dependency on bubble radius, as shown in figure 4.15.

Bubble radius along the jet is found from the ideal gas law, in which the total pressure at a given height is the hydrostatic pressure of the melt, and the moles of gas per bubble are found by taking the ratio of the concentration of gas to the concentration of bubbles

$$V_{sb} = \frac{C_{gas}}{C_{bub}}\frac{RT_{melt}}{P_{jet}} = \frac{\pi}{3}(2+\cos\theta)(1-\cos\theta)^2{r_{bub}}^3 \tag{4.55}$$

$$V_{mb} = \frac{C_{gas}}{C_{bub}}\frac{RT_{melt}}{P_{jet}} = \frac{4}{3}\pi{r_{bub}}^3 \tag{4.56}$$

$$C_{gas} = \sum_i C_i \tag{4.57}$$

$$P_{jet} = P_0 + g\rho_{Cu}(L-z) \tag{4.58}$$

$$A_{sb} = 2\pi r^2(1-\cos\theta)C_{bub} \tag{4.59}$$

$$A_{mb} = 4\pi{r_{bub}}^2 C_{bub}\,, \tag{4.60}$$

where V_{sb} and V_{mb} are the volume of gas per spherical-cap and micro bubble respectively at height z along the jet respectively; $\frac{C_{gas}}{C_{bub}}$ is the ratio of the concentration of gas to the concentration of bubbles at height z; P_{jet} is the hydrostatic pressure of the melt at height z above the tuyere insertion point; A_{sb} and A_{mb} are the surface area of the jet-melt interface per height of jet at an arbitrary height for spherical-cap and microbubbles respectively. One may note that the surface area of the

spherical cap bubble on the wake-side has been ignored. This choice was made because this area is highly uncertain, and it is also moving away from the melt. Additionally, if the mass transfer coefficient is calibrated, the exact area of the bubbles does not need to be known. For both spherical cap bubbles and microbubbles, the rate of oxygen transport ultimately goes as

$$\dot{\omega}_{\underline{O}} = -k_{\underline{O}} B X_{\underline{O}} {r_{bub}}^2 , \tag{4.61}$$

where B is the constant giving the surface area per bubble radius squared for a given bubble geometry. As such, an arbitrary change to B will cause an inversely proportional change to the calibration of $k_{\underline{O}}$. As an additional note, the molar flowrate of any species anywhere in the jet is given by the product of the bubble velocity and the concentration of that species

$$\dot{N}_i = w C_i . \tag{4.62}$$

There are some important points regarding equations 4.52-4.62. First, the surface area to volume ratio of microbubbles is much larger than for spherical-cap bubbles due to the smaller size of the microbubbles. This smaller difference leads to modeled jet interfacial areas about two orders of magnitude greater for microbubbles than for spherical-cap bubbles; suggesting one of two possibilities: either there are different $k_{\underline{O}}$ values for each bubbling regime, or microbubble injection is actually orders of magnitude faster than spherical-cap bubble injection. The latter does not seem to be the case according to industrial observation [48], so the former is assumed in this model. Additionally, the bubble velocity as a function of height will be different for spherical-cap bubbles and micro bubbles. Figure 4.15 shows how injected gas velocity changes over the height of one meter of liquid copper for different initial bubble radii in the spherical-cap bubble and microbubble regimes. The moles of gas in the bubbles is kept constant for each case over the jet height for figure 4.15. The radii of the bubbles were chosen so that the initial velocities of the microbubbles and spherical cap bubbles would be equal. Microbubbles have a higher acceleration than spherical-cap bubbles, which counteracts the effects of the higher surface area to volume ratios for microbubbles

to a small degree, as these bubbles spend less total time in the melt than the spherical cap bubbles, so they have less time to participate in reaction.

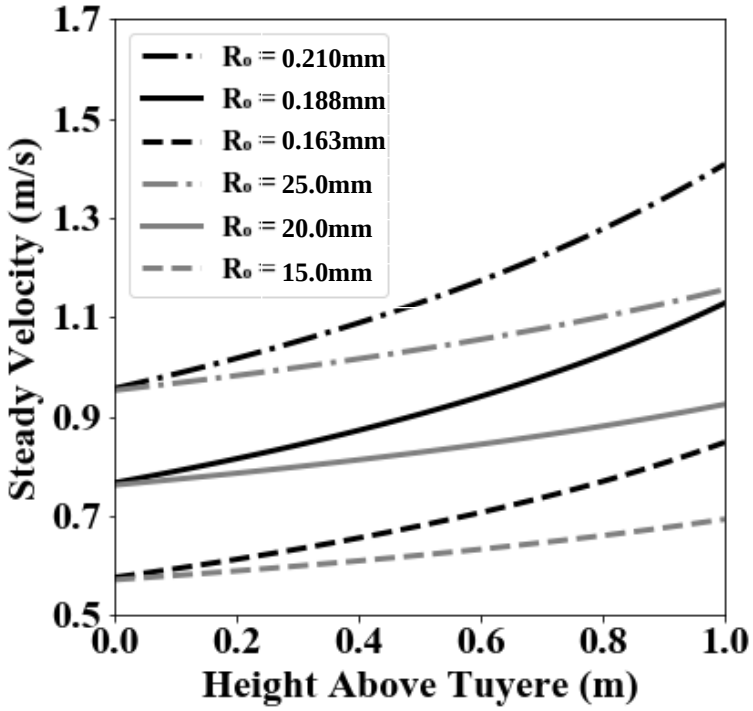

Figure 4.14 - Estimated bubble velocity for spherical-cap bubbles (gray) and microbubbles (black) with a constant bubble molar amount of gas for a given R0 over the height of 1 m of depth of liquid copper

4.2.1.4 Mass conservation for the melt

No species are allowed to dissolve into the melt from the jet because this is thermodynamically unfavorable in the studied system. Oxygen leaves the melt via reaction with CO, H_2, and CH_4 in the jet. Oxygen is removed from the melt as soon as it reaches the jet-melt interface *via* reactions 4.5-7. Copper is neither added to nor removed from the furnace. The rate of change of the mass in the melt of copper and oxygen are thus

$$\frac{dN_{Cu,melt}}{dt} = 0 \tag{4.63}$$

$$\frac{dN_{\underline{O}}}{dt} = \int_0^L \dot{\omega}_{\underline{O}} dz \ , \tag{4.64}$$

where N_i is the molar amount of species i in the melt and L is the distance between the tuyere insertion point and the top melt surface.

4.2.1.5 Initial conditions

The melt is initially comprised of 4090 kmoles (260 tonnes) of liquid copper that has a dissolved oxygen content of 13800 molar ppm (3500 weight ppm); the residual sulfur left after desulfurization is neglected. The melt starts with a specified uniform temperature (1398K for the baseline case). Temperature was kept constant as melt temperature usually only changed by less than 3K over the course of an entire reduction cycle using the calculated heat transfer values (see below). This result is in accordance with the industrial data, which typically saw temperature changes on this order over the whole three hour reduction time. The model considers reduction to start with the entrance of the first bubble into the melt. As such the jet length approaches zero as the time since gas-injection start approaches zero. The jet first reaches the top of the melt after about 2s of gas injection. The initial temperature of the jet is the initial melt temperature.

4.2.1.6 Jet boundary conditions

The model uses boundary conditions for the jet only at the jet inlet because the differential equations describing the jet are first order, so only one condition is needed (a marching problem). The chemical composition and flowrate of the jet is fixed at the jet inlet and is constant over the entire modeled time. The flowrates and compositions used for each study are given in the results section. The inlet gas is a mixture of methane at 298K and steam at 512K. The composition and flowrate of the jet leaving the melt is variable and solved via mass conservation as described earlier. The concentration of bubbles at the jet inlet is given by taking the ratio of the bubble flowrate to the bubble vertical velocity at the jet inlet,

$$C_{bub}|_{z=0} = \left.\frac{\dot{F}_{bub}}{w}\right|_{z=0} \tag{4.65}$$

where C_{bub} is the concentration of bubbles (number of bubbles/m) and $\dot{F}_{bub}$ is the bubble flowrate (number of bubbles per second). The flowrate of bubbles at the inlet is approximated by assuming a monodispersion of bubbles; the initial bubble size used is given in the results section.

4.2.1.7 Heat transfer in the furnace

A steady state radiation heat transfer model was made for heat exchange between the melt, headspace brick, and headspace flame. The full details of the balance can be found in Appendix B. Essential to this model is the net heat transfer rate to the melt and out of the furnace. These are important for establishing an energy balance on the melt and for calculating exergy losses and destruction. Table 4.6 shows these values as a function of melt temperature. The values were found to produce very small melt temperature changes (less than 1K) over the course of a three hour reduction cycle, as seen at FMI Miami Anode Plant.

Table 4.5 - Heat transfer values necessary for model reproduction

Melt Temperature (K)	Net Heat Transfer Rate to Melt (MW)	Net Heat Transfer Rate through Furnace Walls (MW)	Steady State Flame Temperature (K)
1373	-0.69	2.81	1849
1398	-0.73	2.86	1852
1423	-0.78	2.90	1855
1448	-0.82	2.95	1858
1473	-0.87	2.99	1862

4.2.1.8 Exergy Calculations

The exergy balance used for the reduction step of fire refining is the same as that used for the other process models in the current work (described in Chapter 2). For the reduction step of fire refining, exergy is fed to the process as desulfurized blister copper (the product of the desulfurization step of fire refining), the methane-steam mixture used to effect reduction, and the

methane fed to the headspace burner. Exergy leaves the process as anode copper (the product of reduction), offgas, and heat.

4.2.1.9 Solution Method

The reacting flow system was solved *via* a forward-time, back-space solution method (FTBS) [88]. The timestep size used was 0.0005 seconds. The jet-depth increment used was 0.01 m. Use of this method makes sense because there is only one boundary condition for the jet (at the inlet).

4.2.2 RESULTS AND DISCUSSION

This work features a sensitivity study which looks at how the model performs as initial bubble size, methane-steam ratio with a constant total gas injection rate, steady operating temperature, initial oxygen concentration in the melt, steam addition rate at constant methane addition rate, mass transport coefficient for dissolved oxygen change, and soot specific area. These sensitivity studies were done for both spherical-cap bubbles and micro bubbles. Exergy analyses were done for the cases too, and it was found that with the exception of the methane/steam injection ratio case, there was a negligible impact on exergetic performance.

4.2.2.1 The base case

The base case parameter values used for spherical cap and microbubbles cases are shown in table 4.7. The parameter values for the base cases were chosen so that each case would give the same amount of dissolved oxygen after three hours of refining time. With the same starting and ending oxygen content, the shapes of the base case histories could be usefully compared.

Table 4.6 – Parameter values used for the base case

Parameter	Value (Spherical Caps)	Value (Microbubbles)
Tuyere Submergence Depth (m)	1.0	
Temperature of Blow (K)	1398	
Amount of Copper (kmoles)	3918.42	
Initial Oxygen Content (Molar ppm)	13800 (3500 mass ppm)	
Steam Injection Rate (kmoles/s)	0.0234	
Methane Injection Rate (kmoles/s)	9.68×10^{-3}	
Soot Specific Area (m^2/g)	7200	
Bubble Radius (m)	20×10^{-3}	168×10^{-6}
Spherical Cap Angle (^{o})	50	-
$k_{\underline{O}}$ ($kmol \cdot m^{-2} \cdot s^{-1}$)	2.1×10^{-4}	4.0×10^{-6}

For the base cases, contours of the cross-sectional area of the jet over height from tuyeres insertion and time were made; these are shown in figure 4.16. Additionally, contours over height from tuyere insertion and time were made for dissolved species concentrations; these are shown in figures 4.17-4.22.

Figure 4.16 shows that the spherical-cap bubble jet has much greater cross sectional area (and thus jet-melt interfacial area) variance over its height than the microbubble case. The reason for this is that the microbubble jet has a higher average jet velocity over the jet height, as shown in figure 4.15. This means that there is less time for individual bubbles to grow in the microbubble injection case than in the spherical cap bubble case, so the variation in cross-sectional and interfacial area over the depth of the melt for the micro-bubble case is smaller than for the spherical cap bubble case.

Figure 4.15 shows the methane profile of the jet with respect to time. The concentration of methane continuously drops over the jet height. This is because methane pyrolysis and the reduction of the melt with methane continuously occur over the jet height, and there are no

methane-replenishing reactions. As time progresses, the depletion of methane slows because there is less oxygen transport to the jet melt interface, due to there being less dissolved oxygen in the melt. This slows down the rate of methane consumption by its melt-reducing reaction. The microbubble case shows slightly faster methane depletion than the spherical cap bubble case; this is because a larger fraction of the jet-melt interfacial area is in the bottom portion of the jet for the microbubble case, so slightly more reduction of the melt with CH_4 occurs in this region for the microbubble case. This difference is practically insignificant, but explains the slight differences in the concentration profiles between the spherical cap and microbubble cases seen for the other jet species.

Figure 4.16 shows the transient concentration profiles for steam in the jet. As the submergence of the jet decreases, the concentration of steam decreases. This is because steam is consumed by the carbon steam reaction all along the length of the jet. As time progresses, the rate of steam consumption increases. The reason for this is that the rate of consumption of methane decreases with increasing time as described in the preceding paragraph, which in turn means there is more methane to participate in the pyrolysis of methane. This increase in the methane pyrolysis rate with increasing time produces more soot, which increases the net rate of the carbon-steam reaction. The increase in the rate of the carbon steam reaction is responsible for the increased rate of steam consumption with time. The bubbling regime has a negligible impact on the steam concentration.

Figure 4.17 shows the transient profiles for soot. Starting from the jet insertion point, soot concentration first increases along the jet height, reaching a maximum at about 0.3m, and then decreases. The initial increase is caused by soot production *via* methane pyrolysis. The subsequent decrease is caused by the decreasing rate of methane pyrolysis along the jet height combined with soot consumption by the carbon-steam reaction. As time progresses, the concentration of soot increases along the whole jet height. This is because less methane is consumed by melt reduction, allowing for greater rates of methane pyrolysis with increasing time. Bubbling has a negligible impact on soot concentration.

Figure 4.18 shows the transient profiles for hydrogen. Hydrogen concentration increases over about the first 0.8m of jet height and decreases over about the last 0.2m of jet height. This is because the rate of hydrogen production by methane pyrolysis and the carbon-steam reaction is

greater than the rate of hydrogen consumption by melt reduction over the first 0.8m of jet height. Over the last 0.2m, the rate of hydrogen consumption is greater. As time progresses, the concentration of hydrogen increases at all jet heights. This is because less methane is consumed with increasing time, so there is more methane pyrolysis, and subsequently, more carbon-steam reaction with increased time. The increasing rate of these reactions with increased time increases the rate of hydrogen production. The bubbling regime has a negligible impact on hydrogen concentration.

Figure 4.19 shows the transient CO concentration profiles. The explanation of these is the same as for H_2 with the exception that CO is not produced by methane pyrolysis.

Figure 4.20 shows the transient CO_2 concentration profiles. As the jet submergence decreases, the CO_2 concentration increases. This is because oxidation of CO to CO_2 happens along the whole jet height. As time progresses, the concentration of CO_2 decreases all along the jet. This is because the concentration of copper-dissolved oxygen decreases with time, causing the rate of CO conversion to CO_2 to decrease. Bubbling regime had a negligible impact on CO_2 concentration.

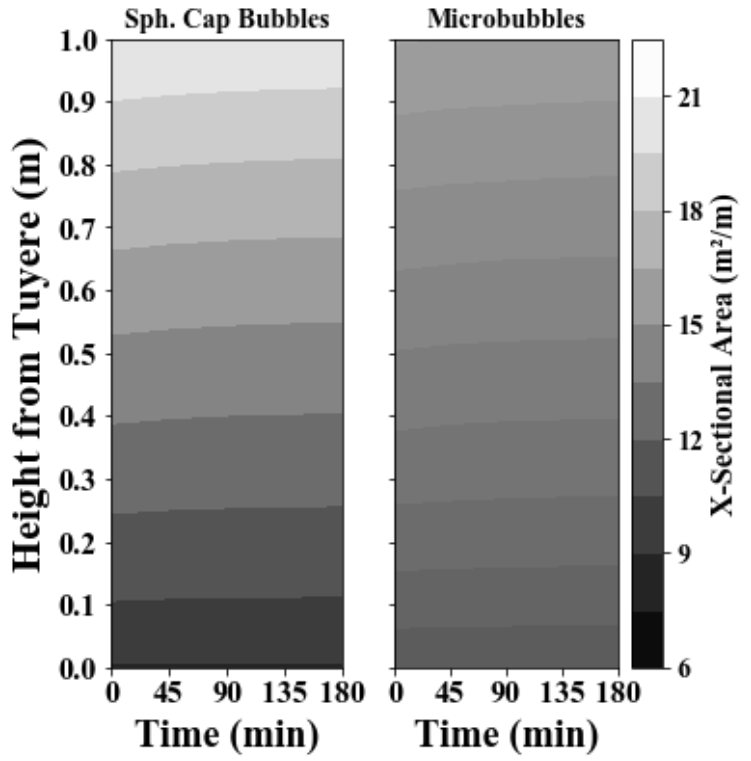

Figure 4.15 – Cross sectional area contours over time and the height of the jet from injection.

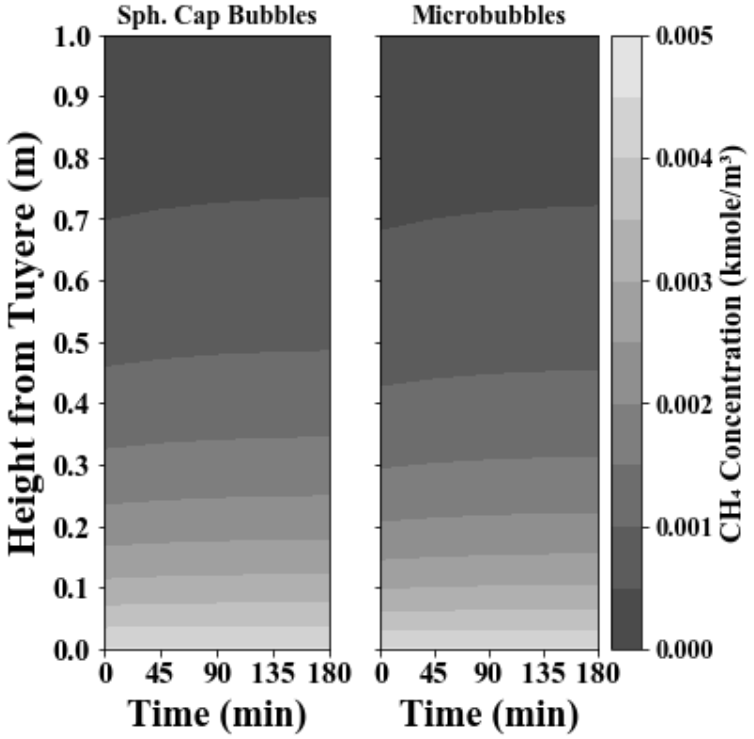

Figure 4.16 – Contours of the methane concentration over the jet height and refining time for the base cases

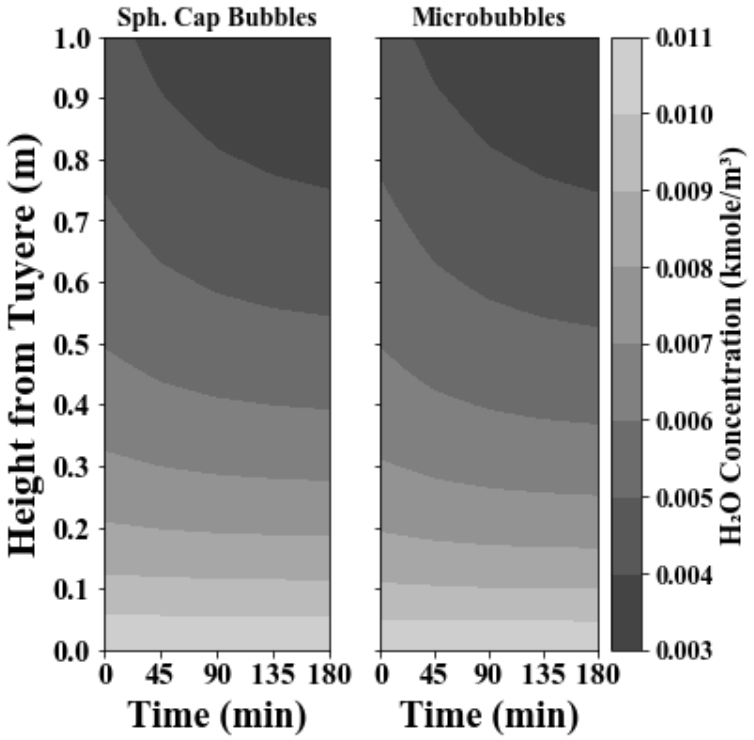

Figure 4.17 - Contours of the steam concentration over the jet height and refining time for the base cases

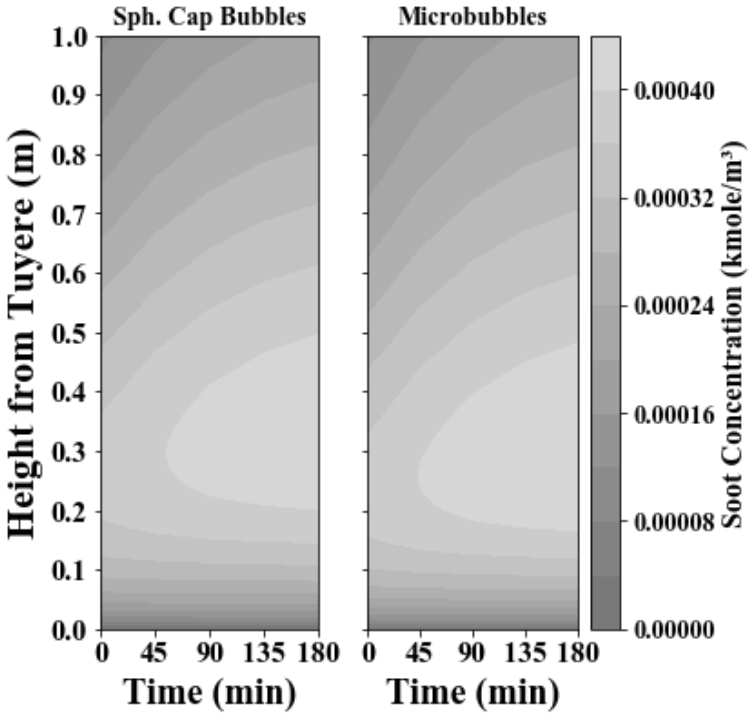

Figure 4.18 - Contours of the soot concentration over the jet height and refining time for the base cases

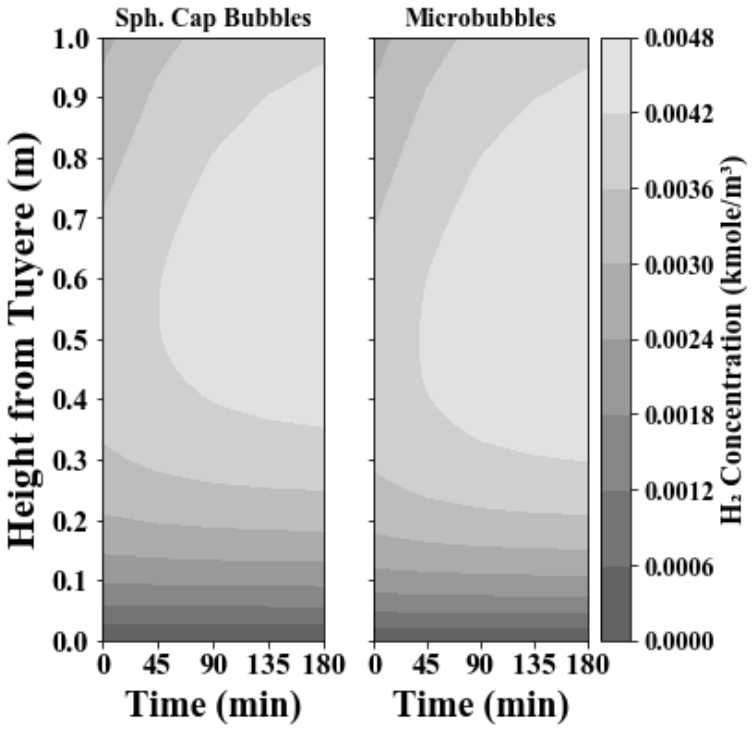

Figure 4.19 – Contours of the H2 concentration over the jet height and refining time for the base cases

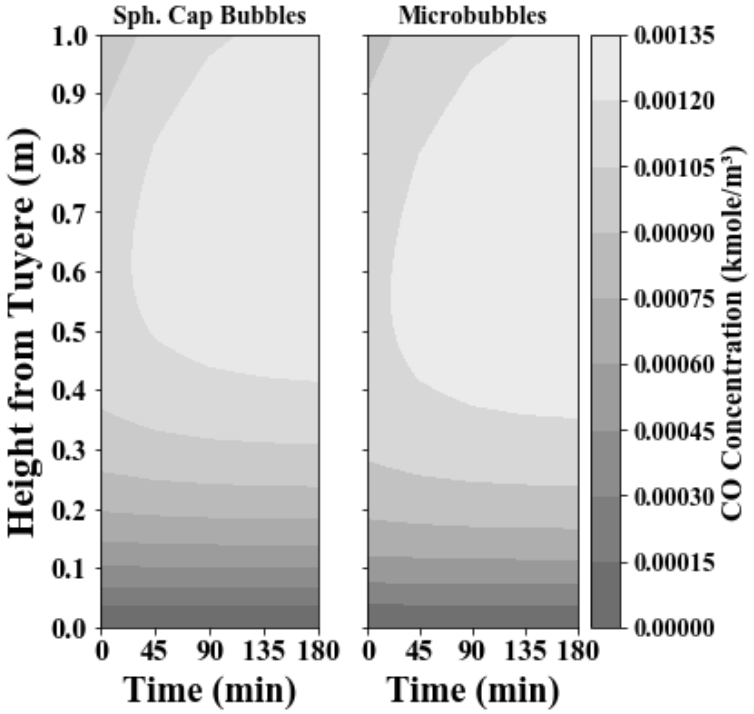

Figure 4.20 - Contours of the CO concentration over the jet height and refining time for the base cases

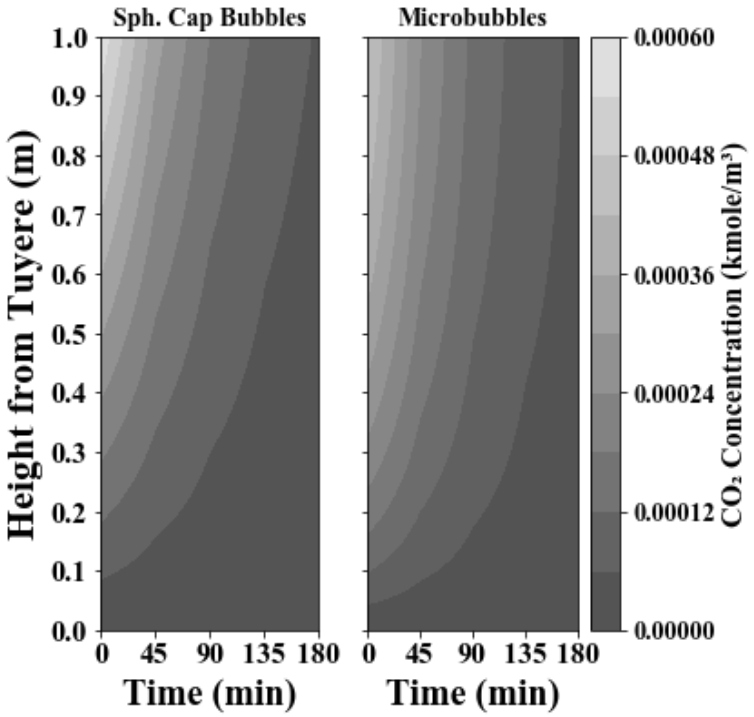

Figure 4.21 - Contours of the CO2 concentration over the jet height and refining time for the base cases

Figures 4.23-24 show the exergetic performance of the base case. The exergy of the dissolved oxygen is negligible. 78% of the exergy fed to and leaving the process is contained in the liquid copper. About 90% of the exergy flowing through the system is chemical exergy. 21% of the exergy fed to the process is lost, and 18% of this 21% is with the offgas. Heat loss represents only 3% of the exergy loss. This suggests targeting the fire-refining offgas for exergy recovery. One possible way of doing this would be using the offgas to preheat the gas injected to the furnace. Only 1% of the exergy fed to the process is destroyed. This make sense considering the small composition change of the process, 0.5 wt%.

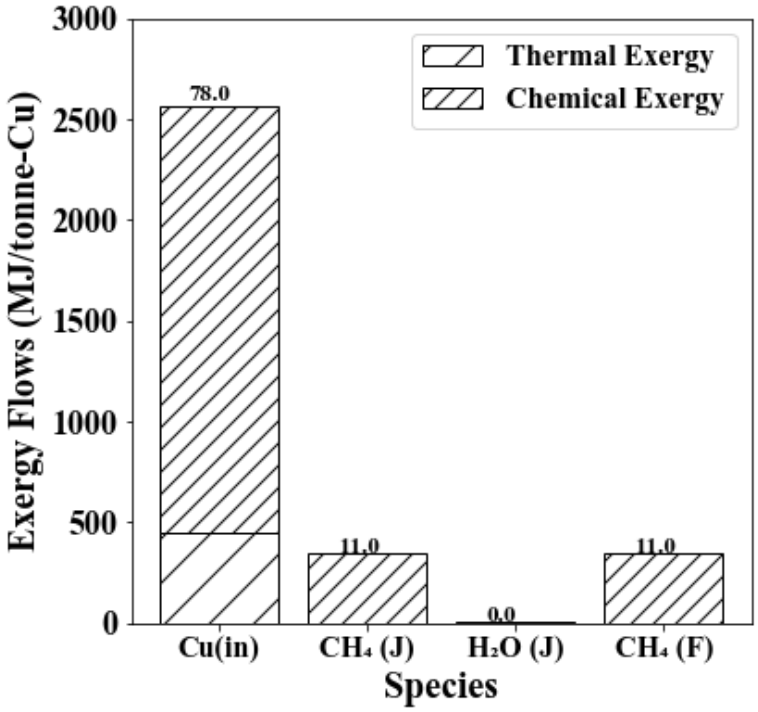

Figure 4.22 - Exergy flows into the reduction step of copper fire refinining. (J) denotes injection with the jet, and (F) denotes injection with the flame. The exergy of dissolved oxygen in the copper is negligible.

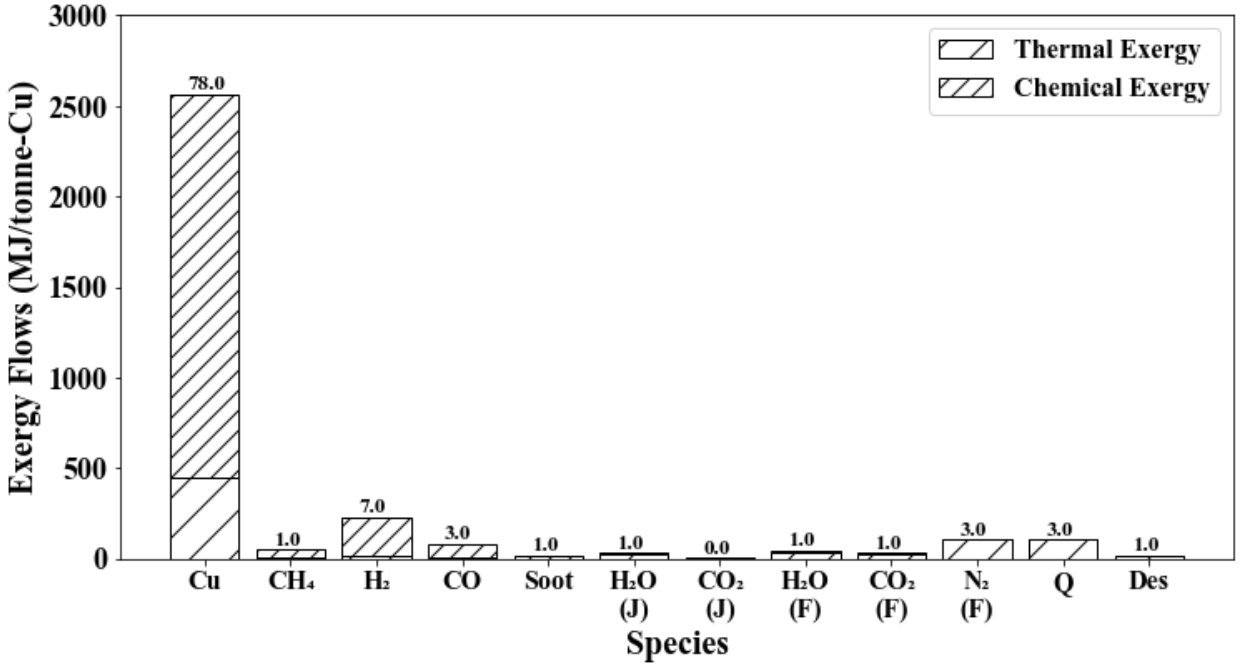

Figure 4.23 - Exergy flows out of the reduction step of fire refining. (J) indicates the exergy associated with flow off the jet, whereas (F) indicates the exergy associated with flow off the flame.

4.2.2.2 Bubble Size Variation

Figure 4.25 shows dissolved oxygen content histories for different bubble sizes. The bubble sizes for both spherical cap and microbubbles were varied +/- 25% about their base case values. Dissolved oxygen content for the base case parameter value set for both spherical cap and microbubbles had almost exactly the same time dependency. This result is not *a priori* guaranteed as the bubble ascension velocities do not have the same submergence depth dependency.

The results show that reduction rate is very sensitive to initial bubble size for both spherical cap and micro bubbles. The reasons for this are first, smaller bubbles have a higher surface area to volume ratio; second, smaller bubbles also have a longer residence time in the melt. The combination of these two features causes higher total gas in the melt at a higher surface area to volume ratio as bubble size is decreased, leading to improved reduction rates. The effect is more pronounced for microbubbles than for spherical cap bubbles. The reason for this is explained by figure 4.15. Microbubble rise velocity is much more sensitive to bubble size than for spherical cap bubbles. Thus, the same percentage change in bubble radius causes the amount of gas held in the melt at any given moment to change to a much greater extent for microbubbles than for spherical cap bubbles. In terms of industrial practice, these results as a whole lend support to the suggestion that attempts at bubble size reduction be done.

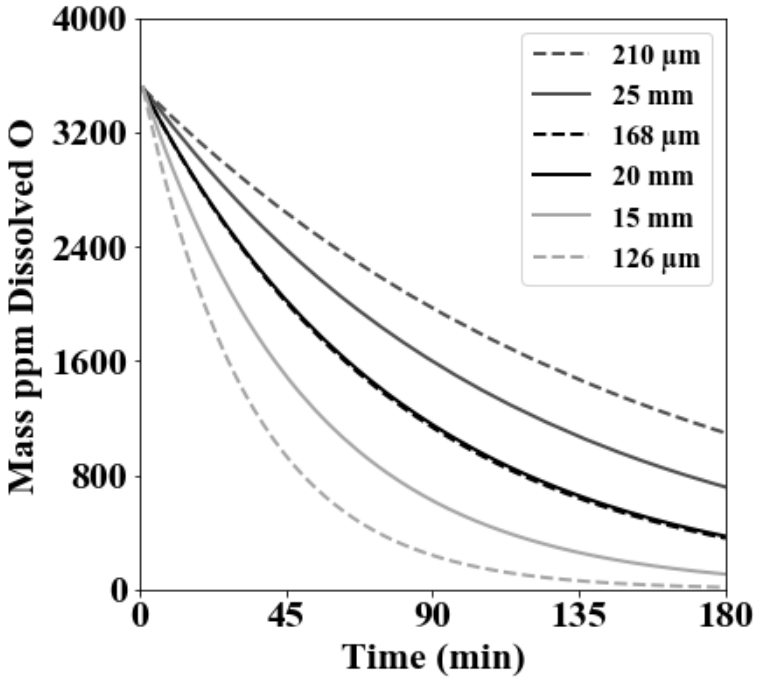

Figure 4.24 – Melt dissolved oxygen content histories as functions of initial bubble size and type of bubble injected.

4.2.2.3 Methane-Steam Ratio with Constant Total Gas Injection Rate

One very interesting possible improvement to the fire-refining process is optimization of the methane-steam ratio used. The authors of this work expect that the reduction step of fire-refining is liquid-phase mass transport controlled. As such, there will be a point where the rate of methane addition becomes high enough that not all of the methane or its reducing product gases will be able to react with dissolved oxygen at the jet/melt interface. This extra methane is thus wasted. Furthermore, because the pyrolysis of methane produces soot, the extra methane can also put increased pressure on the offgas handling system due to extra soot formation. However, the methane addition rate cannot simply be decreased; such a reduction in the total gas injection rate to the furnaces would reduce the jet-melt interfacial area and thus the reduction rate.

A simple solution to this problem is to replace any removed methane with additional steam. Every 1 kmole/s of methane reduction needs to be made up with approximately 1.5 kmole/s of steam. This is because every mole of added methane pyrolyzes into two moles of hydrogen gas (approximately). For this model, making a loss of x kmole/s of methane injection with $1.5x$ kmole/s of steam was found to produce nearly constant reduction rates. The ratio of 1.5 might be different

between each industrial operation; the point is that it should be possible to maintain the same reduction rate while saving on natural gas injection by making up the natural gas with steam.

The cases studied in this section reduced methane addition by 1/6 and 1/3 of the base-case injection rates. The steam addition was correspondingly increased by 1/4 and 1/2 of the base-case value. In an actual plant, if this additional steam is not available, nitrogen produced from the smelter oxygen plant could potentially be used as well. This would ensure approximately the same volume of gas per height of melt over the entire refining time (the gas volume would change slightly because a higher steam to methane ratio causes additional carbon steam reaction) and thus nearly the same reduction rate, assuming that there is enough reducing gas in the jet to accommodate the rate of oxygen transport to the jet melt interface.

This result is shown in figure 13. For both spherical cap and microbubbles, replacement of methane with steam, while maintaining approximately the same if not very slightly improved reduction rate, was possible until the methane addition was a little less than 2/3 of its industrially used value. 2/3 methane injection was the cut-off point on mass balance considerations; below this level, there was not enough reducing gas everywhere in the jet to accommodate the rate of oxygen transport to the jet-melt interface. This powerful results clearly merits exploration at industrial sites. It is safe and easy to implement, although it should be employed incrementally to ensure that methane addition does not go below the minimal needed rate to ensure there is enough reducing gas to accommodate dissolved-oxygen transport.

Along with savings in natural gas addition, savings in soot formation can be expected as well. The original motivation for injecting steam with the natural gas is control of soot formation *via* the carbon steam reaction. As the steam to methane ratio increases, it can be expected that soot production will decrease. This is shown in figure 4.27. The soot production rate was reduced by approximately a factor of three over the methane addition rate studied. At an operation, the headspace flame participates in the capture of soot and other nonreacted reducing gas, so the exact magnitude of the reduction in soot production may not be as high. However, the reduction in the total amount of soot that makes into the offgas handling system is a benefit of decreasing the methane addition rate and replacing it with steam.

Finally, changing the methane/steam ratio to the 2/3 methane case decreased the fed exergy by about 100 MJ/tonne-Cu. This decreased the total exergy lost by approximately the same amount, and changed the proportion of exergy leaving the furnace with the product copper to 81%.

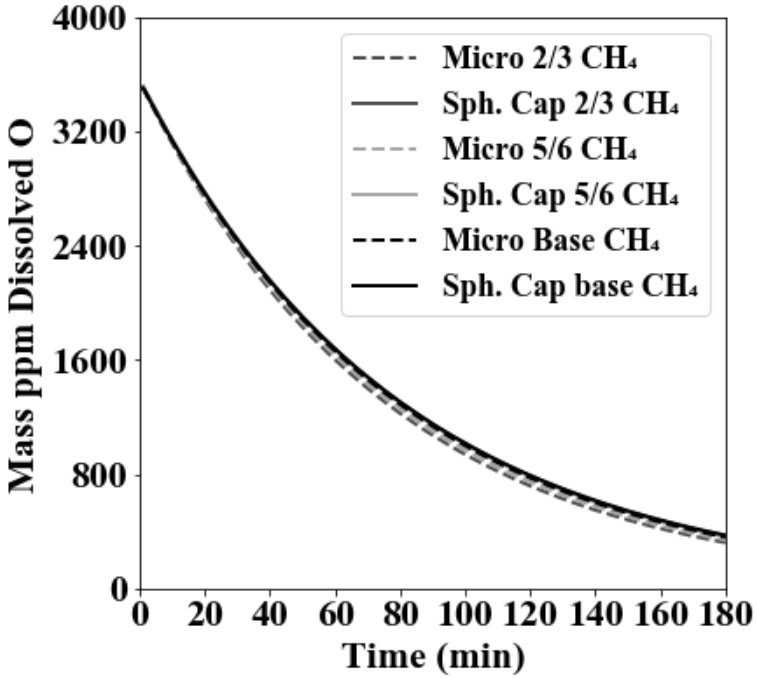

Figure 4.25 – Melt dissolved oxygen content histories for different methane-steam ratios with constant total gas injection rate

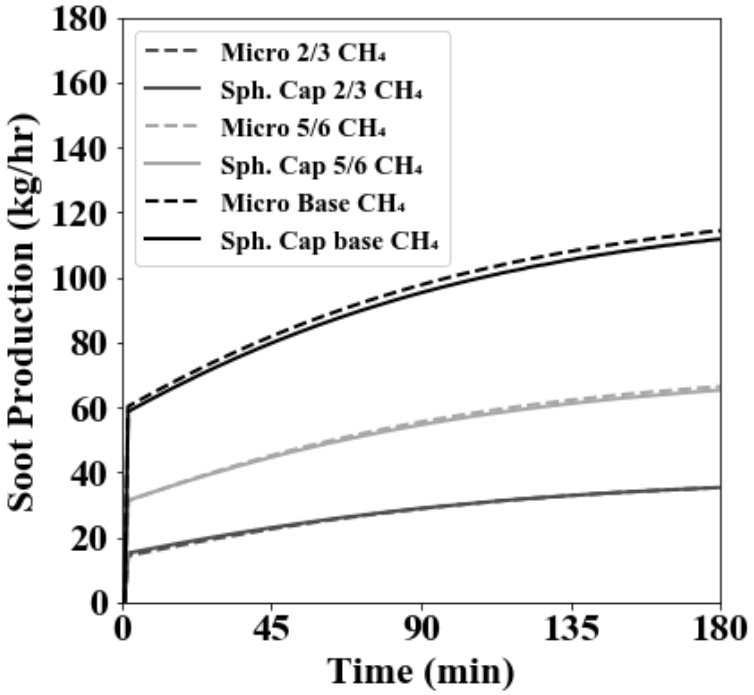

Figure 4.26 – Soot production histories for the methane-steam ratio with constant total gas injection rate case

4.2.2.4 Temperature Variation Cases

Temperature was varied +25 K from the baseline value of 1398 K. The results of this study are shown in figure 4.28. Reduction time is only slightly sensitive to temperature over the studied range. Higher temperatures lead to improved reduction times because the specific volume of the injected gas, and thus the jet-melt interfacial area, is higher. The difference between spherical cap bubble injection and microbubble injection is negligible.

Figure 4.29 shows the effect of temperature on soot production. As temperature is increased, soot production decreases. Although both the pyrolysis of methane and carbon steam reaction speed with increased temperature, the carbon-steam reaction outpaces the rate of methane pyrolysis, causing a decrease in soot production and increase in amount of reducing gas in the jet. This increase in reducing gas would assist attempts to increase the steam-methane ratio while keeping total gas injection constant. Overall, the results of the temperature variation study suggest that plants should try to maximize the temperature of the fire-refining melt; the most economic way to do this may be to run the converters, which precede copper fire refining, at higher temperatures during the copper blow.

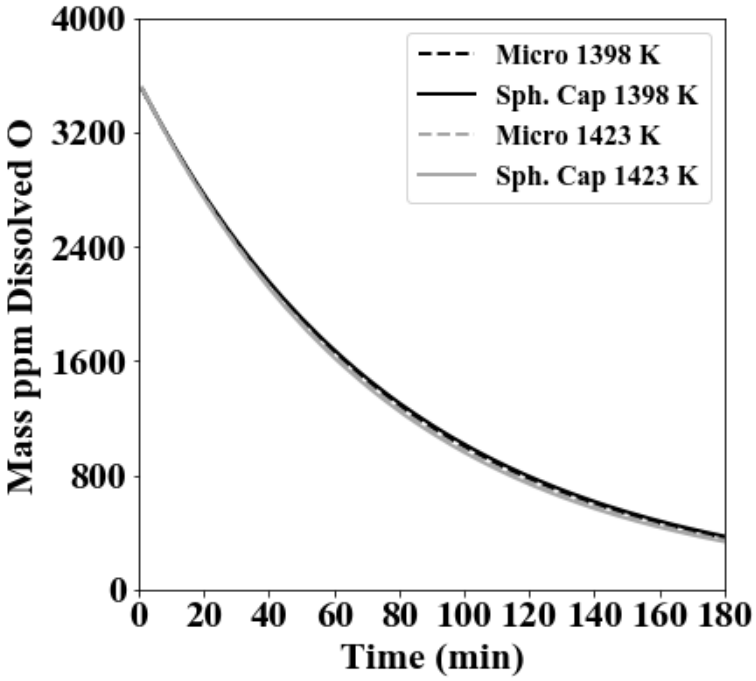

Figure 4.27 – Dissolved oxygen content histories for the temperature variation cases

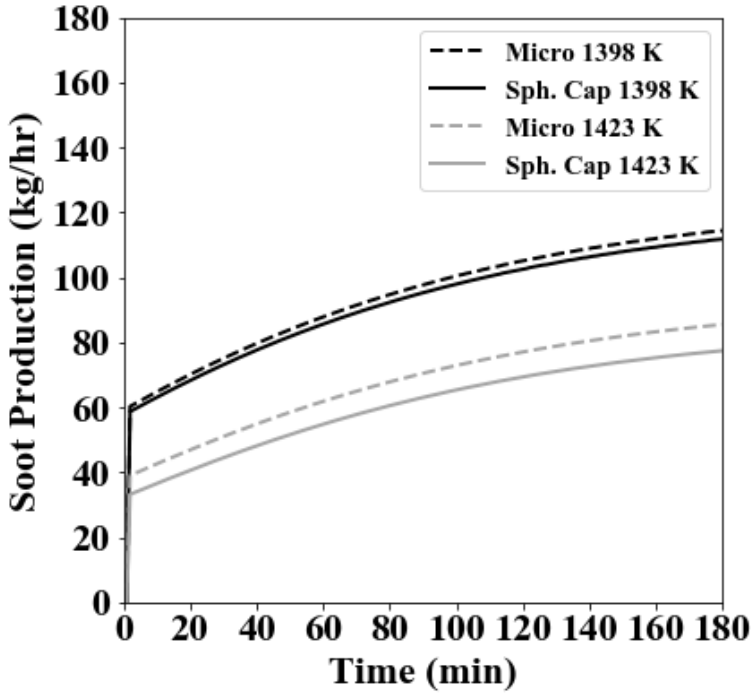

Figure 4.28 - Soot production histories for the temperature variation cases

4.2.2.5 Initial Dissolved Oxygen Variation Cases

The initial oxygen content in the melt was varied +/- 1000 ppm about the base case level of 3500 ppm. These changes to the initial oxygen content had influenced the terminal dissolved oxygen content by +/- 150 ppm dissolved oxygen respectively. The spherical cap bubble cases and microbubble cases had almost exactly the same trend. This suggests that for the same combination of surface area and $k_{\underline{O}}$ the rate of reduction is exactly the same.

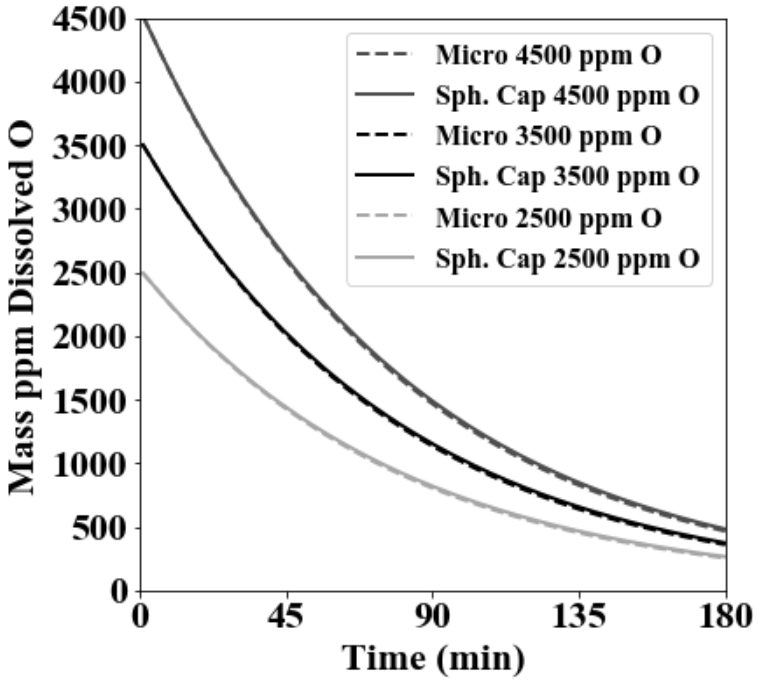

Figure 4.29 - Dissolved oxygen content histories for the initial dissolved oxygen variation cases

4.2.2.6 Oxygen Mass Transport Coefficient Variation

The oxygen mass transfer coefficient ($k_{\underline{O}}$ or OMTC) for both the microbubble and spherical cap bubble cases was varied +/- 20% about its base case values. The effect of this variation on dissolved-oxygen histories are shown in figure 4.31. It is seen that increases and decreases to the oxygen mass transport coefficient (OMTC) increase and decrease, respectively, the reduction rate proportionally. Nevertheless, this study is important because it gives an idea of the spread in the OMTC values that would be obtained *via* model calibration. Additionally, another important but subtle result is that decreases to the OMTC value increase terminal dissolved oxygen by a greater

proportion than the equivalent increases to OMTC decrease the terminal dissolved oxygen. A reduction of 20% in the OMTC increased terminal dissolved oxygen by about one third; the 20% increase in OMTC decreased terminal dissolved oxygen by about 25%. This difference is due to the exponential-decay like behavior of copper reduction.

Also interesting is that the microbubble and spherical cap bubble cases show negligible difference for the same percentage change in the OMTC. This is because what determines the overall reduction rate is the change in the product of the OMTC and the interfacial area of the jet and melt. The specific surface areas of the jet in both bubbling regimes have the same dependency on specific gas volume ($v^{2/3}$). Also, the total moles of gas in the jet scales the same with changes to the OMTC for both bubbling regimes. As such, the same percentage change in OMTC leads to the same percentage change in reduction rate for both bubbling regimes. This highlights the importance of the combined $k_{\underline{O}}A$ term in terms of governing the reduction rate. Finally, this result recommends that any surrogate model used in a Bayesian calibration program give the same percentage change in reduction rate for the same percentage change in OMTC, regardless of the bubbling regime used.

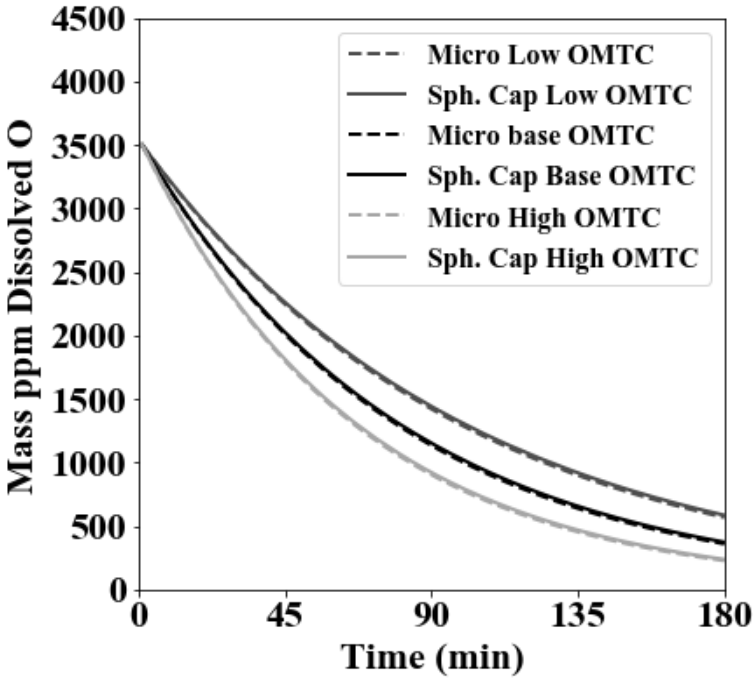

Figure 4.30 – Dissolved oxygen content histories for the oxygen mass transport coefficient (OMTC) variation cases. High and low OMTC values correspond to +/- 20% of the base case values, respectively.

4.2.2.7 Soot Specific Area Variation

Soot specific area (SSA) was varied +/- 20% from the base-case value of 7200 m^2/g. The effect of these variations on dissolved oxygen content is shown in figure 4.32. It can be seen that changes to SSA had a negligible effect on reduction time. Reduction time is determined by the combination of the oxygen mass transport coefficient and jet-melt interfacial area. Changes to SSA have no bearing on the former. Changes to SSA may have a bearing on the later, since both the carbon-steam reaction and Boudouard reactions produce one mole of gas on net. In the SSA range studied, the total difference in gas produced was not enough to substantially change the jet-melt interfacial area.

With regard to soot production rate, figure 4.33 shows that changes to SSA had the expected effect on soot production. Higher SSA led to lower soot production (16% less than the base case), and lower SSA led to higher soot production (23% higher than the base case). Additionally, the microbubble cases have a slightly higher soot production rate for each case because the average velocity of the microbubbles is greater than the spherical cap bubbles. This

means there is less time for formed soot to be consumed by reaction. The difference in soot production rates between the spherical cap bubble cases and microbubble cases would be interesting to study in lab or at an operation, as it could help confirm or deny that different bubbling regimes truly have substantially different average jet velocities.

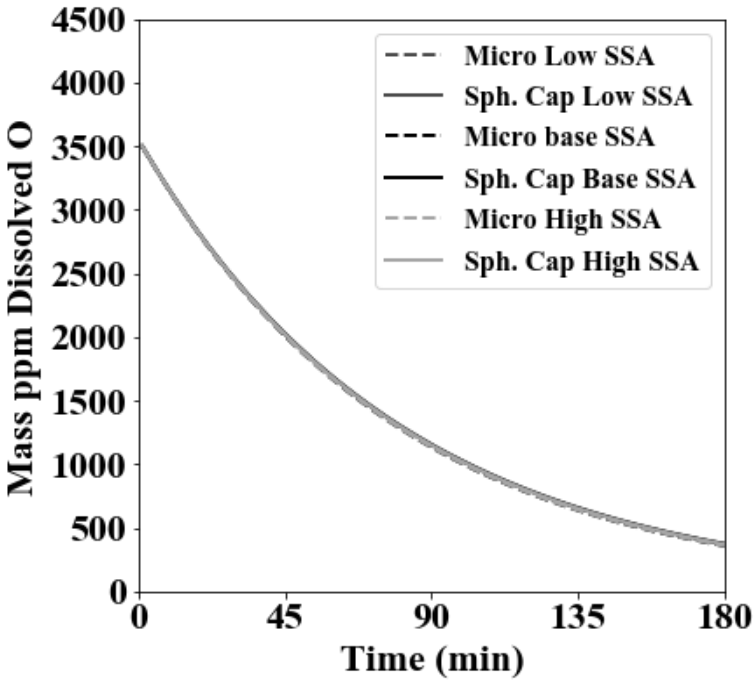

Figure 4.31 – Dissolved oxygen content histories for the soot specific area (SSA) variation cases. Variation to SSA had no effect on reduction rate, so all 6 histories overlap one another, hence the only one red line shown.

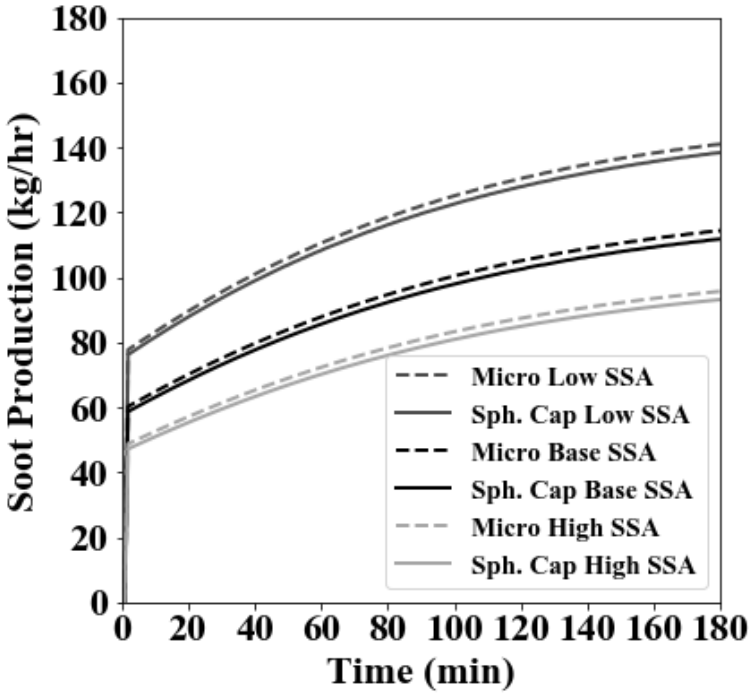

Figure 4.32 – Soot production histories for the soot specific area (SSA) variation cases

4.2.3 Conclusions and Recommendations

A transient reacting flow model was made for the reduction step of copper fire refining. The model looked at both spherical cap bubble injection and microbubble injection. The transient profiles of each species in the reacting jet for base cases were produced. Cases were also studied in which initial bubble size, methane-steam ratio with a constant total gas injection rate, steady operating temperature, initial oxygen concentration in the melt, steam addition rate at constant methane addition rate, mass transport coefficient for dissolved oxygen change, and soot specific area changed about the base-case values. It was found that most of the exergy fed to and leaving the plant is contained in the liquid copper; approximately 18% of the fed exergy leaves the plant as a loss with the offgas. The results show that replacement of some of the added methane with steam may be a viable way to save natural gas. The results of this modeling work recommend the following:

1. Operating fire-refiners should attempt to decrease the natural gas addition rate while increasing the steam injection rate. This saves natural gas costs and reduces soot production. If additional steam is not available, plants may still be able to save on natural gas costs and

soot production by replacing some of the injected natural gas with nitrogen from the smelter's oxygen plant

2. It may be possible to recover some of the exergy lost with the offgas for applications such as preheating the injected gas. This may allow for savings in fuel costs for the headspace burner
3. Laboratory or industrial trials should be done to produce reduction rate data using natural-gas steam mixtures. This would allow the model presented here to be calibrated and give quantified probabilities for estimating plant performance.

CHAPTER 5. THE CONCENTRATE LEACH PROCESS

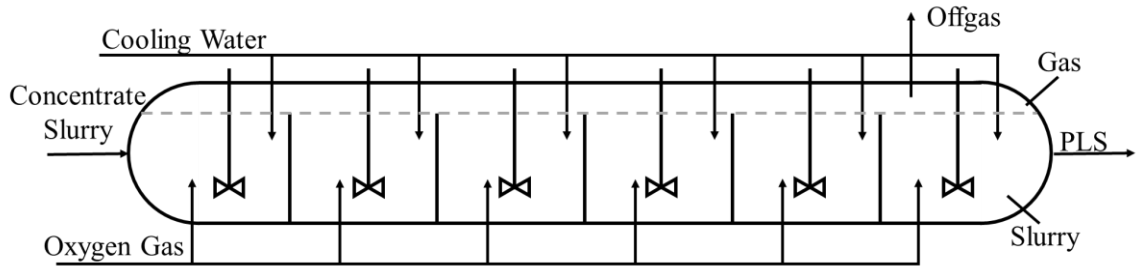

Figure 5.1 - Schematic of a CLP autoclave. Note that the cooling water is actually added through the bottom of each compartment

5.1 Model Description

A CLP autoclave (fig. 5.1) consists of several continuously stirred tank reactors (CSTRs), or compartments, in series with a shared gas phase. Concentrate slurry is fed to the first compartment. Pregnant leach solution (PLS) with residual solids leaves the last compartment. Cooling water and gaseous oxygen (98.5% O_2, 1.5% N_2) are added to each compartment through the compartment floor as needed. Impellers are used to mix the contents of each compartment. Figure 5.1 shows a schematic of the modeled autoclave.

The material flow through the CLP is comprised of three phases: gas, solid minerals, and aqueous solution. The latter two are well mixed at all times, comprising a slurry. The autoclaves are operated to ensure the reaction kinetics in the slurry are independent of gas-phase transport phenomena. Although the modeled kinetics are not functions of the gas-phase properties, the gas phase is important both from exergy and controls perspectives; the gas phase involves significant material flows (and costs upstream *via* the oxygen plant supplying O_2) and it is important that the oxygen efficiency be maximized. The temperature and pressure of all phases is taken to be the same and constant, which is justified by industrial practice [93]. Because the rate of reaction in the slurry determines how to control the gas phase, the slurry is considered first.

5.1.1 Slurry Model

The foundation of the slurry model is the coupling of transient equations describing the particle size distribution of the slurry minerals and moment equations describing the number,

length, surface area, and volume of solids per volume of slurry. The overall method is a *Population Balance* technique [66]. An example of the technique for modeling a gold pretreatment autoclave can be found in the two-part work of Rubisov and Papangelakis [64,65]. The key advantage of this method is it allows modeling of transient slurry behavior, such as would be seen at reactor startup or with process changes. One essential part to employing these methods is a description of the leaching reactions that occur in the autoclave.

5.1.1.1 Slurry Chemistry

The concentrate feed to the CLP is principally made of four sulfide minerals: pyrite, chalcopyrite, covellite (taken as CuS), and digenite.(taken as Cu_9S_5). Gangue mineral is also present, which is modeled as chemically inert, although it does affect the heat balance. The four leaching reactions are:

$$2FeS_{2(s)} + 7.5O_{2(aq)} + 4H_2O_{(aq)} = Fe_2O_{3(s)} + 8H^+_{(aq)} + 4SO^{2-}_{4(aq)} \quad (5.1)$$

$$4CuFeS_{2(s)} + 17O_{2(aq)} + 4H_2O_{(aq)} = 4Cu^{2+}_{(aq)} + 2Fe_2O_{3(s)} + 8H^+_{(aq)} + 8SO^{2-}_{4(aq)} \quad (5.2)$$

$$CuS_{(s)} + 2O_{2,(aq)} = Cu^{2+}_{(aq)} + SO^{2-}_{4,(aq)} \quad (5.3)$$

$$Cu_9S_{5(s)} + 12O_{2(aq)} + 8H^+{}_{(aq)} + 4SO^{2-}_4{}_{(aq)} = 9Cu^{2+}_{(aq)} + 9SO^{2-}_{4(aq)} + 4H_2O \quad (5.4)$$

These oxidative leaching reactions are expected to be mediated by a ferrous-ferric cycle [58,94], *i.e.*, oxygen actually serves to oxidize ferrous ion to ferric, and the ferric then is reduced back to ferrous in an oxidative leaching reaction. For example,

$$2FeSO_4 + O_2 + H_2SO_4 \rightarrow Fe_2(SO_4)_3 + H_2O$$

$$2CuFeS_2 + 16Fe_2(SO_4)_3 + 16H_2O \rightarrow 2CuSO_4 + 34FeSO_4 + 16H_2SO_4$$

Despite this, explicit inclusion of the ferric-ferrous cycle was rejected. There is currently a dearth of information on the influence of the concentrations of ferric and ferrous on the rates of reactions 5.1-4. However, because the reaction rate parameters were calibrated to transient lab batch data which used the same chemistry (see Chapter 6), the rate parameters used for equations 5.1-4 include the average effect of ferrous and ferric on the leaching kinetics over the range of neither

of these ions in solution to the maximum possible amount (complete dissolution of the slurry) in solution. Overall, the level of uncertainty due to lack of publicly available kinetic data for the whole chemical system recommends use of the simplest possible global reaction scheme, which was taken to be equations 5.1-4. This choice helps avoid over-fitting of the model, and also helps keep computational costs down.

Under certain chemical regimes, jarosites and basic ferric sulfates (equations 5.5-8) will form in addition to hematite as the solid iron product. Currently, the thermodynamics for iron precipitation are not well understood in pressure oxidation systems when large amounts of cupric ion are present. Although the base case of the model has only hematite form, jarosite and BFS were the iron precipitate in some cases.

The chemical reactions for jarosite formation are:

$$6FeS_{2(s)} + 22.5O_{2(aq)} + 17H_2O_{(aq)} = 2(H_3O)Fe_3(SO_4)_2(OH)_{6(s)} + 16H^+_{(aq)} + 8SO^{2-}_{4(aq)} \quad (5.5)$$

$$6CuFeS_{2(s)} + 25.5O_{2(aq)} + 11H_2O_{(aq)} = 6Cu^{2+}_{(aq)} + 2(H_3O)Fe_3(SO_4)_2(OH)_{6(s)} + 4H^+_{(aq)} + 8SO^{2-}_{4(aq)} \quad (5.6)$$

The chemical reactions for BFS formation are:

$$2FeS_{2(s)} + 7.5O_{2(aq)} + 3H_2O_{(aq)} = 2Fe(OH)SO_{4(s)} + 4H^+_{(aq)} + 2SO^{2-}_{4(aq)} \quad (5.7)$$

$$2CuFeS_{2(s)} + 8.5O_{2(aq)} + H_2O_{(aq)} = 2Cu^{2+}_{(aq)} + 2Fe(OH)SO_{4(s)} + 2SO^{2-}_{4(aq)} \quad (5.8)$$

In practice, jarosite and BFS do not form individually, but in some combination with each other and hematite. Thus, to analyze these cases, the model results with pure jarosite or BFS formation were averaged with the pure hematite formation case; the results were weighted on the fraction of iron present as each precipitate in the equivalent industrial scenario. It was found that the formation of these iron precipitates had a negligible impact on the process performance indicators looked at.

5.1.1.2 Reaction Product Mass Balances

The reaction product mass balances are used to calculate copper extractions, oxygen consumption rates, iron-compound precipitate and gangue volume fractions, aqueous ion

concentrations, and other performance metrics. In the CLP, cupric ions, hydrogen ions, sulfate ions, and solid hematite (and/or jarosite/BFS) are produced. The transient concentration of each product species in a compartment is found according to:

$$\underbrace{\frac{d(V(1-g)C_i)}{dt}}_{accumulation} = \underbrace{Q_{in}(1-g_{in})C_{i,in}}_{inflow} - \underbrace{Q_{out}(1-g)C_i}_{outflow} + \underbrace{V\sum_j \frac{\varphi_{i,j}}{-\varphi_j}\rho_j\left(\frac{\dot{D}_j}{2}\right)\left(\pi\mu_j^{(2)}\right)}_{Production\ of\ i\ due\ to\ reaction} \qquad (5.9)$$

Equation 5.9 is the accumulation rate of chemical species *i* in a compartment. V is the volume of the tank, g is the solid volume fraction of the slurry, C_i is the concentration of aqueous species *i* in the tank, t is time, Q_{in} is the volumetric flowrate of slurry into the tank, g_{in} is the volumetric fraction of solids in the tank inflow, $C_{i,in}$ is the concentration of chemical species *i* in the tank inflow, Q_{out} is the total volume flowrate out of the tank, $\varphi_{i,j}$ is the stoichiometric coefficient on aqueous species *i* in the chemical reaction with solid species *j* (called chemical reaction *j*), φ_j is the stoichiometric coefficient on species *j* in chemical reaction *j*, ρ_j is the molar density of solid species *j*, $\pi\mu_j^{(2)}$ is the surface area of *j* per volume of slurry, and $\mu_j^{(2)}$ is the second moment (total surface area divied by pi) of species *j*, the calculation of which is described later.

Table 5.1 - Solid mineral species included in the model and their molar densities

Mineral	Chemical Formula	Molar Density (kmol/m^3)
Pyrite	FeS_2	41.8 [74]
Chalcopyrite	$CuFeS_2$	22.8 [74]
Covellite	CuS	49.2 [74]
Digenite	Cu_9S_5	7.65 [95]
Hematite	Fe_2O_3	49.3 [74]
Hydronium Jarosite	$(H_3O)Fe_3(SO_4)_2(OH)_6$	6.45 [96]
Basic Ferric Sulfate	$Fe(OH)SO_4$	19.8 [97]
Gangue	Mix of silicates	19.2 [Plant Data]

For hematite, jarosite, BFS, and the gangue minerals, the volume fraction in the slurry is tracked. This is done according to:

$$\frac{d(Vg_i)}{dt} = Q_{in}g_{i,in} - Q_{out}g_i + \frac{V}{\rho_i}\sum_j \frac{\varphi_{i,j}}{-\varphi_j}\rho_j\left(\frac{\dot{D}_j}{2}\right)\left(\pi\mu_j^{(2)}\right) \tag{5.10}$$

In equation 5.10, g_i is volume fraction of solid species *i*, which is hematite, jarosite, BFS, or gangue. Equation 5.10 gives the rate of accumulation of volume of each of these species. For gangue, the summation term on the right is zero.

5.1.1.3 Population Balance and Moment Equations

The point of the population balance and moment equations is calculation of particle size distribution (PSD) histories. These are important because the overall reaction rate is governed by the total available particle surface area, which can only be calculated from PSDs. This model assumes spherical particles. Copper-sulfide concentrate particles have a wide range of morphologies (see for example, figure 18.a in Perez-Tello et al. [98] or figure 5.2 below). Particles can range from being chip-like to pebbles. However, very few, if any, particles are expected to be flat, thin plates. As such, the characteristic size of the particles is expected to decrease with dissolution. Using spherical particles in the model captures this expected behavior. Because the particle shrinkage rate is calibrated with oxygen consumptions (see chapter 6), the estimated shrinkage rate will capture the effect of the varying particle morphology.

Figure 5.2 – Examples of the varying cross-sections that could be found in a copper sulfide concentrate (after Perrez-Tello et al. [16] and [99])

Assuming all particles are spherical with diameter D_j, the population balance for a particle of type *j* for some compartment is given by:

$$\psi_j = f(D_j, t)$$

$$\underbrace{\left.\frac{\partial(V\psi_j)}{\partial t}\right|_{D_j}}_{\substack{accumulation \\ of\ particles}} = \underbrace{Q_{in}\psi_{j,in}(D_j)}_{inflow} - \underbrace{Q_{out}\psi_j}_{outflow}(D_j, t) - \underbrace{\left. V\frac{\partial}{\partial D_j}(\dot{D}_j\psi_j)\right|_{D_j}}_{\substack{generation\ of\ particles \\ due\ to \\ particle\ shrinkage \\ or\ growth}} . \quad (5.11)$$

Equation 5.11 describes the accumulation rate of particles of species j and diameter D. V is the volume of the compartment, ψ_j is the particle size density in units of number of particles per volume of slurry per length of particle size, t is time, D_j is a diameter of particle of type j, Q_{in} is the volumetric flowrate of slurry into the tank, $\psi_{j,in}$ is the PSD of particles of type j flowing into the tank, Q_{out} is the volumetric flowrate of slurry out of the tank, and $\dot{D}_j$ is the rate of shrinkage of particles of size j. The model assumes the total volume of slurry in the compartment and PSD of the first-compartment feed is constant. The model also assumes chemical reaction control, *i.e.*, the amount of reaction j per surface area of particle type j is always a constant,

$$\frac{d\dot{N}_j}{dA_j} = C \ \rightarrow \ \dot{N}_j = CA_j \, ,$$

where A_j is the surface area of a particle of type j and C the proportionality constant for the amount of reaction. For a spherical particle, the total molar amount of j is given by

$$N_j = \frac{\pi\rho_j D^3}{6} \, ,$$

so

$$\dot{N}_j = \frac{\pi\rho_j}{2} D^2 \frac{dD}{dt} = \frac{\rho_j}{2} A_j \frac{dD}{dt} \, ,$$

and as such,

$$\frac{dD}{dt} = \frac{2C}{\rho_j} = -k_j \, , \quad (5.12)$$

where k_j is the constant rate of particle shrinkage.

Equations 5.11 and 5.12 are sufficient to describe all net rates of reactions and thus the temporal dependence of all PSDs and rates of reaction. The moments of each species, $\mu_j^{(i)}$, could be calculated by the integration:

$$\mu_j^{(i)} = \frac{1}{N} \int_0^{D_{max}} D^i \, \psi_j dD \,, \tag{5.13}$$

where D_{max} is the maximum diameter of ψ_j and N is the total number of particles per unit volume of slurry. Equation 5.13 shows the second moment to be the average particle diameter squared, but it is computationally expensive due to repeated integration and continuously calculation of N as the particles shrink in the reactor. To avoid this cost, the method of moments is used [66], yielding the following equations for the moments of each solid species:

$$\dot{\mu}_j^{(0)} = \frac{Q_{in}}{V} \dot{\mu}_{j,in}^{(0)} - \frac{Q_{out}}{V} \dot{\mu}_j^{(0)} + \dot{D}_j \psi_j \big|_{D=0} \tag{5.14}$$

$$\dot{\mu}_j^{(i)} = \frac{Q_{in}}{V} \dot{\mu}_{j,in}^{(i)} - \frac{Q_{out}}{V} \dot{\mu}_j^{(i)} + i \dot{D}_j \mu_j^{(i-1)} \tag{5.15}$$

Equation 5.14 shows the connection between the population balance and moment calculations; the population balance (eqn. 12) gives $\psi_j\big|_{D=0}$, an otherwise unknown quantity. $\mu_{j,in}^{(i)}$ is the only quantity still needed and can be found *via* eqn. 14; because the PSD of the slurry feed into a compartment is known, use of equation 5.14 for the first compartment does not pose significant computational cost as it only needs to be evaluated once. Equations 5.1-15 are sufficient for characterizing the leaching rate found in any compartment of the autoclave, given an inlet PSD to the first tank.

5.1.1.4 Selection of Inlet Particle Size Distribution

All compartments subsequent to the first take their inlet PSD as the outlet PSD of the immediately preceding tank. In a model of an actual process, the PSD to the first tank is found by a particle size analysis of the slurry feed. The PSD selected should have a value of zero or very

close to zero at D_{max}, the maximum particle size in the feed. The particle fraction distribution (PFD, mass of particles per length of particle size bin) used for this model is described by the sum of two lognormal terms as shows in Figure 5.2 below. The data for this figure was provided the FMI Tucson Technology Center (ref private communication with Pranav).

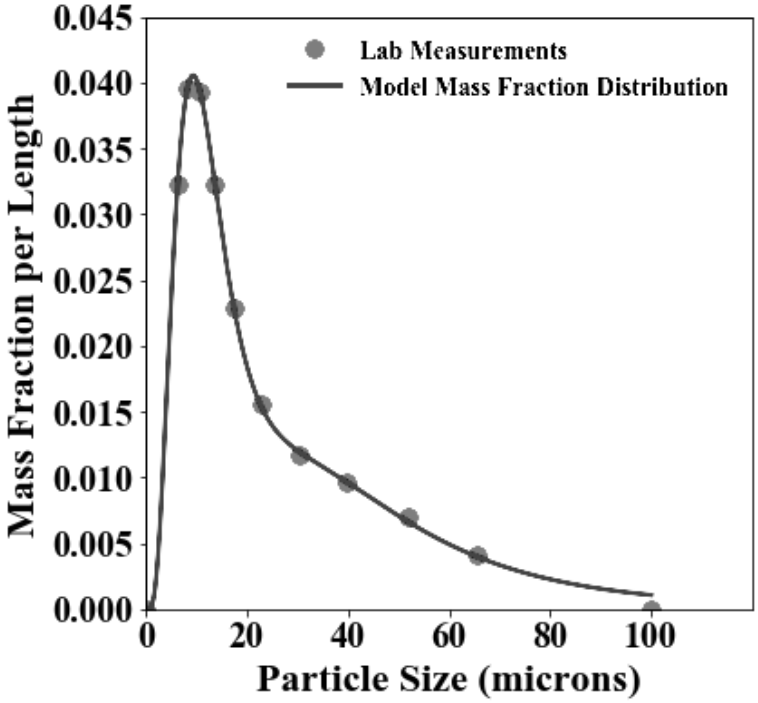

Figure 5.3 - Particle mass distribution for the slurry feed to CLP. The grey curve is described by the sum of two lognormal distributions

The PFD function shown in figure 5.2 is:

$$W_{in} = \frac{A_1}{D} e^{\left[-\frac{(\ln(D)-B_1)^2}{C_1}\right]} + \frac{A_2}{D} e^{\left[-\frac{(\ln(D)-B_2)^2}{C_2}\right]} \tag{5.16}$$

where W is the PFD. The PFD is then transformed to the particle size distribution (PSD). The PSD used for the model is:

$$\psi_{j,in} = N_j C_{norm} \left\{ \frac{A_1}{D^4} e^{\left[-\frac{(\ln(D)-B_1)^2}{C_1}\right]} + \frac{A_2}{D^4} e^{\left[-\frac{(\ln(D)-B_2)^2}{C_2}\right]} \right\} \tag{5.17}$$

where C_{norm} is the normalization constant for the particle fraction distribution. The values of the parameters in eqn. 5.16 are given in table 5.2. Figure 5.3 shows how this PSD looks. Although it appears the tail of the PSD from about 20-100 µm is negligible, it must be remembered that this part of the PSD still accounts for a large fraction of the PMD, or total inlet slurry mass.

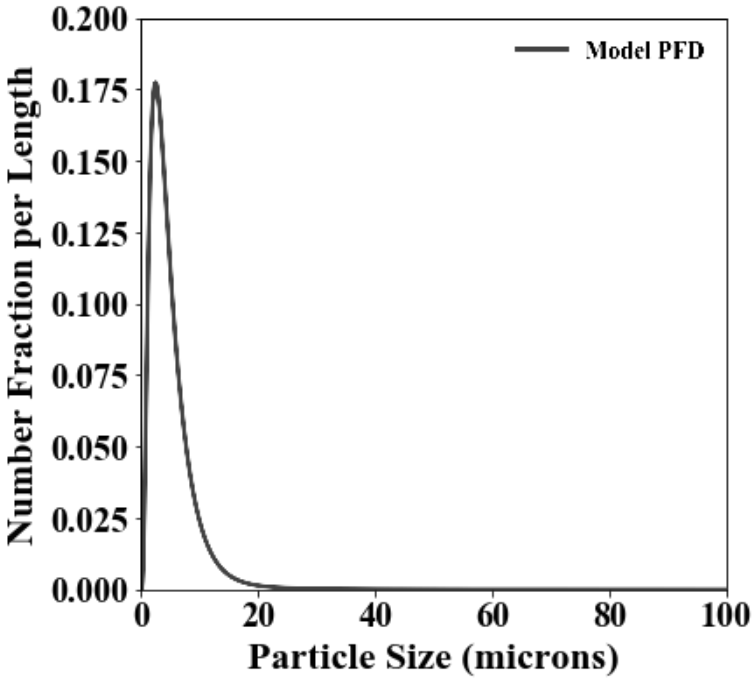

Figure 5.4 - Modeled particle fraction distribution. Although it appears there is negligible fraction of particles above 20 microns, this size range contributes significantly to the particle mass distribution and so can't be ignored

Table 5.2 - Values of the parameters used to describe the particle size distribution of each mineral species into the autoclave

Parameter	Value
C_{norm}	602
A_1	0.913
B_1	3.09
C_1	1.02
A_2	-0.560
B_2	3.13
C_2	0.427
N_{Py}	1.02×10^{20}
N_{Cpy}	1.12×10^{20}
N_{Cov}	6.35×10^{19}
N_{Dig}	7.81×10^{19}

5.1.2 Gas Phase Model

The CLP gas phase is contiguous over the entire surface of the slurry in all compartments; as such, it is treated as a single control volume. The gas phase is comprised of oxygen gas, nitrogen gas, and water vapor. The composition of the gas phase is treated as being at steady state with respect to the rate of consumption of oxygen gas by the leaching reactions and offgassing rate. The temperature and pressure of the gas phase are at steady state along with the rest of the autoclave.

In practice, control of the gas phase pressure is done *via* a valve on the CLP roof that can be opened over a continuous range from entirely closed to entirely opened. There is thus some control over the offgas rate. The functional dependence of the offgas rate on the "openness" of the valve for a given vessel pressure is unknown. Pressure is maintained inside the vessel by pressure regulators, through which the oxygen supply is fed. However, the operators also have manual control of the oxygen addition rate if desired. Gas that leaves the vessel by offgassing or

consumption by reaction is immediately made up by ~98.5% oxygen, 1.5% nitrogen gas. Water vaporizes from the slurry such that its saturation pressure is maintained, *i.e.*, water's rate of vaporization equals its rate of offgassing. The steady state gas phase mass balance is described in Appendix C.

5.1.3 Process Temperature Control

5.1.3.1 Steady Temperature Coolant Water Addition Rate

Plant water is added to the compartments of the autoclave as a coolant to maintain steady temperature. This added water greatly influences the flowrates through and residence times in each compartment, and so is important to process performance. The heat balance for calculating the water addition to a given compartment at steady state temperature is:

$$\frac{dH}{dt} = \sum_i \dot{N}_{i,in} h_{i,in} - \sum_i \dot{N}_{i,out} h_{i,out} + W \tag{5.18}$$

In eqn. 5.18, $\frac{dH}{dt}$ is rate of accumulation of enthalpy in a given compartment at steady-state temperature, $\dot{N}_{i,in}$ is the molar flowrate of species *i* into the compartment, $h_{i,in}$ is the specific enthalpy of *i* at its inlet state, $\dot{N}_{i,out}$ is the flowrate of *i* out of the compartment , $h_{i,out}$ is the specific enthalpy of *i* out of the compartment, and *W* is the added shaft work to move the impellers. Because $\frac{dH}{dt}$ is held by the matter in the compartment, it is also equal to the enthalpy of the species in the compartment at the compartment temperature times the rate of accumulation of each species in the compartment:

$$\frac{dH}{dt} = \sum_i h_{i,out}\left(\dot{N}_{i,in} - \dot{N}_{i,out} + \omega_i\right) \tag{5.19}$$

In equation 5.19, ω_i is the net generation of *i.* Substituting 5.18 into 19 gives:

$$0 = \sum_i \dot{N}_{i,in}\left(h_{i,in} - h_{i,out}\right) + \sum_i h_{i,out}\omega_i + W \tag{5.20}$$

The total rate of water flow into a compartment is separated into the water addition that came from the inlet slurry or previous compartment and the added cooling water:

$$\dot{N}_{a\mathrm{H_2O},in} = \frac{\sum_{i \neq a\mathrm{H_2O}} \dot{N}_{i,in}\left(h_{i,in} - h_{i,out}\right) + \sum_i h_{i,out}\dot{\omega}_i + W}{\left(h_{a\mathrm{H_2O},out} - h_{a\mathrm{H_2O},in}\right)}\ , \tag{5.21}$$

where aH_2O denotes the coolant water. Equation 5.21 can be used to calculate the steady-state coolant water addition rate required to maintain constant temperature. In practice, the exact value of ω_i is not known and water is added in response to slight temperature changes in the vessel. Additionally, the plant has estimated that heat loss due to heat transfer through the autoclave walls is less than 5% of the heat that goes to bringing added water to temperature.

5.1.3.2 Incorporation of Coolant Water Addition into the Numerical Method

Discussions with FMI indicated that the process is practically steady in temperature, and is kept so by adjusting the cooling water addition rate as needed. The practice of coolant water addition rate adjustment in response to temperature changes corresponds to explicit calculation of $\dot{N}_{a\mathrm{H_2O},in}$ in the numerical method. Indeed, with an infinitesimal timestep, eqn. 5.21 exactly gives the instantaneous coolant water addition rate for steady-state temperature operation. With finite sized time-steps, there is a slight lag between heat generation and coolant water addition during transient periods, which would lead to a slightly higher temperature in the vessel than the targeted value. The timestep used was small enough that further decreases to it did not change the results.

5.1.3.3 Thermodynamic Data and Calculation of Elevated Temperature Values

Table 5.3 presents all the modeled chemical species and their relevant thermodynamic properties for the calculation of the steady-state water addition rate and exergy balance. Aqueous ion specie data at elevated temperature was found according the correspondence principle as presented by Criss and Cobble [100,101]. The values for the nonreactive solids are based on the average composition of this material as provided by FMI (ref private comm with Pranav).

5.1.3.4 Shaft Work for each Compartment

A comparatively small amount of shaft work is used in each compartment to drive the impellers. This was included in the heat balance. The power added to each tank as shaft work is given in table 5.4.

Table 5.3 - Modeled Species and their Thermodynamic Properties at the Reference Temperature and 473K

Name	Phase	Chemical Formula	s_{298} (MJ/kmol/K)	h_{298} (MJ/kmol)	s_{473} (MJ/kmol/K)	h_{473} (MJ/kmol)	e_{298} (MJ/kmol)	e_{473} (MJ/kmol)
Pyrite	Solid	FeS_2	0.0529	-172	0.0857	-160.	1429	1431
Chalcopyrite	Solid	$CuFeS_2$	0.125	-190	0.173	-172	1539	1543
Covellite	Solid	CuS	0.0665	-53.1	0.0890	-44.6	690	692
Digenite	Solid	Cu_9S_5	0.548	-365.	0.787	-278	3727	3743
Nonreactive Solids	Solid	—	0.101	-2037	0.156	-2016	0.	4.70
Hematite	Solid	Fe_2O_3	0.0874	-824	0.141	-804	16.5	21.0
Jarosite	Solid	$(H_3O)Fe_3(SO_4)_2(OH)_6$	—	-3770.2[96]	—	-3681.7[96]	—	—
BFS	Solid	$Fe(OH)SO_4$	—	-1160.2 [97]	—	-1119.6 [97]	—	—
Water (L)	Aqueous	H_2O	0.0700	-286	0.112	-271	0.9	3.45
Cupric Ion	Aqueous	Cu^{2+}	-0.0996	64.8	0.0267	113	—	Concentration Variant
Sulfate Ion	Aqueous	SO_4^{2-}	0.0201	-909	-0.239	-1008	—	Concentration Variant

Table 5.3 continued

Proton	Aqueous	H^+	0.000	0.	0.0464	37.5	—	Concentration Variant
Oxygen	Gas	O_2	0.185	0.000	0.200	5.26	11.3	12.13
Nitrogen	Gas	N_2	0.212	0.000	0.225	5.18	-5.12	-3.97
Steam	Gas	H_2O	0.189 ref	-242	0.204	-236	—	8.6

Table 5.4 - Elevated Temperature Exergy Formulas for the Modeled Ions

Ion	Formula for e_{473}
Cu^{2+}	$10.6+2.48\ln\{[Cu^{2+}]/(7.3x10^{-10})\}$
SO_4^{2-}	$-21.8+2.48\ln([SO_4^{2-}]/0.0276)$
H^+	$23.7+2.48\ln([H^+]/10^{-8})$

Table 5.5 - Shaft work used to drive the impellers for each compartment

Compartment	Shaft Work (kW)
1	90
2	94
3	45
4	46
5	44
6	31

5.1.4 Calculation of Exergy Flows

The exergy balance for the autoclave is fundamentally the same as that used for the pyrometallurgical steps. Only chemical exergy is fed to the autoclave in the form of the concentrate sulfide minerals (gangue has negligible chemical exergy), concentrated oxygen (the mechanical exergy of gas compression is negligible for this system), and plant water (taken to be pure, which thus has chemical exergy relative to sea water). Exergy losses from the autoclave are PLS (besides cupric ion) and offgas. Exergy is destroyed as well.

5.1.5 Solution Method

The system of partial differential equations (eqns. 5.1-21) used to describe the slurry, gas addition, and cooling water addition rate were solved using the method of lines described by Rubisov and Papangelakis [66]. A standard fourth order Runge-Kutta method [88] was used for the time discretization of the resulting system of ordinary differential equations. Our modeling work used 1200 nodal points, *i.e.*, the population balance equations (eqn. 5.11) were discretized into 1200 diameter slices. It was found that time-step independence was achieved for $\Delta t<2s$.

5.2 Results and Discussion

The model was used to analyze the effects at steady-state of (i) combining the first two autoclave compartments, (ii) changing the tank size +/- 20% of the base case volume, and (iii) different iron-bearing precipitate formation. The model was also used to look at transient behavior surrounding autoclave startup. Steady state results were obtained by running the transient model for 12 hours of simulation time. Additionally, 95% confidence intervals have been provided for the results where these are signficant. These intervals show the two standard deviation spread of the Bayesian calibrated Monte Carlo results. It must be remembered that the current modeling work assumed uncertainty only in the reaction rate constants; as such, the estimated spread of the results is based on the assumption that uncertainty only in the reaction rate constants is significant. The spread could significantly increase if other uncertain parameters have similar effects.

5.2.1 Steady State Operation at Baseline and with First Two Compartments Combined

Plant operating parameter values and operational data was obtained over the months of April and July 2019; the average parameter values were used in the model, and can be found in Table 5.6.

Table 5.6 - Industrial operating parameters used for the model. Values are the industrial mean over the months of April and July 2019

** $k_{1\text{-}4}$ calibrated from laboratory batch data (see chapter 6)

Model Parameter	Mean Calibrated/Industrial Value
k_1^{**} (m/s)	1.34×10^{-8} (calibrated)
k_2 (m/s)	8.03×10^{-9} (calibrated)
k_3 (m/s)	4.28×10^{-9} (calibrated)
k_4 (m/s)	4.84×10^{-9} (calibrated)
Slurry Volume per Compartment (m^3)	16π (mean measurement)
Slurried Concentrate Addn. Rate (m^3/hr)	17 (mean measurement)
VF Con in Added Slurry	0.15 (mean measurement)
Operating Temperature (℃)	200 (mean measurement)
VF O_2 in Injected Gas	0.985 (mean measurement)
Total Pressure (Mpa, absolute)	2.170 (mean measurement)
H_2O Saturation Pressure (Mpa, absolute)	1.553 (mean measurement)
Oxygen Partial Pressure (Mpa, absolute)	0.500 (mean measurement)

5.2.1.1 Cooling Water Addition Requirement

The model's estimation of the rate of cooling water addition to each compartment of the autoclave is both a strong function of the model parameters, and strongly influences the other model results. It is thus the best model result to compare to industrial data for the purposes of model validation. This comparison is shown in figure 5.4. The deviation between the mean total

water addition rate of the model for the base case and mean total water addition rate for autoclave 1 at the plant is only 8%. This is a good result, as the model estimations are based entirely on first principles with the exception of the reaction rate constants, which were estimated *via* Bayesian inference of batch laboratory pressure leaching data. Furthermore, prior to seeing these modeling results, the plant estimated that the heat transfer out of the autoclave walls is 5% or less of the heat used to bring the added cooling water to temperature. This difference in heat loss is on the order of the difference between the model estimation (done assuming adiabatic conditions) and plant data. The model thus appears to have gained a strong degree of validation.

When the first two compartments are combined into one, the first, larger compartment sees a much higher cooling water addition rate, which happens to accommodate the increased extent of reaction (due to longer residence time), and thus the increased heat release, seen in the first tank. Despite this significant process change, the deviation between the total plant water addition (for the base case) and the model is still only 8%. This makes sense because, as discussed later, total copper extraction is reduced by just 0.3% to 97.8% when the first two compartments are combined. This means the total amount of reaction heat released stayed almost constant between the two cases.

The 95% confidence intervals for the water addition rates were calculated and plotted, although the intervals are to be neatly plotted. Table 5.7 shows the ratio of the uncertainty to the mean result. This small size suggests other model parameters besides the rates of particle shrinkage are sources of uncertainty in the model output for water addition rate. Some possibilities are the concentrate particle size distribution, concentrate composition, aqueous species enthalpies, heat transfer out of the furnace, and the thermochemistry of the aqueous solution.

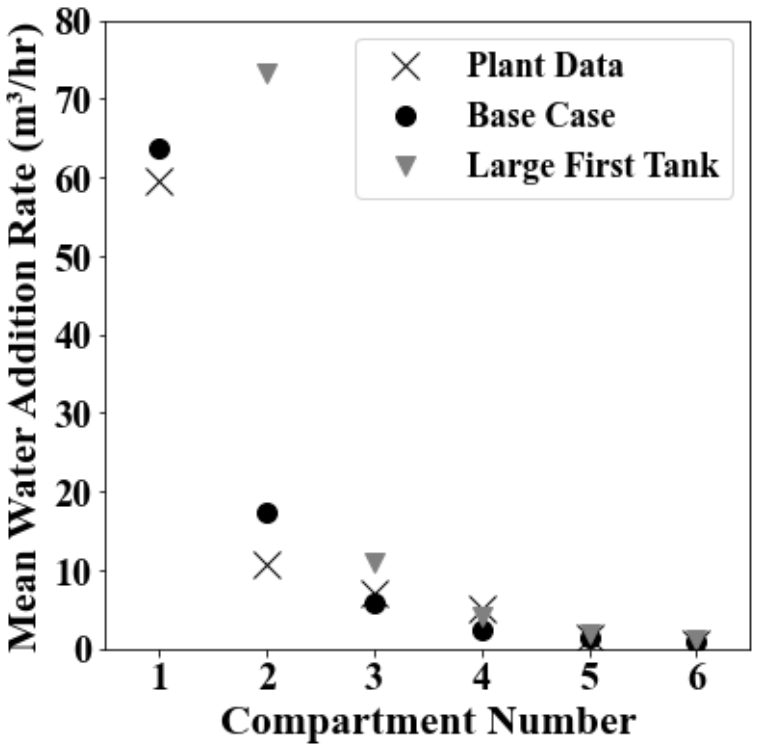

Figure 5.5 - Comparison of model estimated required cooling water addition rate per tank for the baseline case and case where the first two compartments are combined into one. Industrial data, corresponding to the baseline case, is also plotted

Table 5.7 - Ratio of 95% confidence interval radius size to mean result for cooling water addition per tank. σ is the standard deviation of the cooling water addition rate results, and μ is the mean

Compartment Number	1	2	3	4	5	6
$2\sigma/\mu$ Basecase	0.017	0.016	0.040	0.085	0.142	0.215
$2\sigma/\mu$ Large 1st Compartment		0.013	0.017	0.051	0.109	0.190

5.2.1.2 Copper Extraction by Compartment

Fraction of copper extracted through all of the compartments is the most essential performance criterion for evaluating the CLP because that extraction is the purpose of this operation. Copper extraction is defined here as the instantaneous ratio of copper flow out of the

CLP to copper flow into the CLP. For this model, copper leaves the CLP as cupric ion and enters as the minerals chalcopyrite, covellite, and digenite, giving:

$$Total\ \%Cu\ Extracted = \frac{100 Q_{out,6}(1 - g_6) C_{\mathrm{Cu}^{2+}}}{Q_{slurryin,1} \sum_i \nu_i \rho_i X_{Cu,i}} \tag{22}$$

where ν_i is the volume fraction of mineral i into the slurry, ρ_i is the molar density of i, and $X_{Cu,i}$ is the molar fraction of copper in mineral i (e.g., ¼ for chalcopyrite).

Figure 5.5 shows the steady-state copper extraction as a function of compartment number. The terminal copper extraction for the base case is found to be 98.1%. The results show the necessity of each compartment —removing compartment six would reduce the total copper extraction by 1.2%, from 98.7% to 97.6%, an unacceptable loss of copper. Similarly, combining the first two compartments into one reduces the copper extraction by 0.3%, from 98.7% to 98.3%. This copper loss is due to cooling water addition being transferred from the second tank to the first, thus reducing the total residence time of the slurry in the autoclave. Although the total cooling water addition to the autoclave and autoclave slurry volume are approximately the same in the larger first tank case, the additional cooling water added to the first compartment is transferred down the entire autoclave. For example, if all of the cooling water was added to the last compartment, the residence time of the slurry in the autoclave would be much larger than if all the cooling water was added to the first compartment. This is the primary deleterious effect of combining the first two tanks. The 95% confidence intervals were calculated for the copper extraction but were negligible. Inclusion of other model parameters' uncertainty and an estimation of plant measurement noise would broaden the confidence intervals.

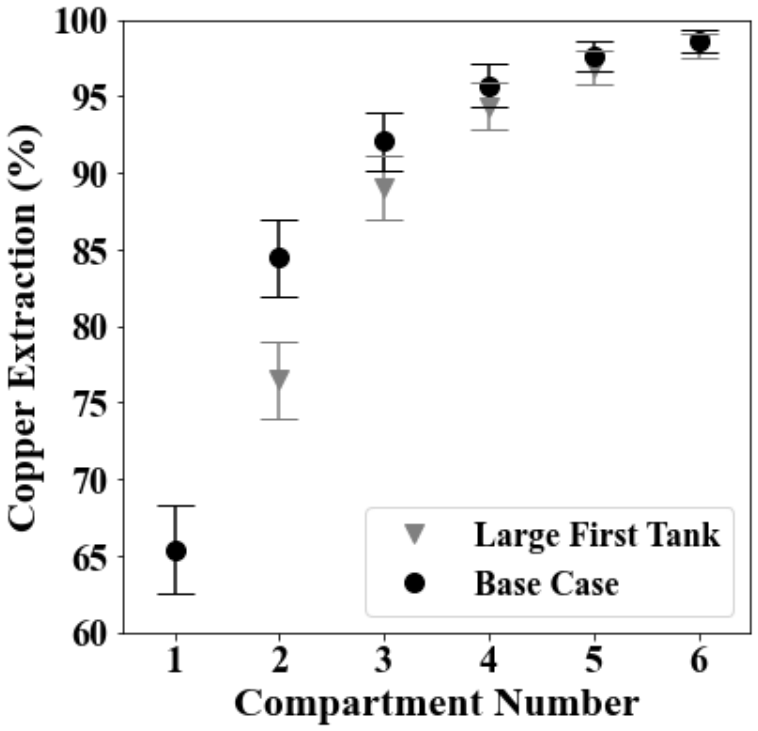

Figure 5.6 - Comparison of model estimated percent copper extraction per tank for the baseline case and case where the first two compartments are combined into one

5.2.1.3 Volume Fraction of Hematite per Compartment

Hematite, jarosite, and BFS are undesirable byproducts of the CLP. The additional solids load that they add to PLS increases downstream PLS processing costs as well as autoclave maintenance costs; indeed, in the case of jarosite formation, the byproducts can manifest as large and potentially operationally harmful scaling phenomenon in the vessel outlet [102]. Figure 5.6 shows how the volume fraction of hematite changes for the base case with compartment number. It was assumed that hematite was the only solid product formed for these cases.

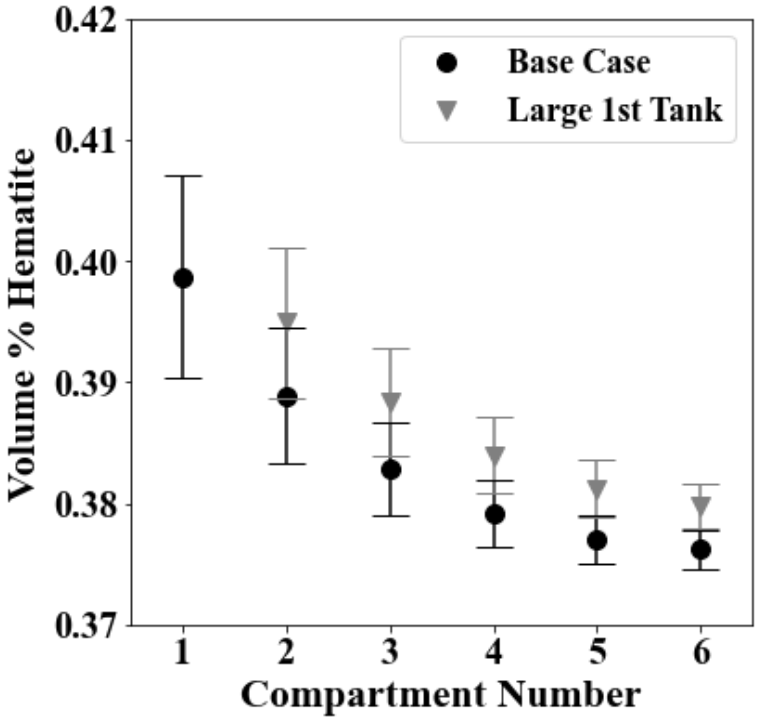

Figure 5.7 - Comparison of model hematite volume fraction per tank for the baseline case and case where the first two compartments are combined into one. The shaded areas are the 95% confidence intervals for each case

The volume fraction of hematite decreases with increasing compartment number, going from a mean result for the baseline case of 0.402% volume in the first compartment to 0.380% volume in the final compartment, despite increasing conversion of iron to hematite with compartment number. The decrease in volume fraction is due to increasing total water flowrate with compartment number, as the water added to cool one compartment flows through all subsequent tanks. All solid species are thus diluted (and have decreased compartmental residence time) with each compartment. The shaded areas show the 95% confidence intervals for hematite volume fraction. They are about 2% of the mean, and so while visible, can probably be ignored.

5.2.1.4 Concentration of Cupric Ion as a Function of Tank Number

Of interest to the operation is the concentration of aqueous species present anywhere in the autoclave. Particularly, cupric concentration is essential for calculating copper extraction. The concentration of cupric as a function of compartment number for the base case and case where the

first two compartments are combined is shown in figure 5.7. It is seen that the cupric iron concentration increases with compartment number, not necessarily a foregone conclusion as the extent of slurry dilution increases with each subsequent compartment due to increasing total water flowrate. The calculated molarity corresponds to 33 gpL copper leaving the final compartment. The uncertainty in cupric concentration in the final tank is about 2% of the mean (0.01 molar). The higher molarities are associated with lower volumetric flowrates, which explains why the uncertainty in cupric ion concentration is not reflected in the copper extraction results.

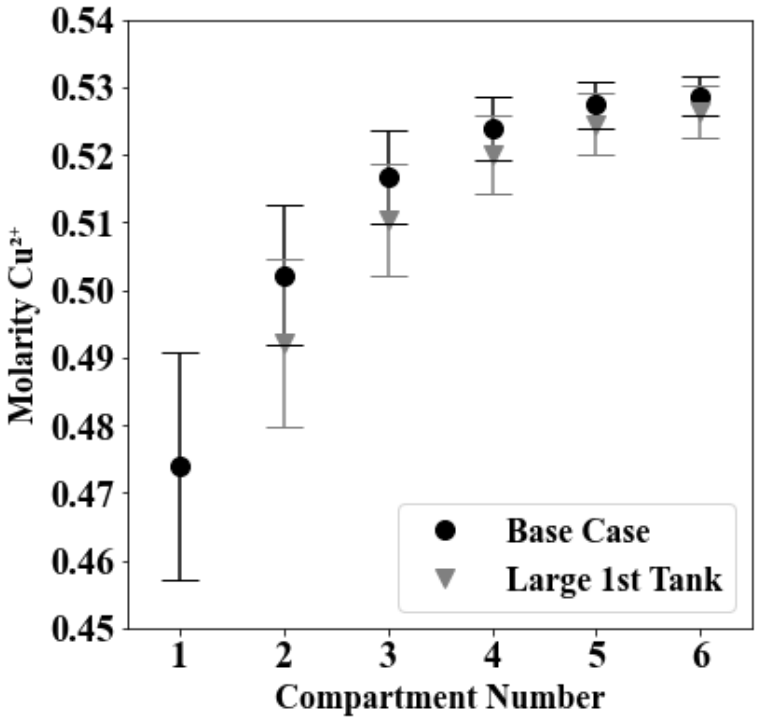

Figure 5.8 - Comparison of model estimated cupric concentration per tank for the baseline case and case where the first two compartments are combined into one. The shaded regions are the 95% confidence intervals for the cases

5.2.1.5 Oxygen Gas Injection Rate

During the months of April and July, 2019, autoclave 1 Morenci injected an average of 225 kmole/hr of oxygen gas. The model estimated 229 kmole/hr of oxygen injection, a 1.8% difference. Graphical comparison of the model estimations and industrial data can be seen in figure 5.8. Interestingly, the model and industrial data do not match for the first two tanks. As the water addition rate data show, much more heat is released by oxygen consuming reactions in the first

compartment than in the second. It can be inferred that a much greater extent of reaction occurs in the first compartment than the second. It thus appears that in the industrial setting, much of the oxygen added to the second compartment transfers to the first compartment via the vessel headspace. Some sort of oxygen transport to the first compartment from the others is at the very least necessary for a proper oxygen mass balance in the first compartment. Combining the first two compartments into one transfers oxygen from the second compartment to the first, due to the increase in copper extraction in the first compartment.

It appears copper extraction for the baseline case could be improved at the plant by directing the excess oxygen from the second compartment to the first. This oxygen transfer would cool the first compartment, meaning less cooling water would be needed to keep it at 200 °C. This same amount of cooling water would be transferred to compartment 2, as it would have less cooling by injected oxygen. However, the effective result of this change would be a higher residence time in compartment 1 and close to the same residence times in compartments 2-6, thus leading to slightly higher copper extractions. This change has been practically difficult to effect at the plant because of lag in the water addition control. At the plant, movement of the oxygen from compartment 2 to 1 causes a drop in the temperature of compartment one. This is followed by a decrease in the cooling water addition rate, but by the time cooling water addition decreases to reestablish steady state, the temperature has dropped enough that the leaching reactions have slowed. Water addition is slowed again but by then temperature has dropped even further. This cycle causes the thermal death of reactions in compartment 1. As such, it appears that the proposed optimization would have to be reached very slowly. Alternatively, the proposed oxygen addition rates from model could be taken into consideration next time the autoclave is down for repair, and the autoclave can be restarted with close to the proposed values. This would hopefully allow the oxygen addition to be optimized.

The plant used slightly less oxygen than the model, so the plant actually operates at a higher oxygen efficiency than estimated. The oxygen efficiency of the plant data is 95.9%; the model estimated oxygen efficiency is 94.3%. This small difference could be due to mass transport limitation in the autoclave, that is, the partial pressure of H_2O is not uniform over the entire autoclave head space. If this condition holds, the partial pressure of water above the first tank, where most of the oxygen consumption occurs, would be slightly lower than over the other tanks. This condition could happen because of the increased concentration of aqueous ions in this tank.

As shown in Appendix C, this slightly smaller oxygen partial pressure is expected to lead to a higher oxygen efficiency. Indeed, the mole fraction of water in the aqueous solution at steady state in the first compartment is 95%. If water behaved ideally at this point (likely a close approximation *per* Raoult's Law), the water saturation pressure would be 1.48 MPa. Using this value while maintaining the total pressure and oxygen partial pressure of 0.5 MPa leads to an estimated oxygen efficiency of 96% as shown in figure 5.9. Also, the oxygen purity of the injected gas could be slightly higher than 98.5%, also leading to increased oxygen efficiency.

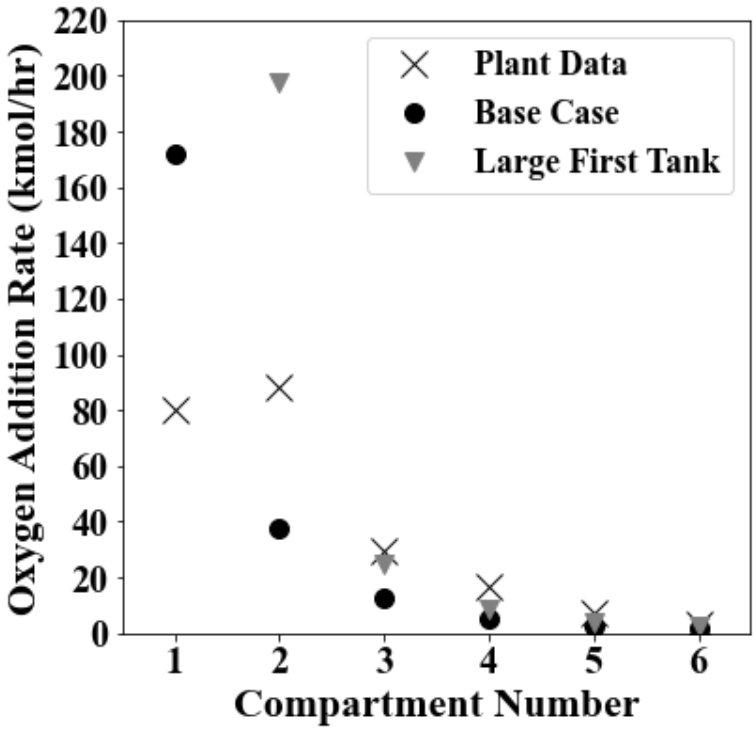

Figure 5.9 - Comparison of model estimated required oxygen addition rate per tank for the baseline case and case where the first two compartments are combined into one. Industrial data, corresponding to the baseline case, is also plotted

Table 5.8 - Ratio of 95% confidence interval radius size to mean result for oxygen addition rate per compartment. σ is the standard deviation of the oxygen addition rate results, and μ is the mean

Compartment Number	1	2	3	4	5	6
$2\sigma/\mu$ Basecase	0.013	0.015	0.039	0.089	0.162	0.250
$2\sigma/\mu$ Large 1st Compartment		0.011	0.016	0.051	0.118	0.212

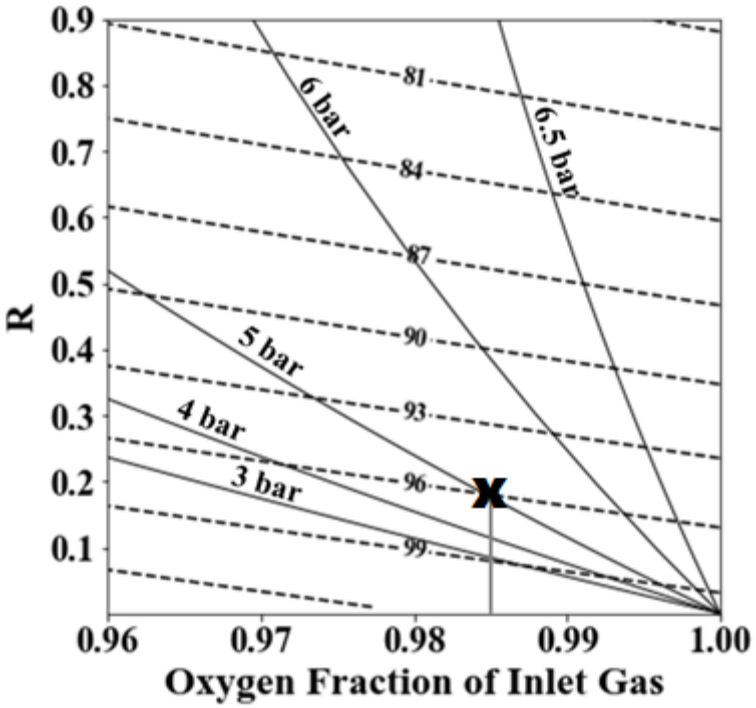

Figure 5.10 - Plot of oxygen efficiency (dashed lines) and oxygen partial pressure (solid lines) as a function of the oxygen fraction of inlet gas and offgassing ratio (R, Appendix C). The gray line and x correspond to the combination of oxygen partial pressure and oxygen grade of inlet gas used by Morenci, which lead to an estimated oxygen efficiency of 96%

5.2.1.6 Particle Size Distributions per Compartment

Two important trends are observed with respect to the PSD as a function of tank number, shown in figure 5.10 for the base case. The first is that the distribution progressively skews to larger particle size, and the second is that the total concentration of particles decreases. The first

phenomenon is due to particle destruction with increased leaching time; the distribution in the first compartment (lower leaching time) has most of its particles at small particle sizes. A large amount of these smaller particles entirely dissolve in the second tank, causing the average particle size in the second tank to slightly increase. The decrease in particle concentration is caused by both the total dissolution of particles and dilution of injected slurry with additional cooling water with each subsequent compartment. This result indicates a substantial slowdown in total reaction rate as tank number increases, because there are much fewer total particles per volume (about an order of magnitude less) with each tank.

When the first two compartments are combined into one, the result is a reduction in the amplitude of the PSD for each tank. This is because the total volumetric flow rate is higher for each tank. The particle flowrate out of each tank, for any particle size, negligibly changes, because the smaller PSD magnitude are compensated by the larger volumetric flowrates.

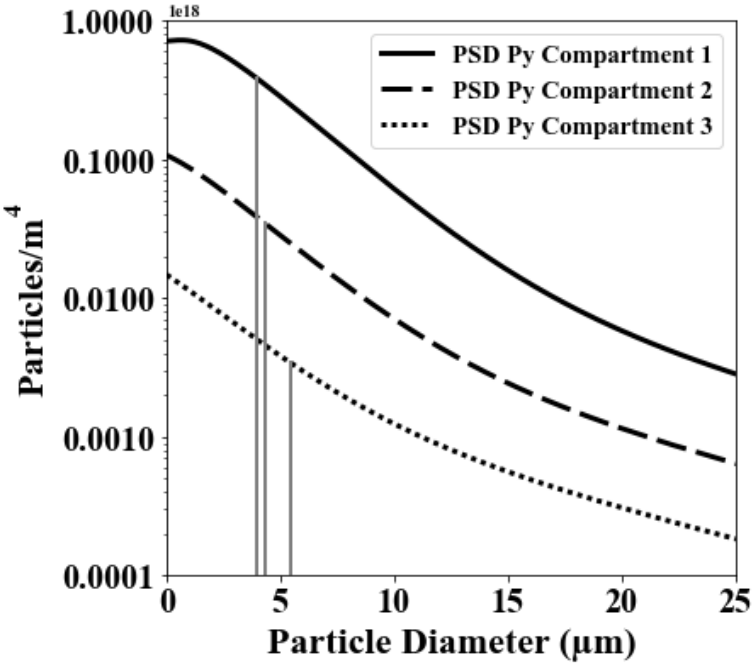

Figure 5.11 - Pyrite particle size distribution as a function of compartment number for the base case. The results for pyrite are representative of the other leached species. The vertical gray lines correspond to the mean particle diameter for each curve. Compartments 4-6 are not shown for clarity

Table 5.9 - Average particle diameter as a function of compartment number

Compartment	1	2	3	4	5	6
Mean Particle Diameter (μm)	4.00	4.32	5.47	6.98	7.54	5.72

5.2.2 Steady State Performance as a Function of Compartment Size

A very important design parameter for the CLP is the size of the compartments. Larger compartments are expected to have higher copper extraction with the same or greater concentrate throughput, due to expected increased slurry residence times. This advantage is countered by increased capital costs.

Figure 5.11 shows how copper extraction per compartment varies with compartment size over the range of compartment size 20% smaller to 20% larger than the baseline. Increased compartment size caused increased copper extraction. The case with the smallest compartments had a terminal copper extraction of 96.8%; the case with the largest compartments had a copper extraction of 99.5%. For a 50 kilo-tonne-per-annum copper production at 100% copper extraction, the difference between the highest and lowest copper extractions is 1400 ktpa of copper. At $5,500/t copper, this is $7.7M per year. The difference between the highest extraction and baseline would amount to 600 tpa copper, or $3.3M per year.

The reason for the increase in copper extraction is increased slurry residence time in each compartment. To confirm this, the cooling water addition rate per compartment as a function of compartment size was calculated. Larger compartments caused greater extent of reaction as a function of compartment number, which in turn caused increased cooling water addition rate to counteract the increased heat release. The decrease in residence time effected by this increased water addition is not enough to counteract the greater increase in residence time due to increased tank volume. As such, the residence time of each compartment increases, allowing for longer leaching times and greater copper extraction.

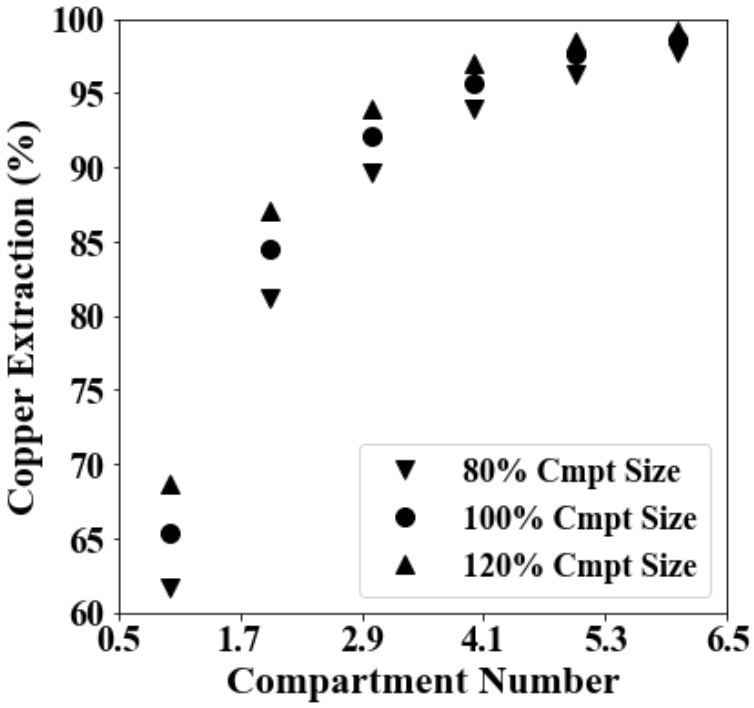

Figure 5.12 - Copper extraction as a function of compartment number and compartment size

5.2.3 Steady State Exergy Performance of the Base Case

Figures 5.12 and 13 show the distribution of flowing into and out of the autoclave. All of the exergy entering the vessel is chemical as the added material is at environmental temperature, and the mechanical exergy added by compressing the injected gas is negligible. The majority of the exergy fed to the autoclave is contained in the minerals which undergo exothermic reaction. Of this fed exergy, only 5% goes to producing the desired cupric ion. Sulfate and hydrogen can be viewed as products or losses, as these can either be used for heap leaching or require neutralization *via* lime. 69% of the fed exergy is destroyed outright. This exergy destruction compares to 18% exergy destruction in copper smelting (chapter 2), 2% in the slag blow of converting (chapter 3), 8% in copper blow of converting (chapter 3), 1% in the desulfurization and reduction steps of copper fire refining (chapter 4), and 20% in copper anode casting (chapter 4). The large difference in exergy destruction between the CLP and the other processes is due to the differences in temperatures and process feeds. The pyrometallurgical processing steps bring all the added material to temperatures that result in six-times greater temperature difference between the processing steps and the environmental temperature, and flowrate of reacting, heat-generating

species to chemical inerts which consume heat in being brought to temperature is also much higher in smelting than the CLP. The CLP for the most part uses the large chemical exergy contents of the added sulfide minerals to heat plant water to relatively low temperature. Unfortunately, the CLP cannot simply be operated at a higher temperature, as this increases the operating pressure of the vessel. Overall, smelting appears to perform much more favorably from an exergetic standpoint.

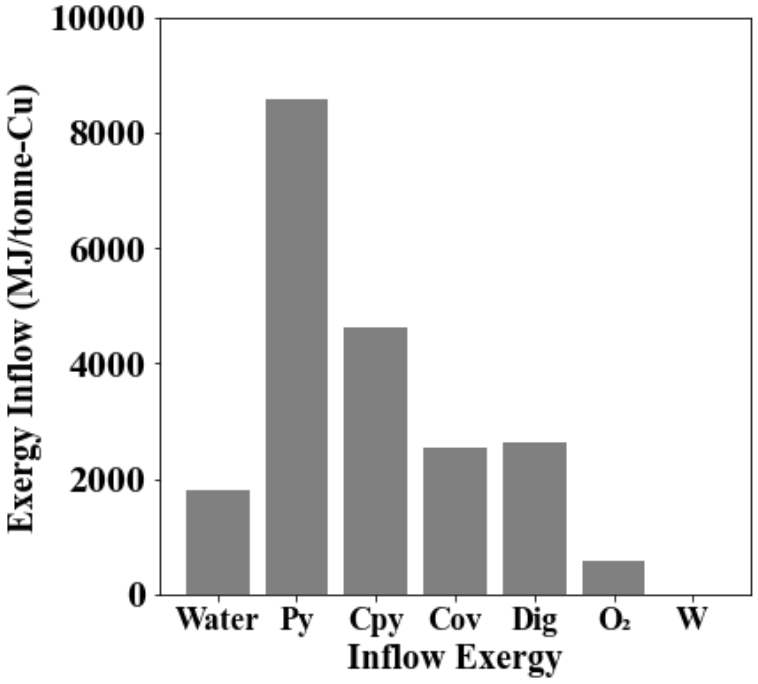

Figure 5.13 - Inflow rates of exergy to the CLP. "Water" is the sum of water in the slurry and the cooling water addition; “W” is shaft work. Missing species (e.g. N_2) had negligible exergy values. All exergies shown are chemical exergies; thermal exergy is zero for all inlet streams

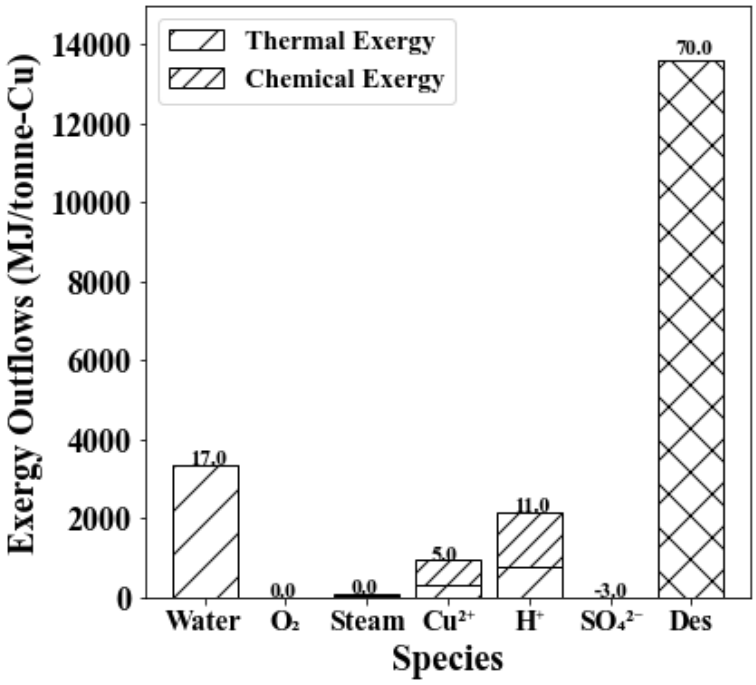

Figure 5.14 - Exergy fate distribution for the base case. Des is destroyed exergy. Nitrogen and solids excluded due to their negligible exergy flow rate out of the autoclave

5.2.4 Jarosite and Basic Ferric Sulfate Formation Cases

The model was evaluated under the base case conditions with jarosite and basic ferric sulfate (BFS) formation. Because the extent of the formation of these reagents as a function of copper CLP thermochemistry is not known the cases were analyzed where only one solid species, jarosite or BFS, was formed. True plant performance, where occasionally all three solid species form together, was then analyzed by averaging the steady state results weighted by the fraction their relative corresponding solid iron precipitate in the outlet slurry. For example, if the situation where the plant exit slurry solids are 50% hematite, 5% jarosite, and 35% BFS, the performance would be estimated by giving a total weight of 90 to the three cases, a weight of 50 to the hematite formation case, 5 to the jarosite case, and 35 to the BFS case.

5.2.4.1 Effect of Jarosite formation on Copper Extraction, Cooling Water Addition, and Oxygen Addition

Jarosite and BFS formation had negligible effect on copper extraction, cooling water addition and oxygen addition. The negligible difference in copper extraction is expected; the

leaching rate of the mineral species did not change and with a negligible difference in heat release rate, water addition per tank did not change and so residence time did not either. The fact that oxygen addition rate did not change is also expected; the ratio of required oxygen per mole of leached mineral stays the same for each leached mineral across all cases, *i.e.*, 3.75 moles of oxygen per mole of pyrite and 4.25 moles of O_2/mole chalcopyrite. Finally, the heat released per mole of chalcopyrite or pyrite reacted also hardly changes, which explains the very similar water addition rates. These results are in agreement with the plant, which does not see significantly different copper extraction, cooling water addition, or oxygen requirement when jarosite and BFS form.

5.2.4.2 Steady State Volume Fraction of Solid Precipitate as a Function of Compartment Number

One major way in which jarosite and BFS formation affects the process is in greatly increased solids load of the outlet slurry. Whereas the base case only saw 0.4% volume hematite in the outlet slurry, the cases with jarosite and BFS formation saw 2% volume percent jarosite and BFS. The fivefold increase in solids loading content is a significant burden on the solid-liquid separation capital employed at the plant. Additionally, jarosite has been reported to form massive deposits in the vessel slurry outlet that can further complicate operation [102].

The reason for increased solids volume follows from the difference in stoichiometry between hematite, jarosite and BFS formation. When hematite is formed, there is no solid sulfate product in the slurry. It thus takes about two moles of oxygen gas to form one mole of aqueous sulfate. When jarosite is formed, it takes approximately 3 moles of oxygen gas to form one mole of aqueous sulfate. The reason for the difference is that a significant amount of the sulfur in the leached mineral species and added oxygen goes to forming solid sulfate and/or hydronium as BFS and jarosite rather than aqueous species. This result motivates future studies that quantify more precisely the thermochemical regime in which jarosite and BFS, rather than hematite, are formed in the chalcopyrite leaching autoclave.

5.2.5 Transient Startup Performance

The transient performance of the model was assessed by examining vessel startup. Cases were run in which the autoclave was filled with hot, dilute sulfuric acid at pH 2. Figure 5.14 shows how the extent of copper extraction and the total cooling water addition rate changes with time

after startup. Extent of copper extraction for the transient case is calculated according to eqn. 5.22. Cooling water addition rate appears to approach steady state much quicker than copper extraction, which is because it takes time for the leached copper to propagate through all six compartments, and the cooling water addition predominantly occurs in the first tank. This result is further illustrated in figure 5.15, which shows the concentration of cupric ion per compartment at time equals one, three, five, and seven hours. The earlier tanks reach steady state well before the final tank, and because these tanks see most of the cooling water addition, the total cooling water addition rate appears to approach steady state more quickly than the copper extraction. Only the cooling water addition for the first few tanks has reached steady state when the total cooling water addition rate has appeared to reach steady state according to figure 5.14.

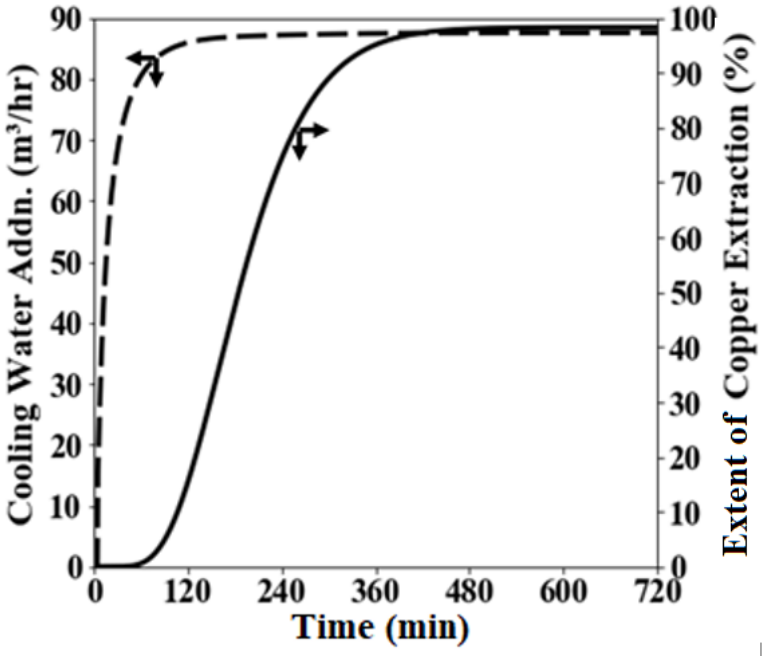

Figure 5.15 - Total cooling water addition rate and copper extraction as a function of time

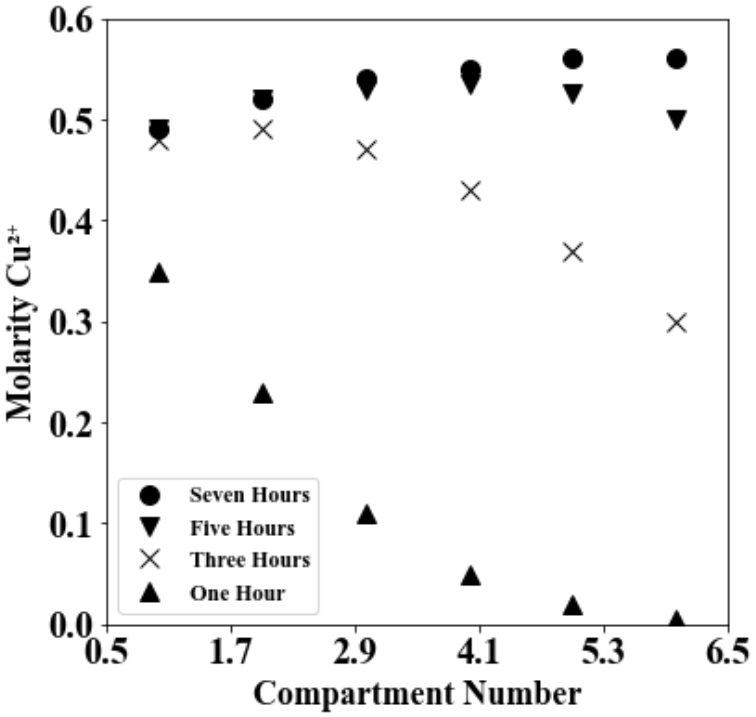

Figure 5.16 - Contours of Cu^{2+} concentration per compartment number over time since start of leaching

5.3 Conclusions and Recommendations

A transient population balance model of the six-tank Freeport-McMoRan Inc. chalcopyrite concentrate leach process was made. Model reliability was estimated via Bayesian inference of the reaction rate constants, which showed that there is very little aleatoric uncertainty expected on the basis of these model parameters, although epistemic uncertainty might be large.

Steady state modeling showed that the model estimated average cooling water addition within 8% of the industrial average rate maesured for the months of April and July of 2019. This closeness in water addition rate is an exceptional result considering the simplicity of the model, and that the reaction rate constants were derived (see Chapter 6) from Bayesian inference of laboratory data. The current work has lead to the following observations and recommendations:

- The current six compartment setup of the CLP is better than the combining of the first two compartments into one large compartment because combination of the first two compartment reduces slurry residence time in the whole autoclave by moving more cooling water to the first tank, which decreases copper extraction;

- increasing compartment size leads to increased copper extraction for a given slurry flowrate;
- pyrometallurgical extraction of copper is much more exergetically favorable than the CLP because of the higher temperature of the pyrometallurgical process and its much higher ratio of exergy-rich feed material to exergy-poor feed material;
- on startup, it takes copper extraction approximately seven hours to reach steady state. Downstream solvent extraction and electrowinning will see lower PLS grades of cupric ion during this time and should be managed accordingly;
- the thermochemistry of the CLP system should be further researched to better determine which solid phases are stable at the CLP operating conditions.

CHAPTER 6. CALIBRATION OF THE CONCENTRATE LEACH PROCESS MODEL

6.1 Overview of Bayesian Inference

Bayesian inference allows one to calculate expected values for model parameters and their variance, both calibrated on experimental and/or industrial data. Although somewhat related to more classic calibration methods such as a least-squares fit, Bayesian inference takes into account both estimations of the noise in the data gathering process, and estimated probabilities for the possible parameter values before any data has been observed. It thus incorporates much more information than a least-squares fit and so gives much more information about the model parameters. Bayesian inference relies on Bayes' theorem, which states:

$$P(A|B)P(B) = P(B|A)P(A) \tag{6.1}$$

This means that the probability of observing a value for A given a value for B times the probability of that value of B independent of A equals the probability of observing a value for B given a value for A times the probability of observing that value for A independent of B. "A" can be substituted with "certain values for parameter **x**" (where bold-faced variables refer to vectors) , for example, mineral particle shrinkage rates, and "B" can be substituted with "observed values **y**," for example, slurry oxygen consumption. Thus the calibrated or *posterior* probability for **x**, the model parameters, can be obtained:

$$P(\boldsymbol{x}|\boldsymbol{y}) = \frac{P(\boldsymbol{y}|\boldsymbol{x})P(\boldsymbol{x})}{P(\boldsymbol{y})} \tag{6.2}$$

$P(\boldsymbol{y}|\boldsymbol{x})$ can be found with a model for how the experiment is expected to behave and an estimation of the measurement noise in the experiment; $P(\boldsymbol{y}|\boldsymbol{x})$ is also referred to as the *likelihood model*. $P(\boldsymbol{x})$ is a probability distribution describing the chance of seeing any set of values for $\boldsymbol{x}$ *before* any experimental data has been observed; it is referred to as the *prior*. $P(\boldsymbol{y})$ is actually divided by itself in the algorithms used to find $P(\boldsymbol{x}|\boldsymbol{y})$, and so can be ignored.

Although $P(\boldsymbol{x}|\boldsymbol{y})$ can be calculated exactly, extracting the probability that $\boldsymbol{x}$ (the particle shrinkage rates) takes on a given set of values requires integrating $P(\boldsymbol{x}|\boldsymbol{y})$. This problem rapidly grows in difficulty as the number of dimensions of $\boldsymbol{x}$ increase. Often times, very small regions of high probability whose locations are not *a priori* known are obtained. This makes direct numerical integration so expensive as to be practically unfeasible. To avoid this, sampling methods are commonly employed, one of the most successful being Markov Chain Monte Carlo methods. The gist of these methods is to explore the space of $P(\boldsymbol{x}|\boldsymbol{y})$ by moving from point to point in this space. At each point, the posterior probability at that point is calculated, and if it passes some acceptance criterion is taken as a "sample" of the posterior. The number of samples in any given region is then equivalent to the integral of the posterior over that region. The goal of a sampler algorithm is to explore the posterior parameter space as efficiently as possible. Efficient here means covering as much of the posterior space in as few computations as possible, with a high (typically about 80%) acceptance rate. This ensures that large regions of posterior probability are not missed while also having a cost-effective exploration method.

Of the Markov-Chain methods, Gibbs-sampling and the Metropolis-Hastings algorithm have historically been very popular, and a good introduction to them is provided by Neal [49]. These algorithms explore the posterior space *via* random-walk behavior. This exploration routine is comparatively simple and can do a good job of estimating posterior distributions assuming enough sampling steps are taken. They suffer the drawbacks of having a very difficult time moving from one high probability area to other high probability areas and also of needing orders of magnitude more iterations than the method used in this paper, Hamiltonian (also called "hybrid") Monte Carlo.

The idea behind Hamiltonian Monte Carlo is to represent the posterior as a potential energy function over $\boldsymbol{x}$. Now, suppose a particle is placed in the space of the posterior and assigned some random initial momentum; the particle thus has some initial potential and kinetic energy. The negative gradient of the potential energy function will be the force, or rate of change in momentum of the particle. The particle will be attracted to the minimum of the potential energy function, which is also the region of highest posterior probability. Furthermore, the path of the particle can be exactly known in theory because energy is conserved. Thus, the Hamiltonian sampler works by numerically estimating the path of the particle and attempting to stop the sampler when the particle

will be at the area of highest posterior probability it can attain. Neal provides a thorough introduction to these methods as well [49].

Recently, the project PyMC3 [103] has become publicly available. PyMC3 employs the No-U-Turn-Sampling algorithm as developed by Hoffman and Gelman [104] to efficiently conduct Hamiltonian Monte Carlo. The samplers used in Hamiltonian Monte Carlo require both a step size for the numerical integrator of the particle path, as well as a stopping criteria for when to test the sample. The No-U-Turn-Sampler automates both of these, optimizing the sampler step size and stopping to test the particle location as soon as it starts to move away from the region of higher probability per its orbit. As will be discussed in the results section of this paper, PyMC3's implementation of NUTS proved an effective solution to estimating the posterior particle shrinkage rates.

6.2 Description of Laboratory Batch-Leaching Experiments

The pressure oxidation experiments' setup and conduction were done by Pranav Attavar, Metallurgist II, at Freeport-McMoRan Inc.'s batch reactor laboratory located at the Technology Center in Safford, Arizona. Both Pranav Attavar and the Author contributed to the experimental design. In an effort to statistically reduce variability, two identical experiments were performed. The experiments were conducted using Morenci copper concentrate collected from the CLP feed tank at Morenci and DI water as the feed liquor. 99% pure oxygen was used to provide an oxygen over pressure of 100 psig.

6.2.1 Experimental Equipment and Setup

A 2L grade 2 PARR titanium reactor was used to conduct the two experiments at 202°C and 320 psig total pressure. The oxygen supply to the reaction was controlled by a pressure regulator which ensured an over pressure of 100 psig oxygen at any point in the experiment. A titanium gas entrainment impeller operated at 1200 rpm was used for both agitation and oxygen sparging into the batch reactor. Regular city water between 10°C and 20°C was used in closed loop to control the temperature of the reaction. A PARR 4848B expanded reactor controller was used for all process control needs of the reaction. The controller was set-up to maintain the contents inside the batch reactor at the required temperature and pressure. A constant venting rate of 0.2

SL/min was used throughout the experiment. An Aalborg gas flow meter was connected to the controller to constantly measure oxygen consumption during the reaction. The following figure depicts the experimental set-up in the batch reactor laboratory.

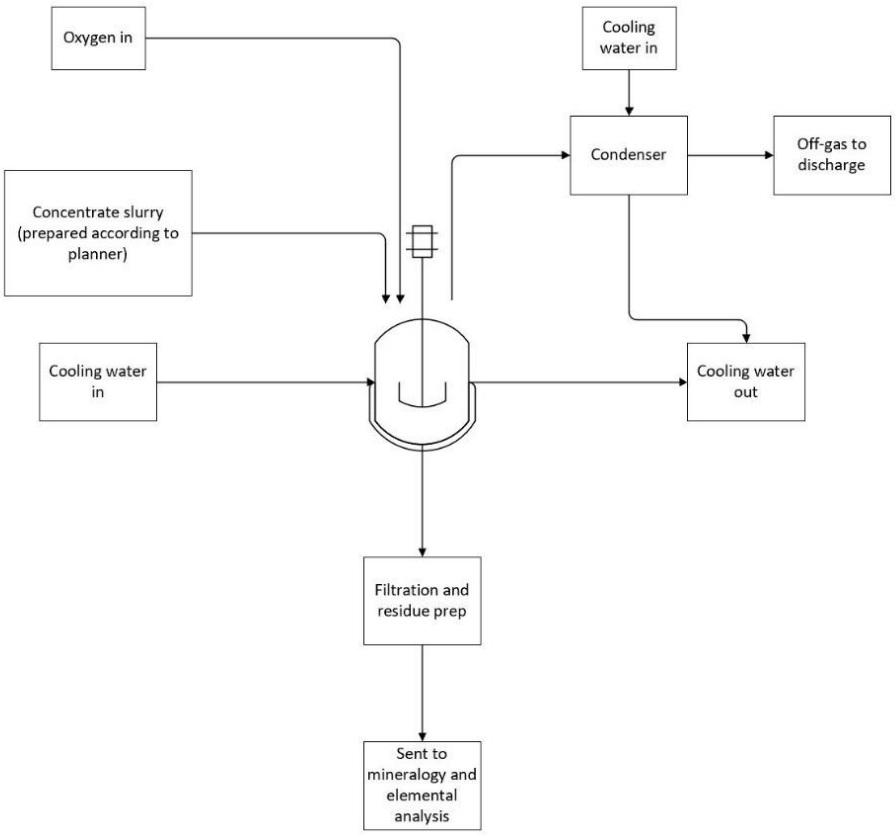

Figure 6.1 Schematic of batch reactor set-up

6.2.2 Experimental Procedure

Morenci copper concentrate was collected from the CLP feed tank in the form of a 45 wt% slurry. The slurry was filtered, dried, screened and rotary split into multiple representative smaller charges of 140 grams each. A portion of the concentrate was sent to mineralogy analysis using XRD at Freeport's AXN department located in Safford, Arizona and another split was sent for solids analysis for a full elemental ICP suite at Freeport's Technology Center in Tucson, Arizona.

The experiment was conducted using 140 grams of dried copper concentrate and 1260 grams of DI water to make the total contents inside the batch rector 1400 grams with 10 wt% solids. The contents of the autoclave were heated using a heating jacket to the required temperature of

202℃ at which point, the observed steam pressure was 220 psig. Once the desired temperatures were reached, oxygen was introduced into the autoclave to maintain an oxygen overpressure of 100 psig to make the total pressure of 320 psig and this marked the start of the 90 minute retention time.

Following the 90 minute experiment planner, the batch reactor was cooled to ambient temperature using a water bath and then dismantled. The contents of the autoclave were filtered for solid liquid separation and the pregnant leach solution was sampled and analyzed for a full element ICP suite. The filtered solids were oven dried and sent for both mineralogy analysis and analytical analysis.

Table 6.1 summarizes the experimental parameters used to run the planner.

Table 6.1 - Experiment summary table

Test number	Feed Liquor	Retention time (min)	Temperature (C)	Total Pressure (psig)	Concentrate mass (grams)	Percent solids in feed (%)	Off-gas rate (SL/min)	O2 overpressure (psig)
1	DI water	90	202	320	140	10	0.2	100
2	DI water	90	202	320	140	10	0.2	100

6.2.3 Experimental Results

The assay results indicate that the 90 minute retention time was sufficient to completely oxidize all the iron in the feed to hematite. The copper recovery as an average for both the experiments was 98.5% (with respect to residue) and the sulfur analysis using a LECO equipment in the residue resulted in a 98.5% copper extraction. The pH of the pregnant leach solution was at 0.62 for both the experiments.

6.3 Laboratory Batch-Leaching Model Description

The purpose of the computational model is transient estimation of the extent of concentrate leaching in a way that includes the unknown rate of particle shrinkages for the modeled leaching chemistry. Inclusion of the rate of particle shrinkages is required for their calibration. Furthermore, the experimental data in this work provide the extent of leaching reaction in terms of oxygen consumption, so the model must estimate transient oxygen consumption as well. The model estimates transient oxygen consumption *via* the population balance and moment method described by Rubisov and Papangelakis [66], with modifications.

6.3.1 Leaching Chemistry

The concentrate used in the experiments is comprised of nonreactive (*i.e.* gangue) minerals and four leachable sulfides: pyrite, chalcopyrite, covellite, and digenite. The chemical reactions used to model the leaching of these minerals, respectively, are:

$$2\mathrm{FeS}_{2,(\mathrm{s})} + 7.5\mathrm{O}_{2,(\mathrm{aq})} + 4\mathrm{H}_2\mathrm{O}_{(aq)} = \mathrm{Fe}_2\mathrm{O}_{3,(\mathrm{s})} + 8\mathrm{H}^+_{(aq)} + 4\mathrm{SO}^{2-}_{4,(\mathrm{aq})} \tag{6.3}$$

$$4\mathrm{CuFeS}_{2,(\mathrm{s})} + 17\mathrm{O}_{2,(\mathrm{aq})} + 4\mathrm{H}_2\mathrm{O}_{(aq)} = 4\mathrm{Cu}^{2+}_{(aq)} + 2\mathrm{Fe}_2\mathrm{O}_{3,(\mathrm{s})} + 8\mathrm{H}^+_{(aq)} + 8\mathrm{SO}^{2-}_{4,(\mathrm{aq})} \tag{6.4}$$

$$\mathrm{CuS}_{(\mathrm{s})} + 2\mathrm{O}_{2,(\mathrm{aq})} = \mathrm{Cu}^{2+}_{(aq)} + \mathrm{SO}^{2-}_{4,(\mathrm{aq})} \tag{6.5}$$

$$\mathrm{Cu_9S_{5(s)}} + 12\mathrm{O_{2(aq)}} + 8\mathrm{H^+_{(aq)}} + 4\mathrm{SO^{2-}_{4\ (aq)}} = 9\mathrm{Cu^{2+}_{(aq)}} + 9\mathrm{SO^{2-}_{4(aq)}} + 4\mathrm{H_2O} \tag{6.6}$$

6.3.2 Oxygen Balance

The rate of oxygen consumption is given by:

$$\frac{dO_{2,cons}}{dt} = V\sum_j \frac{\varphi_{O_2,j}}{-\varphi_j}\rho_j\left(\frac{\dot{D}_j}{2}\right)\left(\pi\mu_j^{(2)}\right) \tag{6.7}$$

In equation 6.7, $\frac{dO_{2,cons}}{dt}$ is the rate of oxygen consumption by leaching reaction, V is the volume of slurry in the batch reactor, $\varphi_{O_2,j}$ is the stoichiometric coefficient on oxygen gas in the chemical reaction involving leached species *j*, φ_j is the stoichiometric coefficient on leached species *j* in its

chemical reaction, ρ_j is the molar density of j, $\dot{D}_j$ is the rate of shrinkage of particles of j, $\pi\mu_j^{(2)}$ is the surface area of particles (taken to be perfect spheres) of j per volume of slurry. Table 6.2 has the values for the molar densities. The total oxygen consumption as a function of time is the integral of eqn. 6.7:

$$O_{2,cons}(t) = V \int_0^t \left[\sum_j \frac{\varphi_{O_2,j}}{-\varphi_j} \rho_j \left(\frac{\dot{D}_j}{2} \right) \left(\pi\mu_j^{(2)} \right) \right] dt \tag{6.8}$$

The oxygen consumption at time = 0 is 0. The integral in eqn. 6.8 is computationally calculated *via* a fourth order Runge-Kutta method [105].

Table 6.2 - Solid mineral species included in the model and their molar densities

Mineral	Chemical Formula	Molar Density (kmol/m^3)
Pyrite	FeS_2	41.8 [74]
Chalcopyrite	$CuFeS_2$	22.8 [74]
Covellite	CuS	49.2 [74]
Digenite	Cu_9S_5	7.65 [95]
Hematite	Fe_2O_3	49.3 [74]
Gangue	Mix of silicates	19.2 [calc. from FMI data]

6.3.3 Population Balance And Moment Equations

These equations calculate particle size density (PSD) histories. These are important because the overall reaction rate is governed by the total available particle surface area, which requires the particle PSDs. The population balance for a particle of type j for some batch reactor is given by:

$$\psi_j = f(D_j, t)$$

$$\underbrace{\left.\frac{\partial(V\psi_j)}{\partial t}\right|_{D_j}}_{accumulation} = \underbrace{-V\left.\frac{\partial}{\partial D_i}\left(\dot{D}_j\psi_j\right)\right|_{D_j}}_{\substack{generation\ due\ to \\ particle\ shrinkage}} \tag{6.9}$$

$$\dot{D}_j = -k_j \tag{6.10}$$

Equation 6.9 describes the accumulation rate of particles of type *j* and size *D* in a batch reactor. V is the volume of the CSTR, ψ_j is the particle size density in units of number of particles per volume per length of particle size bin, *t* is time, and $\dot{D}_j$ is the rate of shrinkage of particles of size *j*. The model assumes the total volume of slurry in the CSTR is constant. This model also assumes that the rate of particle shrinkage is independent of particle size. It is assumed that all particles are spheres comprised of only one mineral.

A constant rate of particle shrinkage was chosen for several reasons. One is that the plant where the CLP is employed has reported that they operate in the oxygen partial pressure independent rate regime [106]; this means the rate of particle shrinkage is not a function of the oxygen partial pressure. Additionally, as mentioned earlier the Bayesian calibration captures the average of any unmeasured variable's effect on the reaction rate. As such, the model with the least inclination to over-fitting and also most general to the modeled process has a minimum of terms in $\dot{D}_j$; this is satisfied by constant, though not necessarily equal values, for each $\dot{D}_j$.

Equations 6.9 and 6.10 are in fact sufficient to describe all net rates of reactions and thus the temporal dependence of all PSDs and rates of reaction. The moments of each species, $\mu_j^{(i)}$, could be calculated by:

$$\mu_j^{(i)} = \frac{1}{N}\int_0^{D_{max}} D^i\,\psi_j\,dD \tag{6.11}$$

D_{max} is the maximum diameter of ψ_j. N is the total number of particles per unit volume of slurry. Equation 6.11 is, however, computationally difficult to implement, due to the requirement of both integrating and continuously calculating *N* as they change in the reactor. To get around this issue, the method of moments as developed by Rubisov and Papangelakis can be used [66], yielding the following equations for the moments of each solid species:

$$\dot{\mu}_j^{(0)} = \frac{Q_{in}}{V}\dot{\mu}_{j,in}^{(0)} - \frac{Q_{out}}{V}\dot{\mu}_j^{(0)} + \dot{D}_j\psi_j\big|_{D=0} \tag{6.12}$$

$$\dot{\mu}_j^{(i)} = \frac{Q_{in}}{V}\dot{\mu}_{j,in}^{(i)} - \frac{Q_{out}}{V}\dot{\mu}_j^{(i)} + i\dot{D}_j\mu_j^{(i-1)} \tag{6.13}$$

Equation 6.12 shows the connection between the population balance and moment calculations; the population balance gives $\psi_j\big|_{D=0}$, an otherwise unknown quantity. Because a batch reactor is used, Q_{in} and Q_{out} are zero, so:

$$\dot{\mu}_j^{(0)} = \dot{D}_j\psi_j\big|_{D=0} \tag{6.14}$$

$$\dot{\mu}_j^{(i)} = i\dot{D}_j\mu_j^{(i-1)} \tag{6.15}$$

Because the laboratory experiments were held at constant temperature, and directly measured the rate of oxygen consumption by the slurry, equations 6.1-15 are sufficient for characterizing the rate of oxygen consumption in the lab batch reactor, provided the initial condition of the reactor is given.

6.3.4 Initial Condition of the Batch Reactor Used in the Model

The model was given the same initial condition as the actual experimental setup described earlier. One key additional piece of information needed for the model not necessarily needed for the description of the experiment itself is the initial particle size distribution of the slurry. This can be found from the mass fraction distribution, shown in figure 6.2 below. The mass density can be converted to the particle size density by dividing the mass density by the particle size cubed and multiplying by a normalization constant. The final functional form of the particle size density (PSD) of the slurry used as the initial condition in the model is the sum of two lognormals divided by D^3:

$$\psi_j\big|_{t=0} = v_j\psi|_{t=0} \tag{6.16}$$

$$\psi|_{t=0} = NC_{norm}\left\{\frac{A_1}{D^4}e^{\left[-\frac{(\ln(D)-B_1)^2}{C_1}\right]} + \frac{A_2}{D^4}e^{\left[-\frac{(\ln(D)-B_2)^2}{C_2}\right]}\right\} \tag{6.17}$$

In these equations, v_j is the initial volume fraction of leached species *j*, *N* is the total number of particles per cubic meter, C_{norm} is the normalization constant, A_1, B_1, C_1, A_2, B_2, and C_2 are all constants describing the particle fraction distribution, and *D* is the particle diameter in microns. Table 3 has the values for all the parameters in eqns. 6.16 and 6.17. With the initial conditions of the experiment and the initial particle size distribution used in the model, the entire initial condition of the model is completely described.

Table 6.3 - Parameter values for eqns. C.16 and C.17

Parameter in C.16 and C.17	Parameter Value
v_{Py}	0.21
v_{Cpy}	0.44
v_{Cov}	0.08
v_{Dig}	0.27
N	3.77×10^{13}
C_{norm}	10.1
A_1	41.8
B_1	2.60
C_1	0.625
A_2	41.6
B_2	4.40
C_2	0.582

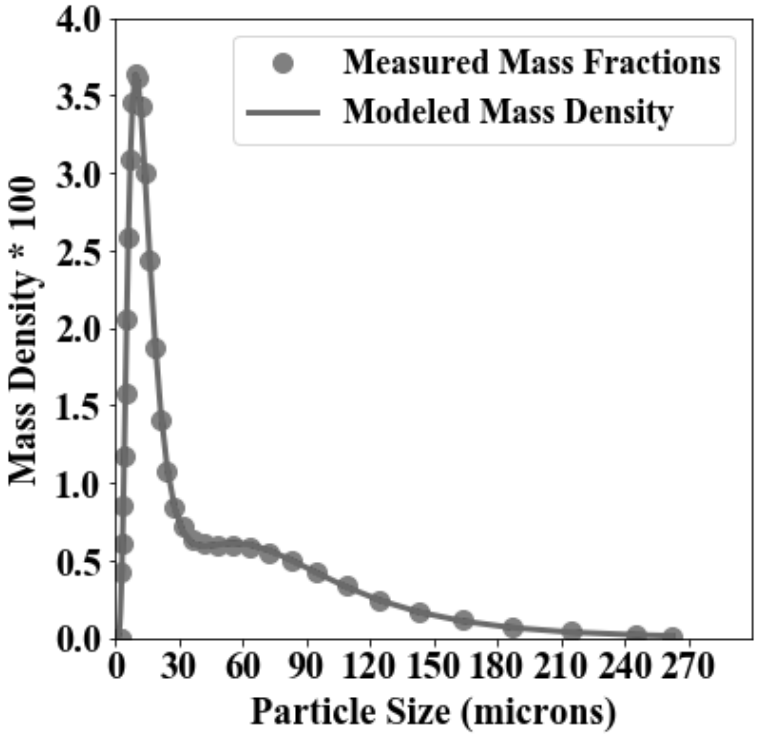

Figure 6.2 - Plots of the measured mass fractions of the concentrate used in the lab-batch leaching experiments and the mass density as a function of particle size used in the model. Particle sizes associated with measured mass fractions are the median of the particle size bins associated with each fraction.

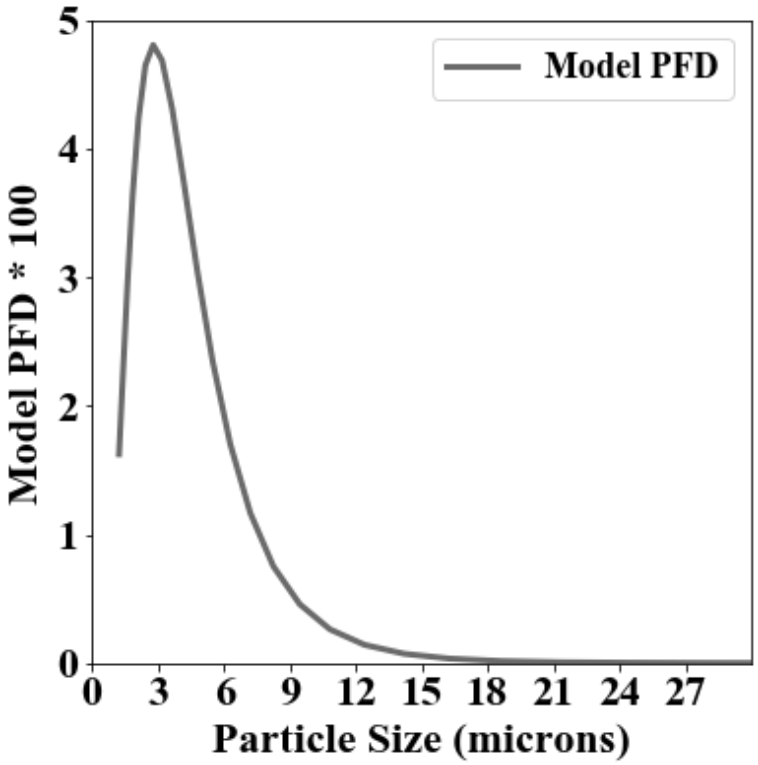

Figure 6.3 - Particle Fraction Distribution used in the model of the laboratory experiments. Derived from the measured particle mass fraction distribution. Maximum particle size is 270 μm, however only 27 μm are shown for clarity.

6.4 Bayesian Calibration of Rate of Particle Shrinkages

Bayes' theorem is:

$$P(\boldsymbol{x}|\boldsymbol{y}) = \frac{P(\boldsymbol{y}|\boldsymbol{x})P(\boldsymbol{x})}{P(\boldsymbol{y})} \tag{6.18}$$

For background on eqn. 6.18, please see the introduction to this chapter. Here, $P(\boldsymbol{x}|\boldsymbol{y})$ is the probability of $k_{1\text{-}4}$ taking on any value given the set(s) of time-series data for oxygen consumption; $P(\boldsymbol{x})$ is the expected probability of $k_{1\text{-}4}$ taking any value based solely on what is known about the physical system before observations of oxygen consumption are made. $P(\boldsymbol{y}|\boldsymbol{x})$ is the expected probability of measuring any oxygen consumption given an estimation of measurement noise and the full or surrogate model for oxygen consumption as a function of time and $k_{1\text{-}4}$. Measurement noise describes the probability of measuring some phenomenon having a

value different from its actual value; in this case for example, it would inform the probability of measuring an oxygen consumption some amount different from the actual oxygen consumption rate.

Bayes' theorem is used in conjunction with the NUTS algorithm developed by Hoffman and Gelman [104] and implemented by PyMC3 [103] for the calculations of expectations of $\boldsymbol{k}$ over arbitrary regions. The introduction provides a more in depth explanation of what these algorithms do in general and why they are necessary. In the light of necessity, one may wonder whether these algorithms are truly needed when the number of uncertain parameters is only 4. It may be possible to use other integration methods for this work, but constructing the model on the foundation of these methods ensures more uncertain variables can be added to the model without worry about confounding the integration method. The same cannot be said of direct integration or other simpler methods, which would exponentially increase in difficulty with each additional uncertain parameter.

6.4.1 Surrogate Model Creation

Bayesian calibration/inference is conducted in this work using the NUTS algorithm (see part C of this section), which typically requires 1-3 orders of magnitude fewer simulation that the Metropolis-Hastings or Gibbs Sampler. However, the full transient model in this work is still too computationally expensive to provide this number of simulations. A surrogate model provides the cost savings necessary by approximating the behavior of the full model with a computationally cheaper mathematical expression.

6.4.2 Description of Sparse Grid Generation for Surrogate Model Fit

Preliminary testing of the full lab model suggested **k** values between $4.5\text{x}10^{-9}$ and $5.5\text{x}10^{-9}$. A sparse grid was made containing the set of all unique combinations of $\{k_1,k_2,k_3,k_4\}$, where k_i takes one of three values: $4.5\text{x}10^{-9}$, $5.0\text{x}10^{-9}$, $5.5\text{x}10^{-9}$. This sparse grid required 81 full model simulations (three values, four variables, or 3^4).

6.4.3 Description of Surrogate Model Fit

The first step in fitting a surrogate model is choosing its functional form. First, the dependent variable of the surrogate model is ratio of oxygen consumed to maximum theoretical consumption of oxygen; the independent variable is time. For the case of batch leaching chalcopyrite concentrate, it makes sense that the net rate of consumption of concentrate is proportional to the amount of concentrate left in the vessel. Furthermore, the conversion of concentrate to leached products has to be between zero and one, zero meaning no leaching has happened and one meaning all of the leachable material in the concentrate has dissolved. Additionally, it seems likely that the reaction rates of the leachable species are not dependent on each other's reaction rates. Finally, because three values were used for each dimension in constructing the sparse grid, 2nd order effects should be capturable. This leads to the following functional form for the surrogate model:

$$X_{O_2} = 1 - \sum_i Y_i \exp\left[-\left(A_i + B_i k_i + C_i {k_i}^2\right)t\right] \tag{6.19}$$

Here, X_{O_2} is the ratio of consumed oxygen to the maximum theoretical consumption of oxygen by the batch of concentrate; Y_i is the maximum contribution of mineral species i to X_{O_2}; A_i, B_i, C_i are coefficients on the second order expression for k_i; t is time.

The surrogate model was fit to the full model output using a maximum likelihood/least squares estimate. This is reasonable since the uncertainty in how the surrogate model should compare with the full model is entirely unknown. Table 6.4 below shows the values of Y_i, A_i, B_i, C_i for each species. The numbers of the subscripts refer to the leached species as follows: 1 is pyrite, 2 is chalcopyrite, 3 is covellite, and 4 digenite. Figure 6.4 shows an example comparison between the full model output and surrogate model output.

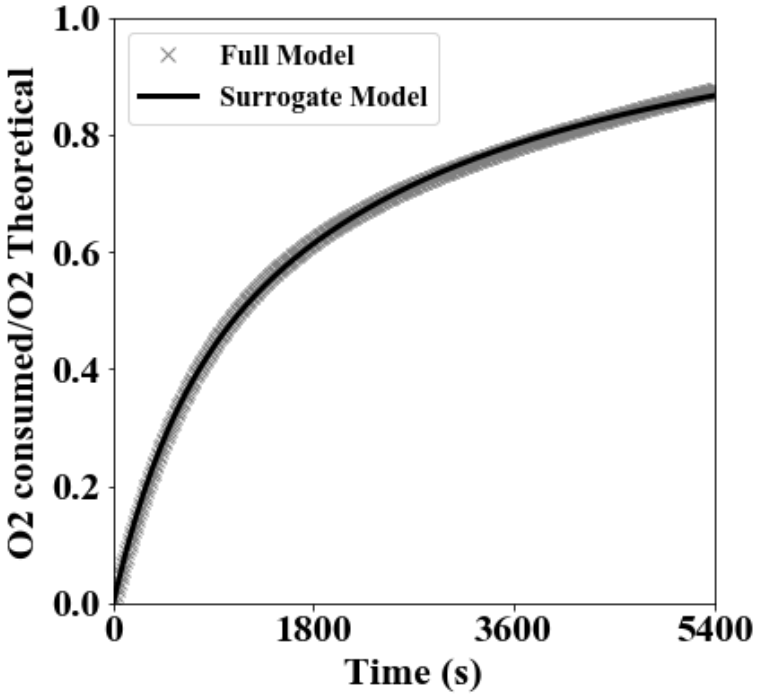

Figure 6.4 – Comparison of surrogate model performance to full model performance

Table 6.4 - Surrogate model parameter values

Surrogate Model Parameter	Parameter Value
Y_1	0.324
A_1	1.11×10^{-4}
B_1	1.02×10^{5}
C_1	0
Y_2	0.408
A_2	5.63×10^{-5}
B_2	3.34×10^{4}
C_2	0
Y_3	0.077
A_3	5.83×10^{-4}
B_3	3.28×10^{5}
C_3	0
Y_4	0.192
A_4	1.91×10^{-4}
B_4	0.324
C_4	1.11×10^{-4}

6.4.4 Calibration Methodology and Results

Calibrating the lab batch model for the rate of particle shrinkages ***k*** was done with the following steps:

1. Calculate the standard deviation of the two laboratory batch data sets to get an estimation of the maximum measurement noise
2. Choose prior probability density functions for the rate of particle shrinkages

3. Run PyMC3 [103] to calculate posterior density functions for ***k***
4. Plot the comparison of the laboratory oxygen consumption data to the model estimated oxygen consumption using the posterior samples of ***k***

6.4.3.1 Calculation of Standard Deviation of Laboratory Results to Estimate Measurement Noise

The standard deviation of the laboratory results at each time point was calculated. Figure 6.5 shows plots of the results of the two experiments. The experimental results nearly duplicate themselves until about 2400s. The results then diverge ultimately being 7% apart by the end of the experiments. The standard deviation increases with time. The maximum standard deviation between the two sets of experimental results is 2.9% oxygen conversion. This value was chosen as the measurement noise; with only two sets of experimental data, it is difficult to say how the measurement noise should change over the time of the experiments, or how random differences in the experiments influence the measurement noise/difference in results. The choice of measurement noise that minimizes the chance of assuming more knowledge than is actually had is thus the maximum standard deviation between the two results.

The experimental oxygen consumption never reaches the theoretical oxygen consumption for complete leaching. When the experimental O_2 consumption is compared to the actual theoretical consumption, there is almost always a difference due to the following:

1. Before the experiment starts, a small portion of the concentrate is shipped out for chemical assay and mineralogy. This is assumed to be the starting point for that particular concentrate. After this, the concentrate is split into small charges of about 200 g each to be utilized for individual experiments. Although sampling variance is attempted to be minimized, it does exist.
2. At the start of experiment, the agitator almost always throws a bit of concentrate into the vessel head during heat up and this does not react completely while the reaction is happening.

These two explanations are the most likely causes why the experiments fall short of theoretical oxidation numbers. As for why the theoretical O_2 consumption decreased near the end of the experiment, the way the O_2 consumption is calculated is that it records the instantaneous mass flow

rate of O_2 in and O_2 out which is communicated back to the data logger. Sometimes, during an experiment there can be a difference between the actual O_2 out reading versus what is displayed on the data logger. Calibration of these two values is attempted before an experiment starts. As such, it is possible that there was no flow going out of the batch reactor during the end of the reaction, but the data logger might have recorded a small flow and this flow causes a drop in the graph.

6.4.3.2 Selection of Prior Probability Distributions for the Rates of Particle Shrinkage

As mentioned in the section on selecting the surrogate model, it was suspected the values of $\boldsymbol{k}$ were near 5.0×10^{-9}. It was also suspected that the probability of $\boldsymbol{k}$ assuming a particular value would decrease with the magnitude of the difference between that value and 5.0×10^{-9}. A probability distribution that takes these considerations into account and conservatively estimates the level of prior uncertainty in these parameters is a normal distribution with a mean of 5.0×10^{-9} and standard deviation of 2.0×10^{-9}. This distribution was chosen as the prior for all elements of $\boldsymbol{k}$.

6.4.3.3 Calculation of Posterior Distributions for the Rates of Particle Shrinkage

PyMC3 was used to calculate posterior distributions for $\boldsymbol{k}$. Table 6.5 shows the mean and standard deviation posterior values for $\boldsymbol{k_i}$. These values were generated by performing the NUTS algorithm twice, with 2000 total samples on each run, and a burn-in of 1500 samples on each run. The "burn-in" is the number of initial samples that are discarded to ensure the algorithm has reached the posterior distribution. This leaves two 500-sample sets of $\boldsymbol{k_i}$. The second set of is checked against the first to ensure the sets are statistically identical. This gives strong validation to either set being from the posterior, as it is very unlikely two independent runs of the NUTS algorithm would produce statistically identical posteriors if the sample-sets were not truly the posteriors. Finally, with the validity of each set checked, the second sample set is discarded, leaving 500 samples of $\boldsymbol{k}$ to perform the Monte-Carlo analysis of the industrial model with. The other 500 samples could be kept, but they are needed for a statistically valid Monte-Carlo analysis. In general, it is ideal to use the minimum number of samples in the Monte-Carlo analysis, as each run of a full industrial model can be expensive.

Table 6.5 - Mean posterior values and posterior standard deviations for the calibrated rate of particle shrinkages

k_i	**Mean Posterior Value of k_i**	**Standard Deviation of Posterior k_i**
k_1	1.34×10^{-8}	7.93×10^{-10}
k_2	8.03×10^{-9}	2.55×10^{-10}
k_3	4.28×10^{-9}	9.26×10^{-10}
k_4	4.85×10^{-9}	4.93×10^{-10}

6.5 Comparison of Calibrated Model to Experimental Data

The surrogate model was run with each set of sampled posterior **k**. Figure 6.5 shows plots of the experimental data along with the mean surrogate model result for all 500 posterior samples of **k**. The plot also shows the 95% confidence intervals for the expected measurement values to be seen in future experiments. The results show that the surrogate model, posterior estimations of **k**, and estimation of the measurement noise using the standard deviation of the experimental results, adequately capture the behavior of the laboratory experiments. This is because the two sets of laboratory experiments fall within the 95% confidence bounds of the calibrated surrogate model.

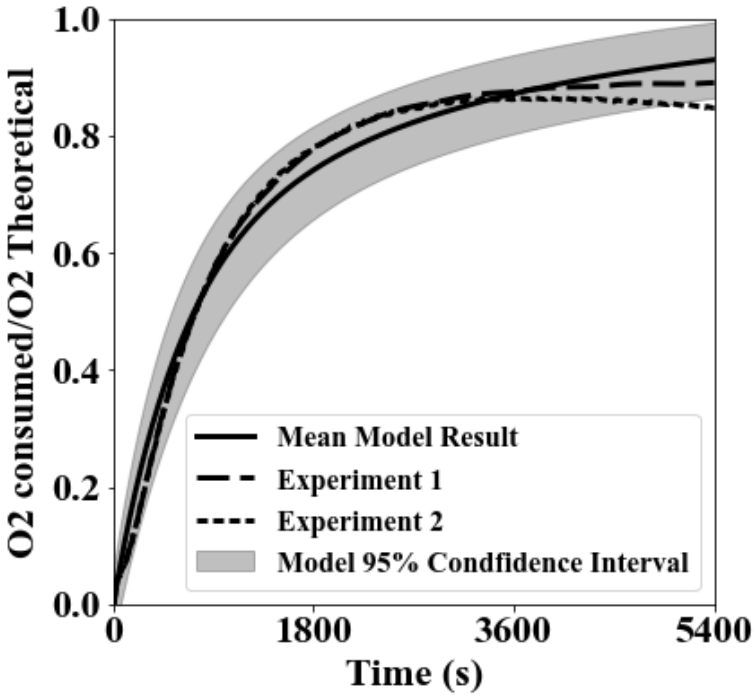

Figure 6.5 - Plots of the experimental results for the conversion of **k,** the mean results of surrogate model having used the complete set of the 500 posterior values for **k**, and the 95% confidence intervals of the surrogate model

6.6 Pitfalls to Avoid

This work has aimed so far to develop an easily deployable, highly intuitive approach to fitting a surrogate model to the full model using tools most engineers are already familiar with or can easily pick up. It follows that to aid the implementation of these tools, possible pit-falls that can be encountered along the way should be described.

6.6.1 Surrogate Model Extrapolation — Valid?

One must be very careful to discern whether the surrogate model being applied can be used to extrapolate parameter values. For this work, the question to ask would be, "Can our surrogate model be used to estimate full model performance outside of the sparse grid?" The answer to this depends on the function chosen for the surrogate model, and has important implications for calibration.

In this work, the surrogate model was a function of k_1-k_4 and time. The surrogate model was made over the entire experimental time domain, so with the laboratory data given for

calibration, extrapolation with respect to time is not a question. k_1-k_4 on the other hand were modeled over a space that *a priori* doesn't necessarily contain the true set of particle shrinkages. Indeed, the Bayesian calibration found a value for pyrite well outside of the sparse grid space. This fact does not necessarily make the value for k_1 wrong; indeed, Bayesian calibration showed that despite the very small *a priori* probability of k_1 taking the mean value of 1.5×10^{-8} m/s, (*i.e.*, 5 standard deviations from the *a priori* mean), the posterior probability was nevertheless maximized here.

There are two reasons why such a calibration can occur. The first is that the surrogate model extrapolates poorly, such as occurs with polynomials of order greater than 1. In this case, the surrogate model can have regions that closely approximate the observations used for calibration, but the calibrated parameter values are outside of the realm of physical possibility. Using this case as an example, with certain surrogate models, it is possible to closely match the experimental data with a combination of positive and negative particle shrinkage rates. Other surrogate models tried led to pyrite shrinkage rate values on the order of 10^{-11} m/s and digenite shrinkages of over 10^{-7} m/s. Both cases are absurd, the first because particle growth does not happen in this system, and the second because pyrite has been observed to completely dissolve in industrial leaching systems. A particle shrinkage rate of 10^{-11} would not even dissolve a one micron particle of pyrite in an industrial autoclave.

The second reason a calibration to values in low probability portions of the prior can occur is that the surrogate model is indeed behaving well and the true value of the parameter is close to its calibrated value. In this case, it is the exceptional performance of the surrogate model for describing the observations, when the true values of the parameters are used, that leads to a high posterior probability value at the true parameter values.

It can be difficult to tell which of these two situations may be applying solely based on the surrogate model function, especially as the number of parameters increases. One helpful way of discerning surrogate model performance is to make contours of the variables that were calibrated to highly *a priori* improbable values. Figure 6.6 below shows how the surrogate model behaves over contours where k_2-k_4 remain at 5×10^{-9} m/s and k_1 (for pyrite) goes to 25×10^{-9}. It is seen that the surrogate model behaves very reasonably over this range, and so it can be supposed that the calibrated value for k_1 is a good candidate for the true value of k_1.

Overall, the good performance of the surrogate model in this case was the combination of its linear dependency on the values of k and exponential dependence on time. Although a 2nd order polynomial was originally chosen to try to optimize the fit of the model over the interpolated space, the linear form found (all constants on the second order terms were zero) ensures that the oxygen consumption fraction changes monotonically with respect to any of the k-values. This is the expected physical behavior. As the rate of particle shrinkage increases, one never expects the rate of oxygen consumption to begin decreasing. This said, it is also important to make sure that the monotonic behavior also has the correct slope. This is talked about more in the next section.

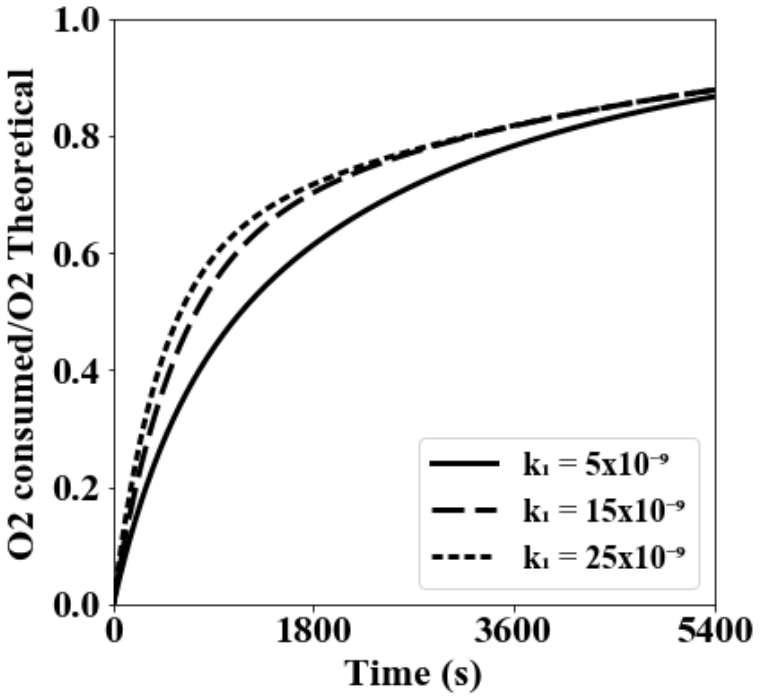

Figure 6.6 - Performance of surrogate model over a range of rates of pyrite shrinkage (in m/s). All other particle shrinkages held at $5x10^{-9}$ m/s

6.6.2 Poor Surrogate Model Fits and Multiple Surrogate Model Fits

One pitfall is a bad or misleading, surrogate model fit. This can happen for multiple reasons. If the sparse grid used to describe the surrogate model covers too large of a space, *i.e.*, the parameter domain chosen for the grid does not have enough analyzed points, one may find that their surrogate model interpolates the parameter space poorly. This can also happen even if many points were used in the sparse grid but a poor functional form of the surrogate model was chosen,

e.g., a very high order polynomial. Such a surrogate model appears to perform well at the sparse grid points but may perform very poorly between them. Such possible behavior motivates minimizing the order of the surrogate model.

Even with a low order surrogate model with close to monotectic behavior, the fit of the surrogate model can be misleading. Indeed, one must be extremely cautious when using premade optimizers, such as the SciPy curve-fit function employed in this work. Different converged surrogate model fits can be had depending on the starting guess used for the surrogate model's parameter values. Indeed, it was observed in this work that when the default starting guess for the optimizer was used (all parameter values equal to one) the surrogate model had a negative β value for some of the minerals. Such a surrogate model says that as the rate of particle shrinkage increases for some mineral, the rate of oxygen consumption due to that mineral's leaching reactions decreases. This is clearly not physical. Although such fits performed well over the interpolated range, they did not perform well during extrapolation and led to erroneous calibrations for the particle shrinkage rates, *e.g.*, a negative rate for covellite. Overall, one must ensure the surrogate model used makes physical sense and performs well during interpolation, and preferably during extrapolation too.

6.6.3 Using too many Observations in the Calibration

Although an abundance of data can be helpful, attempting to use all of it in the calibration can seriously slow down the algorithm without an appreciable change in result. In this work, it was found that the difference in calibration between keeping all of the laboratory (10000 total points) and keeping only every hundredth (100 total points) was negligible; however, using less point sped calibration by somewhere between one and two orders of magnitude. Additionally, using too many observations can lead to an over-confident posterior. In the case of this work, one can argue that every experimental data point is *not* independent. At any given time, random fluctuations in the experimental progress will tend to affect the measured oxygen conversion for longer than the spacing between each data point. This can be seen in the experimental data where the initial sharp rate in oxygen consumption slows down substantially for about one-hundred seconds. Another example is the hypothetical case where an agglomerate suddenly breaks apart during mixing in the experiment and temporarily causes an increase in available particle surface area for leaching. Overall, calibration proceeds more quickly and with less over fitting when a moderate amount of

observations are provided. Too few observations and hardly any calibration would be done. Too many observations and over-calibration can occur. Overall, it is an interesting questions as to how much time-dependent data to keep when the system is measured continuously

6.6.4 Poor Rate of Convergence

Being careful to avoid the errors mentioned in the three proceeding sections should get calibration off to a good start. However, in conducting this work, it has been found that even with a well-fitting, low-order, and physically reasonable surrogate model, calibration nevertheless can proceed to propose posterior parameter values outside of the physically acceptable range. This situation is very frustrating and can be very difficult to debug. In such a situation, one may wish to check the following:

1. That the priors chosen are physically reasonable, both in terms of their functional form, mean, and standard deviation
2. That the data used for calibration is physically reasonable
3. Whether or not a different sampler initialization scheme is available

6.7 Conclusions and Recommendations

Bayesian inference was used to estimate the rate of particle shrinkages for a chalcopyrite-concentrate pressure leaching scheme comprised of four chemical reactions. This was done by:

1. Collecting chalcopyrite-concentrate pressure leaching data in a laboratory batch setting

2. Making a transient population balance model for chalcopyrite-concentrate pressure leaching in a laboratory batch setting

3. Fitting a surrogate model to the full leaching model

4. Using the No-U-Turn-Sampling algorithm, *via* PyMC3, to estimate the posterior distributions of the rate of particle shrinkages

Comparison of the experimental data to the surrogate model with the calibrated rate of particle shrinkage values proved to favorable. As shown in chapter 5, the calibrated rate of particle shrinkages provided for estimation of industrial behavior within 8% using a population balance

model for industrial-scale leaching. It is recommended that Bayesian inference, a rapidly growing field, be explored for future applications in the copper extraction industry.

CHAPTER 7. PROCESSING-ROUTE COMPARISON AND CONCLUDING REMARKS

The pyrometallurgical and hydrometallurgical routes examined in this work have been shown to perform very differently in terms of exergy. The maximum exergy destruction in the pyrometallurgical process was found to be 18% in smelting. In contrast, the CLP destroyed 69% of the exergy fed to it. Although the entirety of the pyrometallurgical and hydrometallurgical processes were not modeled, a first step to comparing both of these extraction routes can be gained by linking the modeled pyrometallurgical steps and comparing the performance of this linked system to the CLP. Figure 7.1 shows the linked pyrometallurgical steps.

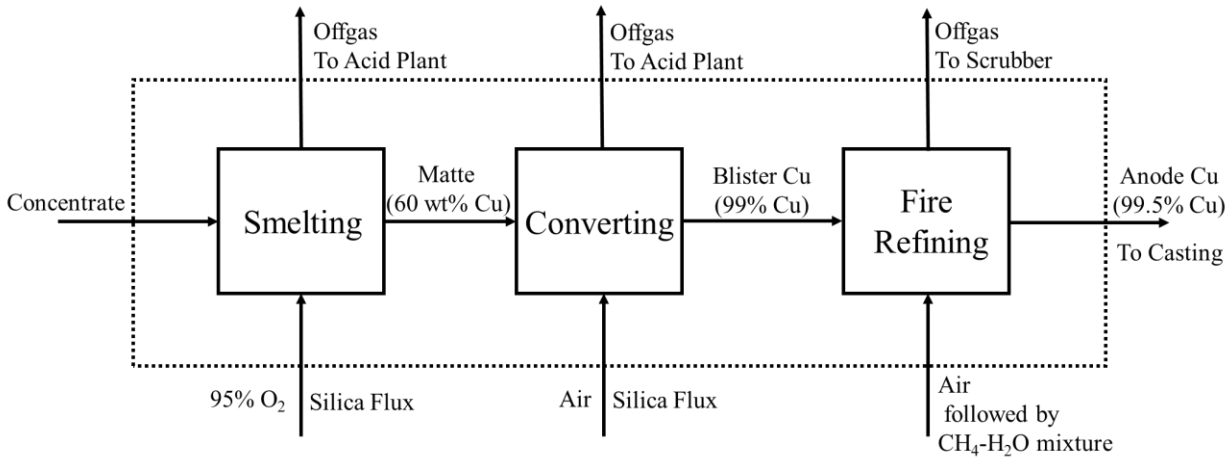

Figure 7.1 - Schematic of the linked pyrometallurgical steps. The dashed box is the system boundary

Table 7.1 - Comparison of exergetic performance of linked pyrometallurgical process to the CLP

Process	Fed (MJ/tonne-Cu)	Lost (MJ/tonne-Cu)	Destroyed (MJ/tonne-Cu)	Product (MJ/tonne-Cu)
Pyrometallurgical (to molten anode Cu)	29,400	7,400 (25%)	6,000 (20%)	16,000 (55%)
CLP	20,800	5,410 (26%)	14,400 (69%)	1,040 (5%)

The pyrometallurgical process appears to perform much more favorably from an exergetic standpoint than the CLP. One may argue that casting the anode copper (a step not included in the above analysis) destroys much of the exergy in the copper. The thermal exergy of the anode copper amounts to 500 MJ/tonne-Cu fed to the pyrometallurgical process, so including this figure would increase the exergy destruction by 1.7% to 21.7%, still much less than for the CLP. Additionally, the processing step immediately following the CLP is a flash-letdown step which brings the PLS to 1 bar pressure and at most 100°C, destroying at least half the thermal exergy of the PLS and bring the total exergy destruction for the CLP to 80%.

The key difference between the CLP and pyrometallurgical processes that causes the large difference in exergy destruction is need to add cooling water to the CLP. This destroys large amounts of exergy because the chemical exergy in the fed concentrate is being used to bring water to 200°C. Smelting uses the chemical exergy of concentrate to bring its product streams to about 1200°C. As such, the difference between the process temperature and environmental temperature (25°C) is about 6.7 times higher for the pyrometallurgical process than the hydrometallurgical process, allowing the smelter to have much more efficient conversion of the chemical exergy in concentrate to thermal exergy in the product streams. In addition to the temperature difference between the processes, the large amount of cooling water in the CLP also significantly dilutes the copper in its product stream; the wt% Cu of the fed concentrate is approximately 25, whereas the PLS at 33 gpL is only 3.3 wt% Cu. This contrasts with the pyrometallurgical processes, which progressively enrich the copper grade of the product stream by removing the iron and sulfur from the copper in the concentrate. Overall, the ability of smelting to operate at high temperature and with comparatively very little dilution of the fed concentrate allows it to exergetically outperform the CLP.

Future work for this project is linking the pyrometallurgical and CLP models to the rest of their respective processes. In particular, both extraction routes require an oxygen plant to produce the oxygen enriched air used by them. Additionally, the SO_2 from the smelter is fed to an acid plant; it would be interesting to see what fraction of the exergy contained in the product offgas from smelting and converting is stored in the product sulfuric acid from the acid plant. Along a similar vein, the acid produced by the CLP is either sent to leaching oxide ore, or is neutralized by gypsum, both of which could be exergetically interesting processes. In addition to exergy, process

economics should also be included in the final analysis to get the most complete picture of which process is best to install in any given circumstance.

In conclusion, this work explored the creation of transient models of the major chemical reactors involved the pyrometallurgical and hydrometallurgical extraction of copper from chalcopyrite-based concentrates. Transient models were made for copper bath smelting, Peirce-Smith converting, fire refining, and the CLP. Sensitivity studies with exergy balances were performed on each of the models. This study produced the following major observations and recommendations:

1. The linked pyrometallurgical process outperforms the CLP due to the CLP's large dilution of the fed concentrate by plant water
2. Injected gas oxygen grade for the smelting furnace should be maximized. This decreases the offgas load of the smelting furnace, increasing possible production of copper at the smelter as whole.
3. Attempts should be made to minimize thermal cycling in the converters. As such, injected gas oxygen grade should not be increased unless there is a critical need for the offgassing capacity this frees
4. Plantwide copper production under a fixed maximum offgas load can be increased by increasing the matte grade fed to the converters. This is because smelting furnaces can use oxygen enriched air, allowing the same amount of copper purification with less offgas production than converters. This has the added benefit of decreasing the thermal cycling in the converters
5. The current six compartment setup of the CLP is better than the combining of the first two compartments into one large compartment because combination of the first two compartment reduces slurry residence time in the whole autoclave by moving more cooling water to the first tank, which decreases copper extraction
6. Bayesian inference, a rapidly growing field, should be explored for future applications in the copper extraction industry

REFERENCES

1. R. F. Tylecote, in *A Hist. Metall.*, 2nd ed. (The Institute of Materials, London, 1992), pp. 1–6.

2. I. Dincer and M. A. Rosen, *Exergy Energy, Environment And Sustainable Development* (Elsevier, 2013).

3. M. Nagamori, W. J. Errington, P. J. Mackey, and D. Poggi, Metall. Mater. Trans. B **25**, 839 (1994).

4. W. J. Errington, J. S. Edwards, and P. Hawkins, J. South African Inst. Min. Metall. **97**, 161 (1997).

5. G. R. Alvear, P. Aurthur, and P. Partington, in *Copp. 2010* (2010), pp. 615–630.

6. G. R. Alvear, S. P. Hunt, and B. Zhang, in *Adv. Process. Met. Mater. Sohn Int. Symp.*, edited by F. Kongoli and R. Reddy (2006), pp. 673–685.

7. P. Tan and C. Zhang, J. Cent. South Univ. Technol. (English Ed. **4**, 36 (1997).

8. J. W. Matousek, JOM **60**, 62 (2008).

9. J. W. Matousek, JOM **61**, 61 (2009).

10. T. Koskinen and H. Torvela, Miner. Eng. **2**, 489 (1989).

11. A. V. Tarasov and V. M. Paretsky, in *Comput. Model. Mater. Miner. Met. Process.* (2001), pp. 563–571.

12. S. Ellor, M. Chamberland, and H. Davies, in *EPD Congr. 1992* (1992), pp. 1125–1145.

13. Y. B. Hahn and H. Y. Sohn, Metall. Trans. B **21**, 945 (1990).

14. Y. B. Hahn, Metall. Trans. B **21**, 959 (1990).

15. K. W. Seo and H. Y. Sohn, Metall. Trans. B **22**, 791 (1991).

16. K. Itagaki, H. Y. Sohn, and M. Perez-Tello, in *Sulfide Smelt. 2002* (2002), pp. 15–40.

17. P. Coursol, P. Mackey, and P. Diaz, Copp. 2010 Conf. June 7th, Hamburg, Ger. 649 (2010).

18. P. Coursol, P. J. Mackey, J. P. T. Kapusta, and N. C. Valencia, JOM **67**, 1066 (2015).

19. A. Pelletier, P. Mackey, L. Southwick, and A. Wraith, in *Proc. Int. Peirce-Smith Convert. Centen. Symp.* (2009), pp. 29–49.

20. M. E. Schlesinger, M. J. King, K. C. Sole, and W. G. Davenport, Extr. Metall. Copp. 127 (2011).

21. A. K. Kyllo, A Kinetic Model of the Peirce-Smith Converter, University of British Columbia, 1995.

22. A. K. Kyllo and G. G. Richards, Metall. Mater. Trans. B **29**, 239 (1998).

23. A. K. Kyllo and G. G. Richards, Metall. Mater. Trans. B **29**, 251 (1998).

24. N. Aminizadeh and S. H. Mansouri, Proc. Inst. Mech. Eng. Part E J. Process Mech. Eng. **221**, 129 (2007).

25. E. A. Peretti, Discuss. Faraday Soc. 179 (1948).

26. B. O. Bjorkman and G. Eriksson, CMQ **21**, 329 (1982).

27. S. Nikolic, P. C. Hayes, and E. Jak, Metall. Mater. Trans. B **39B**, 179 (2008).

28. S. Nikolic, H. Henao, P. C. Hayes, and E. Jak, Metall. Mater. Trans. B **39**, 189 (2008).

29. S. Nikolic, P. C. Hayes, and E. Jak, Metall. Mater. Trans. B **39B**, 200 (2008).

30. S. Nikolic, P. C. Hayes, and E. Jak, Metall. Mater. Trans. B **39**, 2 (2008).

31. S. Nikolic, P. C. Hayes, and E. Jak, Metall. Mater. Trans. B **40B**, 910 (2009).

32. S. Nikolic, P. C. Hayes, and E. Jak, Metall. Mater. Trans. B **40B**, 900 (2009).

33. S. Nikolic, P. C. Hayes, and E. Jak, Metall. Mater. Trans. B **40B**, 892 (2009).

34. P. C. Chaubal, M. Nagamori, and H. Y. Sohn, Can. Metall. Q. **23**, 405 (1984).

35. P. C. Chaubal and M. Nagamori, Metall. Trans. B **19**, 547 (1988).

36. P. C. Chaubal, H. Y. Sohn, D. B. George, and L. K. Bailey, Metall. Trans. B **20B**, 39 (1989).

37. J. A. Pineda and G. Plascencia, J. Sustain. Metall. **2**, 265 (2016).

38. M. E. Schlesinger, M. J. King, K. C. Sole, and W. G. Davenport, in *Extr. Metall. Copp.* (2011), pp. 237–249.

39. L. Díaz-Damacillo, F. Reyes, A. Ingalls, C. Méndez, and G. Plascencia, JOM **69**, 980 (2017).

40. C. R. Nanda and G. H. Geiger, Metall. Trans. **2**, 1101 (1971).

41. R. J. Andreini, R. B. Phillips, and J. S. Foster, Metall. Trans. **8**, 633 (1977).

42. R. Ohno, Metall. Trans. B **10B**, 649 (1979).

43. T. Marin, A. Warczok, G. Riveros, T. Utigard, G. Plascencia, A. Warczok, G. Riveros, T. Utigard, and G. P. Kinetics, Can. Metall. Q. **46**, 379 (2007).

44. T. Marin and T. Utigard, Metall. Mater. Trans. B **41**, 535 (2010).

45. P. Goyal, N. Themelis, and W. Zanchuk, JOM **34**, 22 (1982).

46. E. Kolczyk, Z. Miczkowski, and J. Czernecki, Arch. Metall. Mater. **61**, 521 (2016).

47. J. L. P. T. Kapusta, JOM **69**, 970 (2017).

48. J. Enriquez, R. Walton, A. Deneys, A. Chan, B. Bielec, and V. Kilchyk, in *Extr. 2018 Proc. First Glob. Conf. Extr. Metall.* (Springer International, Web, 2018), pp. 519–531.

49. R. M. Neal, *Probabilistic Inference Using Markov Chain Monte Carlo Methods* (Toronto, 1993).

50. M. E. Schlesinger, M. J. King, K. C. Sole, and W. G. Davenport, in *Extr. Metall. Copp.*, 5th ed. (Elsevier, 2011).

51. C. Green, J. Robertson, and J. O. Marsden, Miner. Metall. Process. **35**, 109 (2019).

52. R. McElroy and W. Young, in *Copp. Leaching, Solvent Extr. Electrowinning Technol.*, edited by G. V. J. II (SME, Littleton, CO, 1999), pp. 29–40.

53. J. O. Marsden, R. E. Brewer, J. M. Robertson, W. W. Hazen, P. Thompson, and D. R. Baughman, (2009).

54. J. O. Marsden and C. I. House, in *Chem. Gold Extr.*, 2nd ed. (Society for Mining, Metallurgy, and Exploration, 2006), pp. 163–175.

55. R. J. Jan, M. T. Hepworth, and V. G. Fox, Metall. Trans. B **7**, 353 (1976).

56. T. M. Woodward, On the Operability of the Sherritt-Gordon Ammonia Leach at the Kwinana Nickel Refinery, 2014.

57. Y. Li, N. Kawashima, J. Li, A. P. Chandra, and A. R. Gerson, Adv. Colloid Interface Sci. **198**, 1 (2013).

58. R. G. McDonald and D. M. Muir, Hydrometallurgy **86**, 191 (2007).

59. S. A. Baldwin, G. P. Demopoulos, and V. G. Papangelakis, Metall. Mater. Trans. B **26**, 1035 (1995).

60. V. G. Papangelakis, D. Berk, and G. P. Demopoulos, Metall. Trans. B **21**, 827 (1990).

61. V. G. Papangelakis and G. P. Demopoulos, Metall. Trans. B **23**, 865 (1992).

62. V. G. Papangelakis and G. P. Demopoulos, Metall. Trans. B **23**, 847 (1992).

63. D. H. Rubisov and V. G. Papangelakis, Hydrometallurgy **39**, 377 (1995).

64. D. H. Rubisov and V. G. Papangelakis, Can. J. Chem. Eng. **74**, 353 (1996).

65. D. H. Rubisov and V. G. Papangelakis, Can. J. Chem. Eng. **74**, (1996).

66. D. H. Rubisov and V. G. Papangelakis, Comput. Chem. Eng. **21**, 1031 (1997).

67. F. K. Crundwell, Hydrometallurgy **39**, 321 (1995).

68. M. E. Schlesinger, M. J. King, K. C. Sole, and W. G. Davenport, Extr. Metall. Copp. 155 (2011).

69. Z. Asaki, Y. Chiba, T. Oishi, and Y. Kondo, Metall. Trans. B **21**, 19 (1990).

70. Z. Asaki, T. Taniguchi, and M. Hayashi, JOM **53**, 25 (2001).

71. Z. ASAKI, Miner. Process. Extr. Metall. Rev. **11**, 163 (1992).

72. J. G. Dunn, Thermochim. Acta **300**, 127 (1997).

73. A. Warczok and T. A. Utigard, in *EPD Congr. 1992* (1992), pp. 729–744.

74. I. Barin, *Thermochemical Data of Pure Substances* (1997).

75. D. R. Morris and J. Szargut, Energy **11**, 733 (1986).

76. T. S. Community, (2019).

77. J. J. More, B. S. Garbow, and K. E. Hillstrom, *USER GUIDE FOR MINPACK-1* (1980).

78. V. M. Glazov, S. G. Kim, and G. K. Mambeterzina, Zhurnal Fiz. Khimii **66**, 2544 (1992).

79. A. A. Bustos, M. Cardoen, and B. Janssens, in *Copp. 95* (Montreal, 1995), pp. 255–269.

80. J. K. Brimacombe and A. Bustos, in *Phys. Chem. Extr. Metall.* (1985), pp. 327–351.

81. J. K. Brimacombe, S. E. Meredith, and R. G. H. Lee, Metall. Trans. B **15**, 243 (1984).

82. A. A. Bustos, J. K. Brimacombe, and G. G. Richards, Metall. Trans. B **17**, 677 (1986).

83. C. W. Bale and J. M. Toguri, CMQ **15**, 305 (1976).

84. B. Hallstedt, D. Risold, and L. J. Gaukler, J. Phase Equilibria **15**, 483 (1994).

85. P. P. Wegener and J.-Y. Parlange, Annu. Rev. Fluid Mech. 79 (1973).

86. W. N. Bond, Philos. Mag. Ser. 7 **4**, 889 (1927).

87. M. J. Assael, A. E. Kalyva, K. D. Antoniadis, R. Michael Banish, I. Egry, J. Wu, E. Kaschnitz, and W. A. Wakeham, J. Phys. Chem. Ref. Data **39**, (2010).

88. J. D. Hoffman, in *Numer. Methods Eng. Sci.*, 2nd ed. (CRC Press, New York, 2001), pp. 587–650.

89. H. B. Palmer, J. Lahaye, and K. C. Hou, J. Phys. Chem. **72**, 348 (1968).

90. K. J. Hüttinger and W. F. Merdes, Carbon N. Y. **30**, 883 (1992).

91. S. Ergun, *Kinetics of the Reactions of Carbon Dioxide and Steam with Coke* (1962).

92. W. M. Graven and F. J. Long, J. Am. Chem. Soc. **76**, 2602 (1954).

93. P. Attavar, (2020).

94. R. G. McDonald and D. M. Muir, Hydrometallurgy **86**, 206 (2007).

95. F. Gronvold, S. Stolen, E. F. Westrum, and G. Galeas, J. Chem. Thermodyn. **19**, 1305 (1987).

96. J. Majzlan, R. Stevens, J. Oerio-Goates, B. F. Woodfield, A. Navrotsky, P. C. Burns, M. K. Crawford, and T. G. Amos, Phys Chem Miner. **31**, 518 (2004).

97. J. Majzlan, E. Dachs, A. Benisek, J. Plasil, and J. Sejkora, Eur. J. Miner. **30**, 259 (2018).

98. M. Perez-Tello, V. R. Parra-Sanchez, V. M. Sanchez-Corrales, A. Gomez-Alvarez, F. Brown-Bojorquez, R. A. Parra-Figueroa, E. R. Balladares-Varela, and E. A. Araneda-Hernandez, **49**, 627 (2018).

99. S. A. Awe, Antimony Recovery from Complex Copper Concentrates through Hydro- and Electrometallurgical Processes, Lulea University of Technology, 2014.

100. C. M. Criss and J. W. Cobble, J. Am. Chem. Soc. **86**, 5385 (1964).

101. C. M. Criss and J. W. Cobble, J. Am. Chem. Soc. **86**, 5390 (1964).

102. L. Becze, M. A. Gomez, J. F. Le Berre, B. Pierre, and G. P. Demopoulos, Can. Metall. Q. **48**, 99 (2009).

103. S. J., T. V. Wiecki, and C. Fonnesbeck, PeerJ Comput. Sci. **2**, (2016).

104. M. D. Hoffman and A. Gelman, J. Mach. Learn. Res. **15**, 1351 (2014).

105. J. D. Hoffman, *Numerical Methods for Engineers and Scientists*, 2nd ed. (Marcel Dekker, New York, 2001).

106. P. H. Yu, C. K. Hansen, and M. E. Wadsworth, Metall. Trans. **4**, 2137 (1973).

107. J. A. Wiebelt and S. Y. Ruo, Int. J. Heat Mass Transf. **6**, 143 (1963).

108. S. N. Rea, AIAA J. **13**, 1122 (1975).

109. C. P. Minning, AIAA J. **17**, 318 (1979).

110. H. B. Keene, Proc. Roy. Soc. **LXXXVIII-A**, 59 (1913).

111. D. C. Hamilton and W. R. Morgan, *Radiant-Interchange Configuration Factors* (NASA TN, 1952).

112. D. . McAdam, A. K. Khatry, and M. Iqbal, Am. Soc. Ag. Eng. **14**, 1068 (1971).

113. M. F. Modest, in *Radiat. Heat Transf.* (2007), pp. 162–197.

114. B. S.K.S., in *Nat. Convect. from Circ. Cylind.* (2014), p. 13.

115. E. W. Lemmon and R. T. Jacobsen, Int. J. Thermophys. **25**, 21 (2004).

116. Y. Saito, K. Kanematsu, and T. Matsui, Mater. Trans. **50**, 2623 (2009).

APPENDIX A: THERMODYNAMIC VALUES USED IN THE MODELS

Table 7.2 - Thermodynamic property values used for smelting and converting. Molar enthalpy calculated according to $h = A + C_pT$; molar entropy calculated according to $s = s_0 + C_p\ln(T/T_0)$

Species	A (MJ/kmole)	C_p (MJ/kmole-K)	s_0 (MJ/kmole-K, T = 1500K)
Cu_2S (l)	-94.822	0.090	0.277
FeS (l)	-84.511	0.063	0.192
Cu_2O (l)	-160.054	0.100	0.258
FeO (l)	-281.435	0.068	0.166
Fe_3O_4 (l)	-1168.112	0.198	0.545
SiO_2 (l)	-936.782	0.073	0.152
N_2 (g)	-13.757	0.035	0.242
O_2 (g)	-14.148	0.037	0.258
SO_2 (g)	-319.896	0.057	0.328
CO_2 (g)	-419.183	0.058	0.292
H_2O (g)	-263.910	0.047	0.251
Cu (l)	-1.800	0.032	0.087
S (Cu)	59.921	0.019	0.257

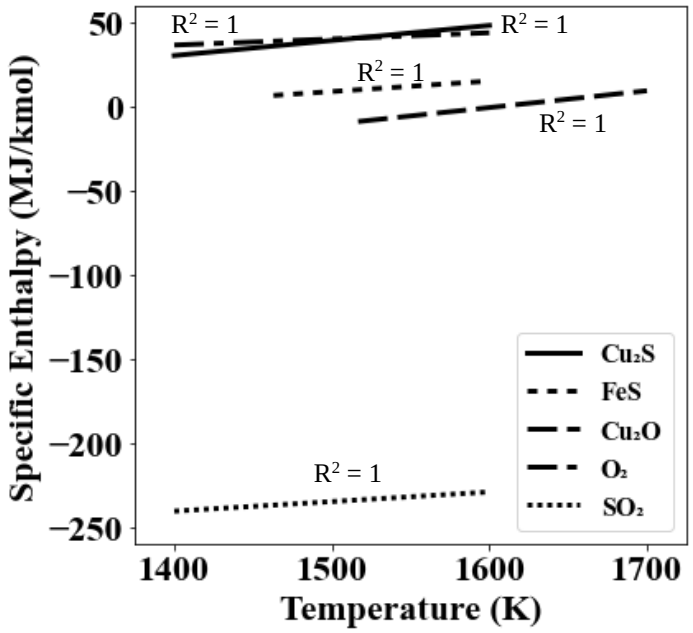

Figure 7.2 – Plot of best fit of specific enthalpies for various species in copper smelting and converting versus temperatures using the data from Barin [74]. The R2 value for each best-fit line is 1.

Table 7.3 - Activity coefficient expressions used for the smelting and converting slag-blow models [26]

Specie	Activity Coefficient
$CuS_{0.5}$	$\gamma = 1.038 {X_{CuS_{0.5}}}^{\frac{1}{4}}$
FeS	$\gamma = 1.079$
$CuO_{0.5}$	$\gamma = \exp\left(\frac{1576\left(1 - X_{CuO_{0.5}}\right)^2}{T}\right)$
FeO	$\gamma = \exp\left(\frac{A}{T}\right)$ $A = 2466 X_{FeO_{1.333}}(1 - X_{FeO}) - 3109 X_{SiO_2}(1 - X_{FeO}) - 396 X_{FeO_{1.333}} X_{SiO_2}$
$FeO_{1.333}$	$\gamma = \frac{1.0429}{{X_{FeO_{1.333}}}^{\frac{1}{2}}}$

APPENDIX B. HEAT TRANSFER IN THE FIRE REFINING FURNACE

All of the parameter/variable values used for this appendix can be found in table B.7 at the appendix end.

B.1 Furnace Description

A copper fire-refining vessel is a closed horizontal cylinder. The furnace wall is composed of refractory brick, encapsulated by a mild-steel shell. The expose brick surface on the furnace interior is coated with soot, produced during fire refining. The furnace is partially filled with metallic copper and possesses a horizontal flame in the furnace headspace. The flame extends through approximately 2/3 of furnace length. Figure B.1 shows a schematic of this geometry.

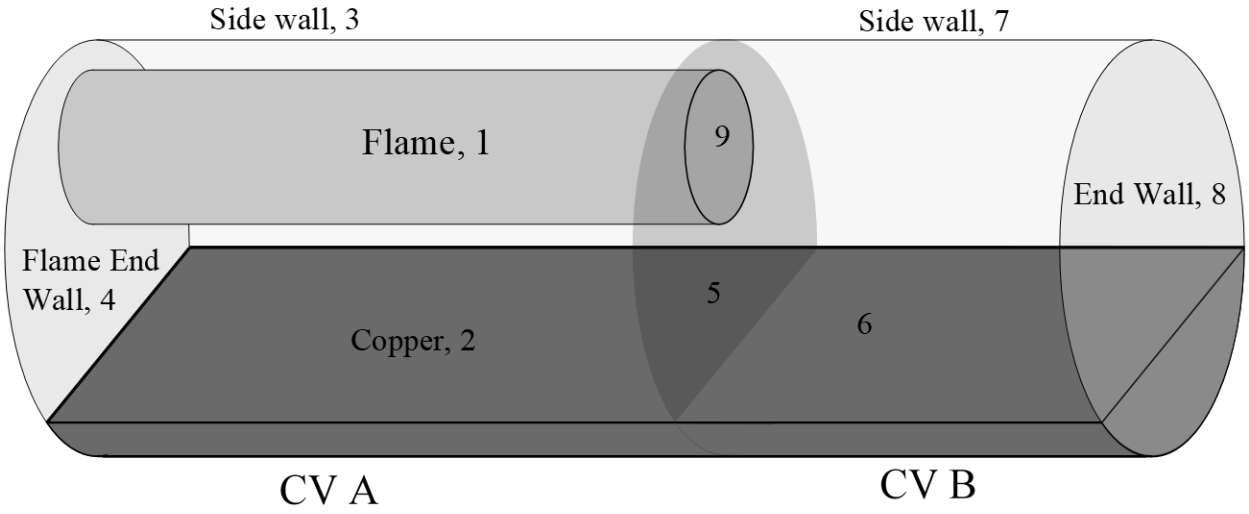

Figure 7.3 - Schematic of the copper fire-refining furnace in 3D

There are several routes of heat transfer in this furnace. This model will consider conduction through the furnace wall, radiation between the melt and wall, melt and flame, and flame and wall. Convection phenomena inside the furnace are ignored due to the expectation that radiation will dominate the furnace's interior heat transfer. Heat is modeled leaving the furnace exterior by both radiation and convection. This model description has three parts: a description of the steady-state heat balance on the headspace flame, the radiation heat transfer network inside of

the furnace, and the conduction-convection network which facilitates heat transfer through the furnace walls and out to the surrounding environment.

B.2 Steady-State Flame Heat Balance

The flame is produced by natural-gas combustion. This modeled as complete methane combustion:

$$\mathrm{CH_4 + 2O_2 \rightarrow CO_2 + 2H_2O} \tag{B. 1}$$

The oxygen source for eqn. B.1 is air at 298K; the methane is fed to the burner at 298K too. The steady-state heat balance on the flame is:

$$0 = \dot{N}_{CH_4} h_{CH_4,298K} - \dot{N}_{CO_2} h_{\mathrm{CO_2},T_f} - \dot{N}_{\mathrm{H_2O}} h_{\mathrm{H_2O},T_f} - \dot{N}_{N_2} h_{N_2,T_f} - \dot{Q}_f \tag{B. 2}$$

In equation B.2, $\dot{N}_i$ is the molar flowrate of species *i* into the furnace (for CH_4) or out of the furnace (H_2O, CO_2 N_2), $h_{\mathrm{i},T}$ is the molar enthalpy of *i* at temperature *T*, and $\dot{Q}_f$ is the net radiation heat transfer off the flame. Oxygen and nitrogen are net present in equation B.2 because their standard enthalpy at 298K is 0. The molar flowrates of each species can be related to the molar flowrate of methane; assuming the stoichiometric amount of oxygen is provided for eqn. B.1 by air, which mimics industrial practice:

$$\dot{N}_{CO_2} = \dot{N}_{CH_4} \tag{B. 3}$$

$$\dot{N}_{\mathrm{H_2O}} = 2\dot{N}_{CH_4} \tag{B. 4}$$

$$\dot{N}_{N_2} = 7.52\dot{N}_{CH_4} \tag{B. 5}$$

The specific enthalpies of each species were approximated by linear functions about 2000K, the initial guess for the flame temperature:

$$h_i = A_i + B_i T \tag{B. 6}$$

The values for *A* and *B* for each species are given in table B.1.

Table 7.4 - Enthalpy values and coefficients used to calculate enthalpies for the chemical species of the flame

Species	A_i (MJ/kmole)	B_i (MJ/kmole-K)
CH_4	h_{298K} = -74.8 MJ/kmole	
CO_2	-424	0.061
H_2O	-273	0.052
N_2	-15.9	0.036

Lastly, $\dot{Q}_f$ is given expression *via* the furnace-interior heat-transfer network, now described.

B.3 Radiation Heat Transfer Inside of the Furnace

B.3.1 Interior Surface Areas

The radiation heat transfer network for the inside of the furnace requires calculation of the view factors between each surface 1-5 shown in fig. 1. To do this, the surface areas of the melt, exposed wall, and flame are needed. The surface area of the melt is:

$$A_{s,melt} = W_{melt} L \tag{B. 7}$$

where $A_{s,melt}$ is the melt surface area, W_{melt} is the width of the melt surface (see fig. 2), and L is the interior length of the furnace. W_{melt} is:

$$W_{melt} = 2r_1 \cos\theta \tag{B. 8}$$

where r_1 is the interior radius of the furnace and θ is angle of the circular section occupied by the melt as shown in figure B.2. θ is found according to the geometry of figure B.2 and noting that the ratio of the volume of the furnace to the volume of the melt equals the ratio of the cross-sectional area of the furnace to the cross sectional area of the melt, $A_{x,melt}$:

$$A_{x,melt} = \pi {r_1}^2 \left(\frac{\theta}{2\pi}\right) - \frac{{r_1}^2}{2}\sin(\pi - \theta) \tag{B.9}$$

$$\frac{A_{x,melt}}{A_{x,furn}} = \frac{V_{melt}}{V_{furn}} \tag{B.10}$$

where $A_{x,furn}$ is the cross sectional area of the furnace, V_{melt} is the volume of the melt, and V_{furn} is the interior volume of the furnace. Combining eqns. B.9 and 10 and substituting the cross-sectional area of the furnace (a circle) and volume of the furnace (a cylinder) with their geometric formulas gives:

$${r_1}^2 \left(\frac{\theta}{2}\right) - \frac{{r_1}^2}{2}\sin(\pi - \theta) = \frac{V_{melt}}{L} \tag{B.11}$$

Equation B.11 can be solved numerically for θ, which is 2.8 radians for the fire refining studies presented in this work. Equations B.7-11 are sufficient for calculating the surface area of the melt (surface 2 in figure B.1), which was found to be 33m^2 for the fire-refining studies presented in this work.

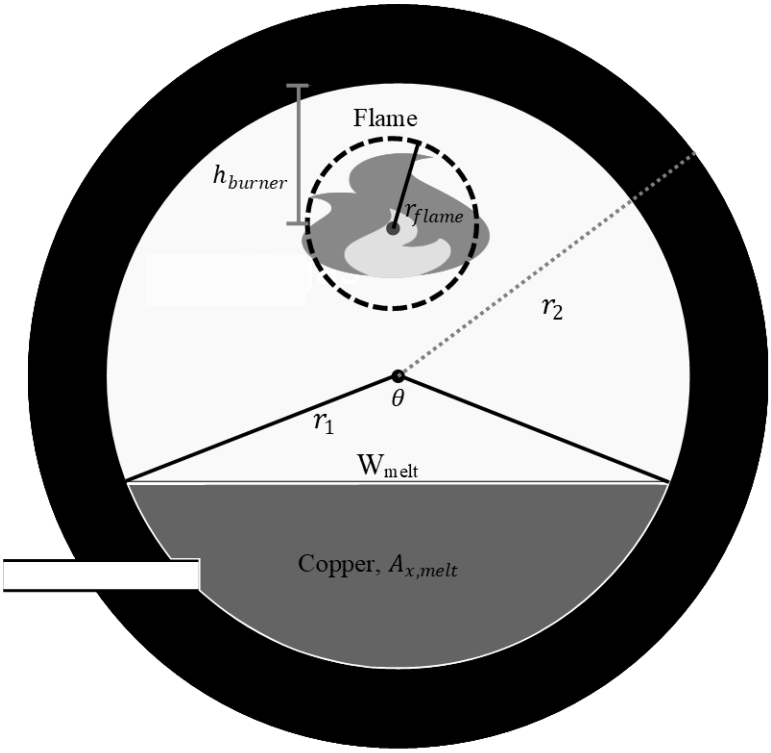

Figure 7.4 - Geometry relevant to view factor calculations

The lateral surface area of the exposed brick (surface 3 in figure B.1) is:

$$A_{LS,brick} = (2\pi - \theta) r_1 L \tag{B.12}$$

The surface area of the brick on the furnace end wall without the flame (surface 5 in figure B.1) is:

$$A_{ES,brick} = 2\pi {r_1}^2 - A_{x,melt} \tag{B.13}$$

$A_{x,melt}$ can be found using equation B.9. The surface area of the brick on the furnace end wall with the flame is:

$$A_{FS,brick} = A_{ES,brick} - \pi {r_f}^2 \tag{B.14}$$

Finally, the surface area of the flame (surface 1 in figure B.1) is found according to:

$$A_{S,flame} = \pi {r_f}^2 + 2\pi r_f L_f \tag{B.15}$$

The radius of the flame was estimated according to industrial observation for the Freeport-McMoRan Inc. Miami anode plant and is given in table B.7. With expressions for the surface areas, the view factors between each surface can be found.

B.3.2 View Factor Relationships for the Furnace Interior

The geometry of the furnace is such that approximations were required to estimate the view factors. To this end, the furnace was divided into two control volumes as shown in fig. 1. Control volume A bears the entire lateral surface area of the flame. Control volume B contains the exposed flame end and the rest of the furnace. The furnace section where the control volumes meet was treated as a completely transparent surface that evenly emits all incoming radiation from one side to the other. This approximation appears to work well for the fire-refining furnace and facilitated overall view factor calculations for the furnace interior. This section of the model description is

divided into three parts. First, the view factors between the surfaces comprising control volume A are described; then, the same is done for control volume B; finally, the view factor relationships through the whole furnace (surface 5 is removed) are given.

B.3.2.1 View Factors in Control Volume A

There are 25 view factors to be found in control volume A. Surfaces 1, 2, 4, and 5 are convex, and so have self-view factors of zero:

$$F_{1,1} = 0 \tag{B.16}$$
$$F_{2,2} = 0 \tag{B.17}$$
$$F_{4,4} = 0 \tag{B.18}$$
$$F_{5,5} = 0 \tag{B.19}$$

Here, $F_{i,j}$ is the view factor of surface *i* looking at surface *j*. Next, view-factor identities allow the following to be written:

$$F_{1,2} + F_{1,3} + F_{1,4} + F_{1,5} = 1 \tag{B.20}$$
$$F_{2,1} + F_{2,3} + F_{2,4} + F_{2,5} = 1 \tag{B.21}$$
$$F_{3,1} + F_{3,2} + F_{3,3} + F_{3,4} + F_{3,5} = 1 \tag{B.22}$$
$$F_{4,1} + F_{4,2} + F_{4,3} + F_{4,5} = 1 \tag{B.23}$$
$$F_{5,1} + F_{5,2} + F_{5,3} + F_{5,4} = 1 \tag{B.24}$$
$$F_{1,2}A_1 = F_{2,1}A_2 \tag{B.25}$$
$$F_{1,3}A_1 = F_{3,1}A_3 \tag{B.26}$$
$$F_{1,4}A_1 = F_{4,1}A_4 \tag{B.27}$$
$$F_{1,5}A_1 = F_{5,1}A_5 \tag{B.28}$$
$$F_{2,3}A_2 = F_{3,2}A_3 \tag{B.29}$$
$$F_{2,4}A_2 = F_{4,2}A_4 \tag{B.30}$$
$$F_{2,5}A_2 = F_{5,2}A_5 \tag{B.31}$$
$$F_{3,4}A_3 = F_{4,3}A_4 \tag{B.32}$$
$$F_{3,5}A_3 = F_{5,3}A_5 \tag{B.33}$$

In addition, surfaces four and five have equal areas, and control volume A is symmetric about them:

$$A_4 = A_5 \tag{B.34}$$

$$F_{1,4} = F_{1,5} \tag{B.35}$$

$$F_{2,4} = F_{2,5} \tag{B.36}$$

$$F_{3,4} = F_{3,5} \tag{B.37}$$

$$F_{5,4} = F_{4,5} \tag{B.38}$$

Equations B.16-38 provide 22 relationships. Three more are needed to be able to solve for the view factors. Wiebelt and Ruo's work [107] is used to calculate $F_{1,2}$, the view factor of the lateral flame area to the surface of the melt. Rea's work [108] is used to estimate $F_{1,4}$, where the flame and exposed furnace end wall are treated as a cylinder with a concentric circle at the cylinder's end. Finally, Minning's work [109] is used to estimate $F_{4,5}$, where the furnace end wall and pseudo-surface at the flame end are treated as concentric circles separated by a solid cylinder. For the cases where the furnace end wall is treated as a concentric circle, the radius for the end wall used in the view factor formulas is estimated as:

$$r_c = \sqrt{\frac{A_4}{\pi}} \tag{B.39}$$

where r_c is the concentric-circle radius. Table B.2 gives the areas used for the surfaces in control volume A. Table B.3 gives the calculated view factors for the surfaces of control volume A.

Table 7.5 - Surface areas for control volume A

Surface	Area (m^2)
1	4.20
2	20.3
3	33.3
4	4.6
5	4.6

Table 7.6 - View factors for control volume A. The surface in the leftmost column is the viewing surface; the surface in the top row is the viewed surface

Surface	1	2	3	4	5
1	0	0.14	0.72	0.07	0.07
2	0.03	0	0.84	0.065	0.065
3	0.09	0.51	0.28	0.06	0.06
4	0.07	0.28	0.45	0	0.2
5	0.07	0.28	0.45	0.2	0

B.3.2.2 View Factors for Control Volume B

The development of the view factors for control volume B follows the same approach as for control volume A. Surfaces 5, 6, 8, and 9 are convex and so have view factors of zero:

$$F_{5,5} = 0 \tag{B.40}$$

$$F_{6,6} = 0 \tag{B.41}$$

$$F_{8,8} = 0 \tag{B.42}$$

$$F_{9,9} = 0 \tag{B.43}$$

Surfaces 5 and 9 are coplanar and so have mutual view factors of zero:

$$F_{5,9} = 0 \tag{B.44}$$

$$F_{9,5} = 0 \tag{B.45}$$

The sum of all the view factors for each surface looking at the rest must add to one:

$$F_{5,6} + F_{5,7} + F_{5,8} + F_{5,9} = 0 \tag{B.46}$$

$$F_{6,5} + F_{6,7} + F_{6,8} + F_{6,9} = 0 \tag{B.47}$$

$$F_{7,5} + F_{7,6} + F_{7,7} + F_{7,8} + F_{7,9} = 0 \tag{B.48}$$

$$F_{8,5} + F_{8,6} + F_{8,7} + F_{8,9} = 0 \tag{B.49}$$

$$F_{9,5} + F_{9,6} + F_{9,7} + F_{9,8} = 0 \tag{B.50}$$

View factors identities relate the view factors and surface areas of each surface to those ofB the other surfaces:

$$F_{5,6}A_5 = F_{6,5}A_6 \tag{B.51}$$

$$F_{5,7}A_5 = F_{7,5}A_7 \tag{B.52}$$

$$F_{5,8}A_5 = F_{8,5}A_8 \tag{B.53}$$

$$F_{6,7}A_6 = F_{7,6}A_7 \tag{B.54}$$

$$F_{6,8}A_6 = F_{8,6}A_8 \tag{B.55}$$

$$F_{6,9}A_6 = F_{9,6}A_9 \tag{B.56}$$

$$F_{7,8}A_7 = F_{8,7}A_8 \tag{B.57}$$

$$F_{7,9}A_7 = F_{9,7}A_9 \tag{B.58}$$

$$F_{8,9}A_8 = F_{9,8}A_9 \tag{B.59}$$

Next, the combined surface 5+9 is symmetric to surface 8, which gives:

$$F_{6,8} = F_{6,5} + F_{6,9} \tag{B.60}$$

$$F_{7,8} = F_{7,5} + F_{7,9} \tag{B.61}$$

So far, there are twenty-two equations for 25 view factors, so three more equations are needed. $F_{9,8}$ was estimated using the work of Keene [110]. $F_{8,5}$ was estimated using Hamilton's and Morgan's work [111] for a disk to coaxial ring on a parallel disk. Finally, $F_{6,8}$ was estimated using the work of McAdam et al. [112]. Table B.4 gives the areas used to in the calculation of the view factors for control volume B. Equation B.39 was used to estimate concentric circle radii. Table B.5 gives the view-factor values.

Table 7.7 - Surface areas for control volume B

Surface	Area (m^2)
5	4.56
6	15.5
7	28.0
8	4.60
9	0.04

Table 7.8 - View factors for control volume A. The surface in the leftmost column is the viewing surface; the surface in the top row is the viewed surface

Surface	5	6	7	8	9
5	0	0.37	0.55	0.08	0
6	0.12	0	0.76	0.12	0
7	0.12	0.42	0.33	0.12	0
8	0.08	0.37	0.55	0	0
9	0	0.20	0.70	0.10	0

B.3.2.3 Overall View Factors

Because surface 5 is treated as a totally transparent and an even distributor of incoming radiation, the view factor of a surface in control volume A looking into control volume B can be

found by the product of the view factor between that surface and surface 5, and surface 5 and the surface in question in control volume B. The equivalent holds true for a surface in control volume B looking into control volume A. For example:

$$F_{2,8} = F_{2,5}F_{5,8} \tag{B.62}$$

Carrying out calculations such as 62 between all surfaces in the furnace gives the view-factors found in table B.6.

Table 7.9 Overall furnace view factors. The row is the viewing surface; the column is the viewed surface

Surface	1	2	3	4	6	7	8	9
1	0.000	0.140	0.720	0.070	0.032	0.033	0.006	0.000
2	0.030	0.000	0.840	0.070	0.029	0.031	0.005	0.000
3	0.090	0.510	0.280	0.060	0.027	0.028	0.005	0.000
4	0.070	0.280	0.450	0.000	0.090	0.094	0.016	0.000
6	0.084	0.034	0.054	0.024	0.000	0.760	0.120	0.000
7	0.084	0.034	0.054	0.024	0.420	0.330	0.120	0.000
8	0.006	0.022	0.036	0.016	0.370	0.550	0.000	0.000
9	0.000	0.000	0.000	0.000	0.200	0.700	0.100	0.000

B.3.3 Radiative Heat Exchange Equations

With the furnace interior surface areas and view factors calculated, the rates of radiative heat exchange between each surface can be calculated as functions of the temperature of each surface. This model takes the entire flame as being at one uniform temperature, the entire melt as being at a second uniform temperature, and the exposed brick wall (surfaces 3, 4, 7, and 8) as being at a third uniform temperature. From Modest [113], the system of equations describing the net heat transfer to each surface 1-4 and 6-9 is developed:

$$\frac{q_i}{\epsilon_i} - \sum_{j=1}^{N} \left(\frac{1}{\epsilon_j} - 1 \right) F_{i,j} q_j = \sigma \sum_{j=1}^{N} F_{i,j} \left({T_i}^4 - {T_j}^4 \right) \tag{B.63}$$

where q_i is the net rate of heat transfer to surface *i*, ϵ_i is the emissivity of surface *i*, *N* is the total number of surfaces, σ is the Stefan-Boltzmann constant, and T_i is the temperature of surface *i*; in equation B.63, the subscript *i* denotes the viewing surface, and the subscript *j* denotes the viewed surface. The total heat transfer to the melt is:

$$q_{melt} = q_2 + q_6 \tag{B.64}$$

The total heat transfer to the flame is:

$$q_{flame} = q_1 + q_9 \tag{B.65}$$

The total heat transfer to the exposed surface of the brick wall is:

$$q_{brick,top} = q_3 + q_4 + q_7 + q_8 \tag{B.66}$$

Now, additional equations are needed to describe the heat transfer through the furnace wall and out to the environment.

B.4 Conduction-Convection Network for Heat Transfer Through the Furnace Wall

Heat leaves the furnace interior in three ways: conduction through the exposed furnace brick, conduction through the brick in contact with the melt, and offgassing. The latter mode of heat transfer is captured as the enthalpy flow out terms in the fire-refining energy balance. The first two terms are now described. Then, the heat transfer from the furnace exterior to the environment is discussed.

B.4.1 Conduction Through the Brick Wall

Conduction was considered to happen through the lateral area of the brick wall only. The furnace ends were ignored both because their surface area is 1/7 of the total furnace exterior surface area and because of the large degree in uncertainty as what convection equations to apply to them. The authors believed any error due to ignoring the furnace ends is less than the uncertainty in the developed model. Additionally, the steel shell surrounding the brick was ignored as it was found to have a negligible impact on the heat transfer results.

Conduction occurs through the exposed brick and the brick in contact with the melt:

$$q_{brick,top} = \frac{(2\pi - \theta)Lk\left(T_3 - T_{os,top}\right)}{\ln\frac{r_2}{r_1}} \tag{B.67}$$

$$q_{brick,bot} = \frac{\theta Lk\left(T_{melt} - T_{os,bot}\right)}{\ln\frac{r_2}{r_1}} \tag{B.68}$$

In equations B.67 and 68, $q_{brick,top}$ is the net rate of heat transfer through the exposed brick to the environment, k is the thermal conductivity of the furnace brick, $T_{os,top}$ is the temperature of the outside furnace area spanned by $2\pi - \theta$, r_2 and r_1 are the outside and inside radii of the furnace respectively, $q_{brick,bot}$ is the net rate of heat transfer through the brick wall in contact with the melt, and $T_{os,bot}$ is the temperature of bottom surface of the furnace, spanned by θ. Heat transfer has been described up to the furnace surface. Now, heat transfer from the furnace surface to the environment is discussed.

B.4.2 Convection and Radiation off the Furnace Surface

The equations for the net rate of heat transfer off the furnace exterior surface are:

$$q_{brick,top} = (2\pi - \theta)r_2L\sigma\left(\epsilon_{st}{T_{os,top}}^4 - \epsilon_{air}{T_0}^4\right) + (2\pi - \theta)r_2Lh_{air}\left(T_{os,top} - T_0\right) \tag{B.69}$$

$$q_{brick,bot} = \theta r_2L\sigma\left(\epsilon_{st}{T_{os,bot}}^4 - \epsilon_{air}{T_0}^4\right) + \theta r_2Lh_{air}\left(T_{os,bot} - T_0\right) \tag{B.70}$$

Now, the convective heat transfer coefficient for air undergoing natural convection off of a horizontal cylinder is needed. The heat transfer coefficient is related to the Nusselt number by:

$$\mathrm{h}_{air} = \frac{\mathrm{N_{ud}k_{air}}}{2r_2} \tag{B.71}$$

The Nusselt number was approximated according to equation 2.55 in Boetcher's work [114]. The temperature-dependent thermal conductivity of air was calculated according to Lemmon and Jacobsen [115]. Equations B.2-71 are sufficient for calculating all rates of heat transfer inside the furnace, through the furnace wall, and from the furnace surface to the environment.

B.5 Heat Transfer Results

The results of the heat transfer model necessary for fire-refining model reproduction are given in Table 4.6 in the fire refining model description.

B.6 Parameter Values Used for the Heat Transfer Model

Table seven lists the parameter values used in the heat transfer model. All of the parameters are highly certain except for the emissivity of the steel shell and emissivity of the liquid copper. Varying the emissivity of the steel shell from 0 to 1 caused a less than 1% change in the heat transfer rates. Varying the emissivity of the liquid copper from 0.3 to 0.5 caused the heat loss rate from the melt to increase by 9 kW to 112 kW. Decreasing the emissivity of the melt to 0.1 from 0.3 caused the heat loss rate to decrease from 103 kW to 60 kW. These heat loss rate differences did not have a significant impact on the transient temperatures of the melt, nor on the exergetic performance of the fire refining operation.

Table 7.10 - Parameter values used for the heat transfer model

Parameter	Value
L, Furnace Length (m)	11.2
r_1, Interior Radius (m)	1.5
r_2, Exterior Radius (m)	1.98
V_{Furn}, Furnace Volume (m^3)	80.4
V_{Melt}, Melt Volume (m^3)	31.1
θ, Angle of Exposed Brick (radians)	2.80
L_{Flame}, Flame Length (m)	6.1
r_{Flame}, Flame Radius (m)	0.1
Burner Vertical Distance from Roof (m)	0.75
k_{brick}, Thermal Conductivity of Brick (W/m-K)	5.6 [116]
ϵ_{st}, Emissivity of Steel	0.7
ϵ_{brick}, Emissivity of Soot Covered Brick	1.0
$\epsilon_{copper(l)}$, Emissivity of Liquid Copper	0.3

APPENDIX C. GAS PHASE MODEL FOR THE CONCENTRATE LEACH PROCESS

C.1 Description of the Gas Phase

The CLP has its gas phase contiguous over the surface of the slurry; as such, it is treated as a single control volume. A schematic a leaching autoclave can be seen in figure C.1.

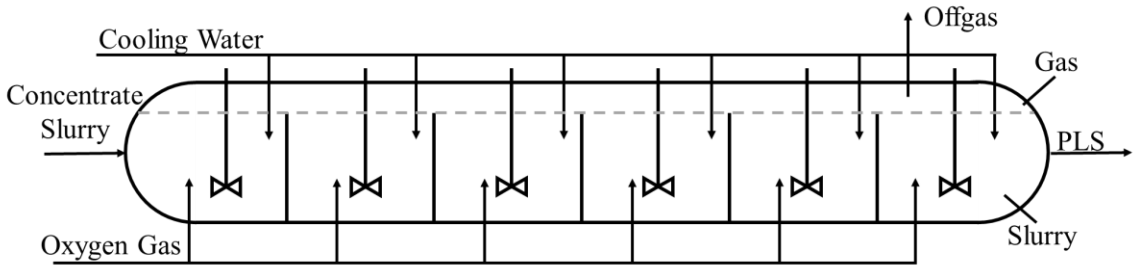

Figure 7.5 - Schematic of a CLP autoclave

The gas phase is comprised of oxygen gas, nitrogen gas, and steam. It is treated as being at steady state with respect to the rate of consumption of oxygen gas by the leaching reactions and offgassing rate; this means the temperature and pressure and composition of the gas phase are steady.

Control of the gas phase is achieved as follows. A valve on the CLP roof can be turned over a continuous range from entirely closed to entirely opened, thus determining the offgassing rate. The functional dependence of the offgassing rate on the "openness" of the valve is unknown. Pressure is maintained inside the vessel via pressure regulators, through which the oxygen supply is fed. Gas that leaves the vessel *via* offgassing or consumption by reaction is immediately made up by 98% pure oxygen. Water vaporizes such that its saturation pressure is maintained, *i.e.*, its rate of vaporization equals its rate of offgassing.

C.2 Gas Phase Mass Balance

The description above of the CLP gas phase yields the following mass balance equations:

$$\dot{N}_{O_{2,in}} = \dot{N}_{O_{2,out}} + \omega_{O_{2,rxn}} \quad (C.1)$$

$$\dot{N}_{N_{2,in}} = \dot{N}_{N_{2,out}} \quad (C.2)$$

$$\omega_{H_2O_{vap}} = \dot{N}_{H_2O_{out}} \quad (C.3)$$

$$\dot{N}_{O_{2,in}} + \dot{N}_{N_{2,in}} + \omega_{H_2O_{vap}} = \dot{N}_{O_{2,out}} + \omega_{O_{2,rxn}} + \dot{N}_{N_{2,out}} + \dot{N}_{H_2O_{out}} \quad (C.4)$$

$\dot{N}_i$ is the injection or removal rate of some gas *i* from the furnace. ω_i is the generation or consumption rate of some gas *i via* reaction. With these equations are also equations relating the species outflow rates to their partial pressures:

$$\dot{N}_{O_{2,out}} = \frac{P_{O_2}}{P_{tot}} \dot{N}_{tot,out} \quad (C.5)$$

$$\dot{N}_{N_{2,out}} = \frac{P_{N_2}}{P_{tot}} \dot{N}_{tot,out} \quad (C.6)$$

$$\dot{N}_{H_2O_{out}} = \frac{P_{H_2O}}{P_{tot}} \dot{N}_{tot,out} \quad (C.7)$$

$$P_{N_2} = P_{tot} - P_{O_2} - P_{H_2O} \quad (C.8)$$

$$\dot{N}_{tot,out} = \dot{N}_{O_{2,out}} + \dot{N}_{N_{2,out}} + \dot{N}_{H_2O_{out}} \quad (C.9)$$

P_i is the partial pressure of gas *i*, P_{tot} is the total pressure in the vessel, and $\dot{N}_{tot,out}$ is net gas flowrate out of the vessel. P_{tot} is a parameter set by the operation via the pressure of the pressure regulators governing gas injection. $\dot{N}_{tot,out}$ is also set (although likely with much less precision) by the operation *via* the opening of the offgas valve. The final equations needed relate the rates of oxygen and nitrogen addition by the pressure regulators:

$$\dot{N}_{O_{2,in}} = Y_{O_{2,in}}\left(\dot{N}_{O_{2,in}} + \dot{N}_{N_{2,in}}\right) \quad (C.10)$$

$$\dot{N}_{N_{2,in}} = Y_{N_{2,in}}\left(\dot{N}_{O_{2,in}} + \dot{N}_{N_{2,in}}\right) \quad (C.11)$$

$$Y_{O_{2,in}} + Y_{N_{2,in}} = 1 \quad (C.12)$$

$Y_{i_{in}}$ is the mole fraction of species *i* in the injected gas.

From equations C.1-12, the steady-state partial pressure of oxygen in the autoclave and the oxygen efficiency can be found. These are functions of the oxygen grade of the injected gas, rate of oxygen consumption, and rate of offgassing. As shown below, the latter two terms appear in the equations as a ratio, allowing the oxygen partial pressure and oxygen efficiency to be more concisely written as functions of this ratio. This ratio is referred to as the "offgassing ratio," denoted by the variable *R*. The offgassing ratio, oxygen partial pressure and oxygen efficiency are given by:

$$R = \frac{\dot{N}_{tot,out}}{\omega_{O_{2,rxn}}} \tag{C.13}$$

$$P_{O_2} = Y_{O_{2,in}}\left(P_{tot} - P_{H_2O}\right) - P_{tot}\left(1 - Y_{O_{2,in}}\right)R^{-1} \tag{C.14}$$

$$OE = 1 - \frac{\dot{N}_{O_2,out}}{\dot{N}_{O_{2,in}}} = \frac{P_{tot}\left(1 - Y_{O_{2,in}}\right)}{Y_{O_{2,in}}\left[P_{tot}(R - YR + 1 - Y) + P_{H_2O}R(Y - 1)\right]} \tag{C.15}$$

Equation C.14 describes P_{O_2} according to expectation: if pure oxygen were fed to the vessel, the only two species in the gas phase would be water and oxygen, so the contribution to the total pressure not made by steam has to be made by oxygen. Alternatively, as the oxygen grade of the injected decreases, the rate of oxygen consumption grows in importance relative to the injection rate of oxygen, causing a lower steady state oxygen partial pressure. The oxygen efficiency equation is more difficult to extract immediate understandings from, however, the results below make its implications clear.

C.3 Results

C.3.1 Base Case – Total Pressure 21.7 Bar Absolute, 200°C H_2O at Saturation

For any combination of oxygen grade of injected gas, offgassing rate, and rate of oxygen consumption by reaction with the slurry, the partial pressure of oxygen and oxygen efficiency can be calculated. This is shown graphically in figure C.2 for 21.7 bar total pressure in the autoclave and steam at 200°C (15.53 bar saturation pressure); this combination of temperature and total pressure corresponds to the current operating conditions at the FMI autoclave.

Graphs such as figure C.2 conveniently allow an operation to estimate autoclave gas-phase performance at a glance. For any combination of two of the four variables displayed on the graph, the required value of the other two can be estimated. For example, suppose a plant knew that at least 5 bar of oxygen partial pressure was needed for leaching rate to be independent of oxygen partial pressure. Also, their inlet oxygen grade is 0.98. This plant would be able to see that they need an offgassing ratio of 0.45 to maintain the required partial pressure of oxygen and maximize the oxygen efficiency, which would have a value of about 91%. One may argue that "R" is practically difficult to know. However, an operation can estimate the rate of consumption of oxygen via an oxygen balance on the slurry entering and leaving the autoclave. This could be accomplished with quantitative mineralogical assays of the inlet and out slurry. The operation can measure the offgassing rate with a flow meter.

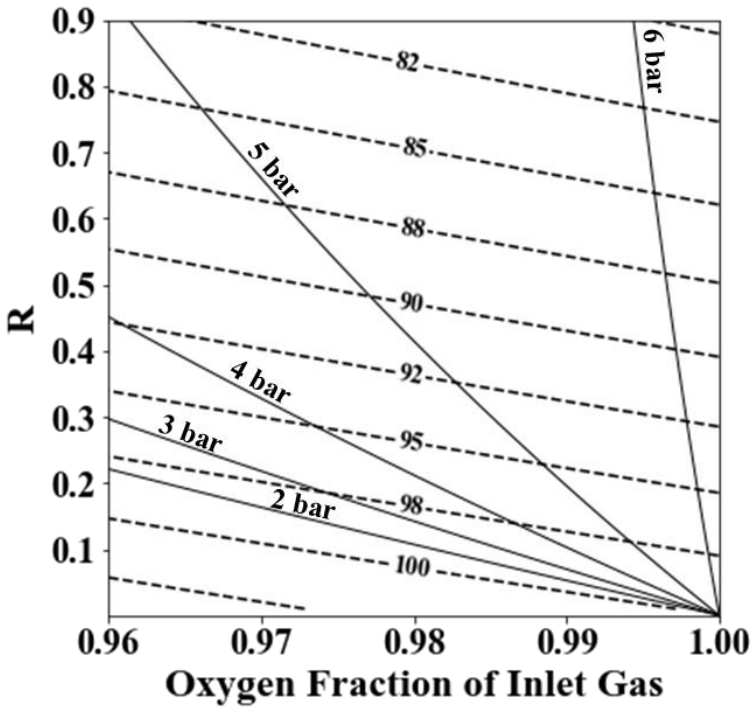

Figure 7.6 - Contour plot of partial pressure of oxygen (solid) and oxygen efficiency (dashed) as a function of the injected gas oxygen grade and offgassing ratio, R. Plot for total pressure of 21.7 bar and saturation pressure of steam at 200 °C, 15.55 bar

C.3.2 Total Pressure 21.7 Bar Absolute, 180°C And 220°C H_2O at Saturation

These two cases explore the effect of changing temperature while keeping total pressure the same. As temperature increases, the saturation pressure of water also increases, and at an increasing rate. This leads to any combination of R and $Y_{O_2,in}$ having smaller oxygen partial pressures and higher oxygen efficiencies with increasing temperatures. The oxygen partial pressure decreases with increasing temperature simply because there is the same amount of total pressure available for the gas phase and H_2O will occupy more of it, meaning oxygen must occupy less. Oxygen efficiency increases with increasing temperature because for a given total rate of offgassing and oxygen consumption by reaction, a lower oxygen partial pressure means less O_2 being offgassed, *i.e.* wasted.

At first glance, these results suggests it could actually be helpful to have an increased steam pressure/temperature in the autoclave. However, this is likely not going to be the case. The reason is that plants are likely already operating near the minimum possible oxygen partial pressure required for the leaching reactions to be independent of the oxygen partial pressure. Thus, an increase in steam pressure may actually push the oxygen partial pressure below its minimum acceptable level.

One important area of future work for modeling the gas phase is getting accurate estimations of steam pressure under autoclave slurry compositions. This work assumed that water behaved as pure water. Saturation pressures of water are likely lower for the highly ionic solutions found in the CLP. This would lead to higher oxygen efficiencies for a given temperature and oxygen partial pressure than shown on the above graphs (the water effectively behaves as though it were at a lower temperature). One should thus take the graphs presented in this works as conservative estimations of oxygen efficiency.

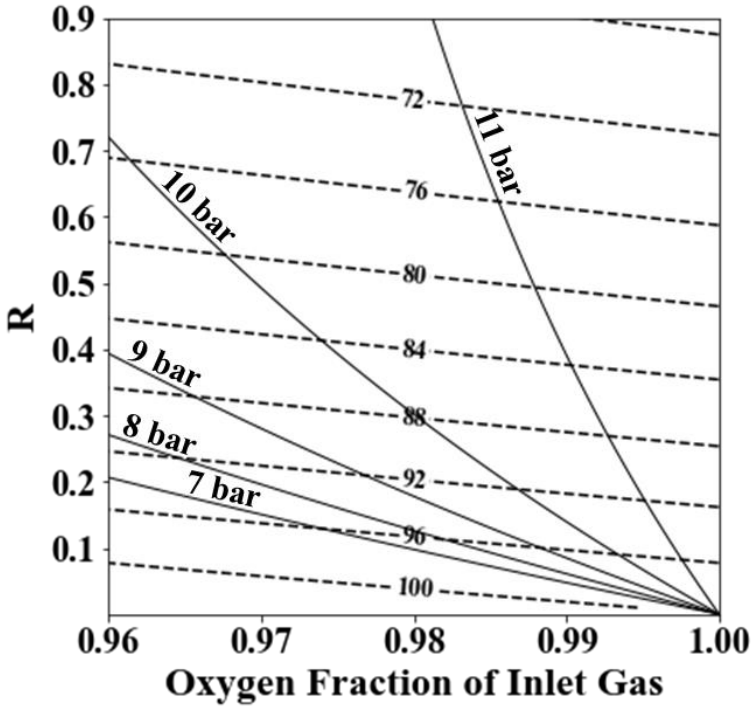

Figure 7.7 - Contour plot of partial pressure of oxygen (solid) and oxygen efficiency (dashed) as a function of the injected gas oxygen grade and offgassing ratio, R. Plot for total pressure of 21.7 bar and saturation pressure of steam at 180 ℃, 10.03 bar

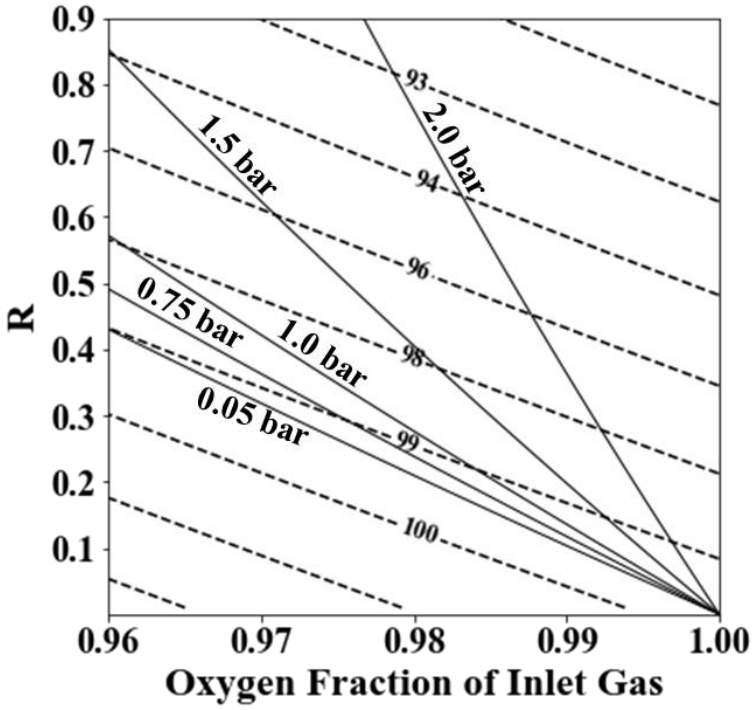

Figure 7.8 - Contour plot of partial pressure of oxygen (solid) and oxygen efficiency (dashed) as a function of the injected gas oxygen grade and offgassing ratio, R. Plot for total pressure of 21.7 bar and saturation pressure of steam at 210 ℃, 19.08 bar

C.3.3 Total Pressure 19.7 And 23.7 Bar Absolute, 200℃ H_2O At Saturation

These two cases explore the effect of changing total pressure while keeping the temperature/steam pressure the same. As the total pressure increases, the partial pressure of oxygen increases and the oxygen efficiency decreases, for any set of R and $Y_{O_2,in}$. The partial pressure of oxygen increases because the total pressure of the vessel increases while the partial pressure of steam remains the same, giving more partial pressure to be occupied by oxygen and nitrogen. The oxygen efficiency decreases because the higher partial pressure of oxygen leads to more oxygen being offgassed for the same amount of oxygen consumed by reaction.

Regarding only the temperature of the operation and total pressure, it appears the best strategy for maximizing oxygen efficiency is keeping the partial pressure of oxygen at the lowest level possible to keep the leaching reaction rates independent of the oxygen partial pressure. This can be done by minimizing the total pressure for the given operating temperature. An operating may experience additional cost reduction by minimizing the temperature too. As temperature is decreased, the total pressure will need to correspondingly be decreased to maintain the minimum

oxygen partial pressure. However, the operation may see reduced costs associated with the mechanical issues inherent in a high pressure operation, as the total pressure has decreased.

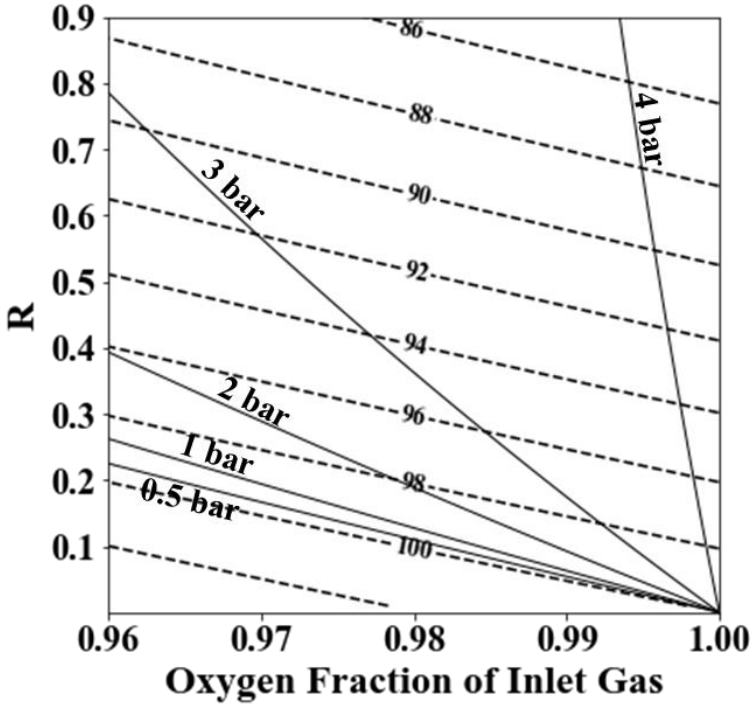

Figure 7.9 - Contour plot of partial pressure of oxygen (solid) and oxygen efficiency (dashed) as a function of the injected gas oxygen grade and offgassing ratio, R. Plot for total pressure of 19.7 bar and saturation pressure of steam at 200 ℃, 15.55 bar

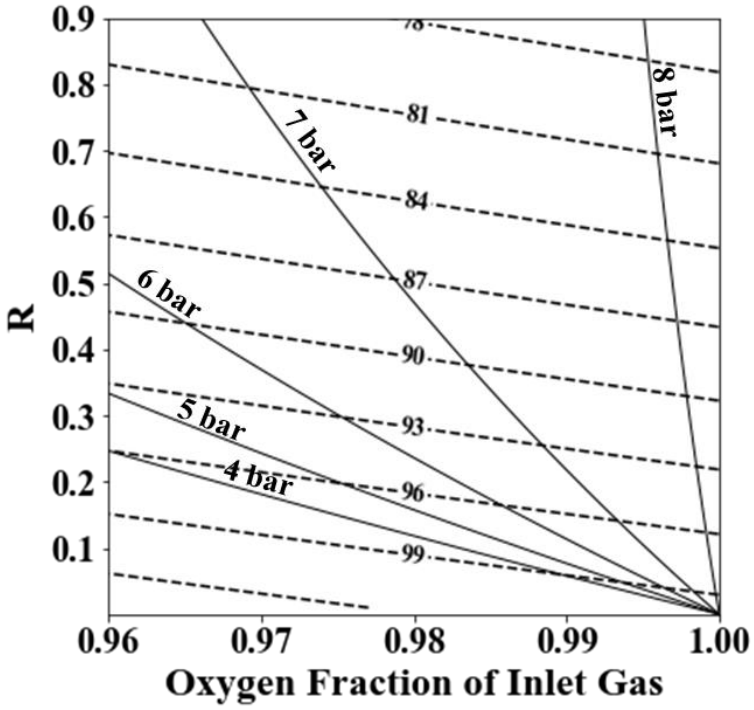

Figure 7.10 - Contour plot of partial pressure of oxygen (solid) and oxygen efficiency (dashed) as a function of the injected gas oxygen grade and offgassing ratio, R. Plot for total pressure of 23.7 bar and saturation pressure of steam at 200 °C, 15.55 bar

APPENDIX D. DERIVATION OF THE TOTAL NUMBER OF PARTICLES PER SLURRY VOLUME

Characterization of slurry typically consists of volume fraction of solids, and of those solids, the weight fractions of each solid species. Additionally, particle size fractions can be obtained *via* sieving or other methods. The question is thus how to calculate the number of particles per slurry volume for each solid species given these three pieces of information. Additionally, it is assumed that all particles are only comprised of one chemical species. First, the definition of the particle size distribution is:

$$\psi_j = N_j \Psi_j \tag{D. 1}$$

Ψ_j is the particle size fraction (PSF) for solid "j", i.e., the PSD normalized to one. Next, the third moment of "j" and volume fraction of "j" are related; for spherical particles:

$$g_j = \frac{\pi}{6} \int_0^{D_{max}} D_j^3 \, \psi_j dD = \frac{\pi N_j}{6} \int_0^{D_{max}} D_j^3 \, \Psi_j dD \implies N_j = \frac{6 g_j}{\pi \int_0^{D_{max}} D_j^3 \, \Psi_j dD} \tag{D. 2}$$

g_j is the volume fraction of "j" in the slurry. It is found according to:

$$g_j = g \frac{X_j v_j}{\sum_i X_i v_i} \tag{D. 3}$$

g is net volume fraction of solids in the slurry, X_j is the weight fraction of "j" in the slurry, v_j is specific volume of "j", and "i" spans all slurry solid species including "j". Equation D.3 is just the total volume fraction of solids times the volume fraction of each species only considering the solids. Now, A3 can be plugged into A2 and N_j solved.

APPENDIX E. TRANSFORMATION OF PARTICLE MASS FRACTION TO PARTICLE SIZE FRACTION

Characterization of the distribution of particle size in a concentrate or concentrate slurry is typically done on a mass, rather than number basis. However, the combined population balance and moment method technique requires a particle size distribution. This necessitates the conversion of interpolated particle mass fraction distributions to particle size fraction distributions. The PSFDs can then be converted to PSDs *via* the method in Appendix D.

The derivation is really just an example of the fundamental theorem of calculus. The first step is writing out the mass of particles in an arbitrarily sized bin; for spherical particles:

$$\frac{\rho_{mass}\pi N}{6}\int_{D}^{D+\Delta D} D^3\Psi dD = M\int_{D}^{D+\Delta D} W dD \tag{E. 1}$$

ρ_{mass} is the mass density of the solid and M is the total mass of particles per volume. Integrating B1, dividing by ΔD, and taking the limit as ΔD goes to zero gives:

$$\begin{gathered}\frac{\rho_{mass}\pi N}{6}[F(D+\Delta D)-F(D)] = M[G(D+\Delta D)-G(D)] \implies \\ \frac{\rho_{mass}\pi N}{6}\lim_{\Delta D\to 0}\left[\frac{F(D+\Delta D)-F(D)}{\Delta D}\right] = M\lim_{\Delta D\to 0}\left[\frac{G(D+\Delta D)-G(D)}{\Delta D}\right] \implies \\ \frac{\rho_{mass}\pi N}{6}D^3\Psi = MW\end{gathered} \tag{E. 2}$$

All that's left is simple rearrangement of B2:

$$\Psi = \frac{CW}{D^3} \tag{E. 3}$$

where C is the normalization constant, found according to:

$$C = \frac{1}{\int_0^{D_{max}} \frac{W}{D^3}\, dD} \tag{B4}$$

Ψ can now be used with methods of Appendix A to develop the expression for ψ.

APPENDIX F. APPLICATION OF THE CORRESPONDANCE PRINCIPLE FOR CALCULATION OF AQUEOUS SPECIES PROPERTIES AT ELEVATED TEMPERATURE

The correspondence principle [100,101] states that for a given type of aqueous ion (*e.g.* single-atom cations), the entropy at some arbitrary temperature is a linear function of the entropy at a reference temperature:

$$s_{i,T} = A + B s_{i,T_{Ref},abs} \quad (F.1)$$

$$s_{i,T_{Ref},abs} = s_{i,T_{Ref}} - 20.935 Z_i \quad (F.2)$$

where "i" denotes some ionic species (*e.g.* Cu^{2+}), *T* is the arbitrary temperature in question, *A* and *B* are constants, and T_{Ref} is the reference temperature; *A* has units of J/mol-K and *B* is unitless. $s_{i,T_{Ref},abs}$ is the absolute specific entropy at the reference temperature, $s_{i,T_{Ref}}$ is the conventional ionic entropy, and is the ionic charge on "i". For example, cupric ion has an entropy of -99.6 J/mol-K at 25 °C. Criss and Cobble [100] give *A* and *B* values for the simple cations, at 200 °C, of 97.6 and 0.711 respectively. Thus, the calculated value of the entropy of the cupric ion at 200 °C is 26.7 J/mol-K.

Specific enthalpy of aqueous ions at elevated temperature is also desired. The intimate relationship between heat capacity and entropy ultimately be used to derive an expression for enthalpy at elevated temperature using the correspondence principle. First, the average heat capacity from a reference temperature to an arbitrary temperature is written in the form of eqn. F3

$$\overline{c_{p,i,T}} = \alpha + \beta c_{p,i,T_{Ref}} , \quad (F.3)$$

where α and β are constants; please see Criss and Cobble's work [101] for a detailed derivation of eqn. F3. With the average heat capacity known over the temperature range of interest, specific enthalpy is found according to:

$$h_T = h_{T_{ref}} + T\overline{c_{p,i,T}} \quad (F.4)$$